Ultrafast Photochemical Dynamics of Azobenzenes Affected by Intra- and Intermolecular Interactions and of a Proton Transfer Switch

Dissertation

zur Erlangung des Doktorgrades

der Mathematisch-Naturwissenschaftlichen Fakultät

der Christian-Albrechts-Universität zu Kiel

vorgelegt von

Julia Bahrenburg

Kiel 2014

Erster Gutachter: Prof. Dr. Friedrich Temps
Zweiter Gutachter: Prof. Dr. Bernd Hartke

Tag der mündlichen Prüfung: 15. Juli 2014
Zum Druck genehmigt: 15. Juli 2014

gez. Prof. Dr. Wolfgang J. Duschl, Dekan

ERKLÄRUNG

Hiermit erkläre ich, dass die vorliegende Abhandlung - abgesehen von der Beratung durch meinen Betreuer Prof. Dr. Friedrich Temps - nach Inhalt und Form meine eigene Arbeit ist. Diese Arbeit hat weder in Auszügen noch in ganzer Form einer anderen Stelle im Rahmen eines Prüfungsverfahrens vorgelegen. Sie wurde in ihrer Gesamtheit nicht veröffentlicht und auch nicht zur Veröffentlichung eingereicht. Teile dieser Arbeit wurden in fachwissenschaftlichen Zeitschriften veröffentlicht oder zur Veröffentlichung eingereicht. Dies bezieht sich auf die folgenden Kapitel:

Kapitel 3
J. Bahrenburg, K. Röttger, R. Siewertsen, F. Renth, F. Temps, Sequential photoisomerisation dynamics of the push-pull azobenzene Disperse Red 1, *Photochem. Photobiol. Sci.* **2012**, *11*, 1210-1219.

Kapitel 4
J. Bahrenburg, F. Renth, F. Temps, F. Plamper, W. Richtering, Femtosecond spectroscopy reveals huge differences in the photoisomerisation dynamics between azobenzenes linked to polymers and azobenzenes in solution, *Phys. Chem. Chem. Phys.*, **2014**, *16*, 11549-11554.

Kapitel 5
J. Bahrenburg, C. M. Sievers, J. B. Schönborn, B. Hartke, F. Renth, F. Temps, C. Näther, F. D. Sönnichsen, Photochemical properties of multi-azobenzene compounds, *Photochem. Photobiol. Sci.* **2013**, *12*, 511-518.

Kapitel 6
J. Bahrenburg, F. Temps, A Femtosecond Time-Resolved Transient Absorption Anisotropy Study of Electronic Coupling in Multi-Azobenzene Photoswitches, *J. Phys. Chem. A*, eingereicht.

Kapitel 8
J. Bahrenburg, M. F. Rode, A. L. Sobolewski, F. Temps, Ultrafast Dynamics of a Bistable Intramolecular Proton Transfer Switch, *Ultrafast Phenomena XIX* **2014**.

Die Arbeit ist unter Einhaltung der Regeln guter wissenschaftlicher Praxis der Deutschen Forschungsgemeinschaft entstanden.

Kiel, im Juni 2014

Julia Bahrenburg

ABSTRACT

The main goal of this Thesis was the investigation of the photochemical properties and ultrafast isomerization dynamics of several azobenzene (AB) derivatives under the influence of different intra- and intermolecular effects by means of femtosecond time-resolved absorption and fluorescence spectroscopy. The influence of electron donating and accepting substituents on the electronic relaxation was investigated for the *push-pull* AB Disperse Red 1 (DR1). The data clearly suggest a stepwise isomerization *via* an intermediate state. The dynamics of DR1 and the bifunctional AB 4,4′-bis(acetamido)-azobenzene (BAAB) were also investigated with the chromophores covalently attached to the side chain or into the main chain of tightly cross-linked polymer colloids, respectively. Due to the strong intermolecular mechanical forces acting on the photoexcited ABs, the excited state lifetimes in the polymeric micronetworks were found to be dramatically longer compared to the lifetimes in solution. The observed effects were more pronounced for the AB in the main chain of the polymer. A systematic study on possible intramolecular interactions between chromophores was performed for the multi-azobenzene compounds bis[4-(phenylazo)phenyl]amine (BPAPA) and tris[4-(phenylazo)phenyl]amine (TPAPA). Transient absorption anisotropy decay measurements allowed to obtain insight into intramolecular chromophore-chromophore interactions on the time scale of several tens of femtoseconds. The data provide clear evidence for strong electronic coupling between the two and three AB units. Previous studies on a magnetically bistable nickel porphyrin functionalized with an azopyridine as photoswitchable unit have shown that the $E \rightleftarrows Z$ isomerization of the AB can lead to the coordination and decoordination of the pyridine nitrogen towards the Ni ion, respectively, resulting in spin switch from the diamagnetic to the paramagnetic state. To obtain insight into the isomerization mechanism of the AB moiety and the possible switch of the spin state a systematic study on the ultrafast dynamics of this system and its building blocks, the Ni(II)-porphyrin and the metal free porphyrin, was performed. The data of the metal free and the metal porphyrin were found to be virtually identical compared to previous studies on related porphyrin derivatives. Due to strong, heavily overlapped and very long-lived absorption bands of the porphyrin itself it was nearly impossible to observe any switching processes. A further goal of this Thesis was the investigation of the bistable excited state intramolecular proton transfer (ESIPT) switch N-(3-pyridinyl)-2-pyridinecarboxamide (NPPCA). The interpretation of the data was supported by ab initio excited state calculations of A. Sobolewski *et al*. The data clearly suggest a stepwise formation of the desired proton transfer product *via* two intermediate states in the aprotic solvent acetonitrile.

ZUSAMMENFASSUNG

Das Hauptziel dieser Arbeit lag in der Untersuchung der photochemischen Eigenschaften und der ultraschnellen Dynamik von Azobenzol (AB)-Derivaten unter dem Einfluss verschiedener intra- und intermolekularer Effekte mittels Femtosekunden-zeitaufgelöster Absorptions- und Fluoreszenzspektroskopie. Der Einfluss elektronenziehender und -schiebender Substituenten auf die elektronische Desaktivierung wurde für das *push-pull* AB Dispersrot 1 (DR1) untersucht. Die Daten weisen eindeutig auf eine stufenweise Isomerisierung über einen Zwischenzustand hin. Außerdem wurde die Dynamik von DR1 und dem bifunktionalen AB 4,4'-Bis-(acetamido)azobenzol (BAAB) in der Seiten- bzw. Hauptkette von stark vernetzten Polymerkolloiden untersucht. Die starken intermolekularen Kräfte, die auf das AB wirken, führen zu einer deutlichen Verlängerung der Lebenszeiten des angeregten Zustands in den polymeren Mikronetzwerken im Vergleich zu den Lebenszeiten in Lösung. Die Effekte für das AB in der Hauptkette waren dabei ausgeprägter. Mögliche intramolekulare Wechselwirkungen wurden in einer systematischen Studie an den Multi-Azobenzol Komponenten Bis[4-(phenylazo)phenyl]amin (BPAPA) und Tris[4-(phenylazo)phenyl]amin (TPAPA) untersucht. Transiente Absorptionsanisotropiemessungen ermöglichten dabei einen Einblick in intramolekulare Chromophor-Chromophor-Wechselwirkungen auf der Femtosekunden-Zeitskala. Die erhaltenden Daten geben deutliche Hinweise auf starke elektronische Kopplung zwischen den zwei bzw. drei Azobenzoleinheiten. Vorherige Studien an einem magnetisch bistabilen Nickelporphyrin, das mit einem Azopyridin als photoschaltbarer Einheit funktionalisiert ist, haben gezeigt, dass die $E \rightleftarrows Z$ Isomerisierung des ABs zu einer Koordination bzw. Dekoordination des Pyridinstickstoffs an dem Ni-Ion und somit zu einem Schalten des Spinzustands von diamagnetisch zu paramagnetisch führen kann. Um einen Einblick in den Isomerisierungsmechanismus und die mögliche Änderung des Spinzustands zu erhalten, wurde die ultraschnelle Dynamik des Systems und die der einzelnen Bausteine untersucht. Die Daten des entsprechenden Ni-Porphyrins und des metallfreien Porphyrins wurden auf der Basis von vorherigen Studien an ähnlichen Derivaten interpretiert. Wegen der stark überlagernden und langlebigen Absorptionsbanden des Porphyrins, war es nicht möglich irgendeinen Schaltvorgang zu beobachten. Ein weiteres Ziel dieser Arbeit war die Untersuchung des bistabilen Protonentransferschalters N-(3-Pyridinyl)-2-pyridincarboxamid (NPPCA), der auf dem ESIPT (excited state intramolecular proton transfer)-Prinzip basiert. Die Interpretation der Daten wurde durch quantenchemische ab initio Rechnungen von A. Sobolewski *et al.* gestützt. Die Ergebnisse weisen deutlich auf die stufenweise Bildung des gewünschten Protonentransferprodukt über zwei Zwischenzustände in dem aprotischen Lösungsmittel Acetonitril hin.

CONTENTS

Part I

INTRODUCTION AND EXPERIMENTAL SECTION

1 INTRODUCTION

The application potential of photochromic molecular switches in natural and artificial systems seems to be endless. Switching is the fundamental process in digital data processing as well as in the operation of engines, sensors or actuators. At the same time, modern technology pursues the aim to minimize and improve electronic and mechanic devices. Today several technical macroscopic functions are based on small artificial molecular switching units embedded in a well defined environment. Often the functions are inspired by nature, where complex biochemical molecular machines form the basis of life. Depending on the necessary requirements for the respective application and the properties of the switchable element, photochromic molecules have been already used in, e.g., light-driven molecular machines,[1–6] optical data storage,[7–11] liquid crystal displays (LCDs)[12,13] and organic light-emitting diodes (OLEDs),[14,15] in biological and medical systems[16–23] and in light sensitive materials for protection against ultraviolet (UV)-A and UV-B components of sunlight.[24,25]

Photochromic molecular switches[5,26] can exist in at least two states, which can be reversibly converted into each other by irradiation with UV or visible (VIS) light due to different UV/VIS absorption spectra. Additionally, the isomerization can induce changes in geometry and shape, in the dipole moment, in conductivity, in the magnetic state or in the acidity of the molecule. Typically one isomer is the thermodynamically stable one and the thermal lifetime of the other depends strongly on the respective system and the surrounding. Light-induced isomerization reactions are generally known to be ultrafast on a femto- to picosecond time scale, especially when intersystem crossing (ISC) is not involved and the reactions obey spin conservation.[27,28] A good photoswitch features low photochemical fatigue, usually a high thermal stability of both isomers, high switching efficiencies and high isomerization quantum yields in both directions. Switches with ultrashort excited state lifetimes and therefore an ultrafast formation of the desired product often reveal better switching efficiencies and higher quantum yields compared to systems with longer excited state lifetimes.[28–30] This can be rationalized with the increasing probability for unwanted side reactions with increasing excited state lifetime. Well known classes of photoswitches are azobenzenes (ABs),[7,29,31–34] fulgides,[28,35–38] spiropyranes,[39,40] diarylethenes,[41,42] and so called proton transfer switches (cf. Figs. 1.1 a) - e).[43–45] The exceptional photochemical properties, the molecular dynamics and possible applications of theses switches have been investigated extensively in the last decades.[5,7,27,28,39,41,46–51]

An example for the application potential of AB was recently shown by Venkataramani *et al.*[23] A nickel porphyrin based system with a covalently attached azopyridine as photoswitchable unit shows magnetic bista-

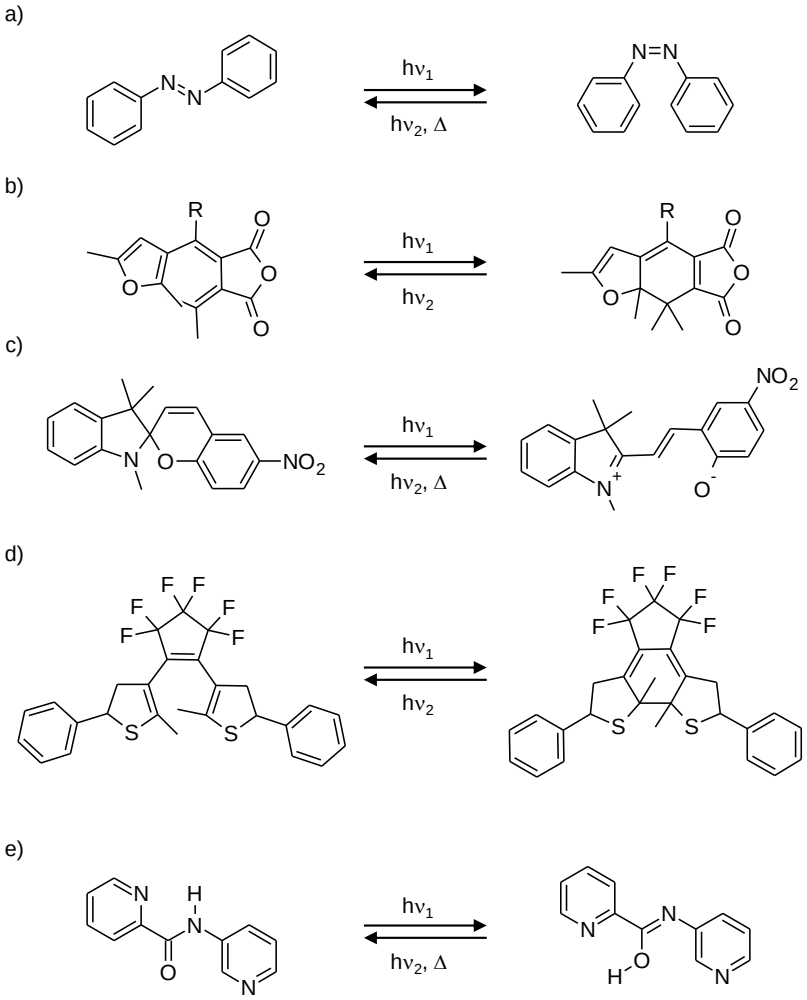

Figure 1.1: Selected photochromic switches and their photo-induced and thermal reactions: a) azobenzenes, b) fulgides, c) spiropyranes, d) diarylethenes and e) an example of a proton transfer switch.

bility in solution at room temperature, a property which was previously restricted to solid bulk materials and to very low temperatures. The Ni(II)-complex in its diamagnetic low-spin and its paramagnetic high-spin state, respectively, is given in Fig. 1.2. The isomerization and change of spin can be reversibly switched back and forth with light at two different wavelengths in the visible range of $\lambda = 500$ nm and $\lambda = 420$ nm. Additionally, the reaction shows no photochemical fatigue. These unique properties are very promising for the application of systems like this as contrast agent in dynamic magnetic resonance imaging (MRI) in vivo.[23]

Fulgide based materials appear to be promising as recording units in optical memory.[9,10] Chen *et al.* developed a dual-wavelength memory device with two different fulgide derivatives embedded in a polymethylmethacrylate (PMMA) matrix, which allows for repeatable parallel recording. The fulgides show different absorption spectra in the visible wavelength region. Figs. 1.3 a) and b) show the clear readout with a 488 nm and a 633 nm laser beam, respectively, after UV irradiation of the sample.

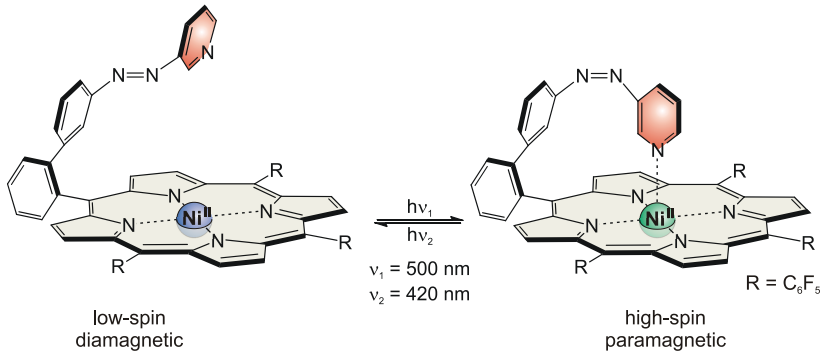

Figure 1.2: Light-induced spin switch in an azopyridine functionalized Ni-porphyrin. The *E*-*Z* and *Z*-*E* isomerization of the AB can lead to coordination and decoordination of the pyridine moiety and is induced with 500 nm and 420 nm, respectively.

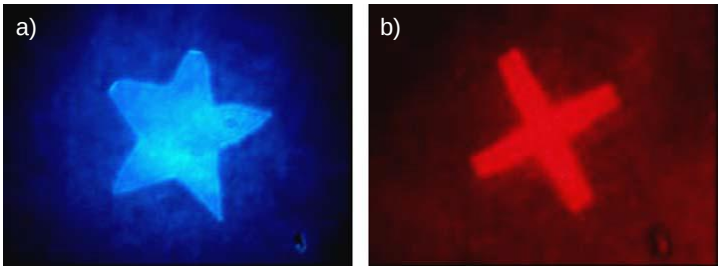

Figure 1.3: Parallel recording with a dual-memory fulgide based PMMA film. The measurements were done at the same position on the film after UV irradiation. First, the blue star was recorded by focusing 488 nm on the sample. The red cross was read out afterwards using a 633 nm laser. Reprinted from Chen, Y.; Xiao, J. P.; Yao, B.; Fan, M. G., Dual-wavelength photochromic fulgides for parallel recording memory, *Opt. Mater.* **2006**, *28*, 1068-1071. Copyright 2006, with permission from Elsevier.

The catalytic generation of chemoluminescence and the photo-induced electrocatalyzed reduction of H_2O_2 using a photoisomerizable spiropyrane functionalized monolayer in the presence of negatively charged Pt nanoparticles as catalysts was developed by Niazov *et al.* and is schematically depicted in Fig. 1.4.[52] UV irradiation induces the isomerization from the closed to the open form of the photoswitch. The protonated positively charged open form leads to a monolayer, which attracts the negatively charged Pt nanoparticles. These modified nanoparticle electrodes catalyze the reduction of H_2O_2. Irradiation of the open form with visible light induces the ring closing reaction and therefore the detachment of the Pt nanoparticles, which are then catalytically inactive. This kind of photoswitchable functionalized surfaces in combination with electrodes might be interesting regarding information storage and processing. Here, the reduction of H_2O_2 and / or the generation of chemoluminescence can be used as selective readout signals.

A fascinating application of a diarylethene derivative was shown by the group of N. R. Branda, who embedded a photoresponsive fluorescent di-

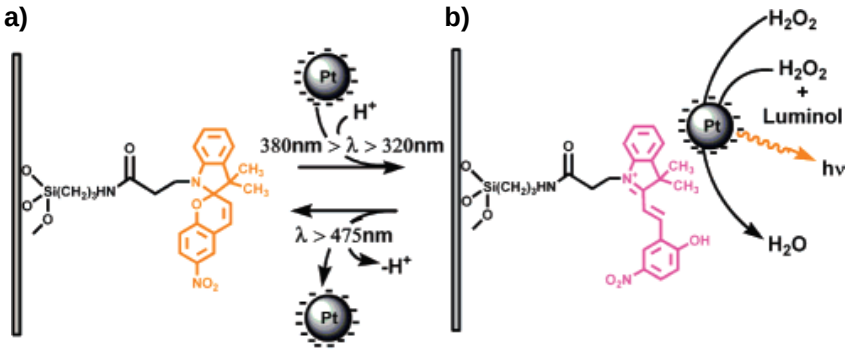

Figure 1.4: Photoswitchable electrocatalyzed reduction of H_2O_2 and the photoswitchable catalytic generation of chemoluminescence in the presence of negatively charged Pt nanoparticles. The closed form of the switch is catalytically inactive (a), whereas the light-induced ring opening reaction is accompanied by the protonation of the open isomer leading to a positively charged monolayer, which is attractive towards the negatively charged Pt nanoparticles (b). This subsequently formed electrode is able to catalyze the H_2O_2 reduction. Adapted with permission from Niazov, T.; Shlyahovsky, B.; Willner, I. *J. Am. Chem. Soc.* **2007**, *129*, 6374-6375. Copyright 2007, American Chemical Society.

thienylethene into the nervous system of a living worm (Caenorhabditis elegans) by feeding the organisms with the ring-open or the closed form of the molecule, respectively. The open form does not influence the mobility of the worm, whereas the closed form leads to immobilization and paralysis. Light exposure with two different wavelengths can trigger the isomerization of the molecules and therefore the condition of the worm back and forth. The state of the switch could be monitored using fluorescence microscopy, which is shown in Fig. 1.5. This type of control of the

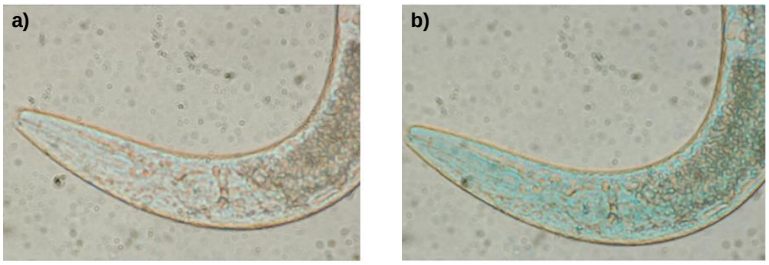

Figure 1.5: Fluorescence microscopy images of the worm (Caenorhabditis elegans) incubated with (a) the colorless open form and (b) the colored closed form of the diarylethene derivative. Switching between the open and the closed form was achieved with UV light at 365 nm and with wavelengths above 490 nm, respectively. Adapted with permission from Al-Atar, U.; Fernandes, R.; Johnsen, B.; Baillie, D.; Branda, N. R. *J. Am. Chem. Soc.* **2009**, *125*, 15966-15967. Copyright 2009, American Chemical Society.

functionality of the nervous system could be a milestone regarding medical applications and therapies.[21]

Proton transfer switches are widely spread in numerous fields and known as highly efficient UV absorbers, which are for example used for the pro-

tection of photodegradable outdoor materials, e.g., wood or plastic against sunlight. Typically, these molecules are dispersed in polymeric coatings for the most applications.[25]

The above mentioned examples represent just a small selection to get an impression of the versatility of molecular photoswitches and their possible applications. It is obvious that for most practical applications the chromophores are embedded in complex environments that may impose specific topographical constraints. The close proximity of the chromophores might additionally lead to cooperative phenomena competing with the desired photoisomerization. Possible intra- and intermolecular effects, which have to be considered in such a complex surrounding, are schematically depicted in Fig. 1.6: Thus, for example, matrix effects like interactions be-

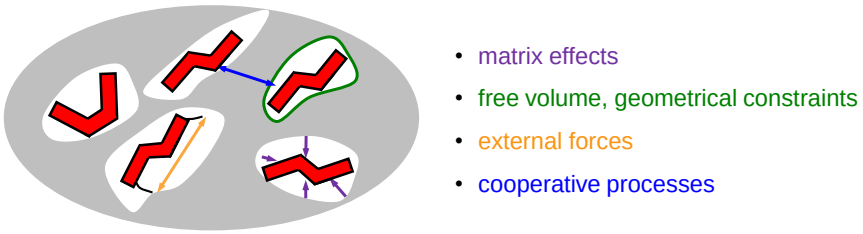

Figure 1.6: Schematic representation of possible effects which act on molecular photoswitches in a complex environment (violet: matrix effects, green: geometrical constraints, orange: external forces, blue: cooperative effects).

tween molecule and matrix can occur. The free volume can be reduced so that there are geometrical constraints affecting the desired reaction. The isomerization can be also influenced by external mechanically pushing and / or pulling forces. If the chromophore density is high enough cooperative processes, e.g., excitonic coupling or charge-transfer (CT) between switches or other surrounding molecules will become possible. Regarding nearly all applications, it is mandatory to design and investigate molecular switches with exceptional properties also in complex environments and not only in solution or in the gas phase, where the molecules are isolated from each other and not exposed to any forces or constraints. A major part of this Thesis therefore constituted the investigation of the photochemical properties and the ultrafast photoisomerization dynamics of several azobenzene derivatives under the influence of the above mentioned intra- and intermolecular effects. For these studies AB derivatives were chosen as molecular photoswitches because of the comparatively simple reaction and their well known switching behaviors[29,32,33,53–66] and the underlying ultrafast dynamics in solution.[30,31,33,34,58,67–75,75–84] Both have been investigated extensively in the last two decades. The following Section 1.1 gives an overview of the photochemical properties and the ultrafast dynamics of AB-based molecular switches in solution and in more complex surroundings. Complex environments are, for example, polymer materials,[46,83,85–96] dendrones and dendrimers[97–102] or surfaces.[103–109] There are also numerous theoretical studies on the isomerization and the dynam-

ics in the involved excited state and the electronic ground state.[110–133] The molecular dynamics have so far been investigated in solution and in the gas phase, although the ultrafast excited state lifetimes and the subsequent isomerization to the electronic ground state could be strongly affected by the surrounding matrix. In this Thesis I will present results to close that gap.

1.1 AZOBENZENES AS MOLECULAR PHOTOSWITCHES

The reversible photo-induced $E \rightleftarrows Z$ isomerization of AB and its derivatives is a well known simple unimolecular reaction. The molecular structures of the two isomers are given in Fig. 1.7. Upon UV irradiation the thermody-

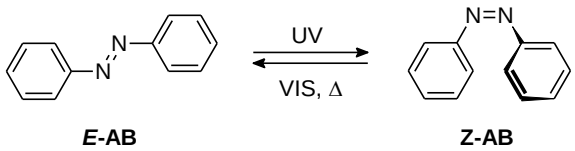

Figure 1.7: UV photo-induced *E*-*Z* isomerization of AB. The *Z*-*E* back-isomerization can be light-induced (VIS) or thermal (Δ).

namically favored, more rod-like *E* isomer transforms to the energetically higher, more compact *Z* isomer. Calculations have shown that the energy of the *E* isomer in the electronic ground state is 0.6 eV lower than the energy of the *Z* isomer[134] and that the isomers are separated by an energy barrier of $\approx$ 1.7 eV.[112,115,134] The back-reaction can be photo-induced with visible light or thermal. The isomerization induces not only large changes in the length from $\approx$ 9Å for the *E* isomer to $\approx$ 6Å for the *Z* isomer but also in the dipole moment. The planar, symmetric *E* isomer has nearly no dipole moment ($\mu \approx 0$ D), whereas the dipole moment of the non-planar *Z* isomer was calculated to be $\mu \approx 3$ D.[135] Furthermore, the chromophore features an extraordinary high photostability and an ultralow photochemical fatigue. All these properties lead to the high application potential of AB as photoswitchable element. The static UV/VIS absorption spectra for each isomer are given in Fig. 1.8.[136] The spectra of both isomers are dominated by a strong $\pi\pi^*$ absorption band at $\lambda \approx 325$ nm and at $\lambda \approx 275$ nm for the *E* and the *Z* isomer, respectively. The weak absorption bands in the visible at $\approx$ 450 nm belong to the respective $n\pi^*$ transition. In the case of the *Z* isomer the intensities of the S_1 and the S_2 are increased and decreased, respectively, compared to these for the *E* isomer. The higher oscillator strength for the nominally symmetry-forbidden $n\pi^*$ transition of *Z*-AB is attributed to the lower symmetry of the molecule (C_{2h} *vs.* C_2[115,118]). Irradiation in the $\pi\pi^*$ absorption band of *E*-AB induces the isomerization to the *Z* isomer. The back-reaction can be achieved by excitation into the $n\pi^*$ band of *Z*-AB. Depending on the substitution of the AB core the absorption bands can exhibit pronounced shifts. The $n\pi^*$ state is typically little affected, whereas the $\pi\pi^*$ transition can be strongly shifted. The thermal lifetime of the *Z* isomer also depends strongly on the

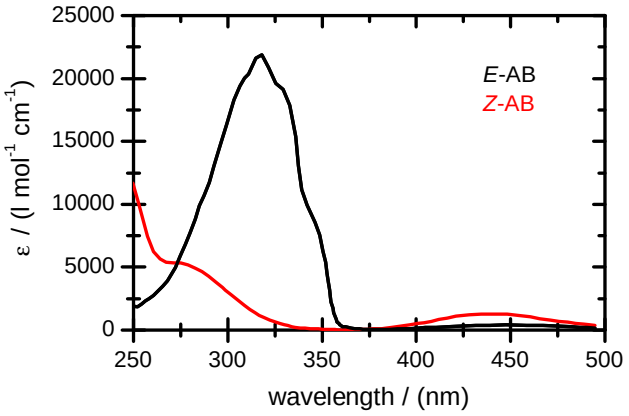

Figure 1.8: Static UV/VIS absorption spectra of *E*- and *Z*-AB in *n*-hexane as solvent.[136]

substitution of the AB.[57] *Push-pull* azobenzenes, for example, are substituted with an electron donating and an electron withdrawing group. This substitution induces a strong CT character in the $\pi\pi^*$ transition leading to a pronounced solvent-dependent red-shift of the respective absorption band.[34,79] At the same time the energy barrier between the two isomers in the electronic ground state is dramatically lowered, therefore the thermal back-isomerization occurs within milliseconds or seconds and is much faster than in plain AB, which has a thermal lifetime of several hours.[56,137]

For applications requiring a large change in the geometry and in the dipole moment of the molecule, AB is typically the first choice. Consequentially, a large a number of azobenzene-based applications have been reported. The above mentioned magnetically bistable azo-functionalized Ni-porphyrin[23] is only one of countless examples. ABs have been used in biochemical and biological systems,[17–20,22,102,138–144] e.g., for the light-induced switching of cell adhesion by reversible changing of the orientation of AB-functionalized peptides[19] or for photocontrol of protein conformation in vivo.[22] The unique properties of AB also have been used for optical data storage or in other optical devices or technical functions and materials.[3,7,8,11,13,15,32,51,145–152] Recently, Sobolewska *et al.* developed a new single-component AB-based liquid crystal with promising properties for application in holographic optical memory devices to allow for ultrahigh density optical data storage.[152] A ternary memory device with an AB derivative as active unit was designed by Li *et al.*[11] Despite the high application potential of AB, there are also disadvantages in comparison with other switches.[28–30,36–38] The absorption bands in the static UV/VIS absorption spectra are not clearly separated for each isomer, therefore quantitative switching is difficult and the isomerization quantum yields are not very high ($\phi_{E\rightarrow Z} \leqslant 0.2$ and $\phi_{Z\rightarrow E} \leqslant 0.6$) and strongly depend on the solvent.[33,55] For most AB derivatives the *E*-*Z* isomerization is induced with UV light, which could lead to photodegradation of linked moieties

or the surrounding matrix. Additionally, the thermal lifetime of *Z*-AB is relatively short compared to other photoswitches.

Azobenzene derivatives have been investigated in complex polymeric environments, with the focus being on the photochemical properties of the photoswitch as well as on the photochromic properties of the polymer.[46,83,85,87–96,153–167] Detailed reviews about the photochemistry of AB-containing coiled, branched or cross-linked polymers in the colloidal or solid state and about the light-induced motions of chromophores and polymer chains in AB polymers were given by Kumar *et al.* and Natansohn *et al.*[46,85] A detailed report on stable polymeric AB materials for the application in nonlinear optics was given by Yesodha *et al.*[157] Some selected examples of AB-functionalized polymeric materials will be given in the following.

Thermosensitve poly(N-isopropylacrylamide) (PNIPAM) cross-linked gels with a bifunctional AB derivative in the polymer main-chain were investigated regarding the swelling behavior and the volume phase transition temperature. In water, the transition temperature of the AB-functionalized polymer shifts to lower temperatures compared to PNIPAM gels without ABs because of the different interactions between solvent and the respective polymer network. Microgels with higher AB concentration and therefore higher cross-linking ratio show a lower degree of swelling and a tighter polymer network. Irradiation with UV light induces the *E*-*Z* isomerization of the ABs and leads to the expulsion of water from the swollen polymeric micronetworks. This behavior was assigned to the entropic changes in the network upon irradiation.[155] A superabsorbent hydrogel with a hydrophilic core and a cross-linked AB-functionalized shell was developed by Mudiyanselage *et al.*[160] The system shows excellent water absorption with the AB units being in their *E* form. Light-induced *E*-*Z* isomerization leads to a contraction of the polymeric network and therefore to an expulsion of the water molecules inside the polymer. Molecular force spectroscopy was used to investigate a polymer-like polypeptide functionalized with AB groups. Switching of the ABs enables a selective change in the length of the polymeric backbone.[87] The isomerization of AB in side chain functionalized polymers can lead to significant changes in the surface activity and viscoelasticity compared to non-AB-functionalized systems in aqueous solution. At low polymer concentrations most of the polymer molecules are monomeric, whereas at higher concentrations (> 0.1 wt%) oligomeric aggregates are formed, which additionally influence the surface activity and solubilization properties of the surrounding aqueous solution. At concentrations above 15 wt% the viscosity is strongly increased indicating the formation of a tight infinite gel network. The structure of these networks can be reversibly changed and rearranged by the light-induced $E \rightleftarrows Z$ isomerization of the ABs resulting in a dramatic change in the viscosity.[163] Non-linear optical thin polymer films with *push-pull* ABs as side chains showing very high second- and third-order non-linear optical parameters were developed and investigated by El Ouazzani *et al.* The observed effects strongly depend on the

structure and the different CT within the molecules of the respective system.[165] Thin polymer films were also investigated by Pakula *et al*. The aim of these studies was to realize high-load PMMA films with AB contents up to 60 wt%. ABs with long branched alkane side chains were found to be promising candidates. Contrary to expectation, the photoisomerization remains fully reversible and nearly unaffected, despite the very close proximity of the chromophores.[166]

Azobenzene switches have also been investigated in multi-chromophoric systems containing at least two AB moieties.[63–65,97–102,161,168–173] A detailed review about AB derivatives in dendrimers and dendrons regarding the photochemical and photophysical properties as well as possible applications was given by Deloncle *et al*.[100] Selected examples will be presented in the following paragraph.

The photochemical properties of linear molecules consisting of two ABs, which were more or less electronically conjugated due to different dihedral angles between the AB units, were investigated experimentally and theoretically. As expected, a larger dihedral angle led to more individual AB units.[63] Another bis-AB derivative with two AB units connected *via* a phenyl ring was investigated by Robertus *et al*.[64] The three possible isomers (*EE*, *EZ* and *ZZ*) were detected in the photostationary state (PSS). The thermal back-isomerization of each respective isomer was followed by NMR spectroscopy. The *Z*-*E* switching behavior seems to be unaffected by the state of the neighboring unit.[64] Kreger *et al.* presented tris-azobenzene chromophores with the ABs connected *via* a benzene core featuring exceptionally stable light-induced orientation. The properties of these compounds appear to be excellent for fabrication of stable holographic volume gratings.[171] Junge *et al.* designed and investigated several dendritic structures with three AB moieties radially configured around the core unit, showing no influence of the close proximity of the single chromophores or any steric hindrance acting on the ABs and the isomerization behavior. However, the dendrimers were found to exist in each of the four possible discrete states, the *EEE*, the *EEZ*, the *EZZ*, and the *ZZZ* isomer by means of NMR spectroscopies.[168] Dendrimers functionalized with four to 32 naphthalene and *E*-AB units were systematically studied by Vögtle *et al*. It was found that fluorescence of the naphthalene units could be quenched by the *E*-ABs *via* electron transfer. Additionally, the *E*-*Z* isomerization becomes more difficult in the dendrimer due to steric hindrance.[98] Dendrimers containing up to 32 AB units have been investigated regarding their photochemical properties. The multi-chromophores show similar switching behavior and virtually identical isomerization quantum yields compared to the monomeric reference compounds.[97] Another fourth generation dendrimer with 32 AB units shows promising properties as photoswitchable dendritic host for eosin molecules.[99]

1.1.1 ULTRAFAST PHOTO-INDUCED DYNAMICS OF AZOBENZENE

The ultrafast dynamics of the $E \rightleftarrows Z$ isomerization of plain unsubstituted AB were investigated extensively. It is known that the electronic deactivation and the isomerization after S_1 and S_2 excitation occur on a subpicosecond time scale.[58,67–72,76,77] The experimental results were supported by numerous computational studies.[110–115,117,118,121,122,124,125,127]

Today the nature and energetic order of the involved excited states as well as the time scale for the isomerization is well known. However, the main focus of most studies on the isomerization of AB was not the nature of the excited states and the related time scales of the dynamics but the isomerization mechanism itself. For a long time it was controversially discussed whether the isomerization occurs *via* the inversion of one phenyl ring with a planar transition configuration or *via* a rotational mechanism.[68,70,71,76,110,113,114,117,118,122,124,174] Today, there is a consensus that the inversion is not the favored deactivation channel. Recent theoretical studies found the rotation or the small amplitude motion of the NN moiety ("hula-twist"), to be the favored photoisomerization mechanism after S_1 and S_2 excitation. The "hula-twist" motion can be imagined as the movement or rotation of a bicycle pedal and was especially found for sterically hindered ABs.[113,114,116,119,122,129]

In the context of this Thesis, the focus was not on the isomerization mechanism but on the effects of intra- and intermolecular interactions on the energetic order of the excited states, the resulting changes in the relaxation pathways and the time scales of the involved dynamics. Satzger *et al.* determined the lifetimes of the involved excited states and suggested relaxation pathways for *E*-AB after excitation to the $n\pi^*$ state and to the $\pi\pi^*$ state which are schematically given in Fig. 1.9 a) and b), respectively.[58,76] Excitation at $\lambda \approx 450$ nm projects the wavepacket from the electronic ground state to the Franck-Condon (FC) region of the $n\pi^*$ state (cf. Fig. 1.9 a). The ≈ 300 fs lifetime component observed by Satzger *et al.* is the lifetime of the initially excited FC state. The S_0 state of the *E* and / or the *Z* isomer is subsequently populated *via* the S_0/S_1 conical intersection (CoIn) within ≈ 3 ps. For the electronic deactivation after $\pi\pi^*$ excitation Satzger *et al.* suggested the scenario shown in Fig. 1.9 b). The initially populated $\pi\pi^*$ state transforms ultrafast to the energetically lower $n\pi^*$ state within ≈ 100 fs. The two slower time constants of ≈ 0.5 ps and ≈ 3 ps were assigned to the subsequent isomerization and radiationless deactivation to the electronic ground state, whereby the component decaying within the shorter time constant is the dominant one. With the exception of the exact decay times these experimentally found time scales are in a good agreement with most experimental studies on the molecular dynamics of AB. Nägele *et al.* observed identical decay times after S_1 excitation and assigned these to the same processes.[68] The dynamics after $\pi\pi^*$ excitation were also followed by Fujino *et al*. The relaxation to the electronic ground state also occurs *via* the intermediate $n\pi^*$ state. The decay times for the S_2 and the S_1 state were found to be ≈ 100 fs and ≈ 500 fs, respectively.[70,71]

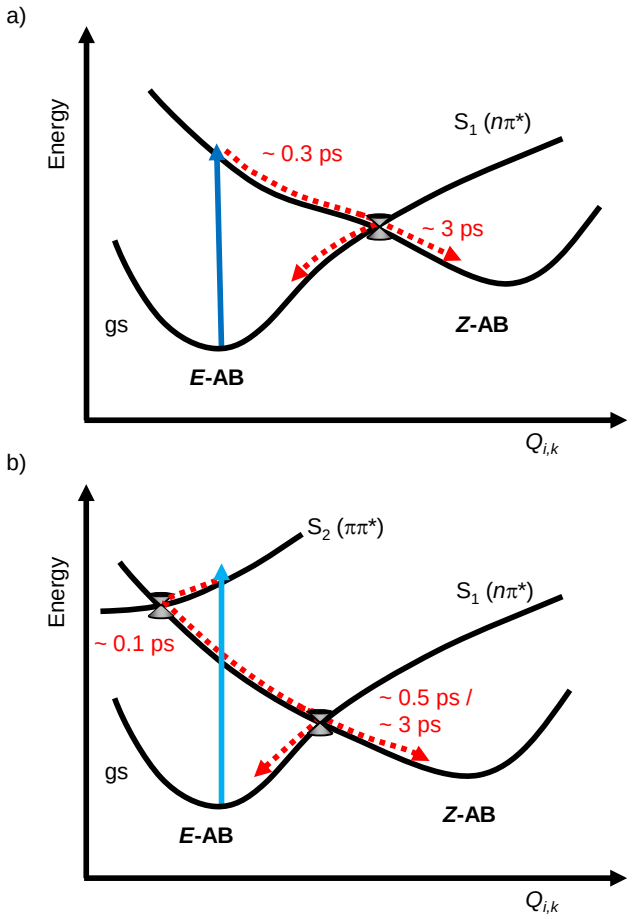

Figure 1.9: Schematic relaxation pathway for *E*-AB after excitation to a) the nπ* state and b) the ππ* state.[58,76]

The dynamics after excitation of *Z*-AB are very similar.[58,68,76] In addition to the experiments in solution, the isomerization dynamics of AB were also investigated in the gas phase by means of femtosecond time-resolved photoelectron spectroscopy.[74,175]

1.1.1.1 *Intra- and intermolecular interactions*

Substituents at the AB core can strongly influence the isomerization dynamics.[30,31,34,75,78,79,83] Due to the induced CT character, the energetic order of the excited states and the molecular dynamics in *push-pull* azobenzenes strongly depend on the solvent.[34,75,79,83] The isomerization pathway is likely to be the rotation around the N=N double bond.[79,118] A more detailed summary regarding the dynamics, the lifetimes and energetic order of the excited states is given in Chapter 3. A comparative study on the ultrafast dynamics of a *push-pull* AB in solution and in a thin polymer film was performed by Hsu *et al*. The excited state dynamics appeared to be almost unaffected by the complex environment, whereas the vibrational relaxation in the electronic ground state was found to be about twice as fast as in solution.[83]

The effects of the substitution with only one electron pushing amino group are small compared to the *push-pull* substitution and the dynamics are more similar to unsubstituted AB, except for a slightly longer S_2 lifetime.[73] In the case of a methoxy and butyl substituted AB derivative, the electronic structure is similar to the amino substituted derivative, therefore the dynamics after $\pi\pi^*$ excitation are also similar to AB. The slower decay of the S_2 state in this case was assigned to a smaller S_1-S_2 energy gap.[27] AB-like behavior was also observed for two different ABs functionalized with two methyl groups or one ethylamine group on one phenyl ring and a carboxyl group on the other ring after $n\pi^*$ excitation.[17,18,176] These AB derivatives were embedded in small mono- and bicyclic peptides exhibiting additional slower decay components. These slower processes mainly arise from the conformational changes of the peptide. The AB switch in the peptide appeared nearly unaffected.[17,18,176,177]

The isomerization dynamics of rotation-restricted AB derivatives were investigated in our work group and by Lu *et al.*[31,78] Pancur *et al.* investigated an *E*-AB derivative capped by a crown ether after excitation to its $n\pi^*$ state and found an increased excited state lifetime by a factor of ≈ 6, which was assigned to a more diffusional motion on the S_1 potential energy hypersurface (PEHS).[31] Large-amplitude rotation is hindered for this system, but the isomerization may still proceed *via* the "hula-twist" mechanism. Nonnenberg *et al.* found a rotational pathway as deactivation channel to the electronic ground state for the same system.[119] Two other AB-based systems with strong rotation restriction show an about ten times slower decay of the $n\pi^*$ state and therefore a slower isomerization. The decay of the initially excited $\pi\pi^*$ state is similar to the unrestricted reference AB derivative because the S_2 state is not directly involved into the isomerization.[78] Although the ABs in these systems seem to be restricted and rotation was predicted to be impossible, theoretical investigations suggest the rotational pathway as the preferred isomerization mechanism.[116] This is possible if the rotational motion involves only the N atoms of the azo-bridge moving to the CoIn. One special example of a strongly restricted system was shown by Siewertsen *et al.*, who investigated a bridged AB-related molecule with an eight-membered heterocyclic ring as central unit with the *Z* isomer being the thermodynamically stable one. The isomerization quantum yields are much higher compared to AB itself.[29,30] Due to the strong intramolecular forces and severe constraints the dynamics are dramatically accelerated compared to unsubstituted AB and the isomerization occurs within only ≈ 300 fs. These investigations were supported by quantum chemical calculations.[128,129,133] Even for this highly constrained bridged AB, a torsional mechanism around the NN bond was found to determine the dynamics. For a better comparison of theoretical calculations and experimental results in solution or in more complex environments, N. O. Carstensen investigated the dynamics of the mentioned bridged AB derivative in a more realistic *n*-hexane environment in a large scale QM/MM surface-hopping study.[133] Compared to previous studies in the gas phase,[129] the obtained results especially regarding the isomerization

quantum yields were in a much better agreement with experimental results.[133] The QM/MM approach has been already used previously for a better description of the molecular dynamics of AB derivatives in a more complex environment.[132]

A comparative study of the molecular dynamics of AB derivatives embedded in nanotubes and nanocavities of mesoporous and zeolite materials and in solution has been performed by Gil *et al.*[178,179] The selected ABs are able to form intra- and intermolecular hydrogen bonds. The time scale for the *E*-*Z* isomerization in the complex environment was found to be slower than in solution, which was assigned to cooperative effects within the solvent cage in the respective framework. The strongest effects could be observed in protic polar solvents because of the slower reorientation and motion of the solvent. Using an non-polar aprotic solvent, no significant changes in the molecular dynamics were observed.[178,179] The isomerization of the AB derivative methyl orange in cyclodextrin nanocavities, where the chromophore was capped at one or both ends, respectively, was found to be up to twice as slow as in solution.[180] Furthermore, the isomerization quantum yields were reduced compared to the situation in solution, depending on the degree of restriction. The observed behavior was assigned to strong intermolecular steric interactions between molecule and surrounding matrix.

Transient absorption and time-resolved anisotropy decay measurements on an AB derivative consisting of three AB units in solution and in thin bulk films were performed by Hao *et al.*[173] The obtained data were compared with the molecular dynamics of a related single AB. The averaged lifetime for the multi-AB in the complex polymeric environment was increased by a factor of more than three compared to solution. The anisotropy in the bulk film remained virtually constant, whereas the anisotropy value in solution decayed slowly. Theses differences are related to the environmental changes within the complex surrounding.

The ultrafast dynamics of dendrimers with terminal AB groups in solution and in solid films were compared by Franckevičius *et al.*[101] Compared to single ABs in solution, the dynamics in the dendrimer are very similar. The branched dendritic structure alone had no significant influence on the *E*-*Z* isomerization reaction, whereas the embedding into the solid film led to a seven times slower reaction times of the respective system, which was assigned to the interactions between the molecule and the surrounding matrix.

These selected studies clearly show potential influences of substituents and / or restrictions. Both affect the switching behavior and the isomerization dynamics of ABs and consequently, the investigation of intra- and intermolecular interactions is of fundamental importance for most applications.

1.1.2 INVESTIGATED AZOBENZENE DERIVATIVES AND AIM OF THIS THESIS

One main goal of this Thesis is the investigation of the photochemical properties and molecular dynamics of azobenzene switches under the influence of specific intra- and intermolecular interactions, which potentially strongly affect the desired photoisomerization. The experimental details of the used femtosecond time-resolved transient absorption and fluorescence up-conversion setups are described in Chapter 2.

In order to shed light on the controversial issue of the role of the involved excited states and the isomerization dynamics of *push-pull* substituted AB derivatives,[34,75,79,83] the *push-pull* AB Disperse Red 1 (DR1) is studied by means of femtosecond absorption and fluorescence spectroscopy. The results of this study are presented in Chapter 3. Although the energetic order of the (compared to unsubstituted AB) strongly red-shifted $\pi\pi^*$ state and the $n\pi^*$ state remains uncertain, the data clearly suggest a stepwise isomerization after $\pi\pi^*$ excitation. The obtained results form the basis for the investigation of the dynamics of DR1 covalently linked to the side chain of tightly cross-linked polymer colloids to study the influence of intermolecular forces acting on the photo-excited AB. In addition, a bifunctional AB derivative is directly attached to the main chain of colloidal polymer particles with two different cross-linking ratios. A schematic depiction of the investigated systems is shown in Fig. 1.10. Femtosecond

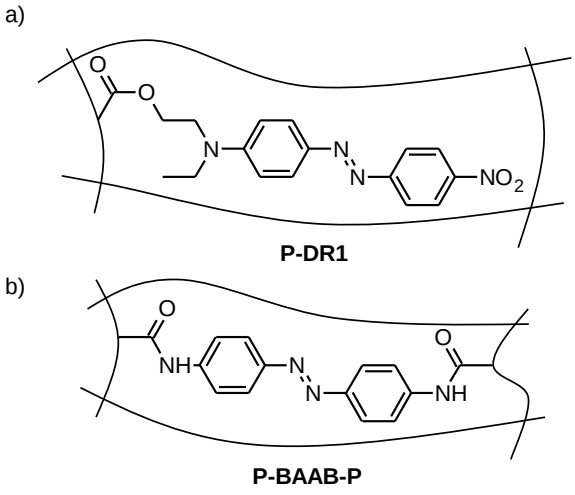

Figure 1.10: a) DR1 linked to the polymer side chain (P-DR1) and b) BAAB linked to the main chain of the polymer (P-BAAB-P).

fluorescence spectroscopy is used to probe and compare the excited state dynamics of the ABs in the complex polymeric micronetworks and in solution. The obtained results reveal dramatic differences in the excited state dynamics and the isomerization of ABs in solution and in the complex environment. The fluorescence lifetimes in the polymer are found to be much longer than in solution. As expected the effects are much more pronounced for the AB in the main chain of the polymer and the stronger

cross-linked particles and are mainly attributed to the extraordinary strong forces in the polymers. The detailed analysis and discussion of the underlying data are given in Chapter 4. Regarding possible applications, the results for the AB derivatives in the polymer are of major importance.

Intramolecular interactions within two multi-AB derivatives consisting of two and three AB units (cf. Fig 1.11), respectively, are investigated by means of static UV/VIS and NMR spectroscopies and by time-resolved transient absorption anisotropy decay measurements. Direct electronic cou-

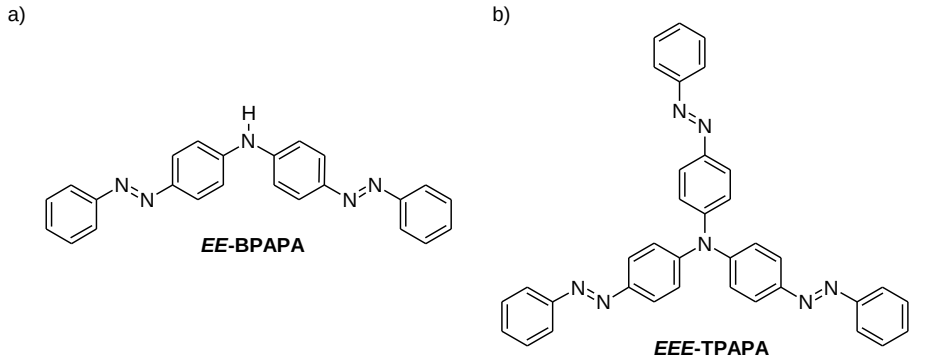

Figure 1.11: Chemical structures of the two multi-azobenzene compounds a) BPAPA and b) TPAPA.

pling between the AB units is enabled *via* the central nitrogen linker. The systems exhibit strong intramolecular chromophore-chromophore coupling between the azo moieties. The observable effects are more pronounced for the tris-AB compared to the bis-AB, which agrees well with previous studies on electronic coupling in multi-chromophoric systems.[181,182] The details of the photochemical properties of the secondary and tertiary amine, BPAPA and TPAPA, respectively, in comparison with the parent compound, the primary amine aminoazobenze are presented in Chapter 5. Chapter 6 deals with the ultrafast dynamics and the anisotropy decay measurements on BPAPA and TPAPA. The obtained results for the multi-AB compounds are of high relevance for numerous applications.

The unique properties of the above mentioned magnetically bistable nickel porphyrin functionalized with an azopyridine as photoswitchable unit shown in Fig 1.2 require an investigation of the nature of the excited states of the porphyrin macrocycle, the metal ion and the AB unit, the isomerization mechanism and the coordination and decoordination of the pyridine unit. Previous studies have shown that the light-induced *E*-*Z* and *Z*-*E* isomerization of the AB can lead to the coordination and decoordination of the pyridine nitrogen resulting in the spin switch of the Ni(II)-ion from its diamagnetic to its paramagnetic state.[23] Within the frame of this Thesis, a systematic study on the ultrafast dynamics of the different building blocks of the molecule, the porphyrin without metal ion, the Ni-porphyrin, the four-coordinate *E* isomer and the five-coordinate *Z* isomer is performed using time-resolved transient absorption spectroscopy. The data of the metal free and the metal porphyrin are very similar to previ-

ous studies on the photochemical properties and the molecular dynamics of related porphyrins and are therefore interpreted on the basis of these studies. A more detailed overview of the important photophysics of porphyrins and the relevant literature is given in Chapter 7. However, further studies on the isomerization mechanism of the molecular spin switch will be needed to elucidate the details of this supposedly complex process.

1.2 Bistable molecular photoswitches based on the excited state intramolecular proton transfer (ESIPT)

Photochromic excited state intramolecular proton transfer (ESIPT) switches consist typically of an acidic and a basic functional group, which are connected *via* intramolecular hydrogen bonds. Electronic excitation can then lead to an increased acidity of the proton donor and basicity of the proton acceptor, respectively, which can induce an intramolecular proton transfer on the electronically excited potential energy hypersurface (PEHS).[43,44,183–185] The reaction between the two states of an ESIPT switch can be driven back and forth by light at suitable wavelengths, thus making these system powerful photoswitches.

In general, proton transfer reactions belong to the most relevant chemical reactions known and are fundamental for numerous biological and biochemical processes.[186–192] Typically, ESIPT reactions are ultrafast on a time scale of only tens to a few hundreds of femtoseconds.[184,191,193–195] Due to the ultrashort excited state lifetimes and the exceptional photostabilities, molecular photoswitches, which can be driven by the ESIPT process, offer huge application potential as photostabilizers, e.g., for the protection of organic materials against the UV-A and UV-B compounds of sunlight.[25,196] One of the most common photostabilizers (2-(2′- hydroxy-5′-methylphenyl)benzotriazole, TINUVIN-P) for varnishes and adhesives shows an overall excited state lifetime of only $\approx$ 200 fs. The proton back-transfer in the electronic ground state occurs within less than $\approx$ 1 ps. Additionally, the reaction was found to be nearly unaffected by a polymeric environment, which is very important for most applications.[197,198] Due to their particularly efficient UV stabilities, several derivatives or related molecules of o-hydroxybenzaldehyde,[199–203] salicylic acid,[200,204–206] 3-hydroxyflavone,[191,204,207,208] 2-(2′-hydroxyphenyl)benzotriazole,[200,204,209–212] hydroxyquinolines[183,193,213,214] and functionalized anthraquinones[204,215–217] have been investigated extensively both from the experimental and the theoretical point of view.[184,191,194,204] The molecular structures of some of the prototypical compounds are given in Fig. 1.12. All these systems are based on an ultrafast ESIPT process after UV excitation, with the key feature being the ultrafast proton transfer in the electronically excited state and the almost barrierless decay of the excited configuration *via* a CoIn to the electronic ground state. Subsequently the photocycle is closed by the proton back-transfer in the electronic ground state. The details of the underlying reaction steps of course depend strongly on the respective systems.[43,44,193,205] Just recently, Rode *et al.* performed a

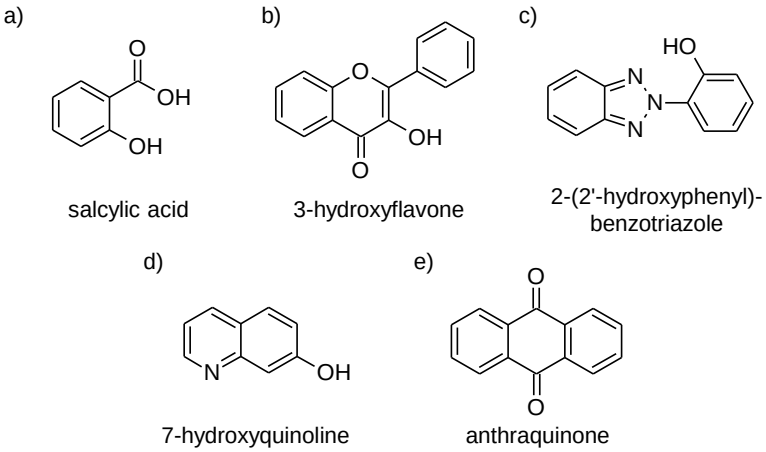

Figure 1.12: Molecular structures of a) salicylic acid, b) 3-hydroxyflavone, c) 2-(2′-hydroxyphenyl)benzotriazole d) 7-hydroxyquinoline and e) anthraquinone.

systematic theoretical study on the influence of electron withdrawing and donating substituents on the structure and the properties on the double ESIPT system 3-hydroxy-picolinic acid, a derivative of salicylic acid. The substitution was found to be able to strongly influence the height of the barrier between the possible tautomers on the S_0 PEHS and the barrierless deactivation *via* the S_1/S_0 CoIn.[185]

A qualitative picture of the basic principle and schematic representation of the potential energy landscape of a bistable molecular photoswitch based on the ESIPT process is given in Fig. 1.13. Optical excitation of **I**

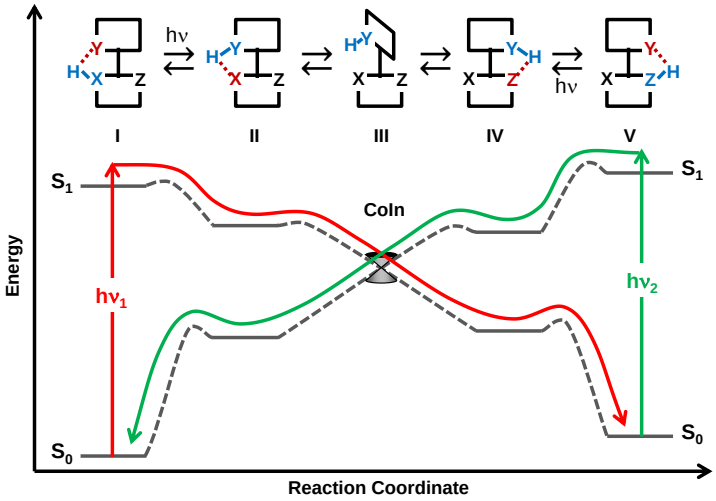

Figure 1.13: Schematic depiction of typical PEHS and possible reaction pathway of a bistable molecular photoswitch, which can be driven by the ESIPT process. Reproduced from[43,44,183].

at wavelength λ_1 promotes the molecule from the S_0 to the S_1 state and induces an ultrafast proton transfer from the proton donating unit **X** to

the proton accepting unit **Y** resulting in form **II**. Subsequently, the system evolves almost barrierless towards the CoIn with the electronic ground state, which is reached *via* a twist around the covalent bond connecting the proton donating and accepting unit. The torsional motion breaks the intramolecular hydrogen bonds. The system on the ground state PEHS then has two possibilities. First, the torsional motion continue, ultimately leading to the formation of form **IV** with a hydrogen bond between **Y** and **Z**. Second, the system can return to the initial form **I**. Typically, structure **IV** is not stable on the S_0 PEHS and the proton is transferred to the proton accepting **Z** atom resulting in the desired final configuration **V**. The back-reaction occurs either thermally or can be switched back by irradiating form **V** at a suitable wavelength (λ_2).[43,44,183] In case of the use as photostabilizers the formation of stable photoproducts is unwanted. Hence, the barrier between the two tautomers **I** and **IV** in the electronic ground state should be low.[205,211]

1.2.1 INVESTIGATED ESIPT SWITCH AND AIM OF THIS THESIS

A second goal of this Thesis is the investigation of a bistable proton transfer switch based on excited state intramolecular proton transfer (ESIPT), which supports the above mentioned general qualitative scheme of the ESIPT phenomenon. The suggested reaction scheme after UV excitation of the thermodynamically stable isomer and the respective intermediate structures on the way to the proton transfer product are shown in Fig. 1.14. Time-resolved absorption and fluorescence measurements are performed

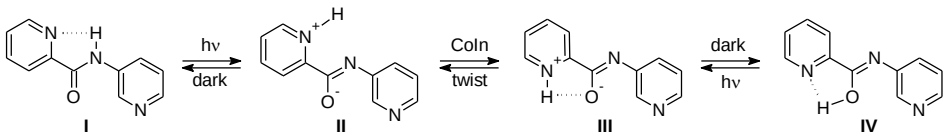

Figure 1.14: Molecular structures and reaction scheme of the bistable proton transfer switch NPPCA after excitation in the UV.

in a protic and an aprotic solvent, respectively. The interpretation of the data is supported by quantum chemical calculations of A. Sobolewski and co-workers. The data clearly suggest a stepwise formation of the desired proton transfer product, the enol form **IV** *via* the forms **II** and **III** after excitation of the keto form **I** in the aprotic solvent acetonitrile. The details of these results are found in Chapters 8 and 9.

Before presenting the results and the discussions for the mentioned molecular photoswitches in the second part of this Thesis (Chapters 3 - 9) , details of the experimental setups will be described in Chapter 2. Finally, a summary of all obtained results and an outlook is given in Part III (Chapter 10).

BIBLIOGRAPHY

[1] Browne, W. R.; Feringa, B. L. *Nat. Nanotechnol.* **2006**, *1*, 25–35.

[2] Muraoka, T.; Kinbara, K.; Aida, T. *Nature* **2006**, *440*, 512–515.

[3] Balzani, V.; Credi, A.; Venturi, M. *Molecular Devices and Machines: Concepts and Perspectives for the Nanoworld*; Wiley-VCH: Weinheim, 2008.

[4] Balzani, V.; Credi, A.; Venturi, M. *Chem. Soc. Rev.* **2009**, *38*, 1542–1550.

[5] Feringa, B. L., Browne, W. R., Eds. *Molecular Switches*; Wiley-VCH: Weinheim, 2011; Vol. 1 & 2.

[6] Iamsaard, S.; Aßhoff, S. J.; Matt, B.; Kudernac, T.; Cornelissen, J. J.; Fletcher, S. P.; Katsonis, N. *Nature chemistry* **2014**,

[7] Kawata, S.; Kawata, Y. *Chem. Rev.* **2000**, *100*, 1777–1788.

[8] Gindre, D.; Boeglin, A.; Fort, A.; Mager, L.; Dorkenoo, K. D. *Opt. Express* **2006**, *14*, 9896.

[9] Chen, Y.; Xiao, J. P.; Yao, B.; Fan, M. G. *Opt. Mater.* **2006**, *28*, 1068–1071.

[10] Dvornikov, A. S.; Walker, E. P.; Rentzepis, P. M. *J. Phys. Chem. A* **2009**, *113*, 13633–13644.

[11] Li, H.; Xu, Q.; Li, N.; Sun, R.; Ge, J.; Lu, J.; Gu, H.; Yan, F. *J. Am. Chem. Soc.* **2010**, *132*, 5542–5543.

[12] Ha, N. Y.; Ohtsuka, Y.; Jeong, S. M.; Nishimura, S.; Suzaki, G.; Takanishi, Y.; Ishikawa, K.; Takezoe, H. *Nat. Mater.* **2008**, *7*, 43–47.

[13] Ma, J.; Xuan, L. *Displays* **2013**, *34*, 293–300.

[14] Zacharias, P.; Gather, M. C.; Köhnen, A.; Rehmann, N.; Meerholz, K. *Angew. Chem. Int. Ed.* **2009**, *48*, 4038–4041.

[15] Shallcross, R. C.; Zacharias, P.; Köhnen, A.; Körner, P. O.; Maibach, E.; Meerholz, K. *Adv. Mater.* **2013**, *25*, 469–476.

[16] Pieroni, O.; Fissi, A.; Angelini, N.; Lenci, F. *Acc. Chem. Res.* **2001**, *34*, 9–17.

[17] Spörlein, S.; Carstens, H.; Satzger, H.; Renner, C.; Behrendt, R.; Moroder, L.; Tavan, P.; Zinth, W.; Wachtveitl, J. *Proc. Natl. Acad. Sci. U.S.A.* **2002**, *99*, 7998–8002.

[18] Wachtveitl, J.; Spoerlein, S.; Satzger, H.; Fonrobert, B.; Renner, C.; Behrendt, R.; Oesterhelt, D.; Moroder, L.; Zinth, W. *Biophys. J.* **2004**, *86*, 2350–2362.

[19] Auernheimer, J.; Dahmen, C.; Hersel, U.; Bausch, A.; Kessler, H. *J. Am. Chem. Soc.* **2005**, *127*, 16107–16110.

[20] Liang, X.; Nishioka, H.; Takenaka, N.; Asanuma, H. *ChemBioChem* **2008**, *9*, 702–705.

[21] Al-Atar, U.; Fernandes, R.; Johnsen, B.; Baillie, D.; Branda, N. R. *J. Am. Chem. Soc.* **2009**, *131*, 15966–15967.

[22] Beharry, A. A.; Wong, L.; Tropepe, V.; Woolley, G. A. *Angew. Chem.* **2011**, *123*, 1361–1363.

[23] Venkataramani, S.; Jana, U.; Dommaschk, M.; Sönnichsen, F.; Tuczek, F.; Herges, R. *Science* **2011**, *331*, 445–448.

[24] Kaczmarek, L.; Borowicz, P.; Grabowska, A. *J. Photochem. Photobiol. A* **2001**, *138*, 159–166.

[25] Zayat, M.; Garcia-Parejo, P.; Levy, D. *Chem. Soc. Rev* **2007**, *36*, 1270–1281.

[26] Bouas-Laurent, H.; Dürr, H. *Pure Appl. Chem.* **2001**, *73*, 639–665.

[27] Tamai, N.; Miyasaka, H. *Chem. Rev.* **2000**, *100*, 1875–1890.

[28] Renth, F.; Siewertsen, R.; Temps, F. *Int. Rev. Phys. Chem.* **2013**, *32*, 1–38.

[29] Siewertsen, R.; Neumann, H.; Buchheim-Stehn, B.; Herges, R.; Näther, C.; Renth, F.; Temps, F. *J. Am. Chem. Soc.* **2009**, *131*, 15594–15595.

[30] Siewertsen, R.; Schönborn, J. B.; Hartke, B.; Renth, F.; Temps, F. *Phys. Chem. Chem. Phys.* **2011**, *13*, 1054–1063.

[31] Pancur, T.; Renth, F.; Temps, F.; Harbaum, B.; Krüger, A.; Herges, R.; Näther, C. *Phys. Chem. Chem. Phys.* **2005**, *7*, 1985–1989.

[32] Russew, M.-M.; Hecht, S. *Adv. Mater.* **2010**, *22*, 3348–3360.

[33] Dhammika Bandara, H. M.; Burdette, S. C. *Chem. Soc. Rev.* **2012**, *41*, 1809–1825.

[34] Bahrenburg, J.; Röttger, K.; Siewertsen, R.; Renth, F.; Temps, F. *Photochem. Photobiol. Sci.* **2012**, *11*, 1210–1219.

[35] Yokoyama, Y. *Chem. Rev.* **2000**, *100*, 1717–1739.

[36] Siewertsen, R.; Renth, F.; Temps, F. *Phys. Chem. Chem. Phys.* **2009**, *11*, 5952–5961.

[37] Siewertsen, R.; Strübe, F.; Mattay, J.; Renth, F.; Temps, F. *Phys. Chem. Chem. Phys.* **2011**, *13*, 3800–3808, to be published.

[38] Strübe, F.; Siewertsen, R.; Sönnichsen, F. D.; Renth, F.; Temps, F.; Mattay, J. *Eur. J. Org. Chem.* **2011**, *2011*, 1947–1955.

[39] Berkovic, G.; Krongauz, V.; Weiss, V. *Chem. Rev.* **2000**, *100*, 1741–1753.

[40] Minkin, V. I. *Chemical Reviews* **2004**, *104*, 2751–2776.

[41] Irie, M. *Chem. Rev.* **2000**, *100*, 1685–1716.

[42] Matsuda, K.; Irie, M. *J. Photochem. Photobiol. C* **2004**, *5*, 169–182.

[43] Sobolewski, A. L. *Phys. Chem. Chem Phys.* **2008**, *10*, 1243–1247.

[44] Lapinski, L.; Nowak, M. J.; Nowacki, J.; Rode, M. F.; Sobolewski, A. L. *ChemPhysChem* **2009**, *10*, 2290–2295.

[45] Bahrenburg, J.; Rode, M. F.; Sobolewski, A. L.; Temps, F. *Ultrafast Phenomena XIX* **2014**, accepted.

[46] Kumar, G. S.; Neckers, D. C. *Chem. Rev.* **1989**, *89*, 1915–1925.

[47] Delaire, J. A.; Nakatani, K. *Chem. Rev.* **2000**, *100*, 1817–1845.

[48] Feringa, B. L. *Molecular Switches*; Wiley-VCH: Weinheim, 2001.

[49] Dugave, C.; Demange, L. *Chem. Rev.* **2003**, *103*, 2475–2532.

[50] Kinbara, K.; Aida, T. *Chem. Rev.* **2005**, *105*, 1377–1400.

[51] Szaciłowski, K. *Chem. Rev.* **2008**, *108*, 3481–3548.

[52] Niazov, T.; Shlyahovsky, B.; Willner, I. *J. Am. Chem. Soc.* **2007**, *129*, 6374–6375.

[53] Bortolus, P.; Monti, S. *J. Phys. Chem.* **1979**, *83*, 648–652.

[54] Asano, T.; Okada, T.; Shinaki, S.; Shigematsu, K.; Kusano, Y.; Manabe, O. *J. Am. Chem. Soc.* **1981**, *103*, 5161–5165.

[55] Rau, H. *J. Photochem.* **1984**, *26*, 221–225.

[56] Gille, K.; Knoll, H.; Quitzsch, K. *Int. J. Chem. Kinet.* **1999**, *31*, 337–350.

[57] Rau, H. In *Photochromism: Molecules and Systems*; Dürr, H., Bouas-Laurent, H., Eds.; Elsevier: Amsterdam, 2003.

[58] Satzger, H.; Spörlein, S.; Root, C.; Wachtveitl, J.; Zinth, W.; Gilch, P. *Chem. Phys. Lett.* **2003**, *372*, 216–223.

[59] Cisnetti, F.; Ballardini, R.; Credi, A.; Gandolfi, M. T.; Masiero, S.; Negri, F.; Pieraccini, S.; Spada, G. P. *Chem. Eur. J.* **2004**, *10*, 2011–2021.

[60] Peters, M. V.; Goddard, R.; Hecht, S. *J. Org. Chem.* **2006**, *71*, 7840–7845.

[61] Norikane, Y.; Tamaoki, N. *Eur. J. Org. Chem.* **2006**, 1296–1302.

[62] Haberhauer, G.; Kallweit, C. *Angew. Chem. Int. Ed.* **2010**, *49*, 2418–2421.

[63] Bléger, D.; Dokić, J.; Peters, M. V.; Grubert, L.; Saalfrank, P.; Hecht, S. *J. Phys. Chem. B* **2011**, *115*, 9930–9940.

[64] Robertus, J.; Reker, S. F.; Pijper, T. C.; Deuzeman, A.; Browne, W. R.; Feringa, B. L. *Phys. Chem. Chem. Phys.* **2012**, *14*, 4374–4382.

[65] Bahrenburg, J.; Sievers, C. M.; Schönborn, J. B.; Hartke, B.; Renth, F.; Temps, F.; Näther, C.; Sönnichsen, F. D. *Photochem. Photobiol. Sci.* **2013**, *12*, 511–518.

[66] Sell, H.; Näther, C.; Herges, R. *Beilstein J. Org. Chem.* **2013**, *9*, 1–7.

[67] Lednev, I. K.; Ye, T.-Q.; Hester, R. E.; Moore, J. N. *J. Phys. Chem.* **1996**, *100*, 13338–13341.

[68] Nägele, T.; Hoche, R.; Zinth, W.; Wachtveitl, J. *Chem. Phys. Lett.* **1997**, *272*, 489–495.

[69] Lednev, I. K.; Ye, T.-Q.; Matousek, P.; Towrie, M.; Foggi, P.; Neuwahl, F. V. R.; Umapathy, S.; Hester, R. E.; Moore, J. N. *Chem. Phys. Lett.* **1998**, *290*, 68–74.

[70] Fujino, T.; Arzhantsev, S. Y.; Tahara, T. *J. Phys. Chem. A* **2001**, *105*, 8123–8129.

[71] Fujino, T.; Arzhantsev, S. Y.; Tahara, T. *Bull. Chem. Soc. Jpn.* **2002**, *75*, 1031–1040.

[72] Lu, Y.-C.; Chang, C.-W.; Diau, E. W.-G. *J. Chin. Chem. Soc.* **2002**, *49*, 693–701.

[73] Hirose, Y.; Yui, H.; Sawada, T. *J. Phys. Chem. A* **2002**, *106*, 3067–3071.

[74] Schultz, T.; Quenneville, J.; Levine, B.; Toniolo, A.; Martinez, T. J.; Lochbrunner, S.; Schmitt, M.; Shaffer, J. P.; Zgierski, M. Z.; Stolow, A. *J. Am. Chem. Soc.* **2003**, *125*, 8098–8099.

[75] Schmidt, B.; Sobotta, C.; Malkmus, S.; Laimgruber, S.; Braun, M.; Zinth, W.; Gilch, P. *J. Phys. Chem. A* **2004**, *108*, 4399–4404.

[76] Satzger, H.; Root, C.; Braun, M. *J. Phys. Chem. A* **2004**, *108*, 6265–6271.

[77] Chang, C.-W.; Lu, Y.-C.; Wang, T.-T.; Diau, E. W.-G. *J. Am. Chem. Soc.* **2004**, *126*, 10109–10118.

[78] Lu, Y.-C.; Diau, E. W.-G.; Rau, H. *J. Phys. Chem. A* **2005**, *109*, 2090–2099.

[79] Poprawa-Smoluch, M.; Baggerman, J.; Zhang, H.; Maas, H. P. A.; De Cola, L.; Brouwer, A. M. *J. Phys. Chem. A* **2006**, *110*, 11926–11937.

[80] Koller, F.; Sobotta, C.; Schrader, T. E.; Cordes, T.; Schreier, W. J.; Sieg, A.; Gilch, P. *Chem. Phys.* **2007**, *341*, 258–266.

[81] Yamaguchi, A.; Nakagawa, N.; Igarashi, K.; Sekikawa, T.; Nishioka, H.; Asanuma, H.; Yamashita, M. *Appl. Surf. Sci.* **2009**, *255*, 9864–9868.

[82] Bao, J.; Weber, P. M. *J. Am. Chem. Soc.* **2011**, *133*, 4164–4167.

[83] Hsu, C.-C.; Wang, Y.-T.; Yabushita, A.; Luo, C.-W.; Hsiao, Y.-N.; Lin, S.-H.; Kobayashi, T. *J. Phys. Chem. A* **2011**, *115*, 11508–11514.

[84] Hoffman, D. P.; Mathies, R. A. *Phys. Chem. Chem. Phys.* **2012**, *14*, 6298–6306.

[85] Natansohn, A.; Rochon, P. *Chem. Rev.* **2002**, *102*, 4139.

[86] Hugel, T.; Holland, N. B.; Cattani, A.; Moroder, L.; Seitz, M.; Gaub, H. E. *Science* **2002**, *296*, 1103–1106.

[87] Holland, N. B.; Hugel, T.; Neuert, G.; Cattani-Scholz, A.; Renner, C.; Oesterhelt, D.; Moroder, L.; Seitz, M.; Gaub, H. E. *Macromolecules* **2003**, *36*, 2015–2023.

[88] Häckel, M.; Kador, L.; Kropp, D.; Schmidt, H.-W. *Adv. Mater.* **2007**, *19*, 227–231.

[89] Bang, C.-U.; Shishido, A.; Ikeda, T. *Macromol. Rapid Comm.* **2007**, *28*, 1040–1044.

[90] Parker, R. M.; Gates, J. C.; Rogers, H. L.; Smith, P. G.; Grossel, M. C. *J. Mater. Chem.* **2010**, *20*, 9118–9125.

[91] Fabbri, F.; Garrot, D.; Lahlil, K.; Boilot, J. P.; Lassailly, Y.; Peretti, J. *J. Phys. Chem. B* **2011**, *115*, 1363–1367.

[92] Willerich, I.; Gröhn, F. *Macromolecules* **2011**, *44*, 4452–4461.

[93] Pardo, R.; Zayat, M.; Levy, D. *Chem. Soc. Rev.* **2011**, *40*, 672–687.

[94] Zaporojtchenko, V.; Pakula, C.; Wahyuni Basuki, S.; Strunskus, T.; Zargarani, D.; Herges, R.; Faupel, F. *Appl. Phys. A* **2011**, *102*, 421–427.

[95] Wiktorowicz, S.; Tenhu, H.; Aseyev, V. *Macromolecules* **2013**, *46*, 6209–6216.

[96] Bahrenburg, J.; Renth, F.; Plamper, F.; Richtering, W.; Temps, F. *Phys. Chem. Chem Phys.* **2014**, *16*, 11549–11554.

[97] Archut, A.; Vögtle, F.; De Cola, L.; Azzellini, G. C.; Balzani, V.; Ramanujam, P. S.; Berg, R. H. *Chem. Eur. J.* **1998**, *4*, 699–706.

[98] Vögtle, F.; Gorka, M.; Hesse, R.; Ceroni, P.; Maestri, M.; Balzani, V. *Photochem. Photobiol. Sci.* **2002**, *1*, 45–51.

[99] Puntoriero, F.; Ceroni, P.; Balzani, V.; Bergamini, G.; Vögtle, F. *J. Am. Chem. Soc.* **2007**, *129*, 10714–10719.

[100] Deloncle, R.; Caminade, A.-M. *J. Photochem. C* **2010**, *11*, 24–45.

[101] Franckevičius, M.; Vaišnoras, R.; Marcos, M.; Serrano, J. L.; Karpicz, R.; Gulbinas, V. *Chem. Phys. Lett.* **2010**, *485*, 158–160.

[102] Chandrasekaran, V.; Lindhorst, T. K. *Chem. Commun.* **2012**, *48*, 7519–7521.

[103] Hagen, S.; Leyssner, F.; Nandi, D.; Wolf, M.; Tegeder, P. *Chem. Phys. Lett.* **2007**, *444*, 85–90.

[104] Ferri, V.; Elbing, M.; Pace, G.; Dickey, M. D.; Zharnikov, M.; Samori, P.; Mayor, M.; Rampi, M. A. *Angew. Chem., Int. Ed.* **2008**, *47*, 3407–3409.

[105] Baisch, B.; Raffa, D.; Jung, U.; Magnussen, O. M.; Nicolas, C.; Lacour, J.; Kubitschke, J.; Herges, R. *J. Am. Chem. Soc.* **2009**, *131*, 442–443.

[106] Jung, U.; Schütt, C.; Filinova, O.; Kubitschke, J.; Herges, R.; Magnussen, O. *J. Phys. Chem. C* **2012**, *116*, 25943–25948.

[107] Gopakumar, T. G.; Davran-Candan, T.; Bahrenburg, J.; Maurer, R. J.; Temps, F.; Reuter, K.; Berndt, R. *Angew. Chem. Int. Ed.* **2013**, *52*, 11007–11010.

[108] Müller, M.; Jung, U.; Gusak, V.; Ulrich, S.; Holz, M.; Herges, R.; Langhammer, C.; Magnussen, O. M. *Langmuir* **2013**, *29*, 10693–10699.

[109] Benassi, E.; Corni, S. *J. Phys. Chem. C* **2013**, *117*, 25026–25041.

[110] Cattaneo, P.; Persico, M. *Phys. Chem. Chem. Phys.* **1999**, *1*, 4739–4743.

[111] Ishikawa, T.; Noro, T.; Shoda, T. *J. Chem. Phys.* **2001**, *115*, 7503.

[112] Cembran, A.; Bernardi, F.; Garavelli, M.; Gagliardi, L.; Orlandi, G. *J. Am. Chem. Soc.* **2004**, *126*, 3234.

[113] Ciminelli, C.; Granucci, G.; Persico, M. *Chem. Eur. J.* **2004**, *10*, 2327–2341.

[114] Diau, E. W.-G. *J. Phys. Chem. A* **2004**, *108*, 950–956.

[115] Gagliardi, L.; Orlandi, G.; Bernardi, F.; Cembran, A.; Garavelli, M. *Theo. Chem. Acc.* **2004**, *111*, 363–372.

[116] Ciminelli, C.; Granucci, G.; Persico, M. *J. Chem. Phys.* **2005**, *123*, 174317.

[117] Toniolo, A.; Ciminelli, C.; Persico, M.; Martinez, T. J. *J. Chem. Phys.* **2005**, *123*, 234308.

[118] Crecca, C. R.; Roitberg, A. E. *J. Phys. Chem. A* **2006**, *110*, 8188–8203.

[119] Nonnenberg, C.; Gaub, H.; Frank, I. *ChemPhysChem* **2006**, *7*, 1455–1461.

[120] Granucci, G.; Persico, M. *Theor. Chem. Acc.* **2007**, *117*, 1131–1143.

[121] Wang, L. X.; Wang, X. G. *J. Mol. Struc. Theochem.* **2007**, *847*, 1–9.

[122] Conti, I.; Garavelli, M.; Orlandi, G. *J. Am. Chem. Soc.* **2008**, *130*, 5216–5230.

[123] Sauer, P.; Allen, R. E. *Chem. Phys. Lett.* **2008**, *450*, 192–195.

[124] Yuan, S.; Dou, Y.; Wu, W.; Hu, Y.; Zhao, J. *J. Phys. Chem. A* **2008**, *112*, 13326–13334.

[125] Yuan, S.; Wu, W. F.; Dou, Y. S.; Zhao, J. S. *Chin. Chem. Lett.* **2008**, *19*, 1379–1382.

[126] Dokic, J.; Gothe, M.; Wirth, J.; Peters, M. V.; Schwarz, J.; Hecht, S.; Saalfrank, P. *J. Phys. Chem. A* **2009**, *113*, 6763–6773.

[127] Wang, L. X.; Xu, W. L.; Yi, C. H.; Wang, X. G. *J. Molec. Graphics Modeling* **2009**, *27*, 792–796.

[128] Böckmann, M.; Doltsinis, N. L.; Marx, D. *Angew. Chem. Int. Ed.* **2010**, *49*.

[129] Carstensen, O.; Sielk, J.; Schönborn, J. B.; Granucci, G.; Hartke, B. *J. Chem. Phys.* **2010**, *133*, 124305.

[130] Jiang, C.-W.; Xie, R.-H.; Li, F.-L.; Allen, R. E. *J. Phys. Chem. A* **2010**, submitted.

[131] Cusati, T.; Granucci, G.; Persico, M. *J. Am. Chem. Soc.* **2011**, *133*, 5109–5123.

[132] Böckmann, M.; Marx, D.; Peter, C.; Delle Site, L.; Kremer, K.; Doltsinis, N. L. *Phys. Chem. Chem. Phys.* **2011**, *13*, 7604–7621.

[133] Carstensen, N. O. *Phys. Chem. Chem. Phys.* **2013**, *15*, 15017–15026.

[134] Tiago, M. L.; Ismail-Beigi, S.; Louie, S. G. *J. Chem. Phys.* **2005**, *122*, 094311.

[135] Füchsel, G.; Klamroth, T.; Dokic, J.; Saalfrank, P. *J. Phys. Chem. B* **2006**, *110*, 16337–16345.

[136] Perkampus, H.-H. *UV-VIS Atlas of Organic Compounds*, 2nd ed.; VCH: Weinheim, 1992; Vol. 1.

[137] Asano, T. *J. Am. Chem. Soc,* **1980**, *102*, 1205–1206.

[138] Kumita, J. R.; Smart, O. S.; Woolley, G. A. *Proc. Natl. Acad. Sci. U. S. A.* **2000**, *97*, 3803.

[139] Liang, X.; Asanuma, H.; Komiyama, M. *J. Am. Chem. Soc.* **2002**, *124*, 1877–1883.

[140] Dohno, C.; Uno, S.; Nakatani, K. *J. Am. Chem. Soc.* **2007**, *129*, 11898–11899.

[141] Sadovski, O.; Beharry, A. A.; Zhang, F.; Woolley, G. A. *Angew. Chem. Int. Ed.* **2009**, *48*, 1484–1486.

[142] Zhang, F.; Zarrine-Afsar, A.; Al-Abdul-Wahid, M. S.; Prosser, R. S.; Davidson, A. R.; Woolley, G. A. *J. Am. Chem. Soc.* **2009**, *131*, 2283–2289.

[143] Schrader, T. E.; Cordes, T.; Schreier, W. J.; Koller, F. O.; Dong, S.-L.; Moroder, L.; Zinth, W. *J. Phys. Chem. B.* **2010**, *115*, 5219–5226.

[144] Goulet-Hanssens, A.; Barrett, C. J. *J. Polym. Sci. A1* **2013**, *51*, 3058–3070.

[145] Liu, Z. F.; Hashimoto, K.; Fujishima, A. *Nature* **1990**, *347*, 658–660.

[146] Ikeda, T.; Tsutsumi, O. *Science* **1995**, *268*, 1873–1875.

[147] Willner, I.; Rubin, S. *Angew. Chem. Int. Ed.* **1996**, *35*, 367–385.

[148] Ikeda, T.; Nakano, M.; Yu, Y.; Tsutsumi, O.; Kanazawa, A. *Adv. Mater.* **2003**, *15*, 201.

[149] Koshima, H.; Ojima, N.; Uchimoto, H. *J. Am. Chem. Soc.* **2009**, *131*, 6890–6891.

[150] Hu, Y.; Zhang, Z.; Chen, Y.; Zhang, Q.; Huang, W. *Opt. Lett.* **2010**, *35*, 46–48.

[151] Min, M.; Seo, S.; Lee, S. M.; Lee, H. *Adv. Mater.* **2013**, *25*, 7045–7050.

[152] Sobolewska, A.; Bartkiewicz, S.; Mysliwiec, J.; Singer, K. D. *J. Mater. Chem. C* **2014**, *2*, 1409–1412.

[153] Van den Mooter, G.; Samyn, C.; Kinget, R. *Int. J. Pharm.* **1994**, *87*, 37–46.

[154] Buffeteau, T.; Lagugné Labarthet, F.; Pézolet, M.; Sourisseau, C. *Macromolecules* **1998**, *31*, 7312–7320.

[155] Kang, M.; Gupta, V. K. *J. Phys. Chem. B* **2002**, *106*, 4127–4132.

[156] Acierno, D.; Amendola, E.; Bugatti, V.; Concilio, S.; Giorgini, L.; Iannelli, P.; Piotto, S. P. *Macromolecules* **2004**, *37*, 6418–6423.

[157] Yesodha, S. K.; Sadashiva Pillai, C. K.; Tsutsumi, N. *Prog. Polym. Sci.* **2004**, *29*, 45–74.

[158] Li, Y.; He, Y.; Tong, X.; Wang, X. *J. Am. Chem. Soc.* **2005**, *127*, 2402–2403.

[159] Tateishi, Y.; Tanaka, K.; Nagamura, T. *J. Phys. Chem. B* **2007**, *111*, 7761–7766.

[160] Mudiyanselage, T. K.; Neckers, D. C. *Soft Matter* **2008**, *4*, 768–774.

[161] Ando, H.; Tanino, T.; Nakano, H.; Shirota, Y. *Mater. Chem. Phys.* **2009**, *113*, 376–381.

[162] Jayalatha, D.; Balamurugan, R.; Kannan, P. *High Perform. Polym.* **2009**, *21*, 139–154.

[163] Deshmukh, S.; Bromberg, L.; Smith, K. A.; Hatton, T. A. *Langmuir* **2009**, *25*, 3459–3466.

[164] Pérez-Martínez, A. L.; Ogawa, T.; Aoyama, T.; Wada, T. *Opt. Mater.* **2009**, *31*, 912–918.

[165] El Ouazzani, H.; Iliopoulos, K.; Pranaitis, M.; Krupka, O.; Smokal, V.; Kolendo, A.; Sahraoui, B. *J. Phys. Chem. B* **2011**, *115*, 1944–1949.

[166] Pakula, C.; Hanisch, C.; Zaporojtchenko, V.; Strunskus, T.; Bornholdt, C.; Zargarani, D.; Herges, R.; Faupel, F. *J. Mat. Sci.* **2011**, *46*, 2488–2494.

[167] Fujii, T.; Kuwahara, S.; Katayama, K.; Takado, K.; Ube, T.; Ikeda, T. *Phys. Chem. Chem. Phys.* **2014**, *16*, 10485–10490.

[168] Junge, D. M.; McGrath, D. V. *J. Am. Chem. Soc.* **1999**, *121*, 4912–4913.

[169] Kim, M.-J.; Seo, E.-M.; Vak, D.; Kim, D.-Y. *Chem. Mater.* **2003**, *15*, 4021–4027.

[170] Abdallah, D.; Whelan, J.; Dust, J. M.; Hoz, S.; Buncel, E. *J. Phys. Chem. A* **2009**, *113*, 6640–6647.

[171] Kreger, K.; Wolfer, P.; Audorff, H.; Kador, L.; Stingelin-Stutzmann, N.; Smith, P.; Schmidt, H.-W. *J. Am. Chem. Soc.* **2010**, *132*, 509–516.

[172] Fatás, P.; Longo, E.; Rastrelli, F.; Crisma, M.; Toniolo, C.; Jiménez, A. I.; Cativiela, C.; Moretto, A. *Chem. Eur. J.* **2011**, *17*, 12606–12611.

[173] Hao, Y.-W.; Wang, H.-Y.; Huang, Y.-J.; Gao, B.-R.; Chen, Q.-D.; Li, L.-B.; Sun, H.-B. *J. Mater. Chem. C* **2013**, *1*, 5244–5249.

[174] Fujino, T.; Tahara, T. *J. Phys. Chem. A* **2000**, *104*, 4203–4210.

[175] Stolow, A. *Annu. Rev. Phys. Chem.* **2003**, *54*, 89–119.

[176] Löweneck, M.; Milbradt, A. G.; Root, C.; Satzger, H.; Zinth, W.; Moroder, L.; Renner, C. *Biophys. J.* **2006**, *90*, 2099–2108.

[177] Ciminelli, C.; Granucci, G.; Persico, M. *Chem. Phys.* **2008**, *349*, 325–333.

[178] Gil, M.; Wang, S.; Organero, J. A.; Teruel, L.; Garcia, H.; Douhal, A. *J. Phys. Chem. C* **2009**, *113*, 11614–11622.

[179] Gil, M.; Organero, J. A.; Peris, E.; García, H.; Douhal, A. *Chem. Phys. Lett.* **2009**, *474*, 325–330.

[180] Takei, M.; Yui, H.; Hirose, Y.; Sawada, T. *J. Phys. Chem. A* **2001**, *105*, 11395–11399.

[181] Qian, W.; Jonas, D. M. *J. Chem. Phys.* **2003**, *119*, 1611–1622.

[182] Hwang, I.; Selig, U.; Chen, S. S.; Shaw, P. E.; Brixner, T.; Burn, P. L.; Scholes, G. D. *J. Phys. Chem. A* **2013**, *117*, 6270–6278.

[183] Rode, M. F.; Sobolewski, A. L. *J. Phys. Chem. A* **2010**, *114*, 11879–11889.

[184] Kwon, J. E.; Park, S. Y. *Adv. Mater.* **2011**, *23*, 3615–3642.

[185] Rode, M. F.; Sobolewski, A. *J. Chem. Phys.* **2014**, *140*, 084301.

[186] Heberle, J.; Riesle, J.; Thiedemann, G.; Oesterhelt, D.; Dencher, N. A. *Nature* **1994**, *370*, 379–382.

[187] Stowell, M.; McPhillips, T.; Rees, D.; Soltis, S.; Abresch, E.; Feher, G. *Science* **1997**, *276*, 812–816.

[188] Luecke, H.; Richter, H.-T.; Lanyi, J. K. *Science* **1998**, *280*, 1934–1937.

[189] Sobolewski, A. L.; Domcke, W. *Phys. Chem. Chem. Phys.* **2004**, *6*, 2763–2771.

[190] Schwalb, N. K.; Temps, F. *J. Am. Chem. Soc.* **2007**, *129*, 9272–9273.

[191] Han, K.-L.; Zhao, G.-J. *Hydrogen bonding and transfer in the excited state*; Wiley: Chichester, UK, 2011; Vol. 1&2.

[192] Migliore, A.; Polizzi, N. F.; Therien, M. J.; Beratan, D. N. *Chem. Rev.* **2014**,

[193] Douhal, A.; Lahmani, F.; Zewail, A. H. *Chem. Phys.* **1996**, *207*, 477–498.

[194] Elsaesser, T.; Bakker, H. J. *Ultrafast hydrogen bonding dynamics and proton transfer processes in the condensed phase*; Kluwer Academic Publishers: Dordrecht, 2002.

[195] Hsieh, C.-C.; Jiang, C.-M.; Chou, P.-T. *Accounts Chem. Res.* **2010**, *43*, 1364–1374.

[196] Pospisil, J.; Nespurek, S. *Prog. Polym. Sci.* **2000**, *25*, 1261–1335.

[197] Wiechmann, M.; Port, H.; Laermer, F.; Frey, W.; Elsaesser, T. *Chem. Phys. Lett.* **1990**, *165*, 28–34.

[198] Wiechmann, M.; Port, H.; Frey, W.; Laermer, F.; Elsaesser, T. *The Journal of Physical Chemistry* **1991**, *95*, 1918–1923.

[199] Sobolewski, A. L.; Domcke, W. *Chem. Phys.* **1994**, *184*, 115–124.

[200] Sobolewski, A. L.; Domcke, W. *Phys. Chem. Chem. Phys.* **1999**, *1*, 3065–3072.

[201] Lochbrunner, S.; Schultz, T.; Schmitt, M.; Shaffer, J.; Zgierski, M.; Stolow, A. *J. Chem. Phys.* **2001**, *114*, 2519–2522.

[202] Stock, K.; Bizjak, T.; Lochbrunner, S. *Chem. Phys. Lett.* **2002**, *354*, 409–416.

[203] Migani, A.; Blancafort, L.; Robb, M. A.; DeBellis, A. D. *J. Am. Chem. Soc.* **2008**, *130*, 6932–6933.

[204] Formosinho, S. J.; Arnaut, L. G. *J Photoch. Photobio A* **1993**, *75*, 21–48.

[205] Sobolewski, A. L.; Domcke, W. *Phys. Chem. Chem Phys.* **2006**, *8*, 3410–3417.

[206] Jankowska, J.; Rode, M. F.; Sadlej, J.; Sobolewski, A. L. *ChemPhysChem* **2012**, *13*, 4287–4294.

[207] Ameer-Beg, S.; Ormson, S. M.; Brown, R. G.; Matousek, P.; Towrie, M.; Nibbering, E. T.; Foggi, P.; Neuwahl, F. V. *J. Phys. Chem. A* **2001**, *105*, 3709–3718.

[208] Douhal, A.; Sanz, M.; Carranza, M.; Organero, J.; Santos, L. *Chem. Phys. Lett.* **2004**, *394*, 54–60.

[209] Lochbrunner, S.; Wurzer, A.; Riedle, E. *J. Chem. Phys.* **2000**, *112*, 10699–10702.

[210] Lochbrunner, S.; Wurzer, A. J.; Riedle, E. *J. Phys. Chem. A* **2003**, *107*, 10580–10590.

[211] Sobolewski, A. L.; Domcke, W.; Hättig, C. *J. Phys. Chem. A* **2006**, *110*, 6301–6306.

[212] Iijima, T.; Momotake, A.; Shinohara, Y.; Sato, T.; Nishimura, Y.; Arai, T. *J. Phys. Chem. A* **2010**, *114*, 1603–1609.

[213] Kim, T. G.; Topp, M. R. *J. Phys. Chem. A* **2004**, *108*, 10060–10065.

[214] Bhattacharya, B.; Samanta, A. *J. Phys. Chem. B* **2008**, *112*, 10101–10106.

[215] Neuwahl, F. V.; Bussotti, L.; Righini, R.; Buntinx, G. *Phys. Chem. Chem. Phys.* **2001**, *3*, 1277–1283.

[216] Schmidtke, S. J.; Underwood, D. F.; Blank, D. A. *J. Phys. Chem. A* **2005**, *109*, 7033–7045.

[217] Nagaoka, S.; Uno, H.; Huppert, D. *J. Phys. Chem. B* **2012**, *117*, 4347–4353.

2

EXPERIMENTAL SECTION

Understanding the ultrafast dynamics of different photochromic molecular switches is of particular importance regarding the ambitious design goals for optimal functional devices. The associated processes typically take place on a femtosecond to picosecond time scale and thus require ultrasensitive spectroscopic techniques with femtosecond time resolutions. Due to the slow response times of electronic detectors, femtosecond time-resolved methods are based on the pump-probe principle which is shown schematically in Fig. 2.1. The sample molecules are electronically excited

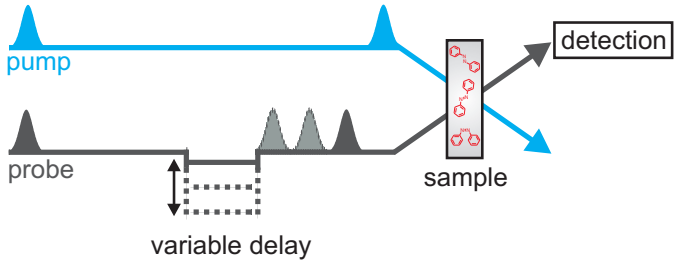

Figure 2.1: Schematic depiction of the pump-probe principle.

by an ultrashort pump pulse. The molecular response at a certain delay time is monitored by a probe pulse, which is temporally delayed with respect to the pump pulse *via* an optical delay line. The time resolution of the experiment is thus only limited by the temporal width of pump and probe pulse and not by the speed of the electronic detection.

In the context of this Thesis, both the deactivation of the electronically excited states and the dynamics in the electronic ground state play a significant role. Therefore, the dynamics of several azobenzene (AB) switches under different circumstances[1–5] and a bistable intramolecular proton transfer switch[6,7] have been investigated by means of femtosecond time-resolved fluorescence and absorption spectroscopy as complementary methods to monitor the dynamics in optically bright and dark states as well as the recovery of the electronic ground sate. The generation of ultrashort laser pulses that are needed for both experiments is based on nonlinear processes. These are described in detail in several previous PhD Theses written in the research group[8–12] and in a number of textbooks.[13–16] This Chapter can therefore be kept relatively brief.

A description of the broadband and single color transient absorption and the single color fluorescence up-conversion setups are given in Sections 2.1 and 2.2, respectively. Both systems are based on a regeneratively amplified Ti:Sa laser (Clark MXR CPA 2001), which delivers pulses with a duration of 120 fs (Full Width at Half Maximum, FWHM) with a repetition rate of 1 kHz and an energy of 1000 µJ at a center wavelength of 775 nm. A detailed description of the entire laser system can be found

elsewhere.[8,10] 500 μJ of the laser output are used to generate the pump and the probe pulses for the transient absorption setup. Three-quarters of the other half (375 μJ) are used in the fluorescence setup. The remaining 125 μJ are needed for an SHG (Second Harmonic Generation) experiment in our laboratory.

Explanation of the data analysis procedures can be found in Sections 2.1 and 2.2.

Further details of the static UV/VIS absorption, fluorescence and NMR measurements and the preparation and the handling of the different samples are given in the respective experimental sections of Chapters 3-9.

2.1 Femtosecond time-resolved single color and broadband transient absorption spectroscopy

A schematic overview of the complete femtosecond time-resolved broadband and single color transient absorption setup in our laboratory in its current status is depicted in Fig. 2.2. Details have been given previously.[17,18] The experiment consists of four major parts: The generation of the pump pulses, the generation of the supercontinuum broadband probe pulses, the generation of the single color probe pulses and the detection units for the respective probe pulses.

(i) Pump pulse generation

A so called non-collinear optical parametric amplifier (NOPA) pumped with $\approx$ 250 μJ of the laser fundamental delivered pulses in a wavelength range from 450 nm $\leqslant \lambda \leqslant$ 700 nm. The NOPA principle[19–21] and the handling of the respective optical setup have been described in detail in former Theses from the work group.[9–12,22] The obtained NOPA pulses with typical energies of $\approx 8-20$ μJ and a duration of $\approx$ 200 fs were temporally compressed in a pair of two BK7 prisms to a temporal width of $\approx 25-40$ fs. The pulse energy after the prism compressor was typically between 5 and 15 μJ depending on the wavelength. A spectrum of a NOPA output at a wavelength of $\lambda = 520$ nm is given in Fig. 2.3 a). The temporal behavior of the NOPA pulses was characterized with an autocorrelator (APE, PulseScope). For the complete characterization of the pulse, an SHG FROG (Frequency-resolved optical gating)[23] system (FROG Scan, Mesa Photonics) was employed, which allows for the characterization of ultrafast laser pulses in the visible and near infrared range. An autocorrelation function and a FROG trace of the NOPA output at $\lambda = 520$ nm are shown in Figs. 2.3 b) and c). In addition to the temporal information of the pulse, which can also be obtained by a simple autocorrelation measurement, the FROG measurement yields the desired spectral information. The resulting FROG trace contains information about the phase of the pulse and the amplitude. Thus the big advantages of the FROG system compared to the simple autocorrelator are that the chirp of a pulse or possible double pul-

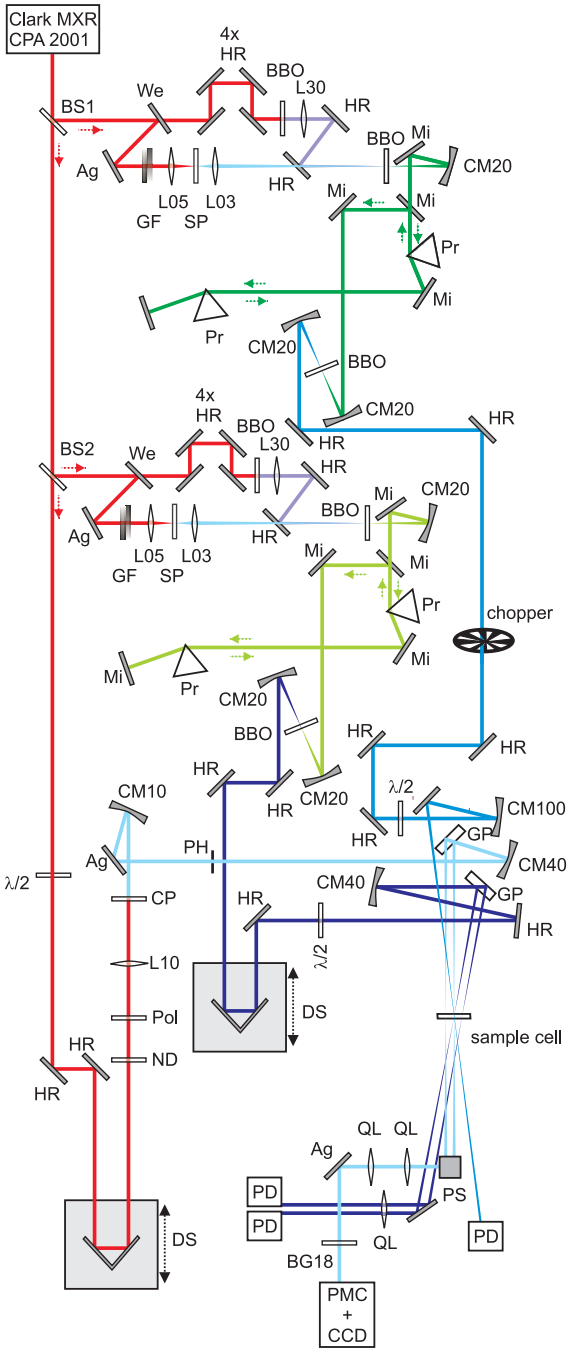

Ag	planar Ag mirror
BBO	β-BaB_2O_4 crystal
BG18	BG18 filter
BS1	beamsplitter, R=50%
BS2	beamsplitter, R=70%
CCD	FFT-CCD cameras
CM20	concave mirror, rcc = 0.2m
CM40	concave mirror, rcc = 0.4 m
CM100	concave mirror, rcc = 1 m
CP	CaF_2 plate (d = 2 mm)
DS	delay stage with retroreflector
GF	gradient filter
GP	quartz glass plate (planar)
HR	high reflective mirror
λ/2	half-wave plate
L03	lens, f = 30 mm
L05	lens, f = 50 mm
L10	lens, f = 100 mm
L30	lens, f = 300 mm
Mi	planar Ag or Al mirror
ND	neutral density filter
PD	photodiode
Pol	polarizer
PH	pinhole
PMC	prism monochromator
Pr	BK7 prism
PS	periscope
QL	quartz lens
SP	sapphire plate
We	wedge (30´)

Figure 2.2: Scheme of the experimental setup of the femtosecond broadband and single color transient absorption experiment (left) and abbreviations of the respective optical components (right). The colors of the beams are chosen arbitrarily and do not necessarily reflect the real wavelength.

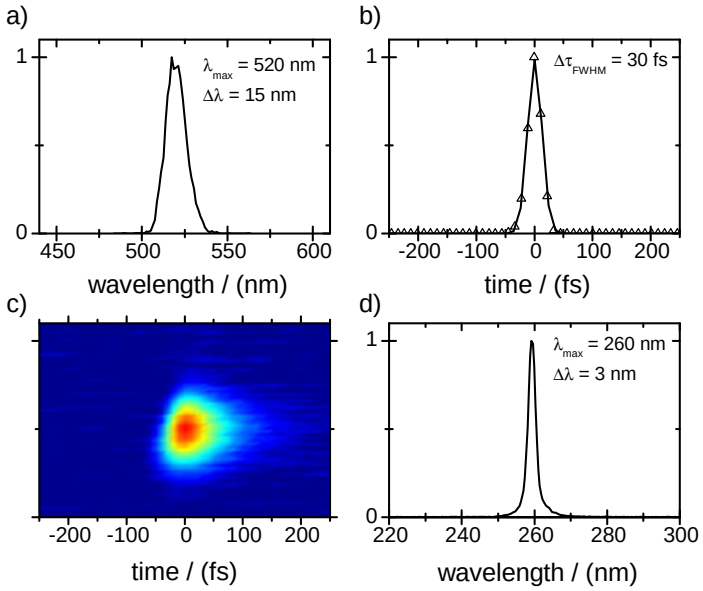

Figure 2.3: a) NOPA spectrum at $\lambda = 520$ nm with a spectral width of $\lambda \approx 15$ nm, b) autocorrelation function of the compressed pulse with a temporal width of $\approx$ 30 fs at $\lambda = 520$ nm, c) typical FROG trace of the compressed $\lambda = 520$ nm pulse and d) spectrum of the frequency-doubled NOPA pulse at $\lambda = 260$ nm with a spectral width of $\lambda \approx 3$ nm.

ses can be easily observed and corrected, making the optimization of the setup much more convenient.

For excitation in the visible wavelength range, the pump pulses were directly delivered from the NOPA and focused into the sample cell immediately after passing the prism compressor. The energy of the pulses had to be reduced to typical values of $\approx 0.2 - 0.5$ µJ depending on the sample molecules. For UV excitation, the compressed NOPA pules were frequency-doubled in a suitable non-linear crystal (usually BBO). A spectrum of a frequency-doubled 520 nm pulse with a center wavelength of $\lambda = 260$ nm is depicted in Fig. 2.3 d). The generated UV pump pulses with typical energies of $\approx 0.1 - 0.7$ µJ were attenuated if necessary and focused into the sample cell. The beam diameter of the pump pulses in the focus was typically in the range of $\approx 200 - 400$ µm. Every second pump pulse was blocked by a chopper to allow for the recording of background spectra of the probe pulses and possible other contributions to the background without the pump pulse.

(ii) Broadband probe pulse generation

After passing the computer controlled delay line equipped with an Al-coated retroreflector, a set of neutral density filters and a polarizer, ≈ 75 µJ of the laser fundamental were attenuated to an energy of ≈ 2 µJ. This part was used to generate broadband supercontinuum probe pulses in CaF_2 between 320 nm $\leqslant \lambda_{\text{probe}} \leqslant$ 750 nm. Due to the low damage threshold of CaF_2, the plate was moved horizontally and vertically without rotation. A detailed description of the whitelight generation and the optimization of

the spectrum and stability of the obtained broadband pulses is given in the Thesis of R. Siewertsen.[12] Only minimal changes in the energy of the incoming 775 nm pulses can involve drastic changes in the resulting spectrum and especially in the stability. Therefore a polarizer in combination with $\lambda/2$ plate instead of two gradient filters was installed into the beam path to adjust the energy very precisely.[18]

The generated pulses were split into probe and reference beam and focused into the sample cell. The probe pulses with a focal diameter of $\approx 100-150$ µm were spatially and temporally overlapped with the pump pulses, hence the reference pulses passed unexcited sample volume.

(iii) Single color probe pulse generation

Single color detection is generally used to follow the ground state recovery (GSR) of sample molecules whose electronic transitions from the electronic ground state to higher electronic states are located in the UV. In these cases the GSR is typically not covered by the broadband detection pulses (320 nm $\leqslant \lambda_{probe} \leqslant$ 750 nm) and has to be followed separately by UV single color probe pulses to obtain information about the overall excited state lifetimes.

The single color probe pulses with energies between $\approx 0.1-0.5$ µJ were also delivered by a frequency-doubled NOPA, which is pumped with $\approx$ 175 µJ of the laser fundamental. Back- and front-side reflection of a quartz glass plate were used to split the pulses into probe and reference. The probe pulses were also focused into the sample cell and overlapped with the pump pulses. The focal diameter was $\approx 100-150$ µm as for the broadband detection pulses. The energy of the probe pulse at the sample cell was $\approx 0.01-0.015$ µJ. The pump-probe time delay was also set with a retroreflector on a computer controlled translation stage. The angles between the pump pulse, the broadband probe pulses and the single color probe pulses were kept as small as possible. The optical pathways and the alignment of the respective pulses in front of the sample cell and after passing the cell at the detection units were described in the Thesis of K. Röttger.[18]

All transient absorption measurements in 2-fluorotoluene, water, *n*-hexane and cyclohexane were performed in home-built flow cells with 0.2 mm quartz windows and optical path lengths of 0.1 mm and 1 mm, respectively, depending on solubility and behavior of the sample molecules in the chosen solvent. The samples in these solvents were pumped through the cell with a peristaltic pump to prevent product deposition on the cell windows. Since the seals of the cells are not resistant against acetonitrile (AcCN), measurements with AcCN were performed in a flow cuvette (Hellma Analytics, Art. No. 170-101-0.1-40) with an optical path length of 0.1 mm and 0.4 mm quartz windows and without any seals. A gear pump equipped with teflon tubes was used to pump the sample through the cuvette.

In general the pump pulse polarization was set to the magic angle polarization (54.7°) with respect to the probe pulse. For anisotropy decay measurements, the parallel and perpendicular pump-probe configuration were selected using a suitable $\lambda/2$ plate. The polarization of the probe pulses was kept fixed.

(iv) Probe pulse detection

After passing the sample cell, the transmitted broadband probe and reference pulses were spectrally dispersed in a prism spectrograph and detected with two FFT-CCD cameras, which are read out with the laser frequency of 1 kHz. The single color probe and reference pulses were detected by a pair of two matched photodiodes. A photodiode in the pump beam path indicates whether the pump beam is blocked or not. The details, the handling and the specifications of the detection parts can be found elsewhere.[17,18]

Further experimental details and conditions for each measurement for the different samples and different excitation and probe wavelengths are given in the respective Chapters 3-9. Unless stated otherwise, each scan was repeated three times to ensure reproducibility of the measurements.

DATA PROCESSING AND ANALYSIS

Calculation of the change in optical density (ΔOD)

The changes in the optical density $\Delta OD(\lambda, \Delta t)$ were calculated directly during the measurements by comparison of the intensities of the probe (I_{pr}) and reference pulses (I_{ref}) according to

$$\Delta OD(\lambda, \Delta t) = \frac{I_{pr}(\lambda, \Delta t) \cdot I^0_{ref}(\lambda, \Delta t)}{I^0_{pr}(\lambda, \Delta t) \cdot I_{ref}(\lambda, \Delta t)} \quad (1)$$

with $I^0_{pr/ref}$ as the intensities of the respective pulses with the sample molecules being unexcited (pump pulse blocked). $I_{pr/ref}$ are the intensities of probe and reference pulses for the excited system (pump pulses unblocked).

Coherent artifacts

The high intensities of the femtosecond laser pulses induce coherent artifacts around the experimental time zero, at which the pump and probe pulses temporally overlap in the sample volume. These non-molecular contributions to the transient absorption signal include several effects: The transient modulation of the refractive index in the cell windows and the solvent (cross-phase modulation (XPM)) by the pump pulse induce a phase shift of the weak probe pulse.[24–26] Additionally, two-photon or multi-photon absorption (TPA or MPA) of pump and probe photons can occur in the windows of the sample cell and the solvent. In case of solvents

with free electron pairs, especially water, this might lead to long-lived solvated electron absorption (SEA). If the difference of the frequency of pump and probe corresponds to the frequency of a vibrational mode of the solvent stimulated Raman scattering (SRS) will be observed. All these effects strongly depend on the excitation wavelength, the energies, the temporal widths and the chirp of the pulses, the optical path length of the sample cell, the thickness of cell windows and the solvent. Measurements of the pure solvent before or after each sample measurement enabled the deconvolution of coherent artifacts and molecular signals. The former were subtracted from the results of the sample measurements with suitable scaling factors.[25] If present, the temporal width of the SRS signal can be used to determine the time resolution of the experiment. Details on the transient artifacts and their correction in our setup can be found elsewhere.[12,18]

Data analysis

To obtain the spectro-temporal two-dimensional transient absorption maps not only the correction of the transient artifacts is needed but also a correction of the experimental time zero, which differs for each detection wavelength due to the chirp of the supercontinuum probe pulses. The correction procedure has been described in detail elsewhere.[12] The wavelength calibration was done with a set of bandpass interference filters.[18] All presented data in this Thesis below are time zero and solvent corrected.

The correction procedures as well as the extraction of selected transient spectra and time profiles were done using self-written MATHEMATICA[27] programs.[12,18] The required non-linear least-squares fitting routines for the global description of the transient absorption-time profiles are based on the Levenberg-Marquardt algorithm and were also self-written[12] and implemented in MATHEMATICA.[27]

In general, the time profiles were analyzed in a global fashion using a sum of exponential decay functions of the form

$$A_\lambda(t) = \sum_i a_i \times \exp\left(-\frac{t - t_0}{\tau_i}\right) \tag{2}$$

whereby a_i is the amplitude and τ_i the decay time. The formation of possible products and permanent bleaches of the electronic ground state were described using additional rise and step functions, respectively.

In the case of the ultrafast dynamics of the *push-pull* azobenzene Direct Red 1 a sequential relaxation pathway after $\pi\pi^*$ excitation was suggested. In this case, the data were fitted using a consecutive kinetic model, which is formally equivalent to the sum of two exponentials. The details can be found in Chapter 3. Further information on this and other fit models can be found in the Thesis of R. Siewertsen.[12]

The temporal width of the pulses was taken into account by the convolution of the exponentials with a Gaussian shaped instrument response function (IRF) of the form

$$G(t, \sigma_{IRF}) = \frac{1}{\sigma_{IRF}\sqrt{2\pi}} \times \exp\left(-\frac{t - t_0}{2\sigma_{IRF}^2}\right). \quad (3)$$

σ_{IRF} can be viewed as the time resolution of the experiment and is correlated to the full width at half maximum of the IRF by

$$IRF_{FWHM} = 2 \times \sqrt{2 \times \ln 2} \times \sigma_{IRF}. \quad (4)$$

The time resolution of the transient absorption experiment was determined from the stimulated Raman scattering (SRS) signal of the solvent or from the IRF fit parameters and was typically in the range of $\approx 30 - 40$ fs and ≈ 60 fs for excitation in the visible and in the UV, respectively.

The contributions of the coherent artifacts at selected probe wavelengths were fitted using a sum of Gaussian shaped functions and if necessary with additional exponentials. Afterwards the correction functions of the solvent were scaled with suitable factors and included in the global fitting routine.[18]

2.2 Femtosecond time-resolved single color fluorescence up-conversion spectroscopy

A schematic overview of the current setup of the femtosecond time-resolved single color fluorescence up-conversion experiment is shown in Fig. 2.4. A detailed description can be found elsewhere.[8,11] The experimental setup can be divided into three major parts: The generation of the pump pulses, the beam path of the gate pulses and the fluorescence up-conversion part with the detection unit.

(i) Pump pulse generation

As for the transient absorption experiment, the UV or visible pump pulses for the fluorescence up-conversion setup were delivered by a frequency doubled NOPA or by a compressed NOPA itself, respectively. The NOPA was pumped with ≈ 250 µJ of the laser fundamental. The resulting pulses were reduced to a maximum energy of 0.25 µJ and then focused into the sample cell, typically a home-built flow cell of 1 mm optical path length with 0.2 mm quartz windows. For the measurements in acetonitrile a 1 mm flow cuvette (Hellma Analytics, Art. No. 137-1-40) with 1 mm quartz was used due to the low resistance of seals against the solvent. The concentrations of the sample solutions were set to an optical density below 0.5 at the excitation wavelength. A bandpass filter (WG320 or OG550, depending on pump and fluorescence wavelength) and a beam stop directly after the sample cell blocked the pump pulses and any scattered pump light.

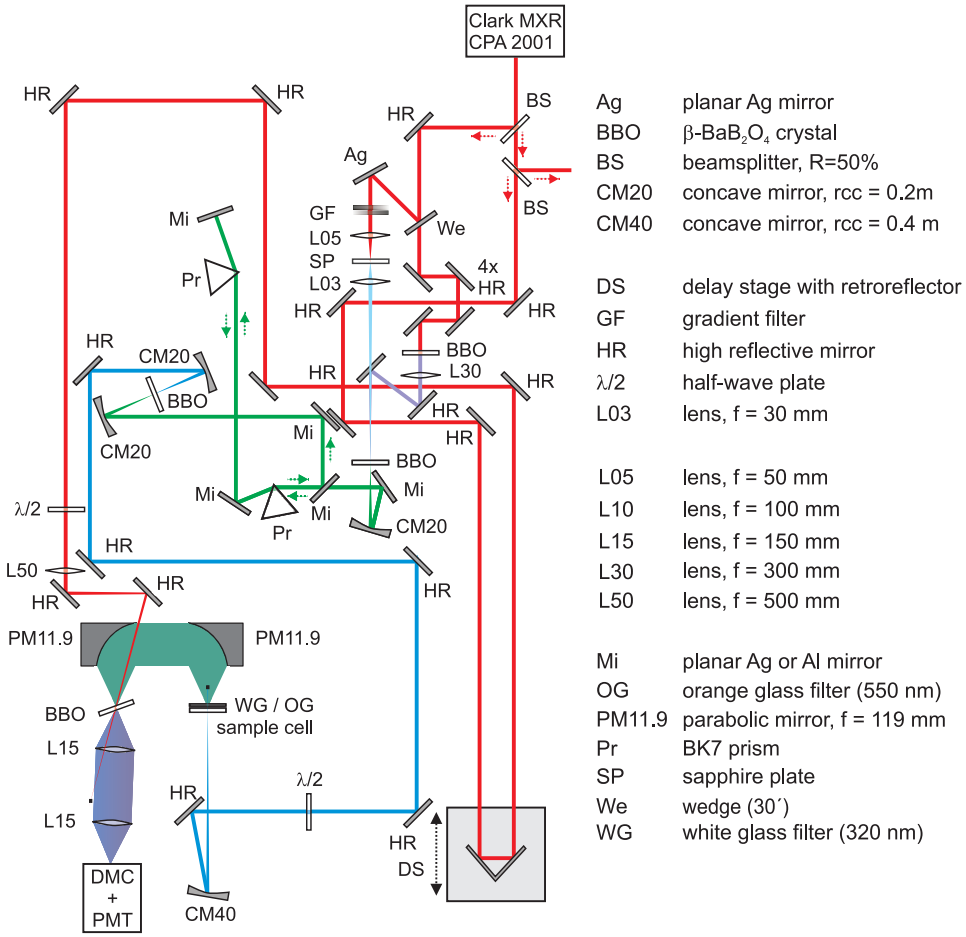

Ag	planar Ag mirror
BBO	β-BaB_2O_4 crystal
BS	beamsplitter, R=50%
CM20	concave mirror, rcc = 0.2m
CM40	concave mirror, rcc = 0.4 m
DS	delay stage with retroreflector
GF	gradient filter
HR	high reflective mirror
λ/2	half-wave plate
L03	lens, f = 30 mm
L05	lens, f = 50 mm
L10	lens, f = 100 mm
L15	lens, f = 150 mm
L30	lens, f = 300 mm
L50	lens, f = 500 mm
Mi	planar Ag or Al mirror
OG	orange glass filter (550 nm)
PM11.9	parabolic mirror, f = 119 mm
Pr	BK7 prism
SP	sapphire plate
We	wedge (30´)
WG	white glass filter (320 nm)

Figure 2.4: Schematic overview of the femtosecond single color fluorescence up-conversion setup (left) and abbreviations of the respective optical components (right). The colors of the beams are chosen arbitrarily and do not necessarily reflect the real wavelength.

For all measurements the pump pulse polarization was set to the magic angle with respect to the gate pulse using a suitable $\lambda/2$ plate.

(ii) Beam path of the gate pulse

125 µJ of the laser fundamental were used as gate pulses. After passing the computer-controlled delay stage equipped with a retroreflector the energy was $\approx 60-70$ µJ. The pulses were then focused into the up-conversion BBO for type I sum frequency generation ($\theta = 54.4°, \phi = 0°$) or type II sum frequency generation ($\theta = 51°, \phi = 30°$ or $\theta = 43.3°, \phi = 30°$) for the different emission wavelength after excitation in the UV or in the visible, respectively. A suitable $\lambda/2$ plate set the polarization of the gate pulses in a way that the *ooe* and *oeo* phase matching conditions for type I and type II sum frequency generation, respectively, were fulfilled.

(iii) Fluorescence up-conversion and detection

The emission by the sample molecules was collected by a pair of off-axis parabolic mirrors, refocused into the up-conversion BBO and spatially and temporally overlapped with the gate pulses. The fluorescence photons were up-converted into photons of sum frequency by type I or type II sum frequency generation (SFG), which depends on the respective fluorescence wavelengths. The intensity of the obtained SFG signal is directly correlated to the intensity of the fluorescence. After passing a double monochromator the up-converted light was detected with a photomultiplier connected to a gated photon counter.

Depending on each fluorescence wavelength and the respective phase matching conditions, the tilt angle Ω of the BBO up-conversion crystal was manually optimized by rotation around the vertical axis.

Additional details of the experimental conditions for each measurement are given in the respective Chapters 3-9. Unless otherwise stated, each scan was repeated at least twice to ensure the reproducibility.

DATA ANALYSIS

The obtained single color fluorescence-time profiles were analyzed as the absorption-time profiles using a sum of exponentials. No further data processing was necessary.

The time resolution of the experiment was determined by the temporal width of a cross correlation signal of the gate pulse and scattered pump light and was typically in the range of $\approx 80-100$ fs for excitation in the visible and $\approx 130-150$ fs for excitation in the UV.

BIBLIOGRAPHY

[1] Bahrenburg, J.; Röttger, K.; Siewertsen, R.; Renth, F.; Temps, F. *Photochem. Photobiol. Sci.* **2012**, *11*, 1210–1219.

[2] Bahrenburg, J.; Sievers, C. M.; Schönborn, J. B.; Hartke, B.; Renth, F.; Temps, F.; Näther, C.; Sönnichsen, F. D. *Photochem. Photobiol. Sci.* **2013**, *12*, 511–518.

[3] Bahrenburg, J.; Temps, F. to be published.

[4] Bahrenburg, J.; Renth, F.; Plamper, F.; Richtering, W.; Temps, F. *Phys. Chem. Chem Phys.* **2014**, *16*, 11549–11554.

[5] Bahrenburg, J.; Böhnke, H.; Bohnsack, M.; Dommaschk, M.; Herges, R.; Temps, F. to be published.

[6] Bahrenburg, J.; Rode, M. F.; Sobolewski, A. L.; Temps, F. *Ultrafast Phenomena XIX* **2014**, accepted.

[7] Bahrenburg, J.; Rode, M. F.; Nowacki, J.; Näther, C.; Sobolewski, A. L.; Temps, F. to be published.

[8] Pancur, T. Investigation of the Isomerization Dynamics of Azobenzenes and the Radiationless Deactivation of Nucleobases Using Femtosecond Fluorescence Spectroscopy. Ph.D. Thesis, Christian-Albrechts-Universität zu Kiel, Kiel, 2004.

[9] Foca, M. Investigations of Ultrafast Photoisomerization of Photochromic Molecular Switches by fs-Time-Resolved Transient Absorption Spectroscopy. Ph.D. Thesis, Christian-Albrechts-Universität zu Kiel, 2005.

[10] Studzinski, H. Ultrafast Radiationless Dynamics of Selected Electronically Excited Aromatic Molecules by Femtosecond Time-Resolved Mass Spectrometry and Photoelectron Imaging. Ph.D. Thesis, Christian-Albrechts-Universität zu Kiel, 2007.

[11] Schwalb, N. K. Ultrafast Electronic Deactivation Dynamics in DNA Model Systems by Femtosecond UV Fluorescence Spectroscopy. Ph.D. Thesis, Christian-Albrechts-Universität zu Kiel, 2009.

[12] Siewertsen, R. Ultrafast Photochromic Reactions of Structurally Modified Furylfulgides and a Bridged Azobenzene. Ph.D. Thesis, Christian-Albrechts-Universität zu Kiel, 2011.

[13] Mukamel, S. *Principles of Nonlinear Optical Spectroscopy*; Oxford Series in Optical and Imaging Sciences; Oxford University Press: New York, 1995.

[14] Demtröder, W. *Laserspektroskopie: Grundlagen und Techniken*; Springer, Berlin, 2000.

[15] Meschede, D. *Optik, Licht und Laser*; Teubner, Wiesbaden, 2005.

[16] Boyd, R. W. *Nonlinear Optics*; Elsevier Inc., Amsterdam, 2008.

[17] Röttger, K.; Siewertsen, R.; Temps, F. *Chem. Phys. Lett.* **2012**, *536*, 140–146.

[18] Röttger, K. Ultrafast Deactivation Dynamics of Structurally Modified and Hydrogen-Bonded DNA and RNA Building Blocks. Ph.D. Thesis, Christian-Albrechts-Universität zu Kiel, 2013.

[19] Wilhelm, T.; Piel, J.; Riedle, E. *Opt. Lett.* **1997**, *22*, 1494–1496.

[20] Riedle, E.; Beutter, M.; Lochbrunner, S.; Piel, J.; Schenkl, S.; Sporlein, S.; Zinth, W. *Applied Physics B: Lasers and Optics* **2000**, *71*, 457–465.

[21] Cerullo, G.; De Sivestri, S. *Rev. Sci. Instrum.* **2003**, *74*, 1–18.

[22] Studzinski, H. Aufbau und Charakterisierung eines nicht-kollinearen optisch-parametrischen Verstärkers. Diploma Thesis, Christian-Albrechts-Universität zu Kiel, 2002.

[23] Trebino, R.; DeLong, K. W.; Fittinghoff, D. N.; Sweetser, J. N.; Krumbügel, M. A.; Richman, B. A.; Kane, D. J. *Rev. Sci. Instrum.* **1997**, *68*, 3277–3295.

[24] Ekvall, K.; van der Meulen, P.; Dhollande, C.; Berg, L.-E.; Pommeret, S.; Naskrecki, R.; Mialocq, J.-C. *J. Appl. Phys.* **2000**, *87*, 2340–2352.

[25] Lorenc, M.; Ziolek, M.; Naskrecki, R.; Karolczak, J.; Kubicki, J.; Maciejewski, A. *Appl. Phys. B: Lasers Opt.* **2002**, *74*, 19–27.

[26] Dobryakov, A. L.; Kovalenko, S. A.; Ernsting, N. P. *J. Chem. Phys.* **2005**, *123*, 044502.

[27] Wolfram Research, I. *Mathematica*, version 8.0 ed.; Wolfram Research, Inc., 2010.

Part II

RESULTS AND DISCUSSION

3

SEQUENTIAL PHOTOISOMERISATION DYNAMICS OF THE PUSH-PULL AZOBENZENE DISPERSE RED 1

Julia Bahrenburg, Katharina Röttger, Ron Siewertsen, Falk Renth* and Friedrich Temps*

Institut für Physikalische Chemie, Christian-Albrechts-Universität zu Kiel, Olshausenstr. 40, 24098 Kiel, Germany

J. Bahrenburg, K. Röttger, R. Siewertsen, F. Renth and F. Temps *Photochem. Photobiol. Sci.*, **2012**, *11*, 1210-1219.

OWN CONTRIBUTIONS TO THIS MANUSCRIPT:

- Time-resolved fluorescence spectroscopy
- Static absorption and fluorescence spectroscopy
- Analysis of the transient absorption and fluorescence up-conversion data
- Writing of the manuscript

* To whom correspondence should be addressed. E-mail: renth@phc.uni-kiel.de, temps@phc.uni-kiel.de

ABSTRACT

The ultrafast dynamics of the push-pull azobenzene Disperse Red 1 following photoexcitation at $\lambda_{pump} = 475$ nm in solution in 2-fluorotoluene have been probed by broadband transient absorption spectroscopy and fluorescence up-conversion spectroscopy. The measured two-dimensional spectro-temporal absorption map features a remarkable "fast" excited-state absorption (ESA) band at $\lambda \approx 570$ nm appearing directly with the excitation laser pulse and showing a sub-100 fs lifetime with a rapid spectral blue-shift. Moreover, its ultrafast decay is paralleled by rising distinctive ESA at other wavelengths. Global fits to the absorption-time profiles using a consecutive kinetic model yielded three time constants, $\tau_1 = 0.08 \pm 0.03$ ps, $\tau_2 = 0.99 \pm 0.02$ ps, and $\tau_3 = 6.0 \pm 0.1$ ps. Fluorescence-time profiles were biexponential with time constants $\tau'_1 = 0.12 \pm 0.06$ ps and $\tau'_2 = 0.70 \pm 0.10$ ps, close to the absorption results. Based on the temporal evolution of the transient spectra, especially the "fast" excited-state absorption band at $\lambda \approx 570$ nm, and on the global kinetic analysis of the time profiles, τ_1 is assigned to an ultrafast transformation of the optically excited $\pi\pi^*$ state to an intermediate state, which may be the $n\pi^*$ state, τ_2 to the subsequent isomerisation and radiationless deactivation time to the S_0 electronic ground state, and τ_3 to the eventual vibrational cooling of the internally "hot" S_0 molecules.

3.1 INTRODUCTION

The reversible E $\rightleftarrows$ Z photoisomerisation reaction of azobenzene (AB) forms the basis for numerous applications of AB derivatives as photochromic molecular switches, tiny light-driven molecular manipulators, actuators and engines, or smallest optical memory and logical devices.[1–6] The high potential of AB as photoswitchable element rests on the large changes in molecular size, shape and dipole moment induced by light at ultraviolet to visible (UV/VIS) wavelengths and on the low photochemical fatigue of the chromophore. To reach many ambitious rational design goals for optimised functional AB devices, however, it is mandatory to have detailed knowledge about the ensuing molecular dynamics under different circumstances.

Of major importance for applications is that substituents at the AB core may hugely affect the photoisomerization dynamics by electronic and by steric effects. A special class are electron donor-electron acceptor substituted AB dyes like Disperse Red 1 [4-(N-ethyl-N-2-hydroxy)amino-4′-nitro-azobenzene, DR1; Scheme 1].

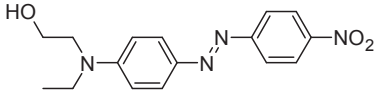

Disperse Red 1 (DR1)

Scheme 1.

DR1 is a so-called push-pull azobenzene, in which the donor-acceptor substitution introduces a strong charge transfer (CT) character into the $\pi\pi^*$ electronic transition.[4,7,8] Compared to unsubstituted AB, this leads to a large red-shift of the $\pi\pi^*$ absorption band from the near-UV into the visible spectrum such that it overlaps with the normally much weaker $n\pi^*$ transition.[9–11] At the same time, the energy barrier between the two isomers in the S_0 electronic ground state is lowered to the extent that the thermal $Z \rightarrow E$ back-isomerisation at room temperature happens in times of just seconds to milliseconds, depending on the solvent, much faster than in normal AB.[12,13] These factors, together with the large photo-induced structural change, determine the specific application profile for, *e.g.*, tailored surface functionalisation, light-induced material deformation, surface-relief formation, nonlinear optics, or charge separation in organic photovoltaic and ferroelectric materials.[7,14–19] DR1 is of particular practical interest because of its hydroxy group, which can be employed as a covalent linker, for example by functionalizing it with a methacrylate group for embedding in a polybutylmethacrylate (PBMA) matrix.[20]

In contrast to plain AB, where the photoisomerisation mechanism is well studied,[21–31] the molecular dynamics of DR1 and related push-pull substituted ABs following excitation in the strong visible $\pi\pi^*$-type absorption band still remains controversial, despite several spectroscopic[32,33] and time-resolved[10,11,34,35] experimental studies and theoretical calculations.[11,36–39] This includes the question of the energetic ordering of the first $n\pi^*$ and $\pi\pi^*$ electronic states of the molecules and their distinctive roles in the photoisomerisation and electronic deactivation processes.[10,11,36,37] It is undoubted at present only that both electronic states are very close. Radiationless interconversion between them should therefore be feasible and fast.

For the case of 4-methoxy-4′-nitro-azobenzene (MNAB), which has been measured by femtosecond transient absorption spectroscopy by Hagiri *et al.*,[9] the $S_1(n\pi^*) < S_2(\pi\pi^*)$ energetic order of states seems established. However, it is not clear whether this also holds for DR1, since methoxy is a much weaker electron donor than a dialkylamino group. A time-resolved fluorescence and absorption study of 4-dimethylamino-4′-nitro-azobenzene (DMANAB) by Schmidt et al. revealed a bi-exponential decay behavior with time constants of $\tau_1 \approx 100$ fs and $\tau_2 \approx 1$ ps.[10] As τ_1 was associated with a rapid departure of the wavepacket from the Franck-Condon (FC) region of the photo-excited $\pi\pi^*$ state and τ_2 with the isomerisation and electronic deactivation to the S_0 state, the photo-induced dynamics was concluded to be analogous to plain AB.[10] A later paper on the ultrafast kinetics and anisotropy of the excited-state absorption of DR1 in different solvents by Poprawa-Smoluch *et al.* assumed that the $n\pi^*$ state was reached from the initially excited $\pi\pi^*$ state,[11] but the experimental time resolution was insufficient to fully resolve the dynamics of both states. More recently, Hsu *et al.* investigated the similar push-pull AB Disperse Red 19 and observed time constants of $\tau_1 = 0.10$ ps and $\tau_2 = 1.11$ ps,[35] which they interpreted in the same way as Schmidt *et al.*[10] for

DMANAB, without much further discussion of the nature or possible sequential dynamics of the involved states. Quantum chemical calculations on the photo-induced reaction routes reported for several push-pull substituted ABs[38,39] including DR1[11,36,37] favour the rotational isomerisation mechanism as in plain AB.[22,25,26,28,31]

Static spectra of DR1 and related push-pull ABs in solution and the quantum chemical calculations generally suggest that the $\pi\pi^*$ state is higher in energy than the $n\pi^*$ state, unless the solute and solvent form strong H-bonds.[11,36,37] The virtual absence of fluorescence from DR1 in aprotic solvents from n-hexane to acetonitrile has been explained by fast internal conversion from the excited $\pi\pi^*$ to the $n\pi^*$ state, which has almost no oscillator strength to the S_0 state. Fluorescence spectra and quantum yields, excitation spectra, and excitation anisotropies of DR1 in a series of alcohols as examples for polar, protic and H-bonding solvents reveal that the $n\pi^*$ and $\pi\pi^*$ states have almost the same adiabatic excitation energies, but that the $\pi\pi^*$ state is reached first upon vertical excitation.[36] However, the picture becomes considerably more complex, if one tries to distinguish between the $\pi\pi^*$-type local optically excited (OE) state and an energetically lower "relaxed" CT state supposed to be formed from the OE state. A resonance Raman study on the solvent influence and the contributions of solvent relaxation and reorganisation on the molecular structure and ultrafast isomerisation dynamics of DMANAB by Biswas and Umapathy showed that the polarity of the solvent plays a decisive role for the excited-state structure and energy and confirmed the strong CT character in the optical transition,[32,33] but a clear and unambiguous picture still remains to be developed.

This paper reports on a study of the photo-induced ultrafast dynamics of DR1 by femtosecond time-resolved broadband absorption spectroscopy and fluorescence up-conversion following excitation at $\lambda_{pump} = 475$ nm. Special attention is directed at the observation of an ultrafast transient excited-state absorption band between $\lambda_{probe} \approx 530 - 580$ nm rising immediately with the excitation laser pulse, earlier than slightly delayed transient excited-state absorptions at other detection wavelengths. This feature provides strong support for a stepwise electronic deactivation and isomerisation mechanism from the $\pi\pi^*$ optically excited state (OE) to the S_0 ground state via an intermediate excited (IE) state. The recorded absorption-time profiles in the range from $\lambda_{probe} = 350 - 680$ nm are therefore analysed in a consistent fashion using a sequential kinetic model and global fitting. The supposed IE state is discussed in the light of the time-resolved results and the evidence from static absorption and fluorescence[36,37] and resonance Raman spectra.[32,33]

3.2 EXPERIMENTAL SECTION

All time-resolved measurements in the present work were performed at room temperature in flow cells of 1 mm optical path length with 0.2 mm quartz windows. The samples of Disperse Red 1 (> 96%) and the sol-

vent 2-fluorotoluene (2FT, > 96%) were used as supplied (Sigma-Aldrich). Solutions at concentrations of 0.03 mM corresponding to an optical density of ≈0.5 at the excitation wavelength were pumped through the probe cells with a peristaltic pump (Ismatec). The solvent 2FT was employed in the present work because it is nearly isorefractive with PBMA, which allows for highly sensitive femtosecond photodynamics measurements on DR1-functionalised PBMA-nanopolymers. These results will be reported elsewhere.[20]

3.2.1 BROADBAND TRANSIENT ABSORPTION MEASUREMENTS

The experimental setup for femtosecond time-resolved broadband absorption spectroscopy in our laboratory is based on a regeneratively amplified Ti:Sa laser (Clark MXR CPA2001).[40,41] Pump pulses at $\lambda = 475$ nm with typically ≈0.5 μJ per pulse and ≈35 fs duration (Gaussian fwhm) were delivered by a home-built non-collinear optical parametric amplifier (NOPA). Supercontinuum probe and reference pulses between 350 nm $\leqslant \lambda_{probe} \leqslant$ 700 nm were generated in CaF_2. The pulses were focused into the sample cell at an angle between pump and probe of 5°. The transmitted probe and reference spectra were taken using an imaging spectrograph with a 1024×127 pixel CCD camera. A BG18 filter before the spectrograph attenuated the intense near-IR part of the supercontinuum. The pump-probe time delay was set using a computer-controlled translation stage.

The pump-induced cross-phase modulation (XPM) and stimulated Raman scattering (SRS) signals were measured independently for the pure solvent. Two-dimensional transient absorption maps were then obtained by subtracting the XPM and SRS contributions from the sample spectra taking into account the pump pulse absorption by the sample and the time-zero correction for each wavelength determined from the XPM signal. The width of the instrument response function (IRF) estimated from the SRS signal was about 110 fs (fwhm), which allows for a time resolution of the experiment of $\Delta t \approx 30 - 40$ fs. The shape of the observed XPM signal around time-zero was taken as input for the non-linear least-squares fitting analysis of the absorption-time profiles.

3.2.2 FLUORESCENCE UP-CONVERSION MEASUREMENTS

Time-resolved fluorescence measurements were performed using the up-conversion technique.[42,43] The emission by the sample molecules excited by a second NOPA (0.3 μJ per pulse) was collected and focused into a BBO crystal for up-conversion by type II sum frequency generation with the 775 nm Ti:Sa gate pulses by a pair of off-axis parabolic mirrors. The up-converted light passed a double monochromator and was detected as function of the pump-gate delay time by a photomultiplier connected to a gated photon counter. An OG550 band pass filter was placed behind the sample cell to remove scattered pump photons. Pump-gate cross correla-

tion determined an IRF width of ≈200 fs (fwhm), corresponding to a time resolution of $\Delta t \approx 80$ fs.

3.3 RESULTS

3.3.1 STATIONARY SPECTRA

The stationary UV/VIS absorption and fluorescence spectra of DR1 in 2FT are displayed in Fig. 3.1. Also plotted are the absorption spectra of DR1

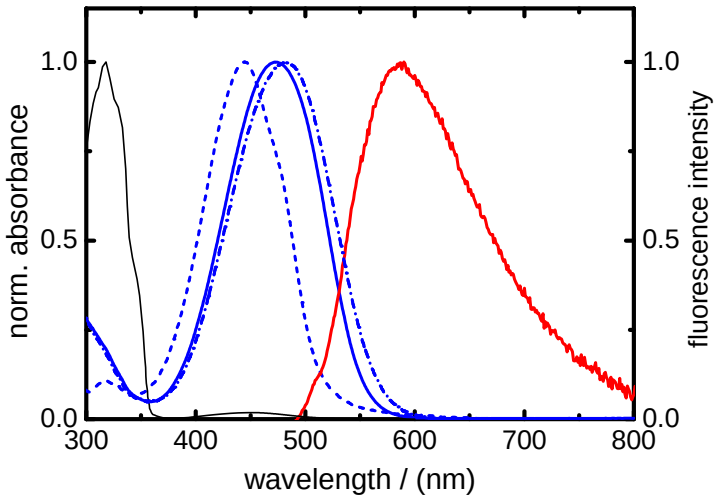

Figure 3.1: Normalised stationary absorption spectrum of DR1 in *n*-hexane (dashed blue), 2FT (solid blue) and ethanol (dash-dotted blue) and stationary fluorescence spectrum of DR1 in 2FT (solid red). The absorption spectrum of plain AB in *n*-hexane is shown by the thin black line for comparison.

in the nonpolar solvent *n*-hexane and in the polar protic ethanol and the absorption spectrum of unsubstituted AB in *n*-hexane for comparison. As shown, the strong $\pi\pi^*$-type absorption band of DR1 has its maximum at $\lambda = 445$ nm in *n*-hexane (dielectric constant $\epsilon = 1.9$), $\lambda = 475$ nm in 2FT ($\epsilon = 4.2$) and $\lambda = 482$ nm ethanol ($\epsilon = 24$),[44] respectively. The CT character of the excited state is reflected by the large solvatochromic red-shift with increasing solvent polarity.[8,11,37] Accordingly, 2FT is ranked as a relatively polar medium. The much weaker $n\pi^*$ transition, observed in plain AB at $\lambda = 450$ nm, remains hidden under the intense $\pi\pi^*$ band. It should be less affected by the *push-pull* substitution and the polarity of the solvent.[11,36]

The fluorescence spectrum of DR1 excited at $\lambda = 475$ nm shows a broad asymmetric emission band between 500 nm $\leqslant \lambda_{fl} \leqslant$ 800 nm with its maximum in 2FT at $\lambda_{fl} \approx 590$ nm. The pronounced Stokes shift by ≈115 nm with respect to the absorption maximum underlines the CT character of the excited state, which experiences significant stabilisation by a polar solvent. The time-resolved measurements in the following will shed more light on the involved excited states.

Fig. 3.2 displays the two-dimensional spectro-temporal map of the change in optical density ΔOD after photoexcitation of the DR1 sample in 2FT at $\lambda_{pump} = 475$ nm for delay times up to $\Delta t = 10$ ps. The pump wavelength coincides with the peak of the $\pi\pi^*$ absorption band of the molecules. The dynamics were followed up to $\Delta t_{max} = 65$ ps, but only little change was observed beyond $\Delta t = 10$ ps. The detection wavelengths range from $\lambda_{probe} = 350 - 680$ nm.

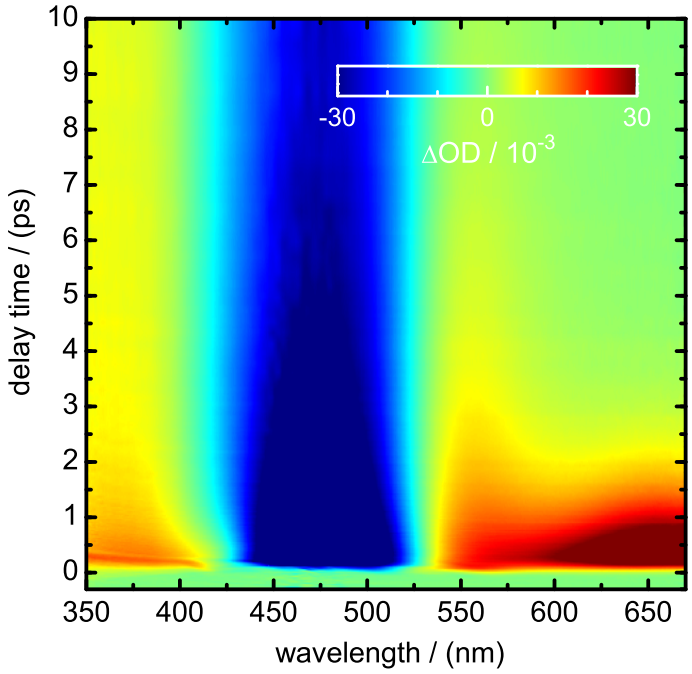

Figure 3.2: Two-dimensional map of the change in optical density (ΔOD) following excitation of the DR1 sample molecules at $\lambda_{pump} = 475$ nm for probe wavelengths in the range 350 nm $\leqslant \lambda_{probe} \leqslant$ 680 nm and delay times of $\Delta t \leqslant 10$ ps. Little change was observed at $\Delta t > 10$ ps up to the maximum experimental delay time of 65 ps.

The spectro-temporal data map (Fig. 3.2) shows an intensive bleach of the absorption around $\lambda = 475$ nm immediately after the pump pulse at $\Delta t = 0$. This so-called ground state bleach (GSB) extends between 420 nm $\leqslant \lambda_{probe} \leqslant$ 525 nm. At the same time, several excited-state absorption (ESA) bands appear. At least three distinctive spectral regions can be distinguished, from $\lambda_{probe} = 350 - 415$ nm, $530 - 580$ nm, and $\approx 580 - 670$ nm. All ESA bands decay almost completely within the first one to two picoseconds. The somewhat longer-lived signal around $530 - 580$ nm is attributed to absorption by vibrationally hot ground state molecules (HGSA) resulting from the electronic deactivation. The ensuing processes lead to a recovery of most of the GSB, but a significant permanent GSB remains at the longest experimental delay time ($\Delta t_{max} = 65$ ps), where all electronic and vibrational relaxation processes are over. This final GSB signal thus

reflects the E $\rightarrow$ Z isomerisation reaction of the DR1 molecules. The formation of Z-DR1 is witnessed by the permanent positive product absorption (PA) band between $\lambda_{probe} = 350 - 400$ nm that can be seen to remain constant at the longest delay times.

The transient spectra at selected delay times displayed in Fig. 3.3 reveal the ensuing photo-induced molecular dynamics in some more detail. The upper panel (Fig. 3.3a) shows the ultrafast spectro-temporal evolu-

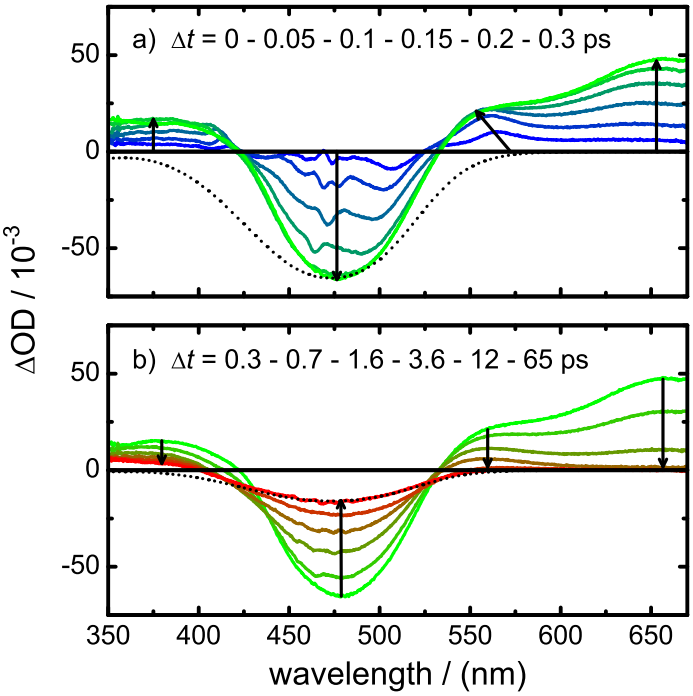

Figure 3.3: Transient spectra of DR1 at different delay times between $0 \leqslant \Delta t \leqslant 0.3$ ps (blue to green, top) and between 0.3 ps $\leqslant \Delta t \leqslant 65$ ps (green to red, bottom) after the pump pulse at $\lambda = 475$ nm. The arrows indicate the temporal evolution of the transient spectra. The circle in the upper panel showcases the rise and blue-shift of the "fast" ESA band from $\lambda_{probe} \approx 570$ to $\approx$550 nm. The black dashed lines show the (negative) absorption of DR1 scaled to the peak GSB (upper panel) and the final absorption at $\Delta t = 65$ ps (lower panel).

tion within the first 300 fs after the excitation laser pulse, the subsequent changes up to $\Delta t_{max} = 65$ ps are given in the lower panel (Fig. 3.3b). The characteristic GSB and ESA bands (as well as HGSA and PA at later delay times) are nicely featured in the distinctive spectral windows identified above. The main changes occur within the first 300 fs and in the next $\approx$1.5 ps thereafter.

The most remarkable feature is the ultrafast, instrument-limited rise of ESA at wavelengths from $530 - 580$ nm (ESA_1, for reference below) that is clearly faster than the rise of the ESA features appearing with some delay at $\lambda \approx 580 - 670$ nm (ESA_2) and $350 - 415$ nm (ESA_3). This is clearly evident from the transient spectra in Fig. 3.3a, where ESA_1 has already reached its maximum at an experimental delay time of no more than $\Delta t \approx$ 125 fs, extremely rapidly, while ESA_2 (and ESA_3) at the same delay time

are still at $\lesssim 50\,\%$ of their eventual maxima. As can be seen, ESA_2 (and ESA_3) need at least $\Delta t \approx 300$ fs to reach their maximal values. Moreover, ESA_1 exhibits a significant spectral blue-shift in the first ≈ 125 fs. ESA_1 is visible despite the fact that its effective peak intensity may be diminished by some overlap with the neighboring negative GSB band and by possible stimulated emission (SE) that might be hidden underneath the excited-state absorption in the spectral window (cf. Fig. 3.1). As will be argued below, the ultrafast rise of ESA_1 from $530-580$ nm and its clearly shorter lifetime compared to ESA_2 at >580 nm strongly suggest a sequential, stepwise isomerisation and electronic deactivation mechanism.

The prompt appearance of the very short-lived ESA_1 band with the excitation pulse without delay has not been given full attention before, presumably because its subsequent decay is partially masked by the blue wing of the rising ESA_2 band and by HGSA appearing at slightly longer times ($\Delta t \gtrsim 1$ ps). The delayed appearance of ESA_2 (and ESA_3), on the other hand, has been noted previously.[10,11] Both observations will be accounted for by the analysis of the absorption-time profiles below.

The second important observation is the permanent final absorption at $\lambda < 400$ nm by the photochemically produced Z-DR1 isomer. As can be seen from the stationary absorption spectrum in Fig. 3.1 and from the spectrum at $\Delta t = 0$ in Fig. 3.3a, there is little absorption by the E-form of DR1 at those wavelengths. Judged from the ratio of the final GSB to the GSB at $\Delta t = 0$ for $\lambda_{probe} = 475$ nm, the photoisoimerisation quantum yield of DR1 is $\phi_{E\rightarrow Z} < 0.25$. The upper limit would apply, if the absorbance by the Z-DR1 product at $\lambda \approx 475$ nm was practically negligible compared to the initial E-DR1.

The temporal development of the transient absorption features is reflected by the absorption-time profiles for four selected probe wavelengths representing the four distinctive spectral windows depicted in Fig. 3.4. Also shown are the best-fit curves to the data from a global nonlinear least-squares analysis assuming a consecutive kinetic scheme of the type

$$E \xrightarrow{+h\nu} E^* \xrightarrow{\tau_1} E^{**} \xrightarrow{\tau_2} [E^{\#} + Z^{\#}] \xrightarrow{\tau_3} [E + Z]$$

where E^* and E^{**} represent the excited molecules in two different "states" which give rise to the prompt and the delayed ESA, respectively, $E^{\#}$ and $Z^{\#}$ denote vibrationally hot S_0 state molecules responsible for HGSA, and E, Z denote the final products in their E- and Z-isomeric forms. The distinction between E^* and E^{**} and the proposition that E^{**} develops consecutively from E^* are made guided by the evidence from the transient spectra (Fig. 3.3a) and the earlier reports of a delayed ESA rise,[10,11] although the question of the nature of those states has to be deferred to the Discussion below. The time profiles included in the global fit are distributed across the probe wavelength range with an emphasis on the "kinetically cleaner" spectral windows, from which the molecular time constants could be well determined. The time-zero and the IRF width, taken into account by convolution, were kept fixed for all time profiles at the values determined by

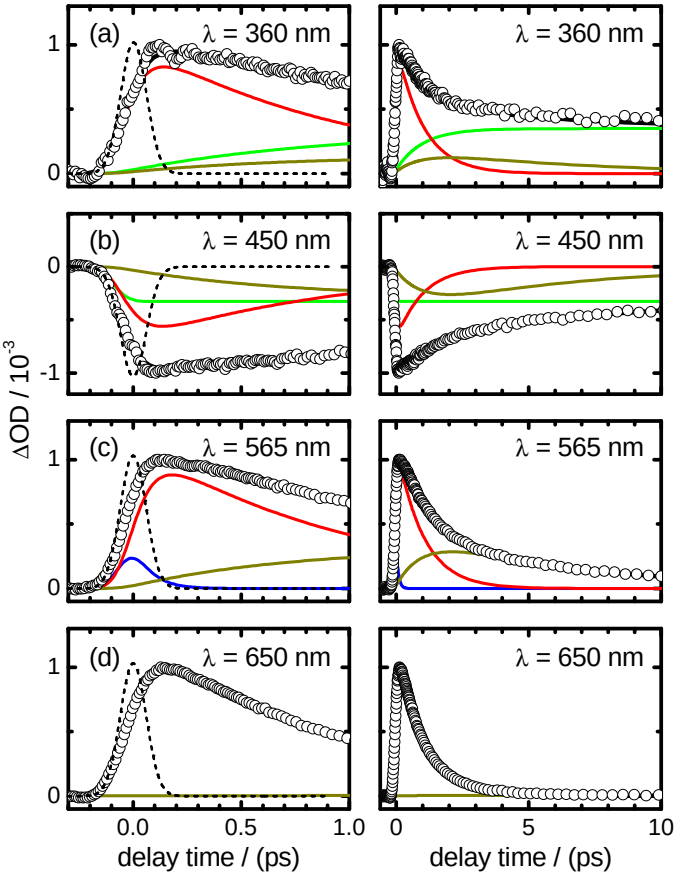

Figure 3.4: Absorption-time profiles at four representative probe wavelengths (a–d) for delay times up to $\Delta t = 1.0$ ps (left column) and $\Delta t = 10$ ps (right column). Open circles are data, solid black lines the overall least-squares fit curves. The different contributions are indicated by coloured lines (blue: ESA_1; red: $ESA_{2,3}$; light brown: HGSA; green: permanent GSB resp. PA.) The thin dashed curves on the left show the IRF.

the XPM and SRS signals to exclude correlation and cancellation effects with time constant τ_1.

The best-fit results for the time constants τ_1-τ_3 in the above kinetic scheme are compiled in Table 3.1. The most important spectral windows with respect to the excited-state dynamics are those from $\lambda_{probe} = 580 - 670$ nm and $530 - 580$ nm. As can be seen from the transient absorption data and the fit for $\lambda_{probe} = 650$ nm in Fig. 3.4d as an example, τ_2 determines the observed single-exponential ESA_2 decay in the first window. The rise of ESA_2 was described by τ_1 to account for the delayed appearance. Here, both ESA_1 and ESA_2 are important at $\lambda_{probe} = 530 - 580$ nm (see Fig. 3.4c), where τ_1 is well determined by the decay of ESA_1 *and* the rise of ESA_2 at the earliest times (Fig. 3.4c left). The distinctive contribution by HGSA in the same wavelength window at later times (Fig. 3.4c right) is well described by τ_2 for its rise and τ_3 for its slower decay. Continuing towards shorter probe wavelengths, all three time constants (τ_1, τ_2, τ_3) determine the transients at $\lambda_{probe} = 450$ nm (Fig. 3.4b) and $\lambda_{probe} = 360$ nm

Table 3.1: Results of the global fit analysis of the absorption-time profiles of DR1 in 2FT. Values in parenthesis give the 2σ standard deviations with respect to the last digits.

λ / nm	τ_1 / ps [1]	A_1 (rel.)	τ_2 / ps	A_2 (rel.)	τ_3 / ps	A_3 (rel.)	A_∞ (rel.)
360	0.076(2)	-	0.99(1)	0.82(3)	6.0(1)	0.12(3)	0.35(2)
450	0.076(2)	-	0.99(1)	−0.56(2)	6.0(1)	−0.26(2)	−0.32(2)
475	0.076(2)	-	0.99(1)	−0.63(1)	6.0(1)	−0.23(2)	−0.28(2)
560	0.076(2)	0.24(2)	0.99(1)	0.86(2)	6.0(1)	0.31(2)	-
565	0.076(2)	0.23(2)	0.99(1)	0.88(2)	6.0(1)	0.28(2)	-
570	0.076(2)	0.25(2)	0.99(1)	0.90(2)	6.0(1)	0.23(2)	-
575	0.076(2)	0.25(1)	0.99(1)	0.90(1)	6.0(1)	0.22(2)	-
580	0.076(2)	-	0.99(1)	0.94(2)	6.0(1)	0.18(2)	-
590	0.076(2)	-	0.99(1)	0.95(1)	6.0(1)	0.12(1)	-
600	0.076(2)	-	0.99(1)	0.95(1)	6.0(1)	0.07(2)	-
625	0.076(2)	-	0.99(1)	0.98(1)	6.0(1)	0.02(3)	-
650	0.076(2)	-	0.99(1)	0.99(1)	6.0(1)	0.01(3)	-

a The small statistical error limits arise because the values for τ_{IRF} and time-zero were kept fixed. Final results with error limits including estimated systematic uncertainties for τ_{IRF} and time-zero are given in the text.

(Fig. 3.4a), but essentially only their amplitudes remain adjustable. The permanent GSB at 450 nm (Fig. 3.4b) is accounted for by a step function with IRF-limited rise time. The resulting final values for the three time constants are

$$\tau_1 = 0.08 \pm 0.03 \text{ ps},$$
$$\tau_2 = 0.99 \pm 0.02 \text{ ps},$$
$$\tau_3 = 6.00 \pm 0.10 \text{ ps}.$$

The quoted error limits include the 2σ statistical uncertainty limits and estimated systematical errors, which may result mostly from the error in the IRF width ($\tau_{IRF} = 0.06 \pm 0.01$ ps) and the uncertainty in the time-zero value ($\approx \pm 0.010$ ps).

Compared with simpler fit models with only one ESA component (and no delayed rise), the consecutive kinetic scheme yielded a much smaller standard deviation (by a factor of 2.5) of the global fit to all twelve data curves. Additionally, we note that the measured time profiles in the $530-580$ nm window could not be modeled well in shape at all assuming of only a single ESA decay component. The derived values for τ_1-τ_3 have low correlation and hold within their respective error limits although the applied fit model comprises quite a number of adjustable parameters, because each τ_i usually governs a time profile in a specific wavelength window. The value for τ_2, for example, is in practice fully determined by the three absorption-time profiles taken between $\lambda = 600-650$ nm (see Table 3.1), where this is the only relevant time parameter. With τ_2 thereby controlled, the values for τ_1 and τ_3 are essentially determined by the four data curves in the $\lambda = 575-560$ nm window at short and at long delay times, respectively. The absorption profiles at shorter wavelengths ($\lambda = 475-350$ nm) are more complex, because they consist of ESA, HGSA, GSB and PA components, but the global fit allows for little variation of the values for $\tau_1 - \tau_3$ without compromising the fits at the above wavelengths. As final additional check, we performed an independent global analysis of the full 2D spectro-temporal absorption map (Fig. 3.2) by taking the spectrally integrated transient absorption-time curves over the four distinctive wavelength windows from $\lambda = 350-380$, $440-520$, $545-575$, and $580-650$ nm. Only the $380-440$ nm region was omitted, because the respective spectro-temporal contributions due to ESA decay, HGSA rise and HGSA decay, PA rise and GSB refill overlap too heavily in wavelengths and time in this range to allow for an unbiased fit without prohibitively large cross-correlations between the resulting parameters. Apart from this narrow range, however, this analysis covered the entire probe spectrum. The results for the time constants from this alternative approach were virtually identical with the ones determined above.

Measured fluorescence decay curves at three selected emission wavelengths, $\lambda_{fl} = 610$, 660 and 700 nm, are shown in Fig. 3.5. The pa-

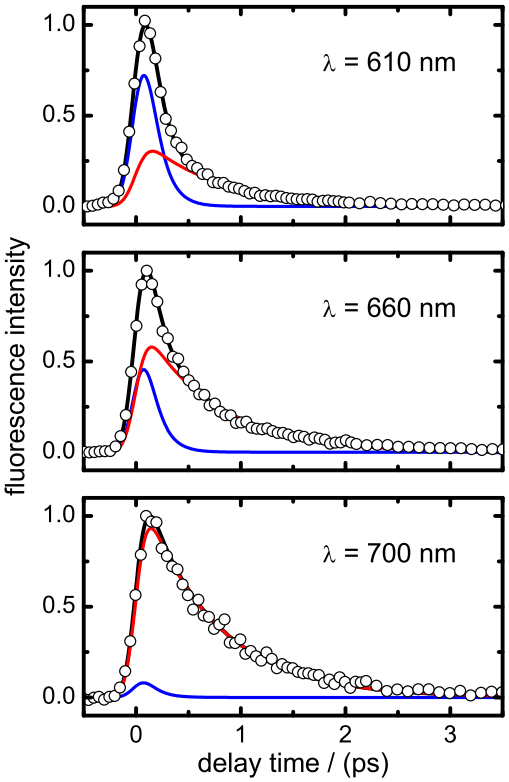

Figure 3.5: Fluorescence-time profiles of DR1 in 2FT excited at $\lambda_{pump} = 475$ nm at three selected emission wavelengths. Open circles are data, solid black lines give the fitted curves, blue and red curves show the individual decay components.

rameters which were extracted by least-squares fitting to the time profiles are collected in Table 3.2. As can be seen, all time profiles require two exponentials for modeling. However, the amplitude of the faster component decreases rapidly with longer emission wavelengths. At $\lambda_{fl} = 600 - 610$ nm, the fluorescence-time profile is almost completely determined by the fast first component, but only the longer-lived second component plays a role at $\lambda_{fl} = 700$ nm. Applying again a consecutive model, similar as above, the fitted fluorescence lifetimes (with 2σ statistical and estimated systematic error limits) of

$$\tau_1' = 0.12 \pm 0.05 \text{ ps},$$
$$\tau_2' = 0.70 \pm 0.10 \text{ ps}$$

correlate well with the excited-state lifetimes τ_1 and τ_2 determined by the transient absorption measurements.

Table 3.2: Results of the global fit analysis of the fluorescence-time profiles of DR1 in 2FT. Values in parentheses give the 2σ standard deviations with respect to the last digits.

λ / nm	τ'_1 / ps	A_1 (rel.)	τ'_2 / ps	A_2 (rel.)
600	0.12(4)	0.74(5)	0.70(8)	0.26(2)
610	0.12(4)	0.71(8)	0.70(8)	0.29(2)
620	0.12(4)	0.63(4)	0.70(8)	0.37(2)
640	0.12(4)	0.47(9)	0.70(8)	0.53(2)
660	0.12(4)	0.43(7)	0.70(8)	0.57(3)
680	0.12(4)	0.30(9)	0.70(8)	0.70(6)
700	0.12(4)	0.08(9)	0.70(8)	0.92(6)

3.4 DISCUSSION

The time-resolved broadband absorption and fluorescence up-conversion measurements presented above provide explicite information on the ultrafast photo-induced dynamics of the push-pull-substituted azobenzene Disperse Red 1. Special attention is directed at the very early dynamics, which has been analysed using a detailed kinetic model.

The obtained transient spectra clearly demonstrate a sequential temporal evolution of the molecules in the excited state within the first 300 fs after the pump pulse. The excited-state absorption in the $\lambda_{probe} = 530 - 580$ nm range (ESA_1) was found to rise earlier than the excited-state absorption at longer wavelengths ($580 - 670$ nm, ESA_2) or in the UV ($350 - 415$ nm, ESA_3). In the latter two regions, the band intensities reach their maxima with some delay, whereas the absorption in the first window has reached its peak in only $\approx 100 - 150$ fs. Moreover, ESA_1 in the $530 - 580$ nm range exhibits a very fast spectral blue-shift in the first $\approx 100 - 150$ fs after the pump pulse, while ESA_2 from $580 - 670$ nm continues to rise without a large spectral shift. Those different pieces of the puzzle add up to a picture that suggests an ultrafast transformation of the wavepacket prepared by the pump laser pulse from the $\pi\pi^*$ optically excited (OE) state to an intermediate excited state (IE), or relaxed excited state (RE), at somewhat lower energy within $\Delta t \lesssim 100$ fs, before the excited molecules may return to the electronic ground state.

The global kinetic analysis of the absorption-time profiles gave quantitative insight into the related processes. The time-resolved experimental data could be nicely modeled assuming a sequential kinetic scheme, where the distinction between two "states" E^* and E^{**} and the proposition that E^{**} arises consecutively from E^* were made based on the transient spectra in Fig. 3.3a and on the earlier reports of a delayed ESA.[10,11] Accordingly, time constant $\tau_1 = 0.08 \pm 0.03$ ps is now assigned to the lifetime of the OE state with respect to its transition to the IE (or RE) state, while time constant $\tau_2 = 0.99 \pm 0.02$ ps gives the lifetime of the IE (or RE) state with respect to the $E - Z$ isomerisation and radiationless electronic conversion

through the conical intersection (CI) connecting it with the S_0 electronic ground state. The resulting internally highly excited S_0 molecules thereafter undergo vibrational cooling described by time constant $\tau_3 = 6.0 \pm 0.1$ ps.

The results of the fluorescence up-conversion measurements, despite their lower temporal resolution, provide further support. The experimental data suggest that the fluorescence arises from two different types of excited states, where the energetically higher one decays faster and appears to populate the lower one by an ultrafast transformation. Most notable in this context is the rapidly decreasing amplitude of the faster fluorescence decay component (τ_1') towards longer wavelengths. This translates into a fast red-shift of the emission spectrum as the wavepacket transforms from the OE to the IE/RE state, which fluoresces at longer wavelengths. The red-shift of the fluorescence correlates with the blue-shift in the excited-state absorption spectrum (ESA_1). On the other hand, the emission near the band maximum in the static spectrum ($\lambda_{fl} \approx 590$ nm, *cf.* Fig. 3.1) is highly predominated by the fast component. The fluorescence decay times $\tau_1' = 0.12 \pm 0.06$ ps and $\tau_2' = 0.70 \pm 0.10$ ps correspond well in magnitude to τ_1 and τ_2 from the absorption measurement. The deviations can be rationalised by differences between the FC windows for the $S_2/S_1 \rightarrow S_0$ transition seen in fluorescence and the $S_n/S_m \leftarrow S_2/S_1$ transitions probed in absorption. Considering the sub-picosecond fluorescence lifetime, we note without going into more detail that it is highly unlikely that solvent relaxation around the excited-state molecules is complete. The observable Stokes shift ($\Delta\lambda \approx 115$ nm) in the static fluorescence spectrum therefore very likely does not reflect the solvent stabilisation of a fully relaxed excited state.

Bi- or multiphasic fluorescence dynamics similar to the experimentally observed behaviour can, in principle, arise from several different mechanisms. The first is vibrational relaxation in the excited state. In view of the well-known much longer time scale (≈10 ps) for typical vibrational energy transfer processes to an organic solvent compared to our τ_1 (≈80 fs), this possibility can be ruled out. The second possibility is a dynamic Stokes shift due to solvation dynamics around the solute molecules after the photoexcitation. Solvent relaxation is known to be multiphasic, with an ultrafast (1 ps) component arising from inertial reorientation of the solvent molecules and longer-lived components associated with slower diffusional motion.[45,46] Both contributions are revealed by corresponding dynamic Stokes shifts in the associated transient fluorescence spectra. In general, it is possible to reconstruct the transient fluorescence spectra from the measured fluorescence-time profiles at a range of emission wavelengths. In our case, however, an intense solvent Raman signal prevented us from recording any fluorescence-time profiles at wavelengths around the maximum of the static fluorescence spectrum at $\lambda_{fl} \approx 590$ nm (cf. Fig. 3.1) and below so that it was not possible to recover the complete transient spectra for DR1. The long-wavelength wings of the transient spectra, which we could reconstruct, do show a time-dependent red-shift as could be expected from

the fluorescence-time profiles. However, several arguments speak against an explanation of this red-shift by solvation dynamics:

First, all fluorescence-time profiles could be well described with only two distinctive decay times, τ_1' and τ_2', over the entire wavelength range. Typical solvation processes show an initial decay at the blue side, a rise at the red side of the fluorescence spectrum, and a wavelength-dependent continuous change of the time constants in between (see, *e.g.*, Ref.[47]). While the rise on the red may have been obscured due to the fast fluorescence decay, we clearly did not observe a continuous evolution of the time constants. Second, known typical solvent reorientation times (with the exception of the special case of water[48]) are usually somewhat longer than $\approx$ 1 ps,[45,47,49] especially considering relatively large molecules such as 2FT, in contrast with our sub-100 fs value of τ_1. Third, the apparent spectral shifts in the recorded 2D absorption map for DR1 are localized to a rather narrow spectral window. Hence, although some contributions by solvent relaxation cannot be excluded, solvation dynamics does not seem to be the major cause for the observed spectral changes.

The third explanation for the biphasic dynamics is an ultrafast radiationless electronic transition. A sequential transformation from the optically excited state *via* an intermediate state to the ground state in push-pull azobenzenes has been presumed in previous studies.[10,11,35] However, the prompt, IRF-limited appearance of the ESA_1 band after the excitation laser pulse has not been fully recognized and taken into account before, probably because of its relatively narrow spectral width, and because its subsequent decay is partially masked by the rising ESA_2 band ($\Delta t < 300$ fs) and the HGSA at longer times ($\Delta t > 1$ ps). Schmidt *et al.*, who reported time-resolved emission and absorption measurements on DMANAB in toluene,[10] observed a biphasic fluorescence decay with a short first lifetime of $\tau_1 \approx 100$ fs and a delayed ESA rise, but based on a comparison with plain AB they associated τ_1 with a rapid departure of the excited wavepacket from the FC region of the photo-excited state instead of a fast internal conversion between two excited states. Poprawa-Smoluch et al. studied the ultrafast kinetics and anisotropy of DR1 in toluene, acetonitrile and ethylene glycol,[11] but could not fully resolve the very early events at the time. In spite of this, they also report a delayed ESA appearance at $\lambda > 600$ nm with a rise time of $\tau_1 < 200$ fs, which they assigned to rapid internal conversion of the initially excited $\pi\pi^*$ state to the energetically lower $n\pi^*$ state. Meanwhile, Hsu *et al.*[35] interpreted their results similar to Schmidt *et al*. The slower second time constant, $\tau_2 \approx 1$ ps, has been commonly accepted as the lifetime of the excited molecules with respect to the isomerisation and radiationless deactivation to the S_0 state.

The kinetic model applied to the experimental data in the present work accounts for the observed photochemical dynamics of DR1 overall in a global fashion. However, the energetic order of the excited states of DR1 and the nature of the intermediate excited state remain under question. For the case of 4-methoxy-4′-nitro-azobenzene (MNAB), the $\pi\pi^*$ state is supposed to be clearly higher (S_2) in energy at vertical excitation than the $n\pi^*$

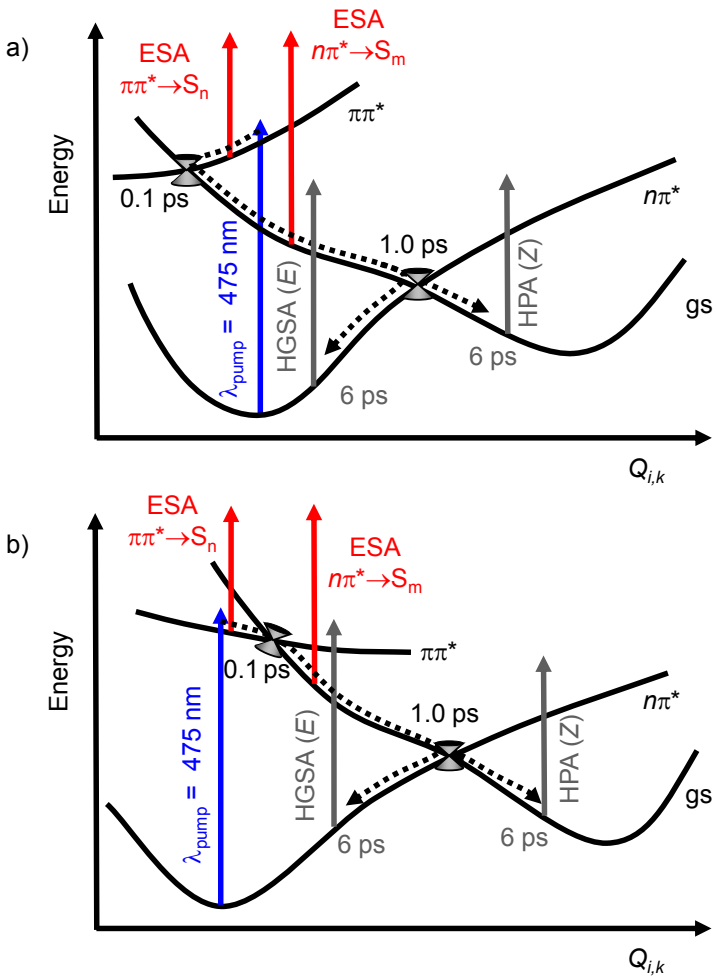

Figure 3.6: Proposed relaxation pathways for DR1 after photoexcitation at $\lambda_{pump} = 475$ nm. (a) The $\pi\pi^*$ state is above the $n\pi^*$ state at vertical excitation and the deactivation to the S_0 state occurs stepwise by internal conversion to the lower-lying $n\pi^*$ state and the CI between the $n\pi^*$ and S_0 states involving the CNNC torsional pathway as in plain AB. (b) The $\pi\pi^*$ state is below the $n\pi^*$ state at vertical excitation, but the deactivation to the S_0 state occurs sequentially by rapid motion of the wavepacket from the $\pi\pi^*$ to the $n\pi^*$ state and the $n\pi^*/S_0$ CI along the CNNC torsional coordinate.

state (S_1).[9] For 4-dimethylamino-4′-nitro-azobenzene (DMANAB) and DR1, the energetic order is less certain and depends on the solvent. Quantum chemical calculations employing basis sets of double-zeta quality indicated that the $n\pi^*$ state is slightly lower than the first $\pi\pi^*$ state,[11,38,39] but larger basis sets would be needed for more conclusive evidence. Based on a spectral decomposition study of the fluorescence spectra, the two states are supposed to keep their order even in highly polar solvents like acetonitrile, but rearrange in alcohols, where the $\pi\pi^*$ state thus falls below the $n\pi^*$ state.[36,37] The rapid internal conversion from the optically bright $\pi\pi^*$ state to the $n\pi^*$ state prior to the return to the S_0 state proposed by Poprawa-Smoluch *et al*. implicitly assumes an energetically higher $\pi\pi^*$ state. On the other hand, the peak absorption wavelength of $\lambda_{max} = 475$

nm of the strong $\pi\pi^*$ transition of DR1 corresponds to lower energy than the known absorption maximum at $\lambda_{max} = 450$ nm of the $n\pi^*$ band of plain AB. The situation might be even more complex, however. A resonance Raman study on DMANAB led Biswas and Umpathy to conclude that the solvent environment strongly influences the $\pi\pi^*$ excited state. They distinguished between the $\pi\pi^*$/OE state reached in *n*-hexane and the solvent-stabilised "relaxed" $\pi\pi^*$/CT state that is reached in <100 fs from the $\pi\pi^*$/OE state in benzene.[32,33] This relaxation is due to an adiabatic change in the electronic structure of the OE/CT state with solvent polarity, rather than a complete change of the electronic character.

In view of the uncertainty about the energetic order of the $\pi\pi^*$ and $n\pi^*$ states, we propose two alternative scenarios for the photo-induced dynamics of DR1 after excitation at $\lambda_{pump} = 475$ nm as depicted in Fig. 3.6. In the first scenario (Fig. 3.6a), the pump laser pulse projects a wavepacket from S_0 to the FC region of the optically bright $\pi\pi^*$ state, which is observable for roughly ≈100 fs in emission around 600 nm and in transient absorption around $\lambda \approx 570$ nm (ESA_1). Very rapid internal conversion, however, takes the wavepacket from the $\pi\pi^*$ (OE) state in 100 fs (τ_1) to the energetically lower $n\pi^*$ (IE) state. The $n\pi^*$ state is well detected by several intense excited-state absorptions (ESA_2, ESA_3). The observation of the weaker longer-lived fluorescence component suggests that the two excited states are vibronically quite strongly coupled. The subsequent isomerisation and radiationless deactivation to the electronic ground state takes place in ≈1.0 ps (τ_2). The reaction coordinate to the $n\pi^*/S_0$ CI likely involves torsional motion around the central CNNC coordinate as in plain AB.

In the second scenario (Fig. 3.6b), the $\pi\pi^*$ (OE) state may be below the $n\pi^*$ (IE) state at vertical excitation. Without an easily accessible $\pi\pi^*/S_0$ CI, however, the relaxation to the S_0 state can occur only *via* the $n\pi^*$ state, which is reached *via* a rapid internal conversion in the time of τ_1 from the $\pi\pi^*$ state at some configuration, where $n\pi^*$ moves below $\pi\pi^*$. The isomerisation and deactivation to S_0 in time τ_2 thus takes place again along the CNNC torsional coordinate *via* the $n\pi^*/S_0$ CI.

3.5 CONCLUSION

In conclusion, we have presented a study of the photo-induced dynamics of the push-pull azobenzene Disperse Red 1 in solution in 2-fluorotoluene by means of femtosecond time-resolved transient absorption spectroscopy and fluorescence up-conversion spectroscopy following photoexcitation at $\lambda_{pump} = 475$ nm. The observed transient excited-state absorption spectra in the first ≈300 fs after the pump laser pulse, the experimental absorption-time profiles, and the observed biphasic fluorescence decay dynamics demonstrate a stepwise electronic deactivation and isomerisation. A consecutive kinetic model allowed for a global analysis of the transient absorption-time profiles with three time constants, $\tau_1 = 80 \pm 30$ fs, $\tau_2 = 0.99 \pm 0.02$ ps and $\tau_3 = 6.0 \pm 0.1$ ps, which account for the present experimental re-

sults and for previously reported data in the literature. Therefore, τ_1 was assigned to the internal conversion and relaxation of the initially excited $\pi\pi^*$ state to the $n\pi^*$ state, τ_2 to the radiationless transformation from the $n\pi^*$ to the ground electronic state and the $E - Z$ isomerisation and τ_3 to the eventual vibrational cooling processes in the electronic ground state. The question of the energetic ordering of the $\pi\pi^*$ and $n\pi^*$ states at vertical excitation remains undecided, both states are clearly very close in energy.

Last but not least, this study of the azo dye DR1 in solution provides a basis for the interpretation of new experimental on the photodynamics of DR1 in complex environments and photoswitchable materials under application-relevant conditions, *e.g.*, in polymeric organic films or glasses. Towards these ends, a time-resolved fluorescence study of the photoisomerisation of DR1 in a polybutylmethacrylate matrix has just been completed in our laboratory to obtain insight into the effects of the topographic constraints by the polymeric micronetwork on the ensuing reaction dynamics.[20]

ACKNOWLEDGMENTS

This work has been supported by the Deutsche Forschungsgemeinschaft through project A1 of the Sonderforschungsbereich 677 "Function by Switching".

BIBLIOGRAPHY

[1] Liu, Z. F.; Hashimoto, K.; Fujishima, A. *Nature* **1990**, *347*, 658–660.

[2] Ikeda, T.; Tsutsumi, O. *Science* **1995**, *268*, 1873–1875.

[3] Willner, I.; Rubin, S. *Angew. Chem. Int. Ed.* **1996**, *35*, 367–385.

[4] Rau, H. In *Photochromism: Molecules and Systems*; Dürr, H., Bouas-Laurent, H., Eds.; Elsevier: Amsterdam, 2003.

[5] Balzani, V.; Credi, A.; Venturi, M. *Molecular Devices and Machines: Concepts and Perspectives for the Nanoworld*; Wiley-VCH: Weinheim, 2008.

[6] Feringa, B. L.; Browne (Eds.), W. R. *Molecular Switches*; Wiley-VCH: Weinheim, 2011; Vol. 1 & 2.

[7] Delaire, J. A.; Nakatani, K. *Chem. Rev.* **2000**, *100*, 1817–1845.

[8] Dhammika Bandara, H. M.; Burdette, S. C. *Chem. Soc. Rev.* **2012**, *41*, 1809–1825.

[9] Hagiri, M.; Ichinose, N.; Zhao, C.; Horiuchi, H.; Hiratsuka, H.; Nakayama, T. *Chem. Phys. Lett.* **2004**, *391*, 297–301.

[10] Schmidt, B.; Sobotta, C.; Malkmus, S.; Laimgruber, S.; Braun, M.; Zinth, W.; Gilch, P. *J. Phys. Chem. A* **2004**, *108*, 4399–4404.

[11] Poprawa-Smoluch, M.; Baggerman, J.; Zhang, H.; Maas, H. P. A.; De Cola, L.; Brouwer, A. M. *J. Phys. Chem. A* **2006**, *110*, 11926–11937.

[12] Asano, T. *J. Am. Chem. Soc,* **1980**, *102*, 1205–1206.

[13] Gille, K.; Knoll, H.; Quitzsch, K. *Int. J. Chem. Kinet.* **1999**, *31*, 337–350.

[14] Natansohn, A.; Rochon, P. *Chem. Rev.* **2002**, *102*, 4139.

[15] Rochon, P.; Batalla, E.; Natansohn, A. *Appl. Phys. Lett.* **1995**, *66*, 136–138.

[16] Yokoyama, S.; Nakahama, T.; Otomo, A.; Mashiko, S. *J. Am. Chem. Soc.* **2000**, *122*, 3174–3181.

[17] Martinez-Perdiguero, J.; Zhang, Y.; Walker, C.; Etxebarria, J.; Folcia, C. L.; Ortega, J.; O'Callaghan, M. J.; Baumeister, U. *J. Mater. Chem.* **2010**, *20*, 4905–4909.

[18] Marinotto, D.; Proutière, S.; Dragonetti, C.; Colombo, A.; Ferruti, P.; Pedron, D.; Ubaldi, M.; Pietralunga, S. *J. Non-Cryst. Solids* **2011**, *375*, 2075–2080.

[19] El-Khouly, M. E.; Chen, Y.; Zhuang, X.; Fukuzumi, S. *J. Am. Chem. Soc.* **2009**, *131*, 6370–6371.

[20] Bahrenburg, J.; Renth, F.; Plamper, F.; Eckert, T.; Richtering, W.; Temps, F.

[21] Satzger, H.; Spörlein, S.; Root, C.; Wachtveitl, J.; Zinth, W.; Gilch, P. *Chem. Phys. Lett.* **2003**, *372*, 216–223.

[22] Chang, C.-W.; Lu, Y.-C.; Wang, T.-T.; Diau, E. W.-G. *J. Am. Chem. Soc.* **2004**, *126*, 10109–10118.

[23] Pancur, T.; Renth, F.; Temps, F.; Harbaum, B.; Krüger, A.; Herges, R.; Näther, C. *Phys. Chem. Chem. Phys.* **2005**, *7*, 1985–1989.

[24] Siewertsen, R.; Schönborn, J. B.; Hartke, B.; Renth, F.; Temps, F. *Phys. Chem. Chem. Phys.* **2011**, *13*, 1054–1063.

[25] Cattaneo, P.; Persico, M. *Phys. Chem. Chem. Phys.* **1999**, *1*, 4739–4743.

[26] Ciminelli, C.; Granucci, G.; Persico, M. *J. Chem. Phys.* **2005**, *123*, 174317.

[27] Nonnenberg, C.; Gaub, H.; Frank, I. *ChemPhysChem* **2006**, *7*, 1455–1461.

[28] Granucci, G.; Persico, M. *Theor. Chem. Acc.* **2007**, *117*, 1131–1143.

[29] Conti, I.; Garavelli, M.; Orlandi, G. *J. Am. Chem. Soc.* **2008**, *130*, 5216–5230.

[30] Carstensen, O.; Sielk, J.; Schönborn, J. B.; Granucci, G.; Hartke, B. *J. Chem. Phys.* **2010**, *133*, 124305.

[31] Pederzoli, M.; Pittner, J.; Barbatti, M.; Lischka, H. *J. Phys. Chem. A* **2011**, *115*, 11136–11143.

[32] Biswas, N.; Umapathy, S. *J. Raman Spectrosc.* **2001**, *32*, 471–480.

[33] Biswas, N.; Umapathy, S. *J. Chem. Phys.* **2003**, *118*, 5526–5536.

[34] Koller, F.; Sobotta, C.; Schrader, T. E.; Cordes, T.; Schreier, W. J.; Sieg, A.; Gilch, P. *Chem. Phys.* **2007**, *341*, 258–266.

[35] Hsu, C.-C.; Wang, Y.-T.; Yabushita, A.; Luo, C.-W.; Hsiao, Y.-N.; Lin, S.-H.; Kobayashi, T. *J. Phys. Chem. A* **2011**, *115*, 11508–11514.

[36] Toro, C.; Thibert, A.; De Boni, L.; Masunov, A. E.; Hernandez, F. E. *J. Phys. Chem. B* **2008**, *112*, 929–937.

[37] De Boni, L.; Toro, C.; Masunov, A. E.; Hernández, F. E. *J. Phys. Chem. A* **2008**, *112*, 3886–3890.

[38] Crecca, C. R.; Roitberg, A. E. *J. Phys. Chem. A* **2006**, *110*, 8188–8203.

[39] Wang, L. X.; Wang, X. G. *J. Mol. Struc. Theochem.* **2007**, *847*, 1–9.

[40] Renth, F.; Foca, M.; Petter, A.; Temps, F. *Chem. Phys. Lett.* **2006**, *428*, 62–67.

[41] Siewertsen, R.; Renth, F.; Temps, F. *Phys. Chem. Chem. Phys.* **2009**, *11*, 5952–5961.

[42] Pancur, T.; Schwalb, N. K.; Renth, F.; Temps, F. *Chem. Phys.* **2005**, *313*, 199–212.

[43] Schwalb, N. K.; Temps, F. *J. Phys. Chem. A* **2009**, *113*, 13113–13123.

[44] Wohlfahrt, C. In *Springer Materials - The Landolt-Börnstein Database*; Madelung, O., Ed.; Springer: Berlin, 1991; Vol. 6; pp 5–228.

[45] Maroncelli, M.; MacInnis, J.; Fleming, G. R. *Science* **1989**, *243*, 1674–1681.

[46] Maroncelli, M.; Fleming, G. R. *J. Chem. Phys.* **1987**, *86*, 6221–6239.

[47] Zhong, D.; Kumar Pal, S.; Zhang, D.; Chan, S. I.; Zewail, A. H. *Proc. Natl. Acad. Sci.* **2002**, *99*, 13–18.

[48] Pal, S. K.; Peon, J.; Bagchi, B.; Zewail, A. H. *J. Chem. Phys. B* **2002**, *106*, 12376–12395.

[49] Stuhldreier, M. C.; Malicki, M.; Böhnke, H.; Öksüz, N.; Keppler, J.; Schwarz, K.; Temps, F.

4

FEMTOSECOND SPECTROSCOPY REVEALS HUGE DIFFERENCES IN THE PHOTOISOMERISATION DYNAMICS BETWEEN AZOBENZENES LINKED TO POLYMERS AND AZOBENZENES IN SOLUTION

Julia Bahrenburg,[a] Falk Renth,[a]* Friedrich Temps,[a]* Felix Plamper,[b] and Walter Richtering[b]

[a] Institute of Physical Chemistry, Christian-Albrechts-University Kiel, Olshausenstr. 40, D-24098 Kiel, Germany

[b] Institute of Physical Chemistry, RWTH Aachen, Landoltweg 2, D-52056 Aachen, Germany

J. Bahrenburg, F. Renth, F. Temps, F. Plamper and W. Richtering *Phys. Chem. Chem. Phys.*, **2014**, *16*, 11549-11554.

OWN CONTRIBUTIONS TO THIS MANUSCRIPT:

- Synthesis of the azobenzene derivatives
- Synthesis and characterization of the polymer colloids (together with F. Plamper)
- Time-resolved fluorescence spectroscopy
- Static absorption spectroscopy and irradiation experiments
- Analysis of the data
- Writing of the manuscript

* To whom correspondence should be addressed. E-mail: renth@phc.uni-kiel.de, temps@phc.uni-kiel.de

ABSTRACT

Femtosecond fluorescence up-conversion spectroscopy of two azobenzenes covalently attached to the side chain or linked by covalent bonds at each end into the main chain of polybutylmethacrylate polymer colloids with different cross-linking ratios reveals dramatic differences in the excited-state dynamics compared to the monomer chromophores in solution due to strong mechanical forces in the complex micronetworks. For the azobenzene derivative **DR1** in the polymer side chain, the measurements determined an increase of the mean excited-state lifetime after irradiation at $\lambda = 475$ nm to $\langle\tau\rangle = 5.5$ ps from $\langle\tau\rangle = 0.5$ ps for the monomer. For the cross-linked **BAAB** in the polymer main chain, an increase of $\langle\tau\rangle$ was found of more than a factor-of-20. Moreover, with a lifetime of $\tau = 430$ ps, $\approx 12\,\%$ of the molecules in the tightly (1:10) cross-linked polymer were found to remain in the excited state about 100 times longer than observed for the monomer chromophore. These results are of high relevance for applications of photoswitchable polymer materials.

4.1 INTRODUCTION

The photoswitching dynamics of azobenzene (**AB**) and derivatives of azobenzene have been extensively studied in solution by ultrafast time-resolved methods for more than a decade.[1–10] For practical applications, however, the photochromic switches are often embedded in complex environments such as liquid crystals,[11–13] polymers,[14–20] thin films[21–23] or composite materials,[24,25] where the photoswitching has not been investigated in much detail to date although the light-induced transformations of the molecules may be very strongly affected by the surrounding matrix. To elucidate the important mechanisms under those much more complex conditions than in solution, we investigated the *trans*-to-*cis* photoisomerisation dynamics of two AB derivatives in cross-linked colloidal polybutylmethacrylate (**PBMA**) micronetworks by femtosecond time-resolved fluorescence up-conversion spectroscopy. The push-pull AB Disperse Red 1 (**DR1**) and the bi-functionalised **AB** 4,4′-bis(acetamido)-azobenzene (**BAAB**) were covalently attached to the polymer chain as side-group (**P-DR1**) and cross-linked by a covalent bond at each end into the polymer network (**P-BAAB-P**), respectively, as sketched in Figure 4.1. In the first case, the **AB** unit is still somewhat flexible as it is fixed to the polymer only at one end. In the second case, in contrast, the **AB** switch is tightly embedded within the cross-linked polymeric network and motionally highly restricted. The two different linkage schemes and the variation of the cross-linking ratio thus allow us to assess the influences of the topographical constraints in the polymer networks on the excited-state dynamics and the ultrafast photo-induced isomerisation reactions of these **AB** switches. The results we are reporting in this paper reveal huge changes in the dynamics compared to the free monomers in solution.

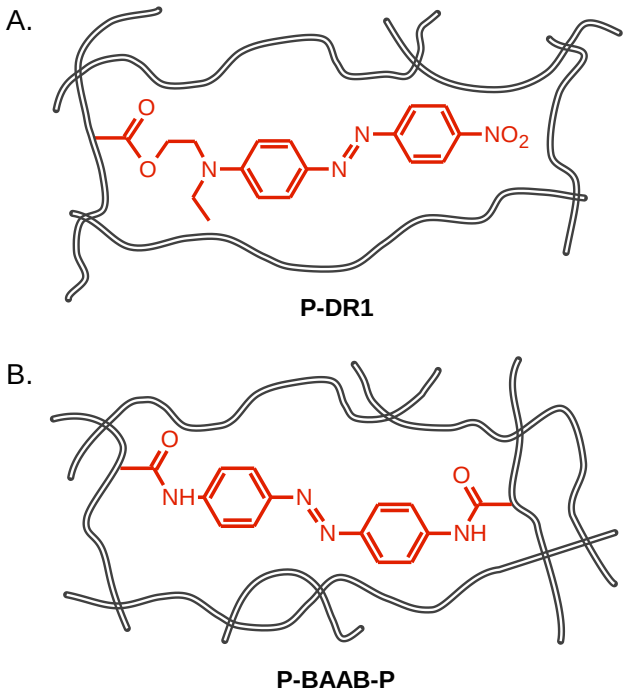

Figure 4.1: A. **DR1** attached as side group by a covalent bond to the PBMA backbone (**P-DR1**) and B. **BAAB** cross-linked covalently at both ends into the main chain of the PBMA polymer (**P-BAAB-P**).

4.2 EXPERIMENTAL METHODS

Colloidal **PBMA** particles with cross-linking ratios of 1:10 for **P-DR1** and 1:10 as well as 1:50 for **P-BAAB-P** were synthesised by radical copolymerisation in surfactant-free emulsion polymerisation as described in the ESI†. The molar ratios of monomer (butyl methacrylate), cross-linker (ethylene glycol dimethacrylate) and co-monomer (**DR1**-methacrylate and 4,4'-bis-(methacryloylamido)-azobenzene, respectively) are given in Table 4.1. To obtain information on the particle size distribution and the swelling behaviour, the particles were measured by light scattering (see ESI†) in water (collapsed) and in toluene (swollen). As expected, the degree of swelling is larger for the more loosely cross-linked particles. The **AB** contents determined by UV/VIS spectroscopy were of the order of $\approx$ 0.3 mol-% for all systems.

Table 4.1: Molar ratios of monomer, cross-linker and co-monomer used for the radical copolymerisation.

	Monomer	Cross-linker	Co-monomer
P-DR1 (1:10)	100	10	1
P-BAAB-P (1:50)	100	2	1
P-BAAB-P (1:10)	100	10	1

The employed femtosecond time-resolved fluorescence up-conversion spectrometer has been described in some detail previously.[6,26] The mea-

surements were performed in 1 mm flow cells with 0.2 mm quartz windows. The required pump pulses at $\lambda = 475$ nm (0.5 µJ) for excitation in the first absorption bands of the molecules in the VIS spectrum were obtained from a Ti:Sa laser pumped non-collinear optical parametric amplifier. The fluorescence decay curves were recorded at wavelengths in the range 600 nm $\leqslant \lambda_{fl} \leqslant$ 700 nm and analysed by global non-linear least squares fitting. The experimental time resolution was of the order of $\Delta t \approx 100$ fs. For all measurements the colloidal particles were re-dispersed at a concentration of $\approx$ 10 mg/mL in 2-fluorotoluene (2-FT) as nearly isorefractive solvent to reduce the intensity of scattered light.

4.3 RESULTS

4.3.1 PHOTOSWITCHING DYNAMICS OF DR1 LINKED TO PBMA

The static UV/VIS spectra of **DR1**, **P-DR1** with cross-linking ratio of 1:10 and neat **PBMA** colloids with the same cross-linking ratio are shown in Fig. 4.2 A. The donor-acceptor substitution in **DR1** is known to induce pronounced charge-transfer (CT) character in the photoexcited state, resulting in a strong red-shift of the intense $\pi\pi^*$ absorption band from the UV into the visible spectrum, where it obscures the much weaker $n\pi^*$ transition.[8–10] The applied 475 nm pump pulses consequently prepare the **DR1** molecules in the $\pi\pi^*$ excited state. Neat **PBMA** colloids show a weak extinction over the whole spectral range due to light scattering. The spectrum of **P-DR1** is very similar to that of **DR1** in solution except for the scattered light contributed by the polymer particles, a slight blue-shift ($\approx$ 2 nm) and the evident broadening of the $\pi\pi^*$ absorption band.

Measured fluorescence-time profiles for **DR1** and **P-DR1** (1:10) in 2-FT at $\lambda_{fl} = 660$ nm after excitation at $\lambda_{pump} = 475$ nm are displayed in Fig. 4.2 B. As shown, the data for **P-DR1** reveal a significantly slower decay than for **DR1**. The time profiles for the monomer in solution are bi-exponential with decay constants of $\tau_1 = 0.18 \pm 0.02$ ps (53 %) and $\tau_2 = 0.83 \pm 0.02$ ps (47 %) with 2σ error limits and relative amplitudes in parentheses. In contrast, the fluorescence data for **P-DR1** require three exponentials for satisfactory fitting, with values of $\tau_1 = 0.18 \pm 0.02$ ps (58 %), $\tau_2 = 1.60 \pm 0.04$ ps (39 %) and $\tau_3 = 160 \pm 15$ ps (3 %). The derived time constants are collected in Table 4.2.

Table 4.2: Experimental fluorescence decay times for **DR1** and **P-DR1** (1:10) in 2-FT.

	τ_1 / ps	τ_2 / ps	τ_3 / ps
DR1	0.18 ± 0.02	0.83 ± 0.02	–
P-DR1 (1:10)	0.18 ± 0.02	1.60 ± 0.04	160 ± 16

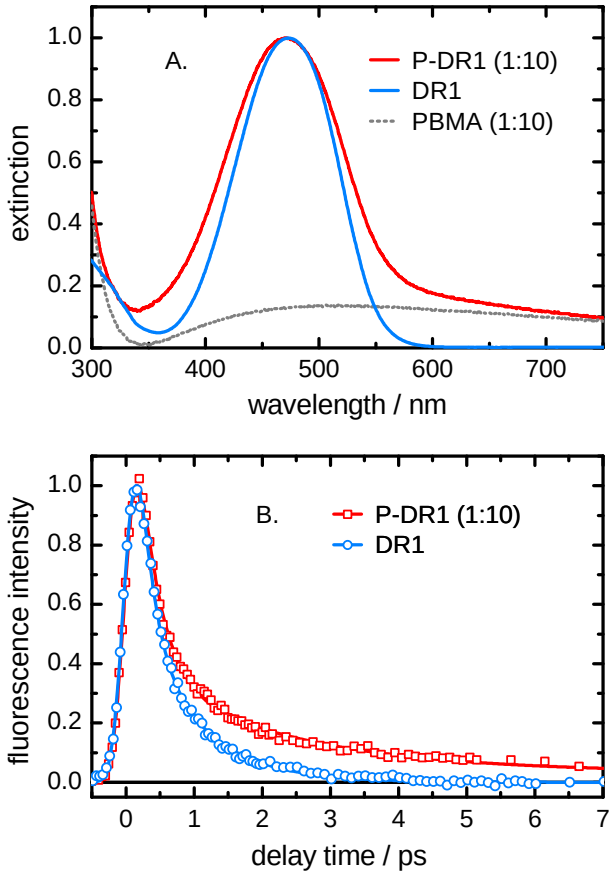

Figure 4.2: A. UV/VIS spectra of **DR1** (blue), **P-DR1** (red) and neat **PBMA** colloids (dotted line) in 2-FT. B. Fluorescence decay curves of **DR1** (blue) and **P-DR1** (red) at $\lambda_{fl} = 660$ nm after excitation at $\lambda_{pump} = 475$ nm. Symbols indicate the data points, solid lines the corresponding non-linear least-square fits. For better comparison the time profiles are shown only up to $\Delta t = 7$ ps, but the scans continued to $\Delta t = 300$ ps, where the dynamics were complete within experimental limits.

4.3.2 PHOTOSWITCHING DYNAMICS OF CROSS-LINKED BAAB IN PBMA

The UV/VIS spectra of **BAAB** and **P-BAAB-P** with cross-linking ratios 1:50 and 1:10 given in Fig. 4.3 A exhibit a strong $\pi\pi^*$ transition in the UV and a weak $n\pi^*$ absorption in the visible similar to plain **AB**. The 1:10 cross-linked sample also shows a contribution by light scattering. Since the 1:50 cross-linked colloids exhibit higher swelling and therefore have more solvent inside the polymer network, the refractive index matching works better and the contribution by scattered light is practically negligible. Additionally, Figure 4.6 (see ESI†) shows the UV/VIS spectra of **BAAB** and **P-BAAB-P** (1:50 and 1:10) in the photostationary states after irradiation at $\lambda = 455$ nm (PSS455) and in the course of the thermal back-isomerisation of the molecules from the photostationary states. From the smaller change in amplitude, the switching efficiency in the cross-linked polymer network appears to be considerably lower than in solution. The observed effects may be related to strong external pulling forces counter-

acting on the isomerising **BAAB** molecule in the main-chain of the polymer. Further, an analysis of the temporal intensity changes shows that with $t_{1/2} \approx 2.0 \pm 0.2$ h the thermal lifetimes of the *cis* isomer in the 1:50 and the 1:10 cross-linked polymer particles is about half as long as for the monomer in solution ($t_{1/2} \approx 4.0 \pm 0.1$ h), hinting at a corresponding lowering of the associated potential energy barrier.

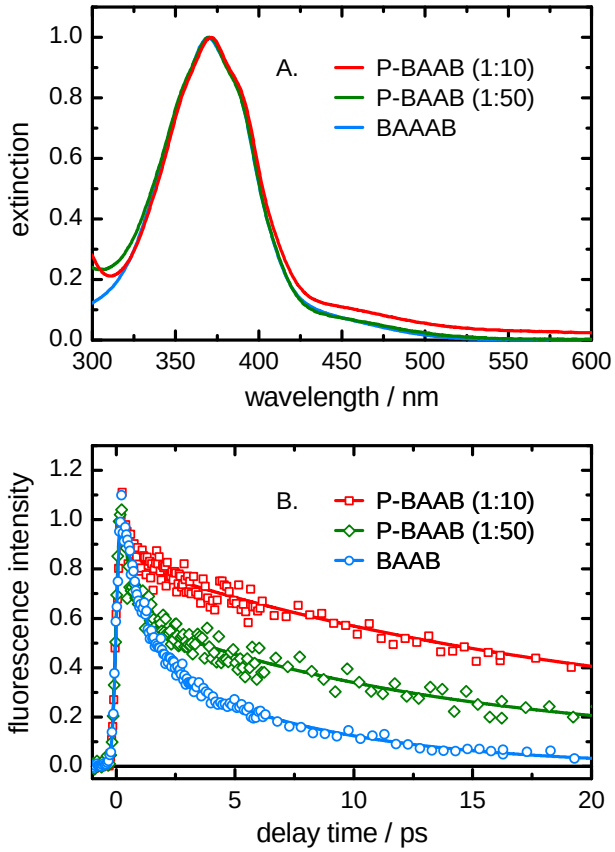

Figure 4.3: A. UV/VIS spectra of **BAAB** (blue), **P-BAAB-P** 1:50 (dark green) and **P-BAAB-P** 1:10 (red) in 2-FT. B. Measured fluorescence-time profiles of **BAAAB** (blue circles), **P-BAAB-P** 1:50 (dark green diamonds) and **P-BAAB-P** 1:10 (red squares) at $\lambda_{fl} = 660$ nm after excitation at $\lambda_{pump} = 475$ nm. Open symbols are data, solid lines the respective least-squares fit curves. For better comparison the curves are shown only to $\Delta t = 20$ ps, but the measurements continued to a delay time of $\Delta t = 350$ ps.

Figure 4.3 B displays recorded fluorescence-time profiles for **BAAB** in solution, **BAAB** in the 1:50 cross-linked polymer and **BAAB** in the 1:10 cross-linked polymer. The excitation at $\lambda_{pump} = 475$ nm leads to the $n\pi^*$ state. As can be seen, **P-BAAB-P** (1:50 and 1:10) exhibit drastically slower fluorescence decays than the monomer. Very similar data were obtained at other emission wavelengths. The fitted time constants are compiled in Table 4.3. **BAAB** decays in a bi-exponential fashion with $\tau_1 = 0.79 \pm 0.04$ ps (50 %) and $\tau_2 = 5.9 \pm 0.1$ ps (50 %), whereas the 1:50 and 1:10 cross-linked polymer colloids require three exponentials for satisfactory descriptions. The respective non-linear least-squares fit analyses gave $\tau_1 = 0.9 \pm 0.1$ ps (41 %), $\tau_2 = 15 \pm 1.0$ ps (50 %) and $\tau_3 = 300 \pm 15$ ps (9 %) for **P-**

Table 4.3: Experimental fluorescence decay times for **BAAB**, **P-BAAB-P** (1:10) and **P-BAAB-P** (1:10) in 2-FT.

	τ_1 / ps	τ_2 / ps	τ_3 / ps
BAAB	0.79 ± 0.04	5.90 ± 0.10	-
P-BAAB-P (1:50)	0.90 ± 0.10	15.0 ± 1.0	300 ± 85
P-BAAB-P (1:10)	1.50 ± 0.10	26.0 ± 1.0	430 ± 100

BAAB-P (1:50) and $\tau_1 = 1.5 \pm 0.1$ ps (20 %), $\tau_2 = 26 \pm 1.0$ ps (68 %) and $\tau_3 = 430 \pm 100$ ps (12 %) for **P-BAAB-P** (1:10).

4.4 DISCUSSION

As in the case of azobenzene itself,[2,4,27–29] the short, sub-picosecond to few picosecond, fluorescence lifetimes of the investigated derivatives **DR1** and **BAAB** are determined by the ultrafast isomerisation and radiationless deactivation of the photoexcited molecules through the conical intersection (CoIn) that connects the excited (S_1) to the ground (S_0) electronic state. The experimental results above thus reveal that the cross-linked, tight polymer network in which the molecules are embedded (**P-DR1**, **P-BAAB-P**) exerts immense influence on the isomerisation dynamics.

An excited-state lifetime for free **DR1** of $\tau < 1$ ps has been found in preceding measurements.[8–10] The observed bi-exponential fluorescence behaviour is rationalised as a step-wise relaxation from the initially excited $\pi\pi^*$ state to the $n\pi^*$ state followed by *trans-cis* isomerisation and radiationless deactivation to the ground state.[10] By comparison, the dynamics of the molecule attached to the polymer matrix (**P-DR1**) are substantially slower. Nevertheless, the isomerisation is likely governed by the same sequential mechanism. Time constant τ_1 is virtually identical for **DR1** and **P-DR1** within experimental errors and related to the internal conversion from the $\pi\pi^*$ to the $n\pi^*$ state in both cases. This first transformation seems to be practically unaffected by the surrounding polymer matrix, which is understandable because the molecule remains in its *trans* form. In contrast, τ_2 for **P-DR1** is longer by a factor of two. This behaviour and the additional long decay time constant of $\tau_3 = 160$ ps are evidently caused by the polymer network. The amplitude-weighted mean fluorescence lifetime increases from $\langle\tau\rangle \approx 0.5$ ps for **DR1** to ≈ 5.5 ps for **P-DR1**. This change by a full order of magnitude shows that the large-amplitude motion required for *trans-cis* isomerisation is substantially hindered in the cross-linked polymer, where the wavepacket motion on the excited potential energy hypersurface (PEHS) *en route* to the CoIn mediating the isomerisation and radiationless transition to the S_0 state becomes more diffuse.

BAAB excited to the $n\pi^*$ state is expected to proceed along a similar route as plain **AB**, where the bi-phasic behaviour of the *trans*-isomer is attributed to fast departure from the Franck-Condon region ($\tau_1 \approx 0.3$ ps) followed by the transformation through the S_1/S_0 CoIn ($\tau_2 \approx 3$ ps).[2,4]

When **BAAB** is cross-linked into a main chain of the polymer, the mean experimental fluorescence lifetime increases from $\langle\tau\rangle = 3$ ps more than 20-fold to $\langle\tau\rangle = 65$ ps in the case of the 1:10 cross-linked **P-BAAB-P**. Specifically, time constant τ_2 grows not only in magnitude but also in relative amplitude. Moreover, the additional third decay time of $\tau_3 = 430$ ps demonstrates that in fact a sizable fraction (≈ 12 %) of the excited AB switches in the polymer remain about a hundred times longer in the S_1 state than in the free **BAAB** case. Those molecules are effectively trapped in the excited state. It is even possible that they are electronically deactivated by other mechanisms than via the main S_1/S_0 CoIn referred to above such that they may not even undergo isomerisation. Further, as shown by the spectra of the photostationary states (see Fig. 4.6, ESI†), it is evident that not only the radiationless dynamics are much slower in the cross-linked polymer, but that the photoswitching yields are smaller as well. Another possibility is that **AB**s in the polymer may follow a variety of reaction pathways on the S_1 PEHS (*e.g.* torsional, hula-twist, inversion or even more complex internal motions). In that case the observed changes reflect the different contributions along those pathways to the overall process. In any case, it is important to keep in mind that the microscopic distribution of the functional AB units in the polymer network is likely quite inhomogeneous.

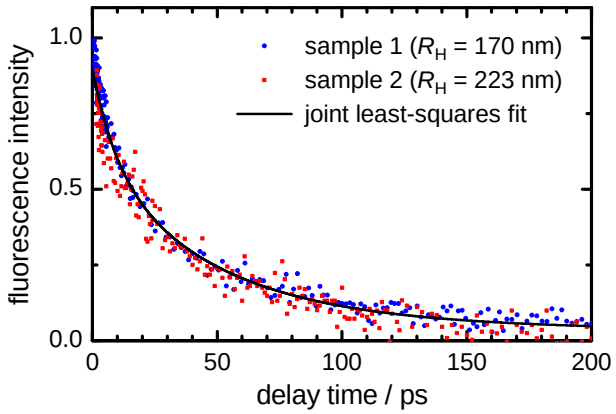

Figure 4.4: Fluorescence-time profiles at $\lambda_{fl} = 660$ nm for two **P-BAAB-P** samples with 1:10 cross-linking ratio, but different hydrodynamic radii R_H from different syntheses. The solid curve shows the joint fit to the data points of both samples.

Figure 4.4 exemplarily displays a comparison of the temporal fluorescence decays for two different **P-BAAB-P** samples with the same cross-linking ratio of 1:10 but different hydrodynamic radii. Both samples were polymerised following slightly different protocols, which led to $R_H = 170 \pm 2$ nm and 223 ± 4 nm, respectively (see ESI†). Nevertheless, the fluorescence decay curves for the smaller and the larger colloid are very similar and both time profiles can be described using one and the same fit curve. These measurements indicate that the photoisomerisation dynamics are not strongly dependent on the particle radius. Additionally, Figure 4.4 nicely demonstrates the long-lived nature of the fluorescing excited state of BAAB in the polymer matrix.

Considering the quantum yields for fluorescence of the photoexcited molecules, $\phi_{fl} = k_{fl}/(k_{fl} + k_{iso} + k_{nr}) = \tau/\tau_{fl}$, where $k_{fl} = \tau_{fl}^{-1}$, k_{iso} and k_{nr} are the rate coefficients for emission, isomerisation and other nonradiative deactivation processes, a Strickler-Berg analysis of the $n\pi^*$ absorption band provides a value for the radiative lifetime of **BAAB** of $\tau_{fl} \approx 300$ ns. Combining this value with the experimentally measured mean lifetimes ($\langle\tau\rangle = 3$ resp. 65 ps), **BAAB** in solution has a fluorescence quantum yield of $\phi_{fl} \approx 10^{-5}$, very similar to plain **AB**.[2] In the 1:10 cross-linked polymer (**P-BAAB-P**), on the other hand, the quantum yield increases to $\phi_{fl} \approx 2 \times 10^{-4}$. Since $k_{fl} \ll k_{iso} + k_{nr}$, this change has to be due to a correspondingly slower molecular motion and reaction (isomerisation and deactivation) through the CoIn. Unfortunately, the quantum yield for photoisomerisation of the molecules in the polymer matrix could not be directly determined by one of the standard methods[30–32] because of the lack of clear signatures of the *cis* product in the UV/VIS spectra and the interference by scattered light.[33] Suitable tools will be developed in future work.

The photoisomerisation dynamics of azobenzenes are known to be influenced by chemical substitution affecting the chromophore electronically and sterically and by the environment around the molecules.[34] For example, a six-fold increase of the fluorescence lifetime τ_2 to 20 ps compared to unsubstituted **AB** has been found in a study of the photoisomerisation of a cyclic, rotation-restricted azobenzene capped by a crown ether and a chemically related open derivative.[6] An effect up to a factor-of-ten has been observed for an azobenzophane, where the isomerisation reaction is sterically strongly hindered.[5] For azobenzene photoswitches in a small cyclic peptide, only a small change of the electronic lifetime of the excited $n\pi^*$ state was observed, while much slower spectro-temporal evolutions thereafter were related to *cis-trans* isomerisation-induced conformational motions of the peptide backbone.[35,36] Further, Chang et al. reported an increase of the fluorescence lifetime of **AB** after $n\pi^*$ excitation with the viscosity of the solvent from *n*-hexane to ethylene glycol accompanied by a large change of the fluorescence anisotropy decay.[4] Both effects have been modeled by mixed quantum-classical dynamics calculations.[28] Intrapolymer exciton aggregate formation has been observed in a sulfophenylazonaphtolsulfonic acid salt attached to a flexible polymer chain,[37] but this mechanism is unlikely to be important in our case due to the very low dye concentration and the heavy cross-linking. An azobenzene derivative in a nanocavity exhibits only slight changes in the isomerisation dynamics and the switching efficiency, with an increase of the excited-state lifetime in the confined environment by just a factor of two.[38] Eventually, restriction of the torsional motion in a benzothiazole-based cationic dye in a nanocavity was found to lead to a similar change.[39] However, none of those works have shown effects anywhere close in magnitude to those found in the present case of **BAAB** in tightly cross-linked **PBMA**, where the measured long fluorescence lifetime constant $\tau_3 = 430$ ps indicates that about 12 % of the photo-excited molecules can hardly reach the CoIn mediating the isomerisation at all. Again, it should be kept in mind here that the local

environment, expecially the local cross-link distribution, around the ABs in the polymer is probably quite inhomogeneous, implying that there will be significant site-to-site variations of the dynamics at the individual molecule level.

Considering the azophotoswitches embedded in the tightly cross-linked polymer environment, the required large-amplitude motion of the molecules on the excited PEHS to the CoIn region mediating the *trans-cis* isomerisation and leading to the S_0 electronic ground state evidently meets severe resistance by the surrounding polymer. Such change of dynamics in a polymer environment are often rationalised by the higher microviscosity. Neutron spin echo experiments, for example, have shown that chain dynamics depend strongly on the cross-link density and the apparent solvent viscosity inside microgels can be significantly higher than in the bulk solvent.[40,41] Alternatively, one may think of the observed striking effect in **P-BAAB-P** to result from strong mechanical restraining forces acting on the photo-excited **AB** switch in the tightly cross-linked polymer network. With the advent of mechanochemistry, where individual azobenzene molecule are submitted to external forces and the consequences are monitored at the single-molecule level,[16,17] this picture appears particularly attractive because it promises to rationalisation at the microscopic, molecular level. First proof-of-principle semiempirical QM/MM dynamics calculations on individual **BAAB** switches in a **PBMA** model matrix indeed indicate order-of-magnitude longer excited-state lifetimes than in solution by the strong external, intermolecular forces acting on the **AB** unit during isomerisation in the polymer.[42] This effect is opposite to that observed in the highly constrained bridged **AB** derivative dihydrodibenzodiazocine,[7,43–45] where the molecular dynamics is strongly accelerated by intramolecular forces directed towards the CoIn and the photo-switching efficiency thus becomes much higher than in plain **AB**.

4.5 CONCLUSIONS

In conclusion, our study revealed dramatic differences between the photoinduced *trans-cis* isomerisation dynamics of azobenzenes in solution and covalently cross-linked in polymeric micronetworks. The excited-state lifetimes in the polymer are drastically longer and can be controlled by varying the tightness of the surrounding matrix. The observed effects are of high practical relevance for applications of photoswitchable azopolymer materials. Optimal design strategies have to provide for sufficient free volume around the switches and avoid conformations, where the switches get constrained and tangled up by the polymer chains.

The unexpected huge matrix effects on the photoswitching dynamics are currently under investigation in other polymer environments, including amorphous thin glass films in addition to colloidal networks, using promising other switches, *e.g.* diazocines, where *trans-cis* isomerisation should be experimentally observable in both directions, and by theoretical means using QM/MM dynamics calculations.

ACKNOWLEDGMENTS

The work of JB, FR and FT has been supported by the Deutsche Forschungsgemeinschaft through the Collaborative Research Centre 677 “Function by Switching”. FP and WR acknowledge support by the Deutsche Forschungsgemeinschaft through the Collaborative Research Centre 985 “Functional Microgels and Microgel Systems”.

BIBLIOGRAPHY

[1] Lu, Y.-C.; Chang, C.-W.; Diau, E. W.-G. *J. Chin. Chem. Soc.* **2002**, *49*, 693.

[2] Satzger, H.; Spörlein, S.; Root, C.; Wachtveitl, J.; Zinth, W.; Gilch, P. *Chem. Phys. Lett.* **2003**, *372*, 216–223.

[3] Satzger, H.; Root, C.; Braun, M. *J. Phys. Chem. A* **2004**, *108*, 6265–6271.

[4] Chang, C.-W.; Lu, Y.-C.; Wang, T.-T.; Diau, E. W.-G. *J. Am. Chem. Soc.* **2004**, *126*, 10109–10118.

[5] Lu, Y.-C.; Diau, E. W.-G.; Rau, H. *J. Phys. Chem. A* **2005**, *109*, 2090.

[6] Pancur, T.; Renth, F.; Temps, F.; Harbaum, B.; Krüger, A.; Herges, R.; Näther, C. *Phys. Chem. Chem. Phys.* **2005**, *7*, 1985–1989.

[7] Siewertsen, R.; Schönborn, J. B.; Hartke, B.; Renth, F.; Temps, F. *Phys. Chem. Chem. Phys.* **2011**, *13*, 1054–1063.

[8] Schmidt, B.; Sobotta, C.; Malkmus, S.; Laimgruber, S.; Braun, M.; Zinth, W.; Gilch, P. *J. Phys. Chem. A* **2004**, *108*, 4399–4404.

[9] Poprawa-Smoluch, M.; Baggerman, J.; Zhang, H.; Maas, H. P. A.; De Cola, L.; Brouwer, A. M. *J. Phys. Chem. A* **2006**, *110*, 11926–11937.

[10] Bahrenburg, J.; Röttger, K.; Siewertsen, R.; Renth, F.; Temps, F. *Photochem. Photobiol. Sci.* **2012**, *11*, 1210–1219.

[11] Ikeda, T.; Tsutsumi, O. *Science* **1995**, *268*, 1873–1875.

[12] Ikeda, T.; Nakano, M.; Yu, Y.; Tsutsumi, O.; Kanazawa, A. *Adv. Mater.* **2003**, *15*, 201.

[13] Fujii, T.; Kuwahara, S.; Katayama, K.; Takado, K.; Ube, T.; Ikeda, T. *Phys. Chem. Chem. Phys.* **2014**, DOI: 10.1039/C4CP00457D.

[14] Kumar, G. S.; Neckers, D. C. *Chem. Rev.* **1989**, *89*, 1915–1925.

[15] Natansohn, A.; Rochon, P. *Chem. Rev.* **2002**, *102*, 4139.

[16] Hugel, T.; Holland, N. B.; Cattani, A.; Moroder, L.; Seitz, M.; Gaub, H. E. *Science* **2002**, *296*, 1103–1106.

[17] Holland, N. B.; Hugel, T.; Neuert, G.; Cattani-Scholz, A.; Renner, C.; Oesterhelt, D.; Moroder, L.; Seitz, M.; Gaub, H. E. *Macromolecules* **2003**, *36*, 2015–2023.

[18] Häckel, M.; Kador, L.; Kropp, D.; Schmidt, H.-W. *Adv. Mater.* **2007**, *19*, 227–231.

[19] Willerich, I.; Gröhn, F. *Macromolecules* **2011**, *44*, 4452–4461.

[20] Wiktorowicz, S.; Tenhu, H.; Aseyev, V. *Macromolecules* **2013**, *46*, 6209–6216.

[21] Sekkat, Z.; Morichère, D.; Dumont, M.; Loucif-Saïbi, R.; Delaire, J. A. *J. Appl. Phys.* **1992**, *71*, 1543–1545.

[22] Hsu, C.-C.; Wang, Y.-T.; Yabushita, A.; Luo, C.-W.; Hsiao, Y.-N.; Lin, S.-H.; Kobayashi, T. *J. Phys. Chem. A* **2011**, *115*, 11508–11514.

[23] Fabbri, F.; Garrot, D.; Lahlil, K.; Boilot, J. P.; Lassailly, Y.; Peretti, J. *J. Phys. Chem. B* **2011**, *115*, 1363–1367.

[24] Pakula, C.; Zaporojtchenko, V.; Strunskus, T.; Zargarani, D.; Herges, R.; Faupel, F. *Nanotechnology* **2010**, *21*, 465201.

[25] Pakula, C.; Hanisch, C.; Zaporojtchenko, V.; Strunskus, T.; Bornholdt, C.; Zargarani, D.; Herges, R.; Faupel, F. *J. Mater. Sci.* **2011**, *46*, 2488–2494.

[26] Schwalb, N. K.; Temps, F. *J. Phys. Chem. A* **2009**, *113*, 13113–13123.

[27] Granucci, G.; Persico, M. *Theor. Chem. Acc.* **2007**, *117*, 1131–1143.

[28] Cusati, T.; Granucci, G.; Persico, M. *J. Am. Chem. Soc.* **2011**, *133*, 5109–5123.

[29] Pederzoli, M.; Pittner, J.; Barbatti, M.; Lischka, H. *J. Phys. Chem. A* **2011**, *115*, 11136–11143.

[30] Rau, H.; Greiner, G.; Gauglitz, G.; Meier, H. *J. Phys. Chem.* **1990**, *94*, 6523–6524.

[31] Uhlmann, E.; Gauglitz, G. *J. Photochem. Photobiol. A* **1996**, *98*, 45–49.

[32] Maafi, M.; Brown, R. G. *Photochem. Photobiol. Sci.* **2008**, *7*, 1360–1372.

[33] For DR1, the thermal lifetime of the *cis* isomer is too short for a straight measurement of the quantum yield at room temperature. See: K. Gille, H. Knoll and K. Quitzsch, *Int. J. Chem. Kinet.* **1999**, 31, 337 – 350.

[34] Dhammika Bandara, H. M.; Burdette, S. C. *Chem. Soc. Rev.* **2012**, *41*, 1809–1825.

[35] Spörlein, S.; Carstens, H.; Satzger, H.; Renner, C.; Behrendt, R.; Moroder, L.; Tavan, P.; Zinth, W.; Wachtveitl, J. *Proc. Natl. Acad. Sci. U.S.A.* **2002**, *99*, 7998–8002.

[36] Wachtveitl, J.; Spörlein, S.; Satzger, H.; Fonrobert, B.; Renner, C.; Behrendt, R.; Oesterhelt, D.; Moroder, L.; Zinth, W. *Biophys. J.* **2004**, *86*, 2350–2362.

[37] Varnavski, O.; Goodson III, T. *Chem Phys. Lett.* **2000**, *320*, 688–696.

[38] Takei, M.; Yui, H.; Hirose, Y.; Sawada, T. *J. Phys. Chem. A* **2001**, *105*, 11395–11399.

[39] Singh, P. H.; Kumbhakar, M.; Pal, H.; Nath, S. *Phys. Chem. Chem. Phys.* **2011**, *13*, 8008–8014.

[40] Hellweg, T.; Eimer, W.; Pouget, S.; Kratz, K. In *Neutron Spin Echo Spectroscopy: Basics, Trends and Applications*; Medzei, F., Pappas, T., Gutberlet, T., Eds.; Springer, 2003; pp 291–301.

[41] Scherzinger, C.; Holderer, O.; Richter, D.; Richtering, W. *Phys. Chem. Chem. Phys.* **2012**, *14*, 2762–2768.

[42] Steffen, J.; Carstensen, N. O.; Hartke, B. unpublished results (2013).

[43] Siewertsen, R.; Neumann, H.; Buchheim-Stehn, B.; Herges, R.; Näther, C.; Renth, F.; Temps, F. *J. Am. Chem. Soc.* **2009**, *131*, 15594–15595.

[44] Carstensen, O.; Sielk, J.; Schönborn, J. B.; Granucci, G.; Hartke, B. *J. Chem. Phys.* **2010**, *133*, 124305.

[45] Carstensen, N. O. *Phys. Chem. Chem. Phys.* **2013**, *15*, 15017–15026.

4.6 ELECTRONIC SUPPLEMENTARY INFORMATION

GENERAL

All commercially available compounds were purchased from Merck and Sigma-Aldrich and used without further purification. The purity of Disperse Red 1-methacrylate was checked by NMR spectroscopy. 4,4'-Bis-(acetamido)azobenzene and 4,4'-bis(methacryloylamido)azobenzene were synthesised in a reaction known from literature between 4,4'-diaminoazobenzene and acetyl chloride and between 4,4'-diaminoazobenzene and methacryloyl chloride, respectively [4.S1, 4.S2]. The purity was checked by NMR spectroscopy. Used solvents were dried according to standard procedures. NMR data were acquired with a Bruker AV-600 spectrometer. UV/VIS absorption spectra were taken on a Shimadzu UV-2401 desktop spectrometer. A light emitting diodes (Nichia) with emission maximum at 455 nm (NS4C107E, 400 mW) was used for the photoisomerisation experiments. The light intensity was attenuated to 150 mW. Dynamic light scattering (DLS) and static light scattering (SLS) measurements in water and in toluene were performed with an ALV 5000 E autocorrelator equipped with a red laser ($\lambda = 633$ nm; in some cases a blue laser with $\lambda = 473$ nm was used; due to dominant absorption, DR1 samples in organic media could only be measured reliably with the red laser). For DLS, the time-resolved signal of two single photon counting modules (SPCM-CD 2969; Perkin Elmer) was cross-correlated (sampling time $\approx$ 2 min) to obtain the intensity autocorrelation function. Hereby, the decay times τ of the field autocorrelation function (as obtained from the intensity autocorrelation function obtained by use of the Siegert relation [4.S3]) were extracted by the second-order cumulant analysis. The inverse of τ, the decay rate Γ, was plotted against the squared length of the scattering vector q^2. The slope gave the diffusion coefficient D and its value was transformed to the hydrodynamic radius R_h by the Stokes-Einstein equation. For SLS, the count rate at each angle was weighted with the scattering volume and corrected for solvent scattering to obtain the scattering intensity $I(q)$ and plotted against q (I in arbitrary units). A collection of the scattering data is given in Table 4.4 and 4.5. Form factor analysis provided the respective hard sphere radius R_{hs}. An exemplary form factor of P-BAAB-P (1:50) (Sample 2) is given in Figure 4.5. It indicates a narrow size distribution both in organic and aqueous dispersion.

SYNTHESES OF THE AZOBENZENE FUNCTIONALISED POLYMER COLLOIDS

Side- and main-chain azobenzene functionalised polymer colloids with a poly(butyl methacrylate) (PBMA) backbone and a cross-linking ratio of 1:10 for P-DR1 and 1:10 as well as 1:50 for P-BAAB-P were synthesised by radical co-polymerisation in surfactant-free emulsion polymerisation. All particles were synthesised twice following slightly different variants.

First synthesis variant for P-DR1 (1:10) and P-BAAB-P (1:10 and 1:50) (Sample 1)

All particles were synthesised in the same way. The different concentrations of monomer, cross-linker and respective co-monomer are given in Table 4.4.

Table 4.4: Ratios of monomer (butyl methacrylate), cross-linker (ethylene glycol dimethacrylate) and co-monomer (Disperse Red 1-methacrylate or 4,4-bis(methacryloylamido)azobenzene) used for the radical copolymerisation in surfactant-free emulsion polymerisation.

	monomer	cross-linker	co-monomer
P-DR1 (1:10)	42 mmol (6 g)	4.2 mmol (0.83 g)	0.42 mmol (0.16 g)
P-BAAB-P (1:50)	42 mmol (6 g)	0.42 mmol (0.083 g)	0.42 mmol (0.13 g)
P-BAAB-P (1:10)	42 mmol (6 g)	3.78 mmol (0.74 g)	0.42 mmol (0.13 g)

Typical synthesis procedure: Butyl methacrylate (BMA), ethylene glycol dimethacrylate (EGDMA) and the respective co-monomer were dissolved in 30 ml acetone in order to solubilise the azobenzene derivative in the mixture. This mixture was added under nitrogen and under stirring to 150 ml of deionised water, which was heated to $\vartheta = 80\,^{\circ}\mathrm{C}$. Not fully dissolved dye was then fully soluble in the monomer droplets. Potassium peroxodisulfate (KPS, 0.10 g) was dissolved in 5 ml of deionised water and then injected to the heated monomer mixture. After 1 h the same amount of radical starter was added to the reaction mixture again to complete the polymerisation. The course of the reaction was followed by DLS measurements. The polymerisation was stopped after about 3 h. Afterwards, formed aggregates were removed by filtration. The filtrate was centrifuged and redispersed in acetone. The filtration/redispergation was repeated a few times in order to remove unreacted monomer until the supernatant was colourless. Then the particles were redispersed in dioxane. Finally this dioxane dispersion was freeze-dried. A small part of the acetone dispersion was diluted then dialysed against water to measure the hydrodynamic radius and the radius of gyration in the collapsed state after further dilution. To measure the hydrodynamic radius in the swollen state a small amount was swollen in toluene. The results of the light scattering measurements are shown in Table 4.5.

Second synthesis variant for P-DR1 (1:10) and P-BAAB-P (1:10 and 1:50) (Sample 2)

All particles were synthesised in the same way. The different concentrations of monomer, cross-linker and respective co-monomer are given in Table 4.4.

Typical synthesis procedure: Butyl methacrylate (BMA), ethylene glycol dimethacrylate (EGDMA) and the respective co-monomer were dissolved in acetone (30 ml) in order to solubilise the azobenzene in the mixture.

This mixture was added to 150 ml of deionised water, which was heated to $\vartheta = 80\,^{\circ}\mathrm{C}$ under stirring and under nitrogen. Not fully dissolved dye was then fully soluble in the monomer droplets. Potassium peroxodisulfate (KPS) as radical starter was dissolved in 5 ml of deionised water and then injected to the heated monomer mixture. During polymerisation, some polymer tends to aggregate, though still a large part of the polymer is dispersed as latex. The polymerisation was stopped after 3 h and the aggregates were removed by filtration. The filtrate was centrifuged and redispersed in acetone. Then, the centrifugation/redispergation was repeated with acetone and dioxane in order to remove unreacted monomer. In the end the supernatant was colourless. For further purification, the dioxane dispersion was freeze-dried and redispersed in toluene in order to dialyse the sample for 3 d against toluene (MWCO 12000) and 2 d against an acetone/isopropanol mixture (1/1 by volume). This mixture was filtered again by use of a syringe filter (0.8 m) and the main part was dialysed against dioxane in order to perform the final freeze-drying. A small part of the acetone dispersion was diluted and then dialysed against water in order to measure the hydrodynamic radius and the radius of gyration in the collapsed state after further dilution. To measure the hydrodynamic radius in the swollen state a small amount was swollen in toluene. The results of the light scattering measurements are shown in Table 4.6.

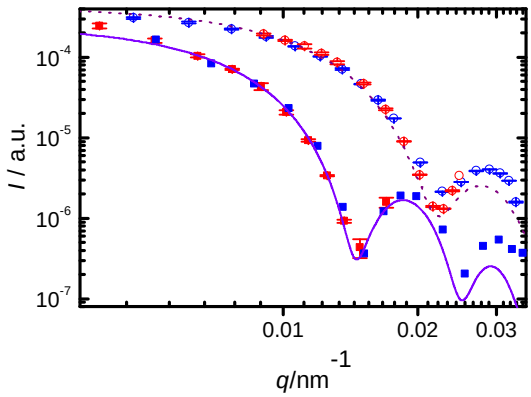

Figure 4.5: Exemplary SLS results: form factor of P-BAAB-P (1:50; sample 2) in toluene (solid squares) and water (open circles) measured with red (red symbols) and blue laser (blue symbols). Lines indicate the fit results of a polydisperse hard sphere form factor model (with radius $R_{hs} = 306 \pm 17$ nm and $R_{hs} = 200 \pm 17$ nm, respectively).

Table 4.5: Sample 1: Hydrodynamic radii (R_h) and hard sphere radii (R_{hs}, obtained from the first minimum of the form factor) in water (aq) and in toluene (tol). Due to a limited q range the form factor minimum could not be reached for all samples. Errorlimits indicate errors in the fitting procedure.

	R_h (aq) / nm	R_h (tol) / nm	R_{hs} (aq) / nm	R_{hs} (tol) / nm
P-DR1 (1:10)	196 ± 2	240 ± 2	0.18	-
P-BAAB-P (1:50)	80 ± 1	150 ± 2	-	-
P-BAAB-P (1:10)	101 ± 1	170 ± 2	-	0.14

Table 4.6: Sample 2: Hydrodynamic radii (R_h) and hard sphere radii (R_{hs}, obtained from the first minimum of the form factor) in water (aq) and in toluene (tol). Due to a limited q range the form factor minimum could not be reached for all samples. Errors indicate errors in the fitting procedure.

	R_h (aq) / nm	R_h (tol) / nm	R_{hs} (aq) / nm	R_{hs} (tol) / nm
P-DR1 (1:10)	196 ± 2	239 ± 1	0.19	-
P-BAAB-P (1:50)	205 ± 2	335 ± 3	0.20	0.30
P-BAAB-P (1:10)	173 ± 1	223 ± 4	0.17	0.22

THERMAL BACK-ISOMERISATION OF BAAB AND P-BAAB-P (1:50 AND 1:10)

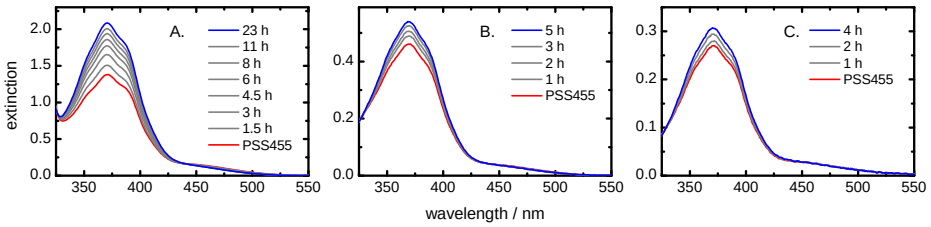

Figure 4.6: UV/VIS absorption spectra of a) **BAAB**, b) **P-BAAB-P** (1:50) and c) **P-BAAB-P** (1:10) in 2-fluorotoluene as of time after excitation to the photostationary state PSS455 at $t = 0$ (red). The spectra of the respective *E* isomer are shown in blue. The thin black lines show the evolution of the spectra in course of the thermal back-isomerisation from the respective PSS after $\Delta t = 1.4$, 3, 4.5, 6, 8, 11 and 23 h for BAAB, $\Delta t = 1$, 2, 3, and 5 h for P-BAAB-P (1:50) and $\Delta t = 1$, 2, and 4 h for P-BAAB-P (1:10). The switching efficiency in the polymer is only $\approx 40 - 50$ % of the value in solution. The observed effects are related to the strong pulling forces acting on the AB in the main-chain of the polymer.

REFERENCES

4.S1. Blevins, A. A.; Blanchard, G. J. *J. Phys. Chem. B* **2004**, *108*, 4962–4968.

4.S2. Van den Mooter, G.; Samyn, C.; Kinget, R. *Int. J. Pharm.* **1992**, *87*, 37–46.

4.S3. Siegert, A. J. F. *MIT Rad Lab Rep* **1943**, No 465.

5

PHOTOCHEMICAL PROPERTIES OF MULTI-AZOBENZENE COMPOUNDS

Julia Bahrenburg,[a] Claudia M. Sievers,[a] Jan Boyke Schönborn,[a] Bernd Hartke,[a] Falk Renth,[a]* Friedrich Temps,[a]* Christian Näther[b] and Frank D. Sönnichsen[c]*

[a] Institut für Physikalische Chemie, Christian-Albrechts-Universität zu Kiel, Olshausenstr. 40, D-24098 Kiel, Germany

[b] Institut für Anorganische Chemie, Christian-Albrechts-Universität zu Kiel, Otto-Hahn-Platz 7, D-24098 Kiel, Germany

[c] Otto Diels-Institut für Organische Chemie, Christian-Albrechts-Universität zu Kiel, Otto-Hahn-Platz 4, D-24098 Kiel, Germany

J. Bahrenburg, C. M. Sievers, J. B. Schönborn, B. Hartke, F. Renth, F. Temps, C. Näther and F. D. Sönnichsen *Photochem. Photobiol. Sci.*, **2013**, *12*, 511-518.

OWN CONTRIBUTIONS TO THIS MANUSCRIPT:

- Syntheses and characterization of the molecules
- Static absorption spectroscopy and irradiation experiments
- Kinetic analysis of one-dimensional ^{1}H NMR and two-dimensional HSQC NMR measurements
- Calculation of ground state structures
- Writing of the manuscript

* To whom correspondence should be addressed. E-mail: renth@phc.uni-kiel.de, temps@phc.uni-kiel.de, fsoennichsen@oc.uni-kiel.de

ABSTRACT

A systematic study is reported of the photochemical properties of the multi-azobenzene compounds bis[4-(phenylazo)phenyl]amine (BPAPA) and tris[4-(phenylazo)phenyl]amine (TPAPA) compared to the parent molecule 4-aminoazobenzene (AAB). The bis- and tris-azobenzenes were synthesised by a variant of the Ullmann reaction and exist in their stable all-*E* forms at room temperature. Striking changes in the spectral positions and intensities of their first $\pi\pi^*$ absorption bands compared to AAB reveal strong electronic coupling between the AB units. The nature of the excited states was explored by quantum chemical calculations at the approximate coupled-cluster (CC2) level. Upon UV/VIS irradiation, the molecules isomerise to the *Z*-isomer (AAB), *ZE*- and *ZZ*-isomers (BPAPA), and *ZEE*-, *ZZE*- and *ZZZ*-isomers (TPAPA), respectively. The photoswitching behaviours were investigated by UV/VIS and NMR spectroscopies. All individual isomers were detected by one-dimensional (1D) ^{1}H NMR spectroscopy (BPAPA) and two-dimensional (2D) HSQC NMR spectroscopy (TPAPA). A kinetic analysis provided the isomer-specific thermal lifetimes. The variance of the thermal lifetimes demonstrates a dependence of the *Z*-*E* isomerisation on the chromophore size and number of AB units.

5.1 INTRODUCTION

The reversible $\mathrm{E} \rightleftarrows \mathrm{Z}$ photoisomerisation of azobenzene (AB) and its derivatives upon irradiation with visible (VIS) or ultraviolet (UV) light forms the basis for a wide range of applications as light-triggered molecular switches or optical memory devices.[1–6] The high application potential of AB as photoswitchable element rests on the reversible, large changes in size, shape and dipole moment between the thermodynamically favoured, stretched *E*-isomer and the energetically higher, more compact *Z*-isomer and on the low photochemical fatigue of the chromophore. These properties have been exploited for, *e.g.*, single molecule optomechanical research,[7,8] photoregulation of biomolecules,[9–12] photoswitching of magnetic bistability,[13] and photocontrol of macromolecular and supramolecular systems, including dendrons and dendrimers,[14–19] molecular wires[20,21] and helices,[22,23] emulsions,[24] and polymer films and materials,[25–28] which are suitable for surface patterning[29–31] or holographic information storage.[32,33] To reach the ambitious design goals for functional AB devices, however, it is mandatory to acquire detailed knowledge about the ensuing molecular dynamics under different circumstances.

In functional systems, photochromic molecular switches are typically embedded in complex environments, where the close proximity of the chromophores leads to cooperative phenomena, *e.g.*, steric interactions, excitonic coupling, charge-transfer (CT), or direct electronic coupling in π-conjugated systems. All of these mechanisms may compete with the desired photoisomerisation. To elucidate the ensuing influences, we initiated an investigation of two prototypical photoswitchable multi-azobenzene

compounds, bis[4-(phenylazo)phenyl]amine (BPAPA) and tris[4-(phenylazo)phenyl]amine (TPAPA), where the AB units are connected *via* an amino linker to enable electronic coupling between the chromophores. The chemical structures of both molecules in their all-*E* forms and the parent 4-aminoazobenzene (AAB) as reference compound are given in Scheme 1.

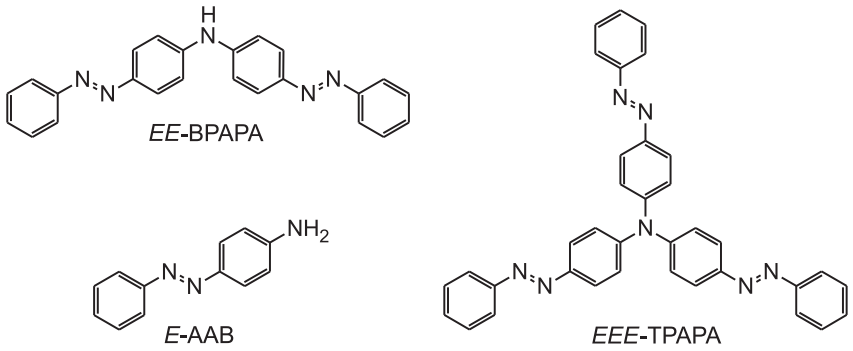

Scheme 1.

The influence of chromophore-chromophore interactions and electronic coupling between several addressable AB moieties connected by a central unit on the photoswitching behaviour has rarely been investigated to date. Several studies involve bis-azobenzenes.[34–37] Work by Cisnetti et al.[34] on the photo- and electrochemical properties of a *meta*- and a *para*-substituted bis-azobenzene showed a difference in the electronic coupling for the two systems. However, it was not possible to determine the composition in the photostationary states (PSS), which should contain three isomers in both cases. The thermal isomerisation of a conjugated *meta*-substituted bis-azobenzene derivative has been investigated by Robertus *et al.*[37] Both AB units seemed to switch independently of each other, and the thermal behaviour was comparable to that of the single AB derivative. Considering much larger systems, Puntoriero et al.[16] determined the photoisomerisation yields of a fourth generation dendrimer containing 32 *trans*-AB units and its complexes with eosin hosted in the dendrimer. Franckevičius *et al.*[18] presented a fluorescence and femtosecond transient absorption study of the excited-state relaxation of dendrimers containing cyano-AB end groups, which indicated rather little effect by the environment. Last but not least, Takahashi *et al.*[30] reported the effect of surface relief grating (SRG) formation by TPAPA. With each AB unit capable of *E*-*Z* isomerisation, this structurally well defined tris-azobenzene may exist in four distinct isomeric forms (*EEE*, *ZEE*, *ZZE*, *ZZZ*). Thus, great potential would arise if the AB units could be individually addressed, a functionality that might be reached by chemical substitutions. Moreover, if TPAPA shows similar hole conductivity as, *e.g.*, the related triphenylamine,[38] it may provide access to logical devices for applications in molecular electronics or to organic light emitting diodes (OLEDs)[39,40] that could be photoswitched to emit at different wavelengths. However, the central question of whether and how the close proximity and electronic interactions of

two or more AB moieties in a molecule influence the photoswitching has remained unanswered.

In the present paper, we report on a systematic investigation of the photoswitching properties of the bis- and tris-azobenzenes BPAPA and TPAPA in comparison to the reference compound AAB by means of UV/VIS absorption and NMR spectroscopy. The study is a prelude to subsequent time-resolved dynamics measurements of the molecules. The target compounds were obtained by a modified, less harsh variant of the Ullmann coupling reaction[41,42] between AAB and 4-iodoazobenzene (IAB). To begin with, the nature of the photoexcited electronic states was explored by quantum chemical calculations. The photostationary states for each system were determined by UV/VIS spectroscopy. The relative concentrations and the thermal lifetimes of the individual *EE*-, *EZ*-, *ZZ*-isomers of BPAPA and the *EEE*-, *ZEE*-, *ZZE*-, *ZZZ*-isomers of TPAPA were investigated in acetonitrile solution by conventional ^{1}H NMR and by two-dimensional (2D) HSQC NMR spectroscopy, respectively. The thermal lifetimes of the different isomers are significantly longer for TPAPA compared to BPAPA, which indicates a dependence of the *Z*-*E* isomerisation on the chromophore size and number of AB units. Large differences in the spectral band positions and in the intensities of the absorption spectra of AAB, BPAPA and TPAPA hint at sizable chromophore-chromophore interactions and electronic couplings between the AB moieties.

5.2 EXPERIMENTAL AND COMPUTATIONAL METHODS

The protocols for the chemical syntheses of BPAPA and TPAPA are given in the ESI. † All commercially available compounds were purchased from Merck, Sigma-Aldrich, Deutero and Lancaster and used without further purification, except for AAB, which was recrystallised from ethanol. Solvents were dried according to standard procedures. ^{1}H-, ^{13}C-, COSY-, HSQC- and HMBC NMR data were aquired with Bruker AC-200 and Bruker AV-600 spectrometers. UV/VIS absorption spectra were taken on a Shimadzu UV-2401 desktop spectrometer. Three light emitting diodes (Nichia) with emission maxima at $\lambda = 365$ nm (NCSU033A, 400 mW), 385 nm (NCSU034A, 400 mW) and 455 nm (NS4C107E, 400 mW) were used for the photoisomerisation experiments. The light intensities were attenuated to 100 mW. The thermal back-isomerisations were followed by UV/VIS and ^{1}H and 2D-HSQC NMR spectroscopies. Quantum chemical calculations of the structures of *EE*-BPAPA and *EEE*-TPAPA in their electronic ground states were performed by density functional theory (DFT) using Gaussian09.[43] AAB had been calculated for another purpose before using the OM2-MRCISD method.[44] The photoexcited electronic states were explored using the second-order approximate coupled-cluster with resolution-of-the-identity (RI-CC2) model of Turbomole.[45,46]

5.3 RESULTS

5.3.1 MOLECULAR STRUCTURES

The calculated B3LYP/6-31+G(d,p) equilibrium structures of *EE*-BPAPA and *EEE*-TPAPA are displayed in Fig. 5.1. As can be seen, the molecules adopt propeller-like configurations. The out-of-plane dihedral angles of the AB units in the electronic ground state are ≈21° for BPAPA and ≈42° for TPAPA.

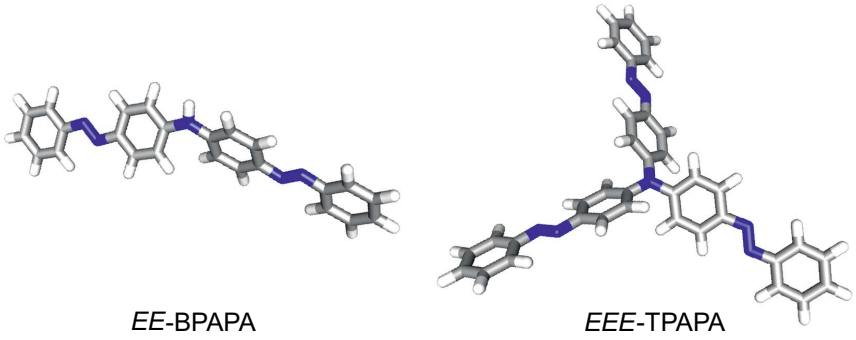

Figure 5.1: Calculated structures of EE-BPAPA and EEE-TPAPA at the B3LYP/6-31+G(d,p) level of theory.

The X-ray diffraction structure of TPAPA (see ESI †) confirmed the calculated propeller-like configuration of the AB units around the central nitrogen. Quite similar configurations are well known for related molecules with a triphenylamine core[47] or triphenylamine itself.[48]

5.3.2 STATIONARY UV/VIS ABSORPTION SPECTRA

The UV/VIS absorption spectra of AAB, BPAPA and TPAPA in their all-*E* forms in *n*-hexane as the solvent are depicted in Fig. 5.2. As for unsubstituted AB, AAB shows a strong $\pi\pi^*$ band in the near UV with a maximum at $\lambda = 361$ nm ($\epsilon_{max} = 2.7 \times 10^4$ $M^{-1}cm^{-1}$) and a weak $n\pi^*$ band at $\lambda \approx 450$ nm in the visible. In contrast, the spectra of BPAPA and TPAPA exhibit pronounced bathochromic and hyperchromic shifts, which increase with the number of AB units. The maxima for BPAPA and TPAPA are at $\lambda = 412$ nm ($\epsilon_{max} = 5.6 \times 10^4$ $M^{-1}cm^{-1}$) and 432 nm ($\epsilon_{max} = 7.0 \times 10^4$ $M^{-1}cm^{-1}$), respectively. The corresponding $n\pi^*$ transitions are obscured by the intense $\pi\pi^*$ bands, but may be located in the extended wings to the red. The red-shift is more pronounced for BPAPA compared to AAB than for TPAPA compared to BPAPA. Thus, the intramolecular coupling of two (three) AB chromophores in BPAPA (TPAPA) has drastic consequences on the resulting excited electronic states and their energies and spectra.

Also given in Fig. 5.2 are the absorption spectra of the molecules in the photostationary states PSS365 (AAB), PSS385 (BPAPA) and PSS455 (TPAPA) after irradiation at the specified wavelengths. Similar to unsubstituted AB, where the *Z*-isomer shows a blue-shifted and much weaker $\pi\pi^*$

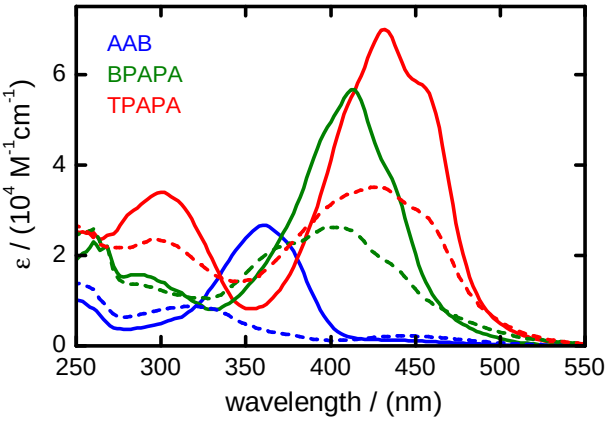

Figure 5.2: UV/VIS absorption spectra of E-AAB (blue), EE-BPAPA (green) and EEE-TPAPA (red; solid lines) and in their photostationary states (dashed lines) after irradiation for ≈ 30 s in the strong first absorption bands at λ = 365 nm (AAB), 385 nm (BPAPA) and 455 nm (TPAPA), respectively, in n-hexane (T = 30 °C).

absorption but a stronger $n\pi^*$ absorption than the *E*-isomer, the spectrum of AAB in the PSS365 exhibits decreased absorption around 360 nm compared to the pure *E* isomer and increased absorption around 450 nm. In the PSS385 for BPAPA and PSS455 for TPAPA, the $\pi\pi^*$ absorptions are much lower as well. At the same time, the presence of several isomers in both cases results in a significant broadening of the bands. Unfortunately, the lack of clear characteristic spectral signatures of the different isomers in the course of the thermal back-reactions hampers a further analysis of the absorption spectra. However, the photoisomerisation yields and isomer-resolved *Z*-*E* back-reactions could be monitored by NMR (below).

Figure 5.3 displays the UV/VIS spectra of the molecules in *n*-hexane, chloroform, acetonitrile and ethanol as solvents. The absorption maximum of AAB can be seen to shift from $\lambda_{max} = 361$ nm in *n*-hexane to 371 nm in chloroform and 380 nm in acetonitrile and ethanol in line with the increasing solvent polarity. The bands in chloroform, acetonitrile and ethanol are broadened compared to *n*-hexane. Likewise, the absorption maxima of BPAPA are at $\lambda_{max} = 412$ nm in *n*-hexane, 424 nm in chloroform, 429 nm in acetonitrile and 455 nm in ethanol. As for AAB, the bathochromic shift is stronger in the more polar solvents. The pronounced red-shift of ≈45 nm in ethanol compared to *n*-hexane can be rationalised by hydrogen bond formation between the solute and solvent. In the case of TPAPA, the influence of the solvent polarity on the absorption behaviour of TPAPA is not as distinctive as for AAB or BPAPA. The absorption maxima are at $\lambda_{max} = 432$ nm in *n*-hexane, 444 nm in chloroform and 434 nm in acetonitrile and ethanol. Compared with the very broad and unstructured band shapes in the more polar solvents, the spectra of BPAPA and TPAPA in *n*-hexane show some very weak structure. The variances in the band shifts and shapes may be partly related to the existence of two resp. three transitions in BPAPA and TPAPA and/or to different basicities and polarities of the primary, secondary and tertiary amine.

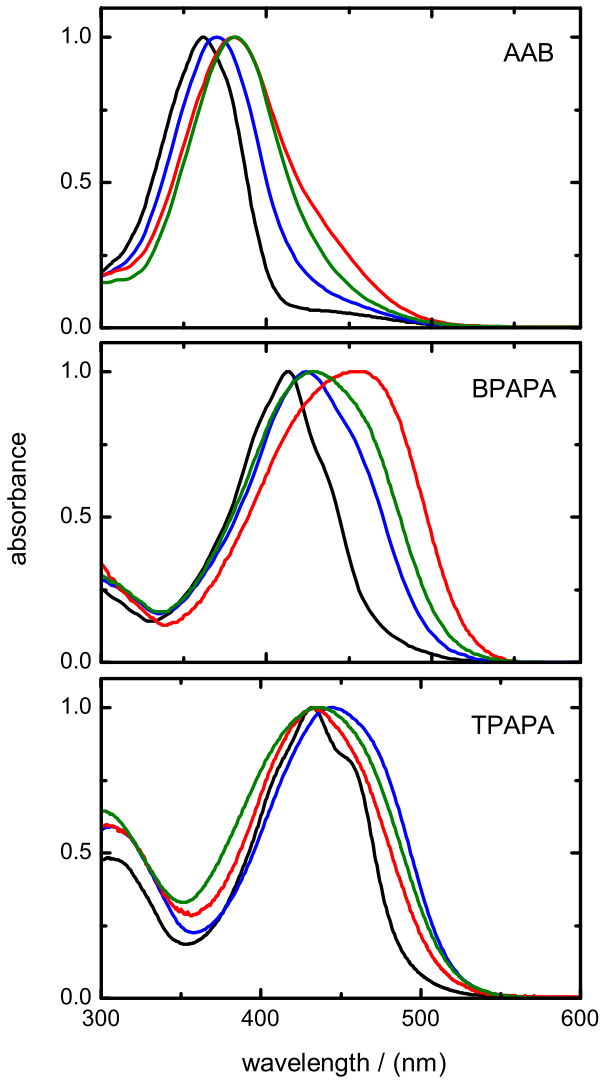

Figure 5.3: UV/VIS absorption spectra of AAB (top), BPAPA (middle) and TPAPA (bottom) in *n*-hexane (black), chloroform (blue), acetonitrile (green) and ethanol (red). The absorption maxima were normalized for better comparison.

5.3.3 EXCITED-STATE CALCULATIONS

The characters of the photoexcited states were studied using the RI-CC2 model[45,46] with the def2-TZVPP basis[49] for AAB and BPAPA and the def2-SVP basis[50] for TPAPA at the aforementioned optimised B3LYP/6-31G+(d,p) structures. The calculations gave the first two excited states of AAB, the first four of BPAPA, and the first six of TPAPA. Table 5.1 in the ESI lists the respective excitation energies, oscillator strengths and dominant excited determinants for these states.

The relevant molecular orbitals are displayed in Fig. 5.4. As can be seen, the energetic order of the states ($n\pi^* < \pi\pi^*$) remains conserved despite the combination of two resp. three AB units. The first excited state of AAB, the first two of BPAPA and the first three of TPAPA are of $n\pi^*$ character,

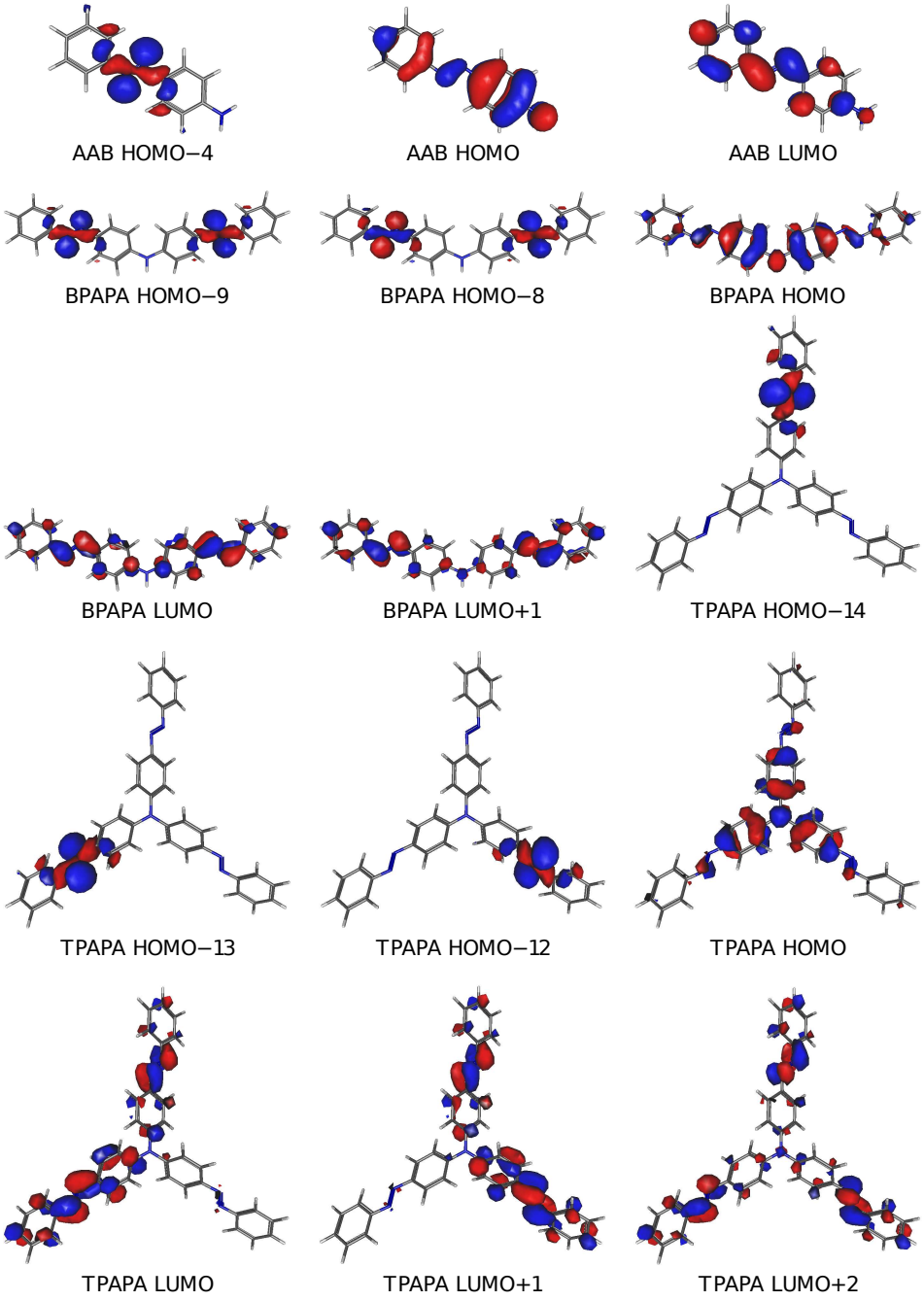

Figure 5.4: Relevant molecular orbitals involved in the electronic transitions in the UV/VIS absorption spectra for AAB, BPAPA and TPAPA.

while the following ones are of $\pi\pi^*$ character. All $n\pi^*$ states carry very low oscillator strengths from S_0. For BPAPA, the calculated excited states appear in pairs of one with higher and one with lower oscillator strength, as one would expect for an excitonic system. While the two $n\pi^*$ states (S_1, S_2) are virtually degenerate, the two $\pi\pi^*$ states (S_3, S_4) are split by about 0.6 eV. The $n\pi^*$ states are calculated to have about the same energy as in AAB, while the first $\pi\pi^*$ state (S_3) is lowered compared to AAB by about 0.75 eV. Since this state carries the bulk of the oscillator strength, its en-

ergic lowering explains the experimentally observed red-shift of the first strong UV/VIS absorption band of BPAPA relative to AAB. In contrast, the $S_4(\pi\pi^*) \leftarrow S_0$ transition of BPAPA is only rather weakly allowed. The results for TPAPA are not quantitatively comparable to the others because of the smaller basis, but qualitative conclusions can nevertheless be drawn. Similar to BPAPA, the $n\pi^*$ states (S_1, S_2, S_3) are virtually degenerate, but the n orbitals remain localised on one of the AB units each instead of taking the form of linear combinations delocalised over the molecule. This difference can be rationalized on the grounds of the larger out-of-plane dihedral angles of the AB chromophores. The calculated energies of the $\pi\pi^*$ states (S_4, S_5, S_6) are comparable to those of BPAPA. Judged by a comparison to results with the same smaller basis set for BPAPA, the excitation energies for TPAPA obtained with the def2-SVP basis are likely slightly overestimated compared to the expected outcome at higher level (def2-TZVPP). The first two are virtually degenerate and carry large oscillator strengths, the third is calculated to be about 0.65 eV higher in energy and has very low oscillator strength.

5.3.4 NMR MEASUREMENTS

The isomer-specific photoisomerisation yields in the photostationary states and the thermal *Z*-*E* back-reactions as function of time were determined by ^{1}H NMR spectroscopy (BPAPA) and by 2D-HSQC NMR spectroscopy (TPAPA).

Figure 5.5 displays ^{1}H NMR spectra of BPAPA in CD_3CN after excitation to the photostationary state PSS385 as a function of time for $T = 15\,^\circ$C. As can be seen, the three singlet peaks of the chemically different NH protons of the three isomers (*EE*, *ZE*, *ZZ*), which co-exist in the PSS, are readily assigned on the basis of their chemical shifts and their time dependence. The NH signal of the *ZZ*-isomer disappears most rapidly, while the NH signal of the *ZE*-isomer shows a slight initial rise due to the *ZE*-production from the *ZZ*-isomer before its subsequent slower decay to zero. The NH signal of the *EE*-isomer slowly rises to its final equilibrium value. All other proton signals can be assigned accordingly (see ESI, Section 5.5.3). Similar spectra were taken at a slightly elevated temperature ($T = 35\,^\circ$C), where the kinetics were correspondingly faster.

The isomer ratio in the PSS385 was found to be 39 % *EE*, 41 % *ZE*, and 20 % *ZZ*. Taking these data, the isomer-specific thermal lifetimes could be determined by a kinetic analysis of the respective integrated singlet signals for the three NH protons using a consecutive kinetic model including the back-reactions of the *ZZ*- and *EZ*-isomers according to the scheme

$$\mathrm{ZZ} \xrightarrow{\tau_{ZZ}} \mathrm{ZE} \xrightarrow{\tau_{ZE}} \mathrm{EE}\,.$$

The experimental time profiles for the three isomers and the best-fit time profiles for $T = 15\,^\circ$C are shown in Fig. 5.6. The resulting isomer-specific

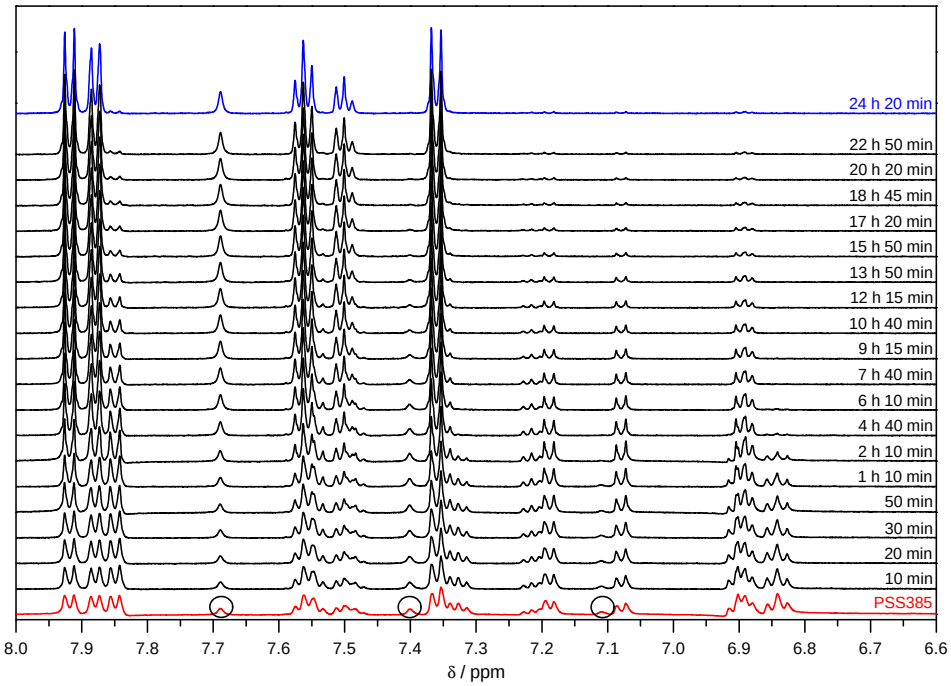

Figure 5.5: ^{1}H NMR spectra of BPAPA in CD_3CN at $T = 15\,°C$ as a function of time after excitation to the photostationary state PSS385 at $t = 0$. The circles in the bottom trace highlight the NH proton signals of the three different isomers.

thermal lifetimes are $\tau_{ZZ} = 1.9 \pm 0.2$ h, $\tau_{ZE} = 7.5 \pm 0.6$ h ($T = 15\,°C$) and $\tau_{ZZ} = 0.5 \pm 0.1$ h, $\tau_{ZE} = 2.4 \pm 0.2$ h ($T = 35\,°C$).

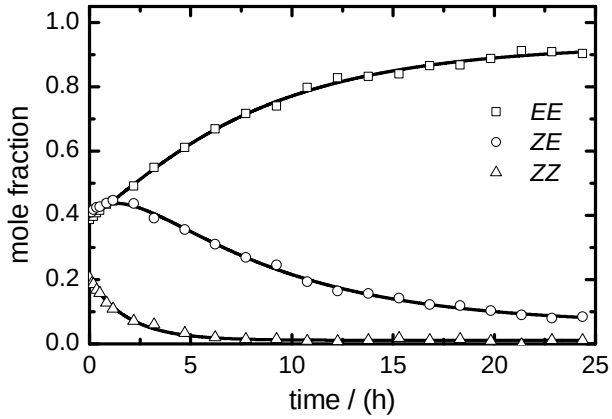

Figure 5.6: Time profiles of the *ZZ*-, *ZE* and *EE*-isomers of BPAPA in the thermal back-reaction starting from the photostationary state PSS385 in CD_3CN at $T = 15\,°C$. The data points (cf. Fig. 5.5) are given by open symbols, the fitted time profiles by solid curves.

Because of the much slower back-reaction compared to BPAPA, similar data for TPAPA were taken only at slightly elevated temperature (T = 35 °C). As for BPAPA, the proton signals belonging to the all-*E* isomer in the spectrum at the longest time are readily recognisable from the time dependence. However, the spectrum of the PSS (see Fig. 5.8, ESI †) is more

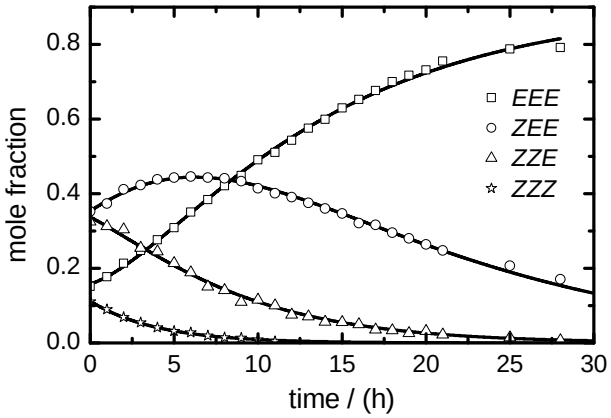

Figure 5.7: Time profiles of the *ZZZ*-, *ZZE*, *ZZE*, and *ZZZ*-isomers of TPAPA in the thermal back-reaction starting from the photostationary state PSS_{455} in CD_3CN at $T = 35\,°C$. The data points are given by open symbols, the fitted time profiles by solid curves.

congested than in the BPAPA case so that a direct identification of the individual photoisomers was not easily possible. The thermal back-reactions were therefore followed by HSQC NMR spectroscopy to resolve the severe overlap in the ^1H NMR spectrum and to assign related cross-peaks to the *EEE*-, *ZEE*-, *ZZE*-, and *ZZZ*-isomers, respectively. The recorded HSQC spectra of the all-*E* isomer, the photostationary state (PSS_{455}), and the photoisomer mixture at three selected times after preparation of the PSS are presented in the ESI (*cf.* Fig. 5.9 †). As shown, the isomer-specific cross-peaks belonging to the aromatic rings next to the central amino-N atom are well separated, the respective concentrations are therefore easily accessible by peak integration. In this way, the photoisomer ratio in the PSS_{455} was found to be 16 % *EEE*, 37 % *ZEE*, 36 % *ZZE*, and 12 % *ZZZ*.

Starting from these values, the respective thermal lifetimes were determined by a kinetic analysis of the time profiles using a consecutive kinetic model including the back-reactions of the *ZZZ*-, *ZZE*-, and *ZEE*-isomers and formation of the *EEE*-isomer of the form

$$\mathrm{ZZZ} \xrightarrow{\tau_{ZZZ}} \mathrm{ZZE} \xrightarrow{\tau_{ZZE}} \mathrm{ZEE} \xrightarrow{\tau_{ZEE}} \mathrm{EEE}\,.$$

The experimental time profiles and the fitted curves for the four isomers are given in Fig. 5.7. The resulting time constants at $T = 35\,°C$ for the *ZZZ*-, *ZZE*-, and *ZEE*-isomers are $\tau_{ZZZ} = 4.0 \pm 0.4$ h, $\tau_{ZZE} = 6.4 \pm 0.9$ h and $\tau_{ZEE} = 12 \pm 1$ h, respectively. For reference, the thermal lifetime of the *Z*-isomer of AAB (τ_Z) under similar conditions determined by UV/VIS spectroscopy is of the order of just ≈5 min.

5.4 DISCUSSION AND CONCLUSIONS

The photoswitching properties of two multi-azobenzene compounds, the secondary amine bis[4-(phenylazo)phenyl)]amine (BPAPA) and the tertiary amine tris[4-(phenylazo)phenyl)]amine (TPAPA), have been investigated

by means of UV/VIS and NMR spectroscopy in comparison to the primary amine 4-aminoazobenzene (AAB). As expected, the UV/VIS absorption spectra of BPAPA and TPAPA show drastic changes which are understandable on the grounds of the larger π-electron systems by the linkage of two resp. three AB chromophores *via* the central amino-N core, despite the non-coplanar orientation of the AB moieties in the molecules. The observed red-shift of the absorption maximum and the increase in absorbance are more pronounced for BPAPA compared to AAB than for TPAPA compared to BPAPA, which stresses the non-additive effects of the added AB units. This may hint at specific intramolecular interactions, *e.g.*, excitonic coupling or charge-transfer (CT), between the different AB units. It has to be taken into account in addition that the twist angle between the AB units is larger in TPAPA than in BPAPA.

The calculated RI-CC2 excitation energies for the $n\pi^*$ and the optically bright $\pi\pi^*$ excited states of BPAPA and TPAPA are in reasonable agreement with the recorded spectra. The observed strong 412 nm absorption band of BPAPA is attributed to the lower of the two $\pi\pi^*$ states, the second $\pi\pi^*$ state 0.6 eV higher lacks high oscillator strength. In contrast, the strong 432 nm absorption of TPAPA appears to arise from two degenerate $\pi\pi^*$ components with comparable oscillator strengths. The next $\pi\pi^*$ state is significantly higher in energy and has only low oscillator strength. The calculated $n\pi^*$ transitions are very weak, but may contribute to the absorptions in the extended wings in the spectra to the red.

Both BPAPA and TPAPA are efficient photoswitches. Starting from the all-*E* isomers, the prepared photostationary states were found to contain $\approx$20 % all-*Z* isomer in the BPAPA case and $\approx$12 % all-*Z* isomer in the TPAPA case. It should be noted that the transformation of the molecules from the all-*E* to the all-*Z* forms require two sequential photoisomerisation steps for BPAPA and three such steps for TPAPA. In the photostationary state, a TPAPA molecule on average has nearly 1.5 of its AB units switched to the *Z*-form.

The isomer-specific concentrations in the photostationary states and the thermal back-isomerisation lifetimes for BPAPA and TPAPA were determined by means of ^{1}H NMR and by 2D-HSQC NMR spectroscopy, respectively. In the BPAPA case, the lifetimes with respect to the thermal back-reactions in CD_3CN at $T = 35\,^\circ$C were found to be $\tau_{ZZ} = 0.5$ h and $\tau_{ZE} = 2.4$ h for the *ZZ*- and *ZE*-isomers, respectively. For TPAPA, the corresponding lifetimes at $T = 35\,^\circ$C were found to be $\tau_{ZZZ} = 4.0$ h, $\tau_{ZZE} = 6.4$ h and $\tau_{ZEE} = 12$ h for the *ZZZ*-, *ZZE*-, and *ZEE*-isomers, respectively. The thermal lifetime of *Z*-AAB under similar conditions is only of the order of a few minutes ($\tau_Z = 5$ min). Thus, the *Z*-isomer lifetimes increase considerably with increasing overall chromophore size and number of AB units. This behaviour is related to the changes in the geometric and electronic structures of the molecules, although it cannot be explained unambiguously at the moment.

Towards applications, it is important to understand the intramolecular couplings between the AB units in more detail. Both BPAPA and TPAPA

are therefore currently under investigation in our laboratoy by femtosecond time-resolved absorption and fluorescence spectroscopy. Ongoing polarisation-dependent decay measurements are expected to provide insight into possible excitonic energy migration processes.

ACKNOWLEDGEMENTS

The support of this work by the Deutsche Forschungsgemeinschaft through the Sonderforschungsbereich 677 "Function by Switching" is gratefully acknowledged.

BIBLIOGRAPHY

[1] Liu, Z. F.; Hashimoto, K.; Fujishima, A. *Nature* **1990**, *347*, 658–660.

[2] Ikeda, T.; Tsutsumi, O. *Science* **1995**, *268*, 1873–1875.

[3] Willner, I.; Rubin, S. *Angew. Chem. Int. Ed.* **1996**, *35*, 367–385.

[4] Rau, H. In *Photochromism: Molecules and Systems*; Dürr, H., Bouas-Laurent, H., Eds.; Elsevier: Amsterdam, 2003.

[5] Balzani, V.; Credi, A.; Venturi, M. *Molecular Devices and Machines: Concepts and Perspectives for the Nanoworld*; Wiley-VCH: Weinheim, 2008.

[6] Feringa, B. L.; Browne (Eds.), W. R. *Molecular Switches*; Wiley-VCH: Weinheim, 2011; Vol. 1 & 2.

[7] Hugel, T.; Holland, N. B.; Cattani, A.; Moroder, L.; Seitz, M.; Gaub, H. E. *Science* **2002**, *296*, 1103–1106.

[8] Holland, N. B.; Hugel, T.; Neuert, G.; Cattani-Scholz, A.; Renner, C.; Oesterhelt, D.; Moroder, L.; Seitz, M.; Gaub, H. E. *Macromolecules* **2003**, *36*, 2015–2023.

[9] Ulysse, L.; Cubillos, J.; Chmielewski, J. *J. Am. Chem. Soc.* **1995**, *117*, 8466–8467.

[10] Pieroni, O.; Fissi, A.; Angelini, N.; Lenci, F. *Acc. Chem. Res.* **2001**, *34*, 9–17.

[11] Spörlein, S.; Carstens, H.; Satzger, H.; Renner, C.; Behrendt, R.; Moroder, L.; Tavan, P.; Zinth, W.; Wachtveitl, J. *Proc. Natl. Acad. Sci. U.S.A.* **2002**, *99*, 7998–8002.

[12] Liang, X.; Asanuma, H.; Komiyama, M. *J. Am. Chem. Soc.* **2002**, *124*, 1877–1883.

[13] Venkataramani, S.; Jana, U.; Dommaschk, M.; Sönnichsen, F. D.; Tuczek, F.; Herges, R. *Science* **2011**, *331*, 445–448.

[14] Archut, A.; Vögtle, F.; De Cola, L.; Azzellini, G. C.; Balzani, V.; Ramanujam, P. S.; Berg, R. H. *Chem. Eur. J.* **1998**, *4*, 699–706.

[15] Vögtle, F.; Gorka, M.; Hesse, R.; Ceroni, P.; Maestri, M.; Balzani, V. *Photochem. Photobiol. Sci.* **2002**, *1*, 45–51.

[16] Puntoriero, F.; Ceroni, P.; Balzani, V.; Bergamini, G.; Vögtle, F. *J. Am. Chem. Soc.* **2007**, *129*, 10714–10719.

[17] Deloncle, R.; Caminade, A.-M. *J. Photochem. Photobiol. C* **2010**, *11*, 25–45.

[18] Franckevičius, M.; Vaišnoras, R.; Marcos, M.; Serrano, J. L.; Karpicz, R.; Gulbinas, V. *Chem. Phys. Lett.* **2010**, *485*, 156–160.

[19] Chandrasekaran, V.; Lindhorst, T. K. *Chem. Commun.* **2012**, *48*, 7519–7521.

[20] Humphrey, J. L.; Lott, K. M.; Wright, M. E.; Kuciauskas, D. *J. Phys. Chem. B* **2005**, *109*, 21496–21498.

[21] Grimes, A. F.; Call, S. E.; Harbron, E. J.; English, D. S. *J. Phys. Chem. C* **2007**, *111*, 14257–14265.

[22] Tie, C.; Gallucci, J. C.; Parquette, J. R. *J. Am. Chem. Soc.* **2006**, *128*, 1162–1171.

[23] King, E. D.; Tao, P.; Sanan, T. T.; Hadad, C. M.; Parquette, J. R. *Org. Lett.* **2008**, *10*, 1671–1674.

[24] Porcar, I.; Perrin, P.; Tribet, C. *Langmuir* **2001**, *17*, 6905–6909.

[25] Kumar, G. S.; Neckers, D. C. *Chem. Rev.* **1989**, *89*, 1915–1925.

[26] Natansohn, A.; Rochon, P. *Chem. Rev* **2002**, *102*, 4139–4175.

[27] Pardo, R.; Zayat, M.; Levy, D. *Chem. Soc. Rev.* **2011**, *40*, 672–687.

[28] Zaporojtchenko, V.; Pakula, C.; Wahyuni Basuki, S.; Strunskus, T.; Zargarani, D.; Herges, R.; Faupel, F. *Appl. Phys. A* **2011**, *102*, 421–427.

[29] Kim, M.-J.; Seo, E.-M.; Vak, D.; Kim, D.-Y. *Chem. Mater.* **2003**, *15*, 4021–4027.

[30] Takahashi, T.; Tanino, T.; Ando, H.; Nakano, H.; Shirota, Y. *Mol. Cryst. Liq. Cryst.* **2005**, *430*, 9–14.

[31] Wang, X.; Yin, J.; Wang, X. *Langmuir* **2011**, *27*, 12666–12676.

[32] Kreger, K.; Wolfer, P.; Audorff, H.; Kador, L.; Stingelin-Stutzmann, N.; Smith, P.; Schmidt, H.-W. *J. Am. Chem. Soc.* **2010**, *132*, 509–516.

[33] Wolfer, P.; Audorff, H.; Kreger, K.; Kador, L.; Schmidt, H.-W.; Stingelin, N.; Smith, P. *J. Mater. Chem.* **2011**, *21*, 4339–4345.

[34] Cisnetti, F.; Ballardini, R.; Credi, A.; Gandolfi, M. T.; Masiero, S.; Negri, F.; Pieraccini, S.; Spada, G. P. *Chem. Eur. J.* **2004**, *10*, 2011–2021.

[35] Peters, M. V.; Goddard, R.; Hecht, S. *J. Org. Chem.* **2006**, *71*, 7846–7849.

[36] Bléger, D.; Dokić, J.; Peters, M. V.; Grubert, L.; Saalfrank, P.; Hecht, S. *J. Phys. Chem. B* **2011**, *115*, 9930–9940.

[37] Robertus, J.; Reker, S. F.; Pijper, T. C.; Deuzeman, A.; Browne, W. R.; Feringa, B. L. *Phys. Chem. Chem. Phys.* **2012**, *14*, 4374–4382.

[38] Visser, S. A.; Gruenbaum, W. T.; Magin, E. H.; Borsenberger, P. M. *Chem. Phys.* **1999**, *240*, 197–203.

[39] Behl, M.; Seekamp, J.; Zankovych, S.; Sotomayor Torres, C. M.; Zentel, R.; Ahopelto, J. *Adv. Mater.* **2002**, *14*, 588–591.

[40] Behl, M.; Zentel, R.; Zen, A.; Lucht, S.; Neher, D. *Polym. Mater. Sci. Eng.* **2004**, *90*, 297–298.

[41] Goodbrand, H. B.; Hu, N.-X. *J. Org. Chem.* **1999**, *64*, 670–674.

[42] Kelkar, A. A.; Patil, N. M.; Chaudhari, R. V. *Tetrahedron Lett.* **2002**, *43*, 7143–7146.

[43] Frisch, M. J. et al. *Gaussian09 Revision A.02*; Gaussian Inc., Wallingford, CT, U.S.A., 2009.

[44] Thiel, W. MNDO program, version 6.1. Max-Planck-Institut für Kohlenforschung, Mülheim an der Ruhr, Germany. 2007.

[45] Hättig, C.; Weigend, F. *J. Chem. Phys.* **2000**, *113*, 5154–5161.

[46] Hättig, C.; Hellweg, A.; Köhn, A. *Phys. Chem. Chem. Phys.* **2006**, *8*, 1159–1169.

[47] Porrès, L.; Mongin, O.; Katan, C.; Charlot, M.; Pons, T.; Mertz, J.; Blanchard-Desce, M. *Org. Lett.* **2004**, *6*, 47–50.

[48] Meijer, G.; Berden, G.; Meerts, W. L.; Hunziker, H. E.; de Vries, M. S.; Wendt, H. R. *Chem. Phys.* **1992**, *163*, 209–222.

[49] Weigend, F.; Häser, M.; Patzelt, H.; Ahlrichs, R. *Chem. Phys. Lett.* **1998**, *294*, 143–152.

[50] Schäfer, A.; Horn, H.; Ahlrichs, R. *J. Chem. Phys.* **1992**, *97*, 2571–2577.

5.5 ELECTRONIC SUPPLEMENTARY INFORMATION

5.5.1 SYNTHESES

All commercially available compounds were purchased from Merck, Sigma-Aldrich, Deutero and Lancaster and used without further purification, except for 4-aminoazobenze which was recrystallised from ethanol. Solvents were dried according to standard procedures. Column chromatography was performed with silica gel (0.06-0.20 mm, Roth). All reactions were carried out under an argon atmosphere. NMR spectra were aquired with Bruker AC-200 and Bruker AV-600 spectrometers. MALDI mass spectra were recorded with a Biflex III instrument (Bruker) with 2,5-dihydroxybenzoic acid as matrix (0.5 mg in 1 ml toluene), CI mass spectra were recorded on a MAT 8200 (Finnigan). UV/VIS absorption spectra were taken on a Shimadzu UV-2401 desktop spectrometer.

4-Iodoazobenzene (IAB)

3.40 mg (15.2 mmol) 4-iodoaniline were added to a solution of 2.01 g (18.2 mmol) nitrosobenzene in 130 ml glacial acetic acid. The mixture was stirred for 96 h at room temperature. Afterwards the mixture was diluted with 500 ml H_2O and extracted five times with 100 ml CH_2Cl_2 each. The organic layer was washed with brine (2 $\times$ 500 ml), dried over Na_2SO_4, filtered and the solvent was removed in vacuo. The product (3.42 g, 11.1 mmol, 72 %) was purified by column chromatography. $R_f = 0.11$ (hexane/ethyl acetate, 200:1). ^{1}H NMR (200 MHz, 300 K, $CDCl_3$): $\delta = 7.89$ (d, 2H), 7.85 (d, 2H), 7.65 (d, 2H), 7.50 (m, 3H) ppm.

Bis[4-(phenylazo)phenyl]amine (BPAPA)

To a solution of 4 ml toluene were added one after the other under stirring 171 mg (0.850 mmol) AAB, 262 mg (0.850 mmol) IAB, 7.7 mg (0.038 mmol) 1,10-phenanthroline, 9.0 mg (0.047 mmol) copper(I)-iodide and 300 mg (2.54 mmol) potassium *tert*-butanolate. The mixture was heated to reflux at 130 °C within 30 min. After 5 h, the mixture was diluted and washed with 500 ml saturated aqueous $NaHCO_3$ solution, 500 ml diluted HCl and 500 ml H_2O and dried with Na_2SO_4. Evaporation of the solvent yielded the crude orange product which was purified by column chromatography ($R_f = 0.14$, toluene/hexane 2:1) and recrystallisation from a hexane-chloroform mixture (4:1). The reaction yielded 157 mg (416 mmol, 49 %) of the crystalline solid. ^{1}H NMR (600 MHz, 300 K, CD_3CN): $\delta = 7.92$ (d, J = 8.82 Hz, 4H, 3-H), 7.88 (d, J = 7.27 Hz, 4H, 6-H), 7.64 (s, 1H, NH), 7.56 (t, J = 7.57, 7.57 Hz, 4H, 7-H), 7.50 (t, J = 7.30, 7.30 Hz, 2H, 8-H), 7.36 (d, J = 8.84 Hz, 4H, 2-H) ppm. ^{13}C NMR (150 MHz, 300 K, $CDCl_3$): $\delta = 152.9$ (C-5), 147.6 (C-1), 144.6 (C-4), 130.4 (C-8), 129.1 (C-7), 124.9 (C-3), 122.6 (C-6), 117.8 (C-2) ppm. MS (CI): m/z = 377. Anal. Calcd. for $C_{24}H_{19}N_5$: C, 76.37; H, 5.07; N, 18.56. Found: C, 76.63; H, 5.61; N, 17.81.

Tris[4-(phenylazo)phenyl]amine (TPAPA)

173 mg (0.860 mmol) AAB, 800 mg (2.60 mmol) IAB, 6.1 mg (0.030 mmol) 1,10-phenanthroline, 9.0 mg (0.047 mmol) copper(I)-iodide and 305 mg (2.58 mmol) potassium *tert*-butanolate were dissolved in 3 ml toluene. The mixture was heated to reflux at 130 °C for 5 h. Afterwards the reaction was quenched by addition of saturated aqueous $NaHCO_3$ solution (50 ml) and washed with 500 ml water and 500 ml of diluted HCl solution. After drying with Na_2SO_4 and filtration, the solvent was removed in vacuo. The product was purified by column chromatography($R_f = 0.31$, toluene/hexane 2:1) and recrystallisation from a hexane-toluene mixture (5:1). The compound (177 mg, 317 mmol, 37 %) was obtained as red crystals. ^{1}H NMR (600 MHz, 300 K, $CDCl_3$): $\delta = 7.91$ (d, 6H, 3-H), 7.91 (d, 6H, 6-H), 7.52 (t, J = 7.54, 7.54 Hz, 6H, 7-H), 7.47 (t, J = 7.28, 7.28 Hz, 3H, 8-H), 7.32 (d, J = 8.82 Hz, 6H, 2-H), 7.36 (d, J = 8.84 Hz, 4H, 2-H) ppm. ^{13}C NMR (150 MHz, 300 K, $CDCl_3$): $\delta = 152.8$ (C-5), 149.0 (C-1 or C-4), 148.9 (C-4 or C-1), 130.8 (C-8), 129.1 (C-7), 124.7 (C-2), 124.5 (C-3), 122.8 (C-6) ppm. MS (MALDI): m/z = 558. Elementary analysis: See Ref. 5.S1.

5.5.2 TABLE OF CALCULATED EXCITED STATES

Table 5.1: Dominant excitations contributing to the lowest $n\pi^*$ and $\pi\pi^*$ excited electronic states of AAB, BPAPA and TPAPA.

compound	state	excitation		contribution	oscillator strength	excitation energy
		from	to	%		eV
AAB[a]	$S_1(n\pi^*)$	HOMO−4	LUMO	90	4×10^{-5}	2.87
	$S_2(\pi\pi^*)$	HOMO	LUMO	91	8×10^{-1}	3.80
BPAPA	$S_1(n\pi^*)$	HOMO−8	LUMO	52	3×10^{-3}	2.82
		HOMO−9	LUMO+1	39		
	$S_2(n\pi^*)$	HOMO−9	LUMO	52	2×10^{-5}	2.82
		HOMO−8	LUMO+1	39		
	$S_3(\pi\pi^*)$	HOMO	LUMO	86	2×10^{0}	3.05
	$S_4(\pi\pi^*)$	HOMO	LUMO+1	83	9×10^{-2}	3.63
TPAPA	$S_1(n\pi^*)$	HOMO−14	LUMO+1	35	1×10^{-3}	2.81
		HOMO−14	LUMO	32		
		HOMO−14	LUMO+2	21		
	$S_2(n\pi^*)$	HOMO−13	LUMO	60	1×10^{-4}	2.81
		HOMO−13	LUMO+2	24		
	$S_3(n\pi^*)$	HOMO−12	LUMO+1	58	2×10^{-4}	2.81
		HOMO−12	LUMO+2	26		
	$S_4(\pi\pi^*)$	HOMO	LUMO	56	1×10^{0}	3.07
		HOMO	LUMO+1	28		
	$S_5(\pi\pi^*)$	HOMO	LUMO+1	57	1×10^{0}	3.08
		HOMO	LUMO	27		
	$S_6(\pi\pi^*)$	HOMO	LUMO+2	83	2×10^{-3}	3.74

a Excited states for AAB at optimised OM2-MRCISD ground state structure with (8, 8) active space (Ref. 5.S2).

^1H *NMR spectra of TPAPA*

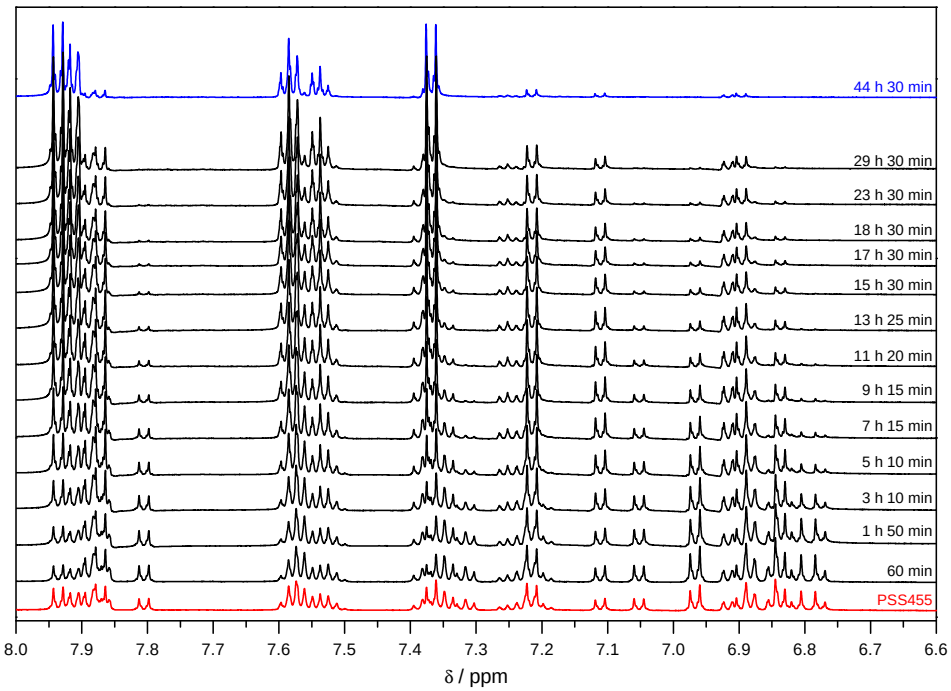

Figure 5.8: ^{1}H NMR spectra of TPAPA in CD_3CN at $T = 35\,^{\circ}C$ as function of time after excitation to the photostationary state PSS455 at $t = 0$.

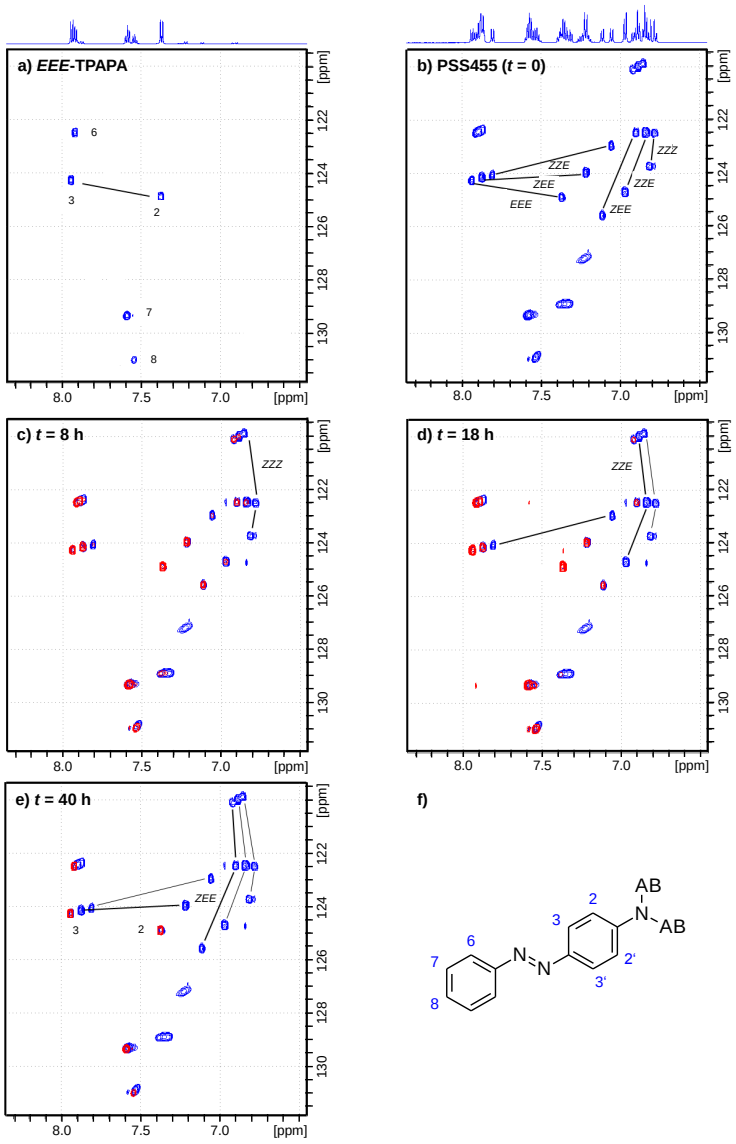

Figure 5.9: 2D-HSQC NMR spectra of TPAPA in CD_3CN at T = 35 °C at different times. a) Spectrum of the pure all-*E* isomer. b) Spectrum of TPAPA in the photostationary state PSS455 (t = 0). c) - e) Spectra after t = 8, 18, and 40 h (red), respectively, together with the spectra in the PSS455 (blue) from panel a) for reference. f) Assignments to the five chemically different proton sites for the all-*E* isomer identified by the labels 2, 3, and 6 – 8.

The 2D-HSQC spectra for the all-*E* isomer, for the photostationary state (PSS455), and for three selected times after preparation of the PSS show the coupling of the ^{13}C signals on the ordinate with the ^{1}H resonances of the H atoms bound the C atoms on the abscissa. The assignments for the *EEE*-isomer (Fig. 5.9a) to the five chemically different sites (labeled 2, 3, 6, 7, 8 in Fig. 5.9f) could be secured by means of COSY spectra. The key to the assignments for the other isomers was the observed change in the spectrum of the pure *EEE*-isomer in Fig. 5.9a to the spectrum of the photostationary state PSS455 in Fig. 5.9b. As can be seen, peaks 6, 7, and 8 show little change in spectral position, because they are associated with the outer aromatic rings that are too far away from the neighboring AB units to respond to their photoisomerisation. In contrast, resonances 2 and 3, which belong to the aromatic rings next to the central amino-N atom, split into several families of cross-peaks arising from the *ZEE*-, *ZZE*-, and *ZZZ*-isomers. The larger number of cross-peaks is due to the fact that the 2,2′- and 3,3′-positions (cf. Fig. 5.9f) are chemically equivalent only in the *EEE*-isomer, but distinguishable in the mixed photoisomers.

Since the thermal back-isomerisation from the PSS occurs sequentially, the additional cross-peaks could be assigned according to their observed time dependences (Figs. 5.9c–d). For example, in the spectrum in Fig. 5.9c shown in red at $t = 8$ h after preparation of the PSS, which has been superimposed on the spectrum of the PSS given in blue, the cross-peaks belonging to the *ZZZ*-isomer have virtually decayed to zero and are thereby identified by their blue color. Likewise, the cross-peaks belonging to the *ZZE*-isomer are reduced to nearly zero after $t = 18$ h (Fig. 5.9d). After $t = 40$ h, (Fig. 5.9d), the cross-peaks belonging to the *ZEE*-isomer eventually disappear as well such that only the *EEE*-isomer is left.

REFERENCES

5.S1. Takahashi, T.; Tanino, T.; Ando, H.; Nakano, H.; Shirota, Y. *Mol. Cryst. Liq. Cryst.*, **2005**, *430*, 9–14.

5.S2. Thiel, W. MNDO program, version 6.1. Max-Planck-Institut für Kohlenforschung, Mülheim an der Ruhr, Germany, 2007.

6

A FEMTOSECOND TIME-RESOLVED TRANSIENT ABSORPTION ANISOTROPY STUDY OF ELECTRONIC COUPLING IN MULTI-AZOBENZENE PHOTOSWITCHES

Julia Bahrenburg and Friedrich Temps*

Institut für Physikalische Chemie, Christian-Albrechts-Universität zu Kiel, Olshausenstr. 40, 24098 Kiel, Germany

submitted to J. Phys. Chem. A

OWN CONTRIBUTIONS TO THIS MANUSCRIPT:

- Synthesis and characterization of the molecules
- Time-resolved broadband transient absorption spectroscopy and transient absorption anisotropy decay measurements
- Analysis of the data
- Writing of the manuscript

* To whom correspondence should be addressed. E-mail: temps@phc.uni-kiel.de

ABSTRACT

The ultrafast dynamics of the bis- and tris-azobenzene photoswitches bis[4-(phenylazo)phenyl]amine (BPAPA) and tris[4-(phenylazo)phenyl]amine (TPAPA) have been investigated by means of femtosecond time-resolved broadband transient absorption spectroscopy and transient absorption anisotropy decay measurements in solution in *n*-hexane. The results show that intramolecular chromophore-chromophore interactions in both molecules play an important role. The relaxation pathway to the electronic ground state after excitation at $\lambda_{pump} = 460$ nm is very similar to that of azobenzene and 4-aminoazobenzene after $\pi\pi^*$ excitation, but the anisotropy measurements reveal strong electronic coupling between the azobenzene moieties. In particular, the anisotropy parameters $r(t)$ decay within $\leqslant 30$ fs from the initial value $r(0) = 0.4$ resp. 0.3 to a value of 0.3 resp. 0.15 for BPAPA and TPAPA. The ultrafast decay and the lower initial anisotropy for TPAPA strongly hint at intramolecular electronic coupling between the chromophore units in the electronically excited state. The observed effects are more distinctive for the tris- compared to the bis-azobenzene derivative. The results have high relevance for applications of photoswitchable materials where the chromophores may be in very close proximity.

6.1 INTRODUCTION

The high application potential of azobenzene (AB) and derivatives of AB as photoswitchable molecules is based on the reversible changes in shape, size and dipole moment between the thermally stable *E*- and the energetically higher *Z*-isomer and on the very low photochemical fatigue of the AB chromophore. AB photoswitches have thus been exploited in copious fields to this day, including the photocontrol of dendrons and dendrimers, polymers, thin films and other materials.[1–15] These examples also demonstrate how in typical functional systems, where multiple molecular switches are embedded in complex environments, the close proximity of the dye molecules can lead to sizable effects competing with the desired photoisomerization. In particular, steric interactions, intermolecular mechanical forces, excitonic coupling, charge transfer or direct electronic delocalization in π-conjugated systems are highly likely to influence the photoisomerization dynamics of the switches compared to the case in dilute solutions. To obtain insight into the isomerization dynamics in the presence of those interactions, we initiated a systematic study of the ultrafast dynamics and intramolecular chromophore-chromophore interactions of two photoswitchable multi-azobenzene compounds, bis[4-(phenylazo)phenyl]amine (BPAPA) and tris[4-(phenylazo)phenyl]amine (TPAPA). The AB units in these molecules are connected *via* a nitrogen linker which enables the electronic coupling between the two and three chromophores, respectively. The chemical structures of both compounds are given in Fig. 6.1. In a preceding paper, we reported on the static photochemical properties of BPAPA and TPAPA compared to their parent molecule 4-aminoazobenzene

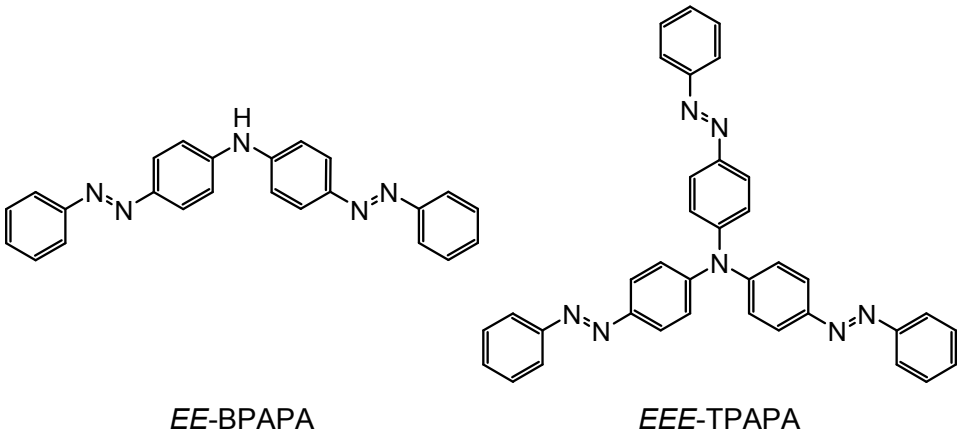

Figure 6.1: Molecular structures of *EE*-BPAPA and *EEE*-TPAPA.

(AAB) as reference system.[16] The UV/VIS absorption spectra of the three compounds are shown in Fig. 6.2. Striking changes in the spectral positions

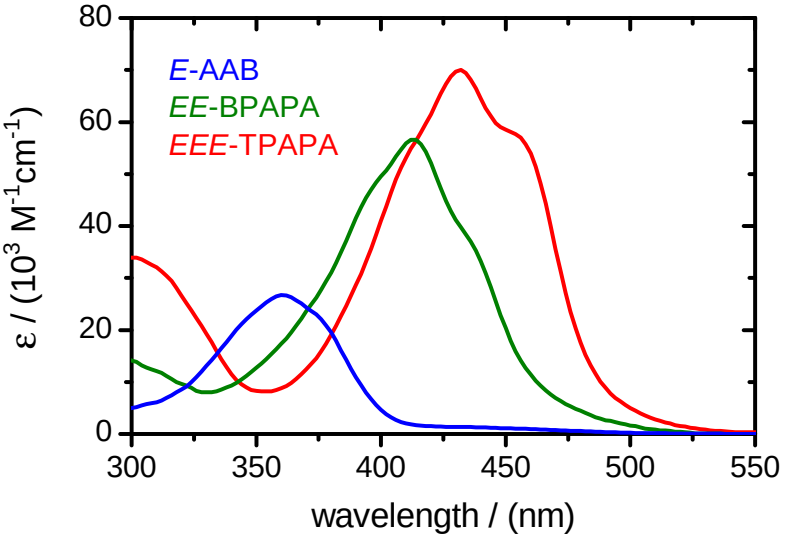

Figure 6.2: UV/VIS absorption spectra of AAB (blue), BPAPA (green) and TPAPA (red) in *n*-hexane as solvent.

and intensities of the first $\pi\pi^*$ absorption bands reveal a sizable influence of intramolecular interactions between the AB moieties, *via* electronic coupling and/or charge-transfer, on the resulting excited states. It is noteworthy that the observed effects are more pronounced for BPAPA compared to AAB than for TPAPA compared to BPAPA. Quantum chemical calculations for the first four excited states of BPAPA and the first six excited states of TPAPA show that the S_1 and S_2 states of BPAPA are degenerate $n\pi^*$ states, which have about the same energy as the $n\pi^*$ state of AAB.[16] The S_3 and S_4 state have $\pi\pi^*$ character and are lower and higher in energy (split by

$\approx$ 0.6 eV), respectively, compared to the $\pi\pi^*$ state of AAB, which is typical for an excitonic system. In the case of TPAPA, the S_1, S_2 and S_3 states are degenerate and of $n\pi^*$ character. The S_4 and the S_5 state are degenerate $\pi\pi^*$ states and have large oscillator strengths compared to the S_6 state, which is 0.65 eV higher in energy. The energetic order of the electronically excited states for BPAPA and TPAPA thus remains conserved ($n\pi^* < \pi\pi^*$) compared to plain AB despite the combination of several AB units. The calculated excitation energies for the respective states were found to be in reasonable agreement with the measured absorption spectra.[16] Furthermore, the photoswitching properties were investigated by means of UV/VIS and NMR spectroscopies. The three and four individual isomers of BPAPA and TPAPA, respectively, were readily detected and identified by one- and two-dimensional NMR spectroscopy. A kinetic analysis yielded the thermal lifetimes for all isomers. The variance of the results demonstrated a dependence of the isomerization on the chromophore size and number of AB units.[16]

Intrigued by the observed effects, we now systematically investigated the excited-state dynamics and the chromophore-chromophore interactions of the two and three AB units in BPAPA and TPAPA, respectively, by means of femtosecond time-resolved transient absorption and anisotropy decay measurements. The anisotropy measurements provide insight into details of the possible intramolecular couplings, in particular electronic energy transfer or exciton hopping,[17–27] between the individual AB chromophores within BPAPA and TPAPA in their electronically excited states. Both molecules were found to exhibit very rapid initial anisotropy decays. Additionally, TPAPA shows a lower initial anisotropy value.

6.2 EXPERIMENTAL SECTION

BPAPA and TPAPA were synthesized as published recently.[16] The purities of the samples were checked by one- and two-dimensional NMR spectroscopy. All measurements were performed in *n*-hexane (Sigma-Aldrich, spectroscopic grade). Solutions at concentrations of 0.1 mM corresponding to optical densities of 0.1 for BPAPA and 0.5 for TPAPA at the applied excitation wavelength were measured in flow cells with 0.2 mm fused silica windows and 1 mm optical pathlength.

The experimental setup for the femtosecond time-resolved broadband transient absorption measurements has been described in some detail previously.[28] The pump pulses at $\lambda_{pump} = 460$ nm with typical energies of $\approx$ 0.5 µJ were delivered by a home-built non-collinear optical parametric amplifier (NOPA). Broadband probe pulses were generated *via* supercontinuum generation in CaF_2, split into probe and reference beams and detected with two FFT-CCD cameras. The polarization of the pump pulses relative to the probe pulses was set to parallel, perpendicular or the magic angle by rotating a $\lambda/2$ plate. The measurements in parallel, perpendicular and magic angle configuration were done directly one after the other so

that they can be compared quantitatively. Further, all runs were repeated three times to ensure reproducibility.

The pump-induced cross-phase modulation (XPM) and stimulated Raman scattering (SRS) were measured independently for the pure solvent for each polarization. 2D transient absorption maps were then obtained by subtracting the XPM and the SRS contributions from the sample spectra taking into account the pump pulse absorption by the sample molecules and the time-zero correction for each wavelength individually for each polarization. The experimental time resolution was determined from the SRS signal and found to be $\Delta t \approx 30$ fs.

To check the setup, the magic angle transient absorption maps (I_{ma}) were also calculated from the parallel ($I_{\parallel}$) and the perpendicular ($I_{\perp}$) data sets according to

$$I_{ma} = \frac{I_{\parallel} + 2I_{\perp}}{3}$$

and compared with the measured data. Both were found to be virtually identical. The anisotropy value $r(t)$ was calculated from $I_{\parallel}$ and $I_{\perp}$ by taking

$$r(t) = \frac{I_{\parallel} - I_{\perp}}{I_{\parallel} + 2I_{\perp}}.$$

To allow for a quantitative analysis of the anisotropy decays at the earliest delay times, the respective time profiles were analyzed very carefully regarding the effects of the time-zero correction, the temporal width of the instrument response function (IRF) and the subtraction of the solvent signal.

6.3 RESULTS

6.3.1 BROADBAND TRANSIENT ABSORPTION MEASUREMENTS

The two-dimensional spectro-temporal transient absorption maps of BPAPA and TPAPA in *n*-hexane following excitation at $\lambda_{pump} = 460$ nm with the pump polarization at the magic angle with respect to the probe are displayed in Figs. 6.3 a and b. Since the respective data for parallel and perpendicular configuration showed little polarization dependent spectral changes except for the first 50 fs after excitation (see below), only the magic angle maps are shown. The absorption maps for BPAPA and for TPAPA exhibit similar behavior. Slight changes are mainly related to the differences in the static absorption spectra. Immediately after the pump pulse at $\Delta t = 0$, the negative ground state bleach (GSB) can be observed at $\lambda_{probe} = 370 - 435$ nm for BPAPA and at $\lambda_{probe} = 385 - 460$ nm for TPAPA. At the same time two excited state absorption (ESA) bands appear between $330 - 365$ nm and $440 - 700$ nm for BPAPA and between $330 - 380$ nm and $465 - 700$ nm for TPAPA, respectively. All ESA bands decay almost completely within the first three picoseconds. The longer-lived signals at $\lambda \approx 470 - 560$ nm belong to the absorption of vibrationally excited molecules in the electronic ground state (hot ground state absorp-

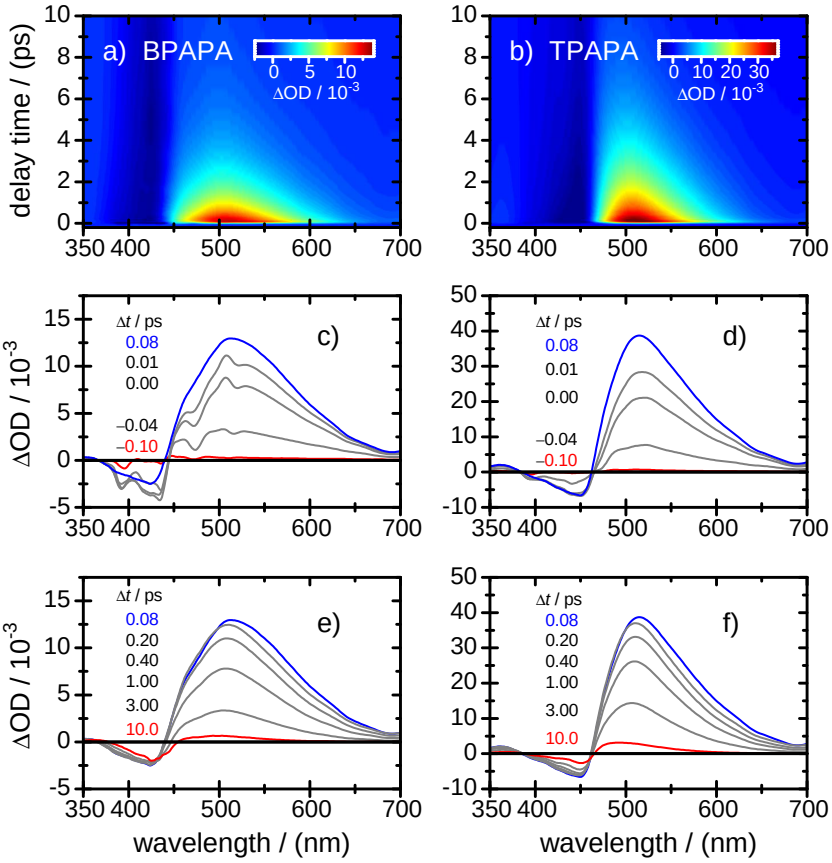

Figure 6.3: Two-dimensional maps of the transient absorption changes ΔOD of a) BPAPA and b) TPAPA in *n*-hexane after excitation at $\lambda_{pump} = 460$ nm for probe wavelengths in the range of 350 nm $\leqslant \lambda_{probe} \leqslant$ 700 nm and delay times of $\Delta t \leqslant 10$ ps with the pump polarization at the magic angle relative to the probe polarization. c) and e) Transient absorption spectra of BPAPA at different delay times between -0.10 ps $\leqslant \Delta t \leqslant 0.08$ ps and 0.08 ps $\leqslant \Delta t \leqslant 10$ ps, respectively. The features in the spectra at short delay times are attributed to scattered pump light and other artifacts. d) and f) Transient absorption spectra of TPAPA at different delay times between -0.10 ps $\leqslant \Delta t \leqslant 0.08$ ps and 0.08 ps $\leqslant \Delta t \leqslant 10$ ps, respectively.

tion, HGSA) after electronic deactivation. The vibrational relaxation of the "hot"molecules leads to a partial recovery of the GSB, but a significant permanent negative bleach remains at the longest delay time of $\Delta t_{max} = 1000$ ps. This final GSB reflects the isomerization of at least one AB moiety in the molecules, which is further confirmed by the persistent weak positive product absorption (PA) band at $\lambda_{probe} \approx 350$ nm.

The transient absorption spectra for BPAPA and TPAPA at selected delay times are given in Figs. 6.3 c – f and reveal the ensuing molecular dynamics in some more detail. Figs. 6.3 c and d show the early ultrafast spectro-temporal evolution up to 80 fs after the excitation, while the subsequent changes up to 10 ps are given in Figs. 6.3 e and f, respectively. The characteristic ESA and GSB absorption bands as well as HGSA at later

delay times are nicely featured in their respective spectral windows. Little spectral shifts can be observed during the rise and decay of the bands.

The quantitative temporal development of the transient absorption features is reflected by the transient absorption *vs.* time profiles, which are shown for parallel and perpendicular pump-probe configuration at six selected probe wavelengths for BPAPA and TPAPA in Figs. 6.4 and 6.5. The

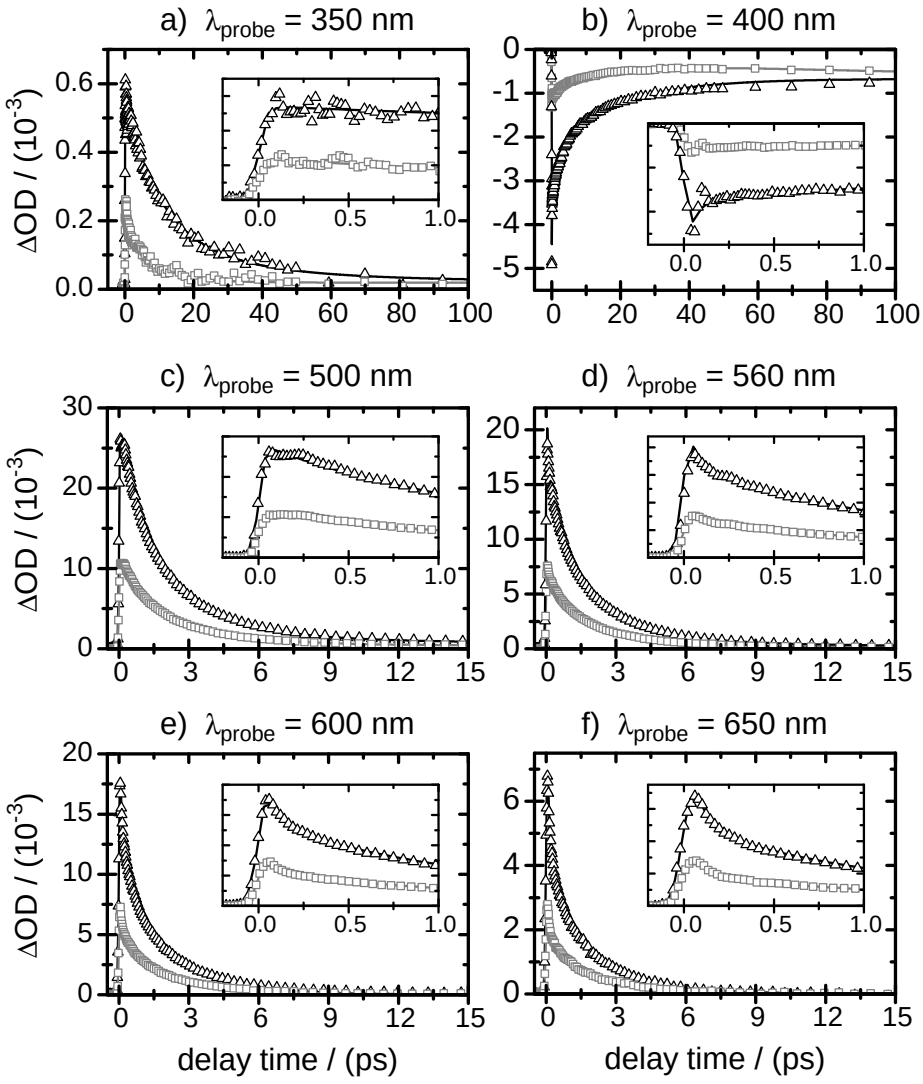

Figure 6.4: Transient absorption-time profiles of BPAPA in *n*-hexane after excitation at $\lambda_{pump} = 460$ nm at six selected wavelengths from $\lambda_{probe} = 350 - 650$ nm with the pump polarization parallel (black) and perpendicular (gray) relative to the polarization of the probe. Open symbols show the data, solid lines the overall least-squares fit curves. The insets give the same data on a shorter time scale up to 1 ps.

corresponding data for magic angle polarization are given in the electronic supplementary information (see Figs.6.7 and 6.8). Taking the experimental data for BPAPA and TPAPA for magic angle polarization at eight selected

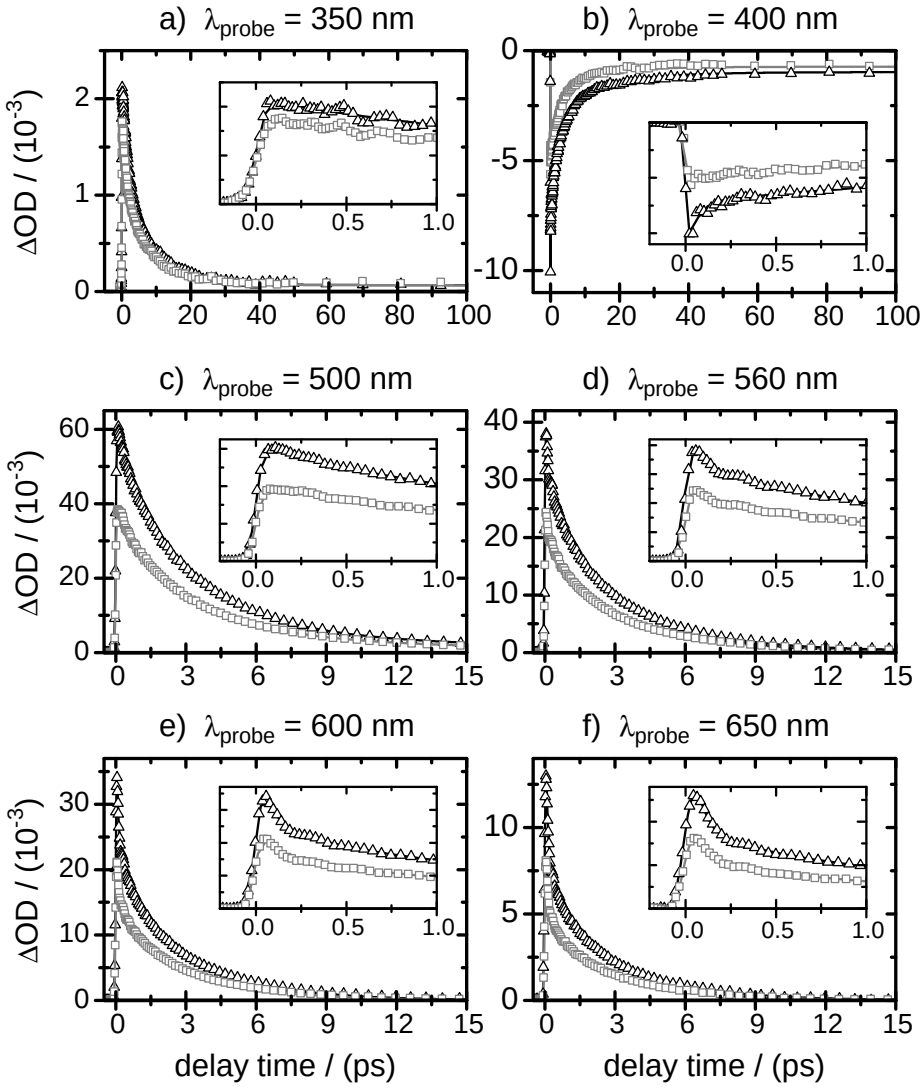

Figure 6.5: Transient absorption-time profiles of TPAPA in *n*-hexane after excitation at $\lambda_{pump} = 460$ nm at six selected wavelengths from $\lambda_{probe} = 350 - 650$ nm with the pump polarization parallel (black) and perpendicular (gray) with respect to the probe. Open symbols show the data, solid lines the overall least-squares fit curves. The insets give the same data on a shorter time scale up to 1 ps.

wavelengths distributed over the probe spectrum, a global analysis yielded the time constants

$$\tau_1 = 0.05 \pm 0.01 \text{ ps},$$
$$\tau_2 = 0.90 \pm 0.10 \text{ ps},$$
$$\tau_3 = 2.60 \pm 0.10 \text{ ps},$$
$$\tau_4 = 10.0 \pm 1.00 \text{ ps}$$

for BPAPA and

$$\tau_1 = 0.05 \pm 0.01 \text{ ps},$$
$$\tau_2 = 0.47 \pm 0.02 \text{ ps},$$
$$\tau_3 = 3.00 \pm 0.10 \text{ ps},$$
$$\tau_4 = 14.0 \pm 1.00 \text{ ps}$$

for TPAPA, respectively. The detailed fit results together with the corresponding relative amplitudes are compiled in Tables 6.1 and 6.2. Except for the evolution in the first $\leqslant$ 50 fs (see below), the time profiles for the three different polarizations for each system are virtually identical, only the relative amplitudes change depending on the probe wavelength and the pump-probe polarization. Tiny oscillations within the first 500 fs hint at coherent wavepacket motions, but the effects are too small to be analyzed in detail in this paper. At long times, the permanent PA at $\lambda_{\text{probe}} \approx 350$ nm and the GSB at $\lambda_{\text{probe}} \approx 430$ nm were each described with a step function accounting for the *E*-*Z* isomerization reactions. Time constants τ_{1-3} were thus attributed to the dynamics in the excited states and the subsequent radiationless deactivation to the electronic ground state, while τ_4, which becomes less important with increasing probe wavelength and can only be observed up to $\lambda_{\text{probe}} \approx 560$ nm, belongs to the vibrational cooling in the electronic ground state. τ_1 becomes more important with increasing detection wavelength for both molecules and can only be observed at $\lambda_{\text{probe}} \geqslant 560$ nm. The main decay components in the time profiles of BPAPA are τ_2 and τ_3, the dominating contribution in the case of TPAPA is the process decaying within $\tau_3 = 3$ ps.

6.3.2 TRANSIENT ABSORPTION ANISOTROPY DECAY MEASUREMENTS

The analysis of the absorption-time profiles shows quite complex excited state dynamics for the two investigated systems. To understand the details of possible ultrafast energy transfer, e.g., exciton hopping and/or exciton delocalization, the time dependent transient absorption anisotropy decay curves were calculated for four selected probe wavelengths in the intense ESA bands from $\lambda_{\text{probe}} = 470 - 650$ nm, where the observed transients are dominated by processes in the excited state (ESA) and not in the ground state (GSB or PA). The anisotropy decay curves at 600 nm and 500 nm for BPAPA and TPAPA are displayed in Fig. 6.6. Fig. 6.6 a shows the data for 500 nm and 600 nm on a time scale up to 1 ps. The 500 nm data are also presented on a longer time scale up to 100 ps in Fig. 6.6 b. The initial anisotropy for BPAPA was $r(t = 0) \approx 0.4$ for all probe wavelengths. Immediately thereafter, $r(t)$ can be seen to decay to a value of ≈ 0.3 within less than 0.1 ps. An exponential fit of this ultrafast process gave a time constant of $\tau < 0.03 \pm 0.01$ ps. This value should be seen as an upper limit due to the time resolution of the experiment ($\sigma_{\text{IRF}} \approx 30$ fs). Afterwards, the anisotropy remains nearly constant up to one picosecond, before it slowly decays to zero. The decay time for this much slower process is in

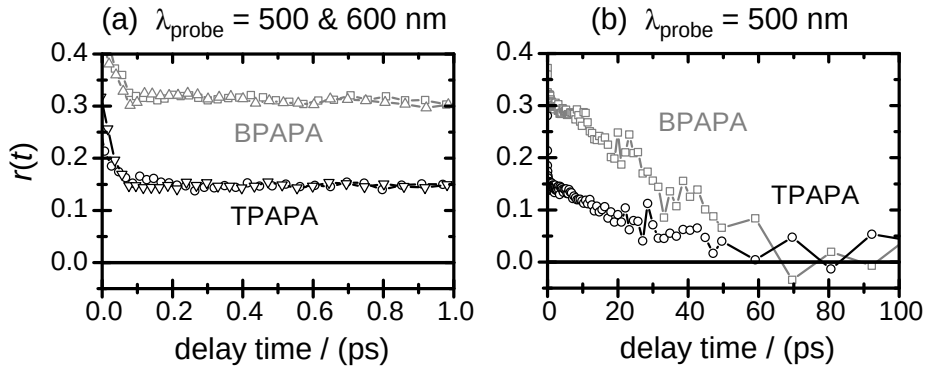

Figure 6.6: a) Transient absorption anisotropy decay curves up to $\Delta t = 1$ ps for BPAPA (gray) and TPAPA (black) after excitation at $\lambda_{pump} = 460$ nm at two selected wavelengths ($\lambda_{probe} = 600$ and 500 nm, shown on top of each other). b) Transient absorption anisotropy decay curves of BPAPA and TPAPA at $\lambda_{probe} = 500$ nm up to 100 ps.

the range of $\tau = 40 \pm 5$ ps. The obtained results showed no important wavelength-dependence of the anisotropy decay.

The anisotropy decay curves for TPAPA show a lower initial anisotropy of $r(t = 0) \approx 0.3$, but also a very fast initial decay with the same time constant of $\tau \leqslant 0.03 \pm 0.01$ ps to a value of ≈ 0.15 at all probe wavelengths. The subsequent decay to zero occurs within $\approx 40 \pm 5$ ps as for BPAPA.

6.4 DISCUSSION

The ultrafast dynamics and intramolecular chromophore-chromophore coupling effects of the two multi-azobenzene compounds bis[4-(phenylazo)-phenyl]amine (BPAPA) and tris[4-(phenylazo)phenyl]amine (TPAPA) have been investigated by means of femtosecond time-resolved broadband transient absorption spectroscopy and transient absorption anisotropy decay measurements. Special attention was directed at the very early dynamics in the polarization dependent measurements, which indicate strong electronic coupling between the two and three AB units, respectively.

6.4.1 OBSERVED TIME CONSTANTS AND ELECTRONIC DEACTIVATION

According to quantum chemical calculations the excitation at $\lambda_{pump} = 460$ nm should lead mainly to the population of the optically bright $\pi\pi^*$ state, which is red-shifted compared to AB and AAB and carries the bulk of the oscillator strength.[16] This implies that the relaxation to the electronic ground state after $\pi\pi^*$ excitation likely occurs *via* the energetically lower $n\pi^*$ state. The global kinetic analysis of the transient absorption-time profiles for parallel, perpendicular and magic angle pump-probe configuration gave quantitative insight into the related processes. The obtained time constants are virtually the same for each polarization for BPAPA as well

as for TPAPA and also very similar for BPAPA and TPAPA compared with each other. Therefore, it can be assumed that the *E-Z* isomerization of at least one AB unit and the relaxation to the S_0 state is probably governed by the same mechanism for both molecules. Sequential deactivation of the optically excited states *via* the energetically lower $n\pi^*$ states was already suggested for several *push-pull* azobenzenes which also feature strongly red-shifted $\pi\pi^*$ states compared to unsubstituted AB[29–32] and for the *E-Z* isomerization of AB and AAB after S_2 excitation.[33–36]

Hirose *et al.* and Satzger *et al.*, for example, probed the ultrafast *E-Z* photoisomerization of AAB and AB after UV excitation to the $\pi\pi^*$ state and found four time constants, $\tau \approx 0.15$ ps, ≈ 0.5 ps, ≈ 2.5 ps and ≈ 15 ps, respectively.[35,36] The ≈ 150 fs decay time was assigned to the transformation of the initially excited $\pi\pi^*$ state to the intermediate $n\pi^*$ state. The two time constants of ≈ 0.5 ps and ≈ 2.5 ps were found to belong to the subsequent *E-Z* isomerization and radiationless deactivation to the electronic ground state. Finally, the vibrational cooling of the "hot " S_0 molecules in the electronic ground state evidently occurred within ≈ 15 ps. Since the four time constants found in the global analysis of the transient absorption-time profiles for BPAPA and TPAPA are similar to the AB and AAB values after $\pi\pi^*$ excitation, the relaxation pathways could in principle be similar as well. Accordingly, the pump laser pulse projects the molecules from the electronic ground state to the Franck-Condon (FC) region of the respective $\pi\pi^*$ state, the decay of which is observed within τ_1 at detection wavelengths of $\lambda_{probe} \geqslant 560$ nm. The subsequent deactivation from the resulting $n\pi^*$ state to the electronic ground state may occur within τ_2 and τ_3. Those components were found to be the dominant ones over the whole probe wavelength range. Finally, τ_4 is safely assigned to the vibrational cooling in the electronic ground state.

6.4.2 TRANSIENT ABSORPTION ANISOTROPY DECAY MEASUREMENTS

To obtain insight into the details of possible intramolecular electronic coupling processes between the AB chromophores in the electronically excited state, the anisotropy decay curves were analyzed at selected probe wavelengths. Here, the primary focus lies on both the initial anisotropy values and the very early dynamics up to 100 fs. BPAPA shows an initial anisotropy value of $r(0) \approx 0.4$, whereas the initial anisotropy $r(0) \approx 0.3$ for TPAPA is lower. Afterwards, the anisotropy decays within less than $\leqslant 30$ fs to a value of ≈ 0.3 for BPAPA and a value of ≈ 0.15 for TPAPA. The lower $r(0)$ for TPAPA and the ultrafast initial anisotropy decays for both molecules hint at strong intramolecular interactions.[19–22] The subsequent slower processes with ≈ 40 ps decay time probably play only secondary roles regarding electronic energy redistribution or excitonic delocalization.[17–22,25–27] The slower processes are often attributed to several overlapping processes, including slow rotational diffusion.[19,21,22,27] In the present case, it should also be taken into account that the observed absorp-

tion at $\lambda_{probe} \approx 500$ nm on the 10 ps time scale arises from molecules back in the S_0 state (i.e., HGSA), where anisotropy should be lost.

The fact that the ultrashort time scale of $\leqslant 30$ fs for the anisotropy decay is in the same range as the decay time of $\tau_1 \approx 50$ fs should not be disregarded. On the basis of previous studies on the dynamics of AB and AAB after $\pi\pi^*$ excitation, τ_1 was assigned to the first electronic deactivation step of the initially excited state. The transition to the energetically lower intermediate state ($n\pi^*$) could also lead to a more or less pronounced change in the anisotropy depending on the transition dipole moments of the respective states. The fast change in anisotropy in the case of BPAPA and TPAPA could therefore be due partly to the transition between the two states. Nevertheless, the data more likely suggest electronic energy exchange by couplings between the AB units within BPAPA and TPAPA for several reasons. First, the lower initial anisotropy for TPAPA is an indication for energy transfer or exciton hopping within the excitation pulse duration. Second, the determined decay time of $\leqslant 30$ fs is an upper limit in view of the experimental time resolution ($\sigma_{IRF} \approx 30$ fs). The determined error (± 10 fs) may be larger. The data of TPAPA (cf. Fig. 6.6 a) show that the plateau of $r(t) \approx 0.15$ is actually reached within less than 70 fs. Third, the component decaying with τ_1 is not visible at probe wavelengths below $\lambda_{probe} \leqslant 560$ nm, where the ultrafast anisotropy decay $r(t)$ was clearly observable.

In conjugated molecules containing a number of chromophores, energy transfer between the chromophores or the formation of delocalized excitons is typically related to excitation spread over several chromophores.[23] For example, Hwang, *et al.* investigated the energy redistribution after excitation in multi-carbazole compounds and observed lower initial anisotropies arising from electronic coupling and excitonic delocalization between the chromophores in the excited state.[27] An explanation for a lower initial anisotropy is that the excitation is delocalized over several chromophores whose transition dipole moments are not necessarily identically oriented, therefore the "overall" dipole moment is different from the monomeric one. This kind of excitonic delocalization can lead to a depolarization by fast electronic energy transfer between the chromophores. This may already occur within the excitation pulse duration and will therefore lead to a lower initial anisotropy, or to a very fast anisotropy decay, if the time-resolution of the experiment is high enough.[21,25,27] The lower initial $r(0)$ value for TPAPA and the very short (≈ 30 fs) anisotropy decay time for both molecules thus give an indication for the electronic coupling between the AB moieties that can lead to rapid energy exchange. The lower initial anisotropy of TPAPA compared to BPAPA ($r(0) \approx 0.3$ *vs.* $r(0) \approx 0.4$) and the ultrafast decay to a lower value in the case of TPAPA ($r(t) \approx 0.15$ *vs.* $r(t) \approx 0.3$) suggest stronger coupling in the tris-AB compared to the bis-AB, which has been found by theoretical studies of Qian *et al.*[37] Their investigations showed that coupled chromophores exhibit an anisotropy value of 0.1 and uncoupled chromophores a value of 0.4, respectively. A value in between means that the chromophores are partially coupled. This

effect was observed as well for the above mentioned carbazole compounds, which also show lower initial anisotropy and/or very rapid anisotropy decay with increasing chromophore number and therefore increasing intramolecular chromophore-chromophore coupling.[27]

6.5 CONCLUSION

In conclusion, our study of the femtosecond time-resolved transient absorption anisotropy decay of the two multi-azobenzene compounds bis[4-(phenylazo)phenyl]amine (BPAPA) and tris[4-(phenylazo)phenyl]amine (TPAPA) in solution in *n*-hexane indicates substantial intramolecular interactions between the AB units in the excited states. Both molecules show a very fast anisotropy decay within $\leqslant$ 30 fs to values of $r(t) \approx 0.3$ (BPAPA) and $r(t) \approx 0.15$ (TPAPA). Furthermore, the initial anisotropy value of BPAPA is in the range of 0.4, whereas TPAPA shows a lower initial anisotropy value of 0.3. Both the ultrafast anisotropy decay and the lower initial anisotropy in the case of TPAPA suggest sizable electronic coupling between the AB moieties, which becomes more pronounced with higher number of chromophores within the respective system. The sequential deactivation to the electronic ground state after $\pi\pi^*$ excitation at $\lambda_{pump} = 460$ nm is assumed to be similar to the cases of 4-amino-AB and AB itself after $\pi\pi^*$ excitation. The initially populated $\pi\pi^*$ state of BPAPA resp. TPAPA decays within $\tau_1 = 0.05 \pm 0.01$ ps, likely to the respective $n\pi^*$ state. This probably additionally contributes to the ultrafast anisotropy decay. Subsequently, the electronic ground state is reached from the $n\pi^*$ state within $\tau_2 = 0.90 \pm 0.10$ ps and $\tau_3 = 2.60 \pm 0.10$ ps (BPAPA) and within $\tau_2 = 0.47 \pm 0.02$ ps and $\tau_3 = 3.00 \pm 0.10$ ps (TPAPA). Vibrational relaxation in the electronic ground state occurs within $\tau_4 = 10.0 - 14.0$ ps.

The observed effects related to the intramolecular coupling between the AB units are of practical relevance for the application of AB-based materials in optimally designed photoswitchable materials, where close proximity of the chromophores may also lead to inter- and intramolecular interactions competing with the desired photoizomerisation reactions.

ACKNOWLEDGMENTS

The support of this work by the Deutsche Forschungsgemeinschaft through the Sonderforschungsbereich 677 "Function by Switching" is gratefully acknowledged.

BIBLIOGRAPHY

[1] Archut, A.; Vögtle, F.; De Cola, L.; Azzellini, G. C.; Balzani, V.; Ramanujam, P. S.; Berg, R. H. *Chem. Eur. J.* **1998**, *4*, 699–706.

[2] Vögtle, F.; Gorka, M.; Hesse, R.; Ceroni, P.; Maestri, M.; Balzani, V. *Photochem. Photobiol. Sci.* **2002**, *1*, 45–51.

[3] Puntoriero, F.; Ceroni, P.; Balzani, V.; Bergamini, G.; Vögtle, F. *J. Am. Chem. Soc.* **2007**, *129*, 10714–10719.

[4] Deloncle, R.; Caminade, A.-M. *J. Photochem. C* **2010**, *11*, 24–45.

[5] Sekkat, Z.; Morichère, D.; Dumont, M.; Loucif-Saïbi, R.; Delaire, J. A. *J. Appl. Phys.* **1992**, *71*, 1543–1545.

[6] Kumar, G. S.; Neckers, D. C. *Chem. Rev.* **1989**, *89*, 1915–1925.

[7] Natansohn, A.; Rochon, P. *Chem. Rev.* **2002**, *102*, 4139.

[8] Hugel, T.; Holland, N. B.; Cattani, A.; Moroder, L.; Seitz, M.; Gaub, H. E. *Science* **2002**, *296*, 1103–1106.

[9] Kim, M.-J.; Seo, E.-M.; Vak, D.; Kim, D.-Y. *Chem. Mater.* **2003**, *15*, 4021–4027.

[10] Takahashi, T.; Tanino, T.; Ando, H.; Nakano, H.; Shirota, Y. *Mol. Cryst. Liq. Cryst.* **2005**, *430*, 9–14.

[11] Häckel, M.; Kador, L.; Kropp, D.; Schmidt, H.-W. *Adv. Mater.* **2007**, *19*, 227–231.

[12] Pardo, R.; Zayat, M.; Levy, D. *Chem. Soc. Rev.* **2011**, *40*, 672–687.

[13] Fabbri, F.; Garrot, D.; Lahlil, K.; Boilot, J. P.; Lassailly, Y.; Peretti, J. *J. Phys. Chem. B* **2011**, *115*, 1363–1367.

[14] Zaporojtchenko, V.; Pakula, C.; Wahyuni Basuki, S.; Strunskus, T.; Zargarani, D.; Herges, R.; Faupel, F. *Appl. Phys. A* **2011**, *102*, 421–427.

[15] Wang, X.; Yin, J.; Wang, X. *Langmuir* **2011**, *27*, 12666–12676.

[16] Bahrenburg, J.; Sievers, C. M.; Schönborn, J. B.; Hartke, B.; Renth, F.; Temps, F.; Näther, C.; Sönnichsen, F. D. *Photochem. Photobiol. Sci.* **2013**, *12*, 511–518.

[17] Jonas, D. M.; Lang, M. J.; Nagasawa, Y.; Joo, T.; Fleming, G. R. *J. Phys. Chem* **1996**, *100*, 12660–12673.

[18] Varnavski, O.; Menkir, G.; Goodson III, T.; Burn, P. *Appl. Phys. Lett.* **2000**, *77*, 1120–1122.

[19] Varnavski, O.; Samuel, I.; Pålsson, L.-O.; Beavington, R.; Burn, P.; Goodson III, T. *J. Chem. Phys.* **2002**, *116*, 8893–8903.

[20] Ranasinghe, M. I.; Wang, Y.; Goodson, T. *J. Am. Chem. Soc.* **2003**, *125*, 5258–5259.

[21] Goodson III, T. G. *Acc. Chem. Res.* **2005**, *38*, 99–107.

[22] Wang, Y.; He, G. S.; Prasad, P. N.; Goodson, T. *J. Am. Chem. Soc.* **2005**, *127*, 10128–10129.

[23] Ahn, T. S.; Thompson, A. L.; Bharathi, P.; Müller, A.; Bardeen, C. J. *J. Phys. Chem. B* **2006**, *110*, 19810–19819.

[24] Kuroda, D. G.; Singh, C.; Peng, Z.; Kleiman, V. D. *Science* **2009**, *326*, 263–267.

[25] Collini, E.; Scholes, G. D. *Science* **2009**, *323*, 369–373.

[26] Badaeva, E.; Harpham, M. R.; Guda, R.; Suzer, O.; Ma, C.-Q.; Bauerle, P.; Goodson III, T.; Tretiak, S. *J. Phys. Chem. B* **2010**, *114*, 15808–15817.

[27] Hwang, I.; Selig, U.; Chen, S. S.; Shaw, P. E.; Brixner, T.; Burn, P. L.; Scholes, G. D. *J. Phys. Chem. A* **2013**, *117*, 6270–6278.

[28] Röttger, K.; Siewertsen, R.; Temps, F. *Chem. Phys. Lett.* **2012**, *536*, 140–146.

[29] Hagiri, M.; Ichinose, N.; Zhao, C.; Horiuchi, H.; Hiratsuka, H.; Nakayama, T. *Chem. Phys. Lett.* **2004**, *391*, 297–301.

[30] Poprawa-Smoluch, M.; Baggerman, J.; Zhang, H.; Maas, H. P. A.; De Cola, L.; Brouwer, A. M. *J. Phys. Chem. A* **2006**, *110*, 11926–11937.

[31] Crecca, C. R.; Roitberg, A. E. *J. Phys. Chem. A* **2006**, *110*, 8188–8203.

[32] Bahrenburg, J.; Röttger, K.; Siewertsen, R.; Renth, F.; Temps, F. *Photochem. Photobiol. Sci.* **2012**, *11*, 1210–1219.

[33] Lednev, I. K.; Ye, T.-Q.; Matousek, P.; Towrie, M.; Foggi, P.; Neuwahl, F. V. R.; Umapathy, S.; Hester, R. E.; Moore, J. N. *Chem. Phys. Lett.* **1998**, *290*, 68–74.

[34] Fujino, T.; Arzhantsev, S. Y.; Tahara, T. *Bull. Chem. Soc. Jpn.* **2002**, *75*, 1031–1040.

[35] Hirose, Y.; Yui, H.; Sawada, T. *J. Phys. Chem. A* **2002**, *106*, 3067–3071.

[36] Satzger, H.; Root, C.; Braun, M. *J. Phys. Chem. A* **2004**, *108*, 6265–6271.

[37] Qian, W.; Jonas, D. M. *J. Chem. Phys.* **2003**, *119*, 1611–1622.

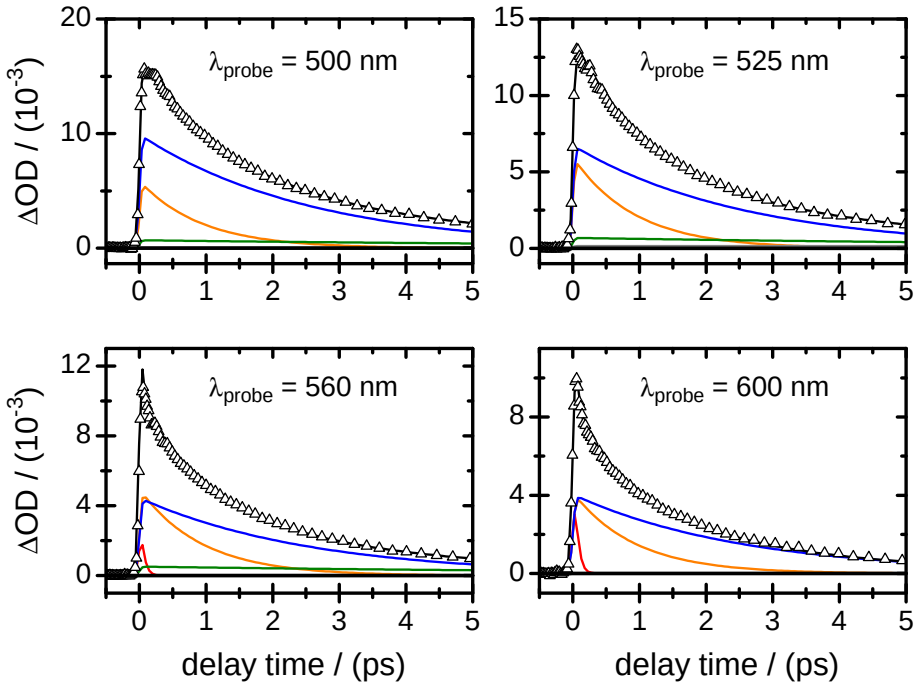

Figure 6.7: Transient absorption-time profiles of BPAPA in *n*-hexane after excitation at $\lambda_{pump} = 460$ nm at four selected wavelengths with the pump polarization at the magic angle relative to the probe. Open symbols are the data, solid lines represent the overall least-squares fit curves. The different contributions are indicated by colored lines (red: τ_1, orange: τ_2, blue: τ_3 and green: τ_4).

Table 6.1: Results of the global fit analysis of the absorption-time profiles between 500 nm $\leqslant \lambda_{probe} \leqslant$ 650 nm of BPAPA with the pump polarization at magic angle with respect the probe. Values in parenthesis give the 2σ standard deviations with respect to the last digits.

λ / nm	τ_1 / ps	A_1 (rel.)	τ_2 / ps	A_2 (rel.)	τ_3 / ps	A_3 (rel.)	τ_4 / ps	A_4 (rel.)
500	0.05(1)	-	0.9(1)	0.36(2)	2.6(1)	0.60(1)	10(1)	0.07(1)
525	0.05(1)	-	0.9(1)	0.45(1)	2.6(1)	0.50(2)	10(1)	0.05(2)
560	0.05(1)	0.30(1)	0.9(1)	0.35(2)	2.6(1)	0.30(1)	10(1)	0.05(1)
600	0.05(1)	0.48(2)	0.9(1)	0.26(2)	2.6(1)	0.26(2)	10(1)	-
650	0.05(1)	0.60(1)	0.9(1)	0.22(1)	2.6(1)	0.18(3)	10(1)	-

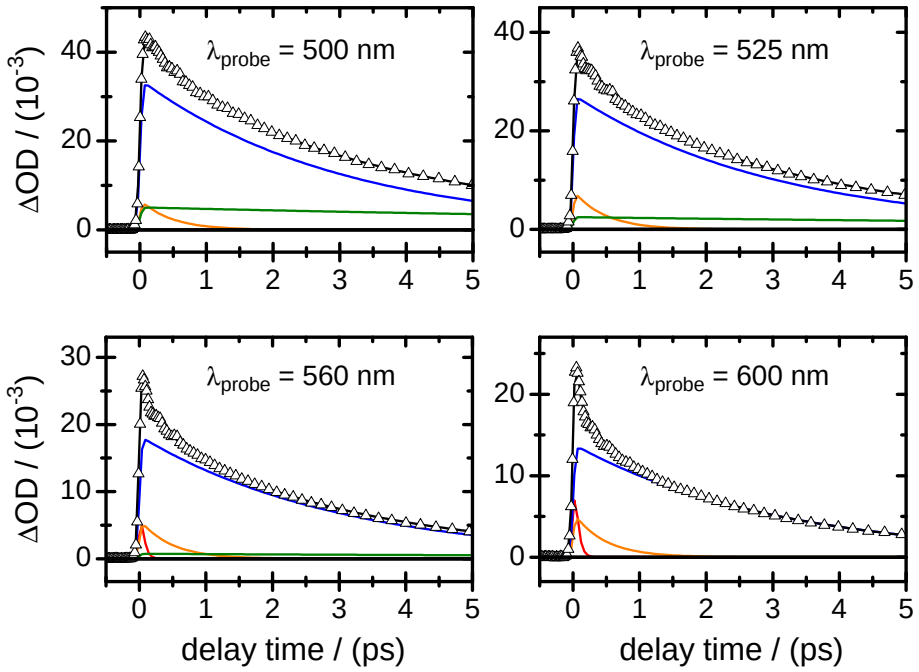

Figure 6.8: Transient absorption-time profiles of TPAPA in *n*-hexane after excitation at $\lambda_{pump} = 460$ nm at four selected wavelengths with the pump polarization at the magic angle with respect to the probe. Open symbols are the data, solid lines represent the overall least-squares fit curves. The different contributions are indicated by colored lines (red: τ_1, orange: τ_2, blue: τ_3 and green: τ_4).

Table 6.2: Results of the global fit analysis of the absorption-time profiles between 500 nm $\leqslant \lambda_{probe} \leqslant$ 650 nm of TPAPA with the pump polarization at magic angle relative to the probe. Values in parenthesis give the 2σ standard deviations with respect to the last digits.

λ / nm	τ_1 / ps	A_1 (rel.)	τ_2 / ps	A_2 (rel.)	τ_3 / ps	A_3 (rel.)	τ_4 / ps	A_4 (rel.)
500	0.05(1)	-	0.47(2)	0.15(1)	3.0(1)	0.74(1)	14(1)	0.11(2)
525	0.05(1)	-	0.47(2)	0.21(2)	3.0(1)	0.72(1)	14(1)	0.07(2)
560	0.05(1)	0.32(2)	0.47(2)	0.16(3)	3.0(1)	0.50(1)	14(1)	0.02(2)
600	0.05(1)	0.47(1)	0.47(2)	0.16(2)	3.0(1)	0.37(1)	14(1)	-
650	0.05(1)	0.57(2)	0.47(2)	0.16(1)	3.0(1)	0.27(2)	14(1)	-

7

ULTRAFAST DYNAMICS OF A NICKEL PORPHYRIN BASED MAGNETICALLY BISTABLE MOLECULAR SPIN SWITCH AND ITS BUILDING BLOCKS

Julia Bahrenburg,[a] Hendrik Böhnke,[a] Mats Bohnsack,[a] Marcel Dommaschk,[b] Rainer Herges,[b] and Friedrich Temps[a]*

[a] Institute of Physical Chemistry, Christian-Albrechts-University of Kiel, Olshausenstr. 40, D-24098 Kiel, Germany

[b] Otto Diels-Institut für Organische Chemie, Christian-Albrechts-Universiy of Kiel, Otto-Hahn-Platz 4, D-24098 Kiel, Germany

OWN CONTRIBUTIONS TO THIS MANUSCRIPT:

- Time-resolved absorption spectroscopy
- Static absorption spectroscopy
- Analysis of the data
- Writing of the manuscript

* To whom correspondence should be addressed. E-mail: temps@phc.uni-kiel.de

ABSTRACT

The photo-induced ultrafast dynamics of the *E*- and *Z*-isomer of the bistable Ni porphyrin based molecular spin switch Azo-NiTPPF$_{15}$ and its respective building blocks, the nickel porphyrin NiTPPF$_{20}$ and the metal free porphyrin H$_2$TPPF$_{20}$, were followed by means of femtosecond time-resolved transient absorption spectroscopy after excitation into the Q band at $\lambda_{pump} = 520$ nm. In the case of H$_2$TPPF$_{20}$ the excitation leads to the population of the Q_y state of the macrocycle. The subsequent deactivation to the Q_x state occurs within the time resolution of the experiment. The vibrational relaxation within the Q_x state is followed by two intersystem crossings to a lower triplet state and the electronic ground state. The results for the four-coordinate NiTPPF$_{20}$ and *E*-Azo-NiTPPF$_{15}$ are virtually identical. Q band excitation populates the S_1 / Q_y state of the macrocycle with the metal remaining in the $(d_{z^2})^2$ configuration. Afterwards the excitation energy is transferred to the metal ion, leading to the electronic ground state of the porphyrin and an excited metal state (porphyrin ground-metal excited state, $|S_0, ^{1,3}(d,d)\rangle_{hot}$). The subsequent vibrational relaxation occurs within $2-5$ ps. The resulting semi-excited state shows the typical derivative-shaped absorption bands and decays on a time scale of hundreds of picoseconds. The states being involved in the relaxation of the five-coordinate *Z*-Azo-NiTPPF$_{15}$ are different due to the paramagnetic triplet ground state. The deactivation occurs *via* a $((d_{z^2})^2)^*$ state. Additionally a triplet state of the porphyrin is involved in the dynamics. The predicted spin switch of Azo-NiTPPF$_{15}$ could not be observed during these experiments since the involvement of the dynamics of the porphyrin macrocylce leads to complex dynamics and very broad, intense and superimposed contributions in the transient absorption spectra over the entire spectral detection range.

7.1 INTRODUCTION

Porphyrins and metal porphyrins play important roles in numerous fields and applications including biology, chemistry, engineering, materials science, medicine and physics.[1–9] An extraordinary example of a metal porphyrin system is a recently designed molecular spin switch based on a Ni porphyrin and an isomerizing azobenzene (AB) unit. This compound shows magnetic bistability at room temperature in homogeneous solution upon irradiation and therefore has application potential as contrast agent in magnetic resonance imaging (MRI).[10] In the past, magnetic bistabilty has been restricted to bulk materials at very low temperatures. The molecular structures of the *E*- and the *Z*-isomer of the mentioned photoswitchable system (*E*-Azo-NiTPPF$_{15}$ and *Z*-Azo-NiTPPF$_{15}$) and the respective porphyrin derivatives NiTPPF$_{20}$ and H$_2$TPPF$_{20}$ with and without metal center are shown in Figs. 7.1 a - d). In the case of the azopyridine functionalized system, one of the pentafluorophenyl groups in meso position of the Ni(II)-porphyrin meso-tetrakis-(tripentafluorphenyl,2-[biphenyl-3-

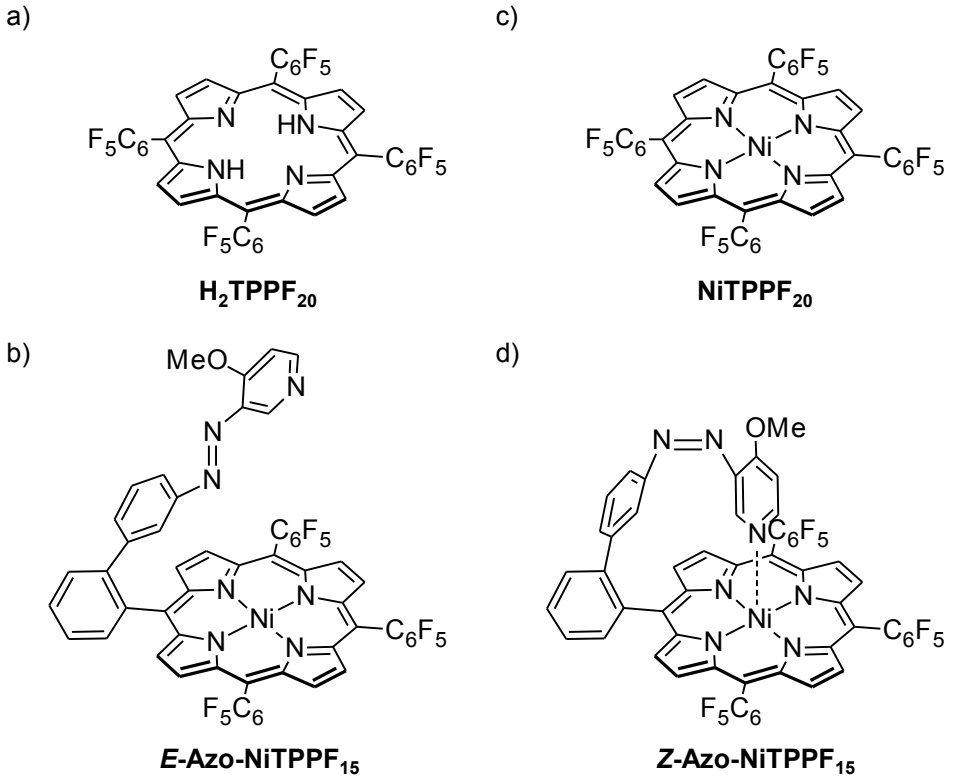

Figure 7.1: Molecular structures of a) the metal free porphyrin (H_2TPPF_{20}), b) the Ni porphyrin ($NiTPPF_{20}$), c) the azopyrindine functionalized Ni porphyrin in the low-spin state (*E*-Azo-$NiTPPF_{15}$) and d) the azopyrindine functionalized Ni porphyrin in the high-spin state (*Z*-Azo-$NiTPPF_{15}$).

azo]-4-methoxypyridine)-nickel(II)porphyrin (cf. Fig. 7.1 b) is substituted by an azobiphenylpyridine unit with a methoxy group in the ortho position of the pyridine ring.

The four-coordinate Ni(II) porphyrins $NiTPPF_{20}$ and *E*-Azo-$NiTPPF_{15}$ have a singlet ($(a_{1u})^2(a_{2u})^2$) electronic ground state. Depending on the relative spin of the promoted electron, the excited configurations ($a_{1u}e_g$) and ($a_{2u}e_g$) can either be singlet or triplet states.[11] The Ni(II) d^8 ion has vacant d orbitals energetically located between the S_0 and the initially excited S_1 state of the π system of the porphyrin.[12] The coordination of the Ni(II) ion into the porphyrin macrocycle leads to interactions between the π and the d orbitals of the macrocycle and the metal ion, respectively, resulting in mixed excited states. 8-states calculations of the *E*-Azo-$NiTPPF_{15}$ at the MCSCF level of theory show that the lowest excited state is a doubly excited mixed state including both a $d_{z^2} \rightarrow d_{x^2-y^2}$ and a $\pi \rightarrow \pi^*$ transition.[13] For the sake of clarity the respective mixed excited states of the π and the d system for the four- and the five-coordinate system are depicted separately in Fig. 7.2 in a schematic manner. In the electronic ground state of *E*-Azo-$NiTPPF_{15}$, the Ni(II) is surrounded by a square planar environment leading to a doubly occupied $3d_{z^2}$ orbital

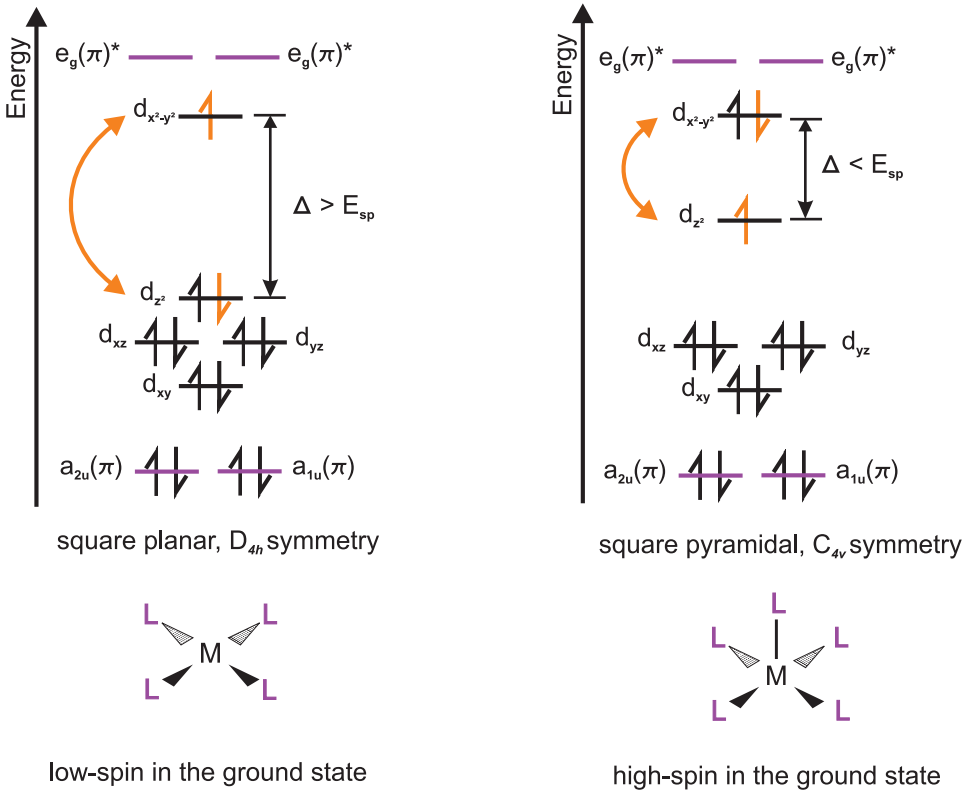

Figure 7.2: Scheme of the spin state configurations of the four-coordinate *E*-Azo-NiTPPF$_{15}$ (left) and the five-coordinate *Z*-Azo-NiTPPF$_{15}$ (right).

as HOMO and a vacant $3d_{x^2-y^2}$ orbital.[14] This ground state configuration gives a low-spin diamagnetic $(d_{z^2})^2$ state, because the energetic gap Δ between the highest filled and the lowest unfilled orbital of the metal system is significantly larger than the spin pairing energy E_{SP}. Compared to the four-coordinate system, the five-coordinate *Z*-Azo-NiTPPF$_{15}$ has an additional axial ligand and exhibits a square pyramidal geometry. In this configuration the Ni(II) ion moves out of the plane of the four nitrogen atoms. Due to the interaction with the p orbitals of the nitrogen atom of the axial ligand the doubly occupied d_{z^2} orbital becomes destabilized and gets energetically closer to the empty $d_{x^2-y^2}$ orbital.[11] The energetic gap Δ between the d_{z^2} and the $d_{x^2-y^2}$ orbital becomes smaller than the spin pairing energy E_{SP} resulting in a paramagnetic high-spin ground state.

The square planar saddled shape in the four-coordinate systems enables a shortening of the bond length between the nitrogen atoms of the porphyrin and the nickel. Upon axial coordination and switching to the high-spin *Z*-Azo-NiTPPF$_{15}$ the $d_{x^2-y^2}$ orbital gets occupied. The N-Ni bond length is then increased within the macrocyclic plane due to the interactions of the d orbitals of the metal manifolds with the π orbitals of the macrocycle, forcing the latter into a planar conformation. The reversible light-driven coordination-induced spin-state switching (LD-CISSS) *via* the coordination or photo-induced decoordination of the pyridine moiety can be achieved by irradiation at $\lambda \approx 500$ nm and $\lambda \approx 435$ nm, inducing the *E*→*Z* and the

$Z \rightarrow E$ isomerizations of the AB, respectively.[10] As typical for AB based switches, the system exhibits very high photostability and ultralow photochemical fatigue.[15–17] Evans measurements allowed for determination of the paramagnetic and diamagnetic states of the *Z*- and the *E*-isomer, respectively. The fact that the isomerization takes place, although the AB itself is not excited, gives evidence for some kind of energy transfer process probably from the excited $\pi\pi^*$ of the porphyrin macrocyle to the $n\pi^*$ transition of the AB enabling the desired isomerization.[10]

The characteristic structure of the absorption spectra of tetrapyrroles in the VIS spectrum can be explained by the four orbital model.[18] A schematic depiction for the metal free and the metal porphyrin are shown in Figs. 7.3 a and b). Essentially, the interactions of one-electron states that

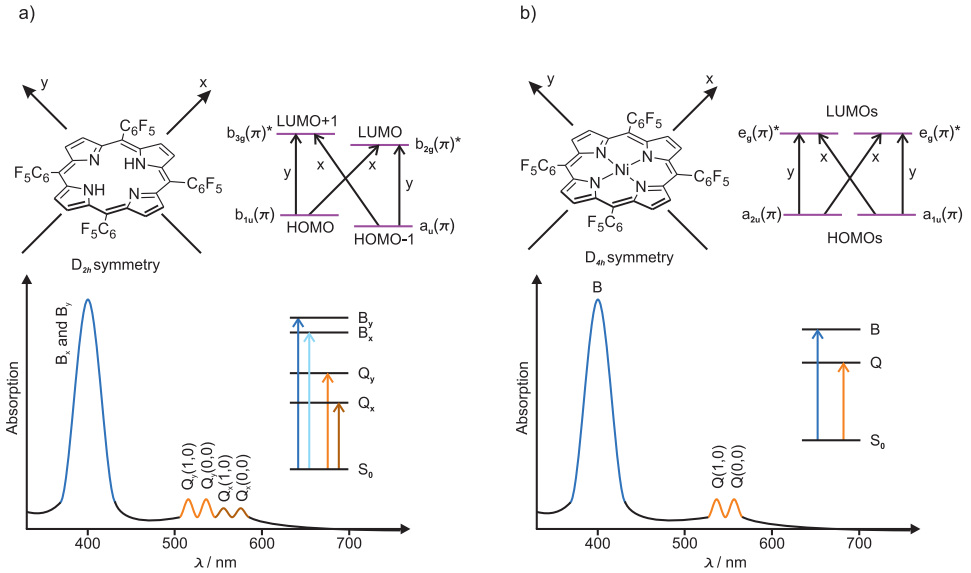

Figure 7.3: Schematic depiction of the four orbital model for the metal free porphyrin H_2TPPF_{20} showing D_{2h} symmetry (a) and for the metal complex $NiTPPF_{20}$ (D_{4h} symmetry) (b).

are MO configurations are parametrized resulting in an absorption spectrum. The excited configurations are formed by promotion of one electron from the HOMO and the HOMO-1 to the LUMO and the LUMO+1. Electron-electron repulsion causes interacting MO configurations giving rise to a 2×2 matrix, whose elements are the parameters of this model. These parameters are the energies and and dipole moments of the excited state MO configurations.[19] As stated in the four orbital model, there are four allowed $\pi \rightarrow \pi^*$ transitions in a porphyrin derivative for electronic excitation. In the case of the metal free porphyrin the involved molecular orbitals are the HOMO $b_{1u}(\pi)$ and the HOMO-1 $a_u(\pi)$ as well as the LUMO $b_{2g}(\pi^*)$ and the LUMO+1 $b_{3g}(\pi^*)$ of the macrocyclic π system. The resulting four allowed transitions are either x- or y-polarized. Linear combination of the associated wave functions of the excited state MO configurations leads to the formation of the B_x, B_y, Q_x and Q_y absorption

bands. While the parallel combination of the dipole moments gives rise to the strongly absorbing B bands, the antiparallel combination results in the formation of the weakly absorbing Q bands as shown in Fig. 7.3 a).[11,18–22] By increasing the complexity of the porphyrin derivative upon incorporation of a central Ni(II) ion, the symmetry of the macrocyclic framework is also increased from D_{2h} in the metal free system to D_{4h} in the metal porphyrin. Therefore, the HOMOs and LUMOs of the macrocyclic π system become degenerate, resulting in overall singular B and Q absorption bands, respectively, as depicted in Fig. 7.3 b). The appearance of the two Q bands ^{1}Q(1,0) and ^{1}Q(0,0) is related to vibronic coupling with the intense B band and strongly depends on the substituents within the porphyrin macrocycle.[11,18]

There are many of previous experimental and theoretical studies on the photochemical properties and the ultrafast dynamics of (Ni-)porphyrin derivatives, which will be summarized roughly in the following.[1,9,11,14,23–47] Ni(II) porphyrins are known to be "non-luminescent". Since neither fluorescence nor phosphorescence ($\Phi < 10^{-5}$) from the usually emissive $\pi\pi^*$ excited states of the porphyrin system can be observed, there is general agreement that a radiationless decay of the excited macrocycle occurs rapidly after photo-excitation resulting in the formation of metal-centered (d,d) excited states.[11,14,23–27,31,34–36,38–40,45,46] In the d^8 electronic configuration of the metal ion, the d_{z^2} and the $d_{x^2-y^2}$ orbitals are the highest occupied and the lowest unoccupied ones, respectively, in the absence of coordinating ligands. The effective suppression of luminescence suggests a low-lying singlet and / or triplet (d_{z^2}, $d_{x^2-y^2}$) excited state as the first excited metal state.[11,14,23–26,35,39] This (d,d) excited state is formed by conversion of the excitation energy from the initially excited macrocycle in the metal manifold within several tens of femtoseconds.[23] Therefore, the $|S_1, (d_{z^2})^2\rangle$ state has often been unresolved in transient absorption experiments due to poor time resolution.[21,47] The first spectrally detectable intermediate state was supposed to be a successor state of S_1 formed by internal conversion.[21] If the porphyrin macrocycle is still excited or reaches the electronic ground state after the energy transfer to the metal ion, is discussed controversially.[21,34] However, it seems to be more likely that the porphyrin ring reaches its electronic ground state within less than one picosecond, which is in agreement with the non-observable emission from the π system.[11,14,23,24,26,34,35,45,48] In general the ultrafast relaxation via the π- and metal-centered excited states is known to occur *via* an internal conversion cascade, probably conserving the overall multiplicity during the deactivation pathway. There is still a disagreement whether the deactivation occurs *via* a singlet ^{1}(d,d) state[14,23] or a triplet ^{3}(d,d) state.[11,24,25,39] The subsequent vibrational relaxation of the metal excited states is related to a change in the size of the central nickel ion and is reported to be in the magnitude of tens of picoseconds.[21,23,24,34,37,39,47,49] The formation of the $d_{x^2-y^2}$ excited state causes changes in the geometrical structure of the porphyrin macrocycle because of changes in the Ni-N bond lengths. In this excited state the electron den-

sity is located on the pairs of diagonally opposite N atoms in the macrocycle. Thus, the central Ni(II) ion is pulled down into the macrocycle plane, destabilizing the Ni-N bonds. The ionic radius in diamagnetic low-spin Ni(II) porphyrins is ≈ 0.6 Å. In the paramagnetic metal-excited (d,d) state the ionic radius is about ≈ 0.7 Å with the macrocycle in a planar geometry.[21,23,24,26,37,47] The geometrical reorganization due to the change in size of the central Ni(II) ion and the repopulation of the electronic ground state of the macrocycle occur most likely simultaneously. As the $(d_{z^2}, d_{x^2-y^2})$ state probably favors a more planar configuration of the macrocycle than the $(d_{z^2})^2$ ground state, the transient absorption spectra belonging to this state are expected to show a progressive blue-shift within the first picoseconds. This blue-shift of the transient absorption bands probably overlaps with the shifting of the bands due to vibrational relaxation accompanied with spectral narrowing. The spectra of Ni(II) porphyrins in the metal excited (d,d) states are expected to show derivative-shaped absorption changes. The transient absorption spectrum of the (d,d) excited state should be governed by the same $\pi\pi^*$ transitions as the absorption spectrum of the electronic ground state, but shifted in energy due to the still excited metal. Most of the (d,d) spectra of the (nearly) planar compound show transient absorption bands red-shifted to the bleach of the bands of the ground state B and Q bands.[23] The intrinsically high absorption coefficients are not significantly affected by the metal center configuration.[35] The red-shifted absorption bands in the absorption spectrum of the $(d_{z^2}, d_{x^2-y^2})$ excited state compared to the ground state absorption spectrum can be understood in terms of the repulsive interaction between the $d_{x^2-y^2}$ orbital and the $a_{2u}(\pi)$ HOMO of the porphyrin ring. This interaction raises the energy of the $a_{2u}(\pi)$ orbital relative to the $e_g(\pi^*)$ LUMOs, and leads to a red-shift of both the Q and the B band.[23] For Ni(II) porphyrins the transition to the overall ground state is supposed to be the $|S_0, (d_{z^2}, d_{x^2-y^2})\rangle \rightarrow |S_0, (d_{z^2})^2\rangle$ transition and occurs typically within several hundreds of picoseconds.[24,26,34,39] The deactivation of the (d,d) state and the entire recovery of the electronic ground state is accompanied by the complete decay of the derivative-shaped absorption changes with one or more apparent isosbestic points. Furthermore, transient absorption and resonance Raman studies of four-coordinate Ni(II) porphyrins have shown that the (d,d) excited states have a strong affinity for ligands like nitrogenous bases. The binding of the axial ligands to the central Ni(II) ion can be described predominantly as a σ interaction of the axial ligand with the $3d_{z^2}$ orbital of the Ni, which favors the coordination of electron donating ligands as long as the $3d_{z^2}$ orbital is only half occupied in the metal excited state. In presence of coordinating solvents, coordination results mainly in six coordinate species.[14,23,34,46] In contrast to the relatively short-lived Ni(II) porphyrins, the metal free porphyrins show lifetimes of $10 - 20$ ns, which are attributed to intersystem crossing between singlet and triplet states.[23,24,29,32]

Our strategy was to study the ultrafast dynamics of the azopyridine func-

tionalized Ni porphyrin and its different building blocks to obtain first insight into the nature of the excited states and possible deactivation mechanisms such as photoisomerization and the associated switch of the spin state, charge- and energy-transfer, or intersystem crossing between singlet and triplet states by means of femtosecond time-resolved transient absorption spectroscopy after excitation to the Q_y absorption band at $\lambda_{pump} = 520$ nm.

7.2 EXPERIMENTAL SECTION

The metal free porphyrin H_2TPPF_{20}, the Ni porphyrin $NiTPPF_{20}$ and the azopyrindine functionalized Ni porphyrin *E*-Azo-$NiTPPF_{15}$ were synthesized by M. Dommaschk according to Venkataramani *et al.*[10] To obtain the *Z*-form of the Azo-$TPPF_{15}$, the sample solution was irradiated before and during the time-resolved transient absorption measurements using a light emitting diode with emission maximum at $\lambda = 495$ nm. The photostationary state (PSS495) contains $\approx$ 80% of *Z*-Azo-$NiTPPF_{15}$. All measurements were performed in cyclohexane (Sigma Aldrich, spectroscopic grade) as solvent in a flow cell with 0.2 mm fused silica windows and an optical pathlength of 1 mm. The concentrations of the different solutions and the resulting optical densities (OD) at the excitation wavelength of $\lambda_{pump} = 520$ nm are given in Table 7.1.

Table 7.1: Concentrations of the sample solutions and resulting optical densities at $\lambda_{pump} = 520$ nm.

	concentration	OD @ 520 nm
H_2TPPF$_{20}$	0.25 mM	0.02
NiTPPF$_{20}$	0.50 mM	0.06
***E*-Azo-NiTPPF$_{15}$**	0.30 mM	0.06
***Z*-Azo-NiTPPF$_{15}$**	$\approx$ 0.24 mM	0.02

The setup for the femtosecond time-resolved transient absorption measurements in our laboratory has been described previously.[50] The excitation pulses at $\lambda_{pump} = 520$ nm ($\leqslant$ 200 nJ per pulse) were delivered by a home-built non-collinear optical parametric amplifier (NOPA). Supercontinuum probe and reference pulses in the wavelength range of 320 nm $\leqslant \lambda_{probe} \leqslant$ 695 nm were generated in CaF_2. The pulses were focused into the sample cell and the angle between them was kept as small as possible. The transmitted probe and reference spectra were detected by two FFT-CCD cameras. All measurements were repeated three times to ensure reproducibility. The pump-induced cross-phase modulation (XPM) and the stimulated Raman scattering (SRS) were measured independently for the pure solvent. The experimental time resolution of the experiment was determined from the SRS signal and was of the order of $\Delta t \approx 40$ fs.

7.3.1 UV/VIS ABSORPTION SPECTRA

The normalized stationary UV/VIS absorption spectra of H_2TPPF_{20}, $NiTPPF_{20}$, *E*-Azo-$NiTPPF_{15}$ and *Z*-Azo-$NiTPPF_{15}$ are depicted in Fig. 7.4. As typical for porphyrins, all investigated systems feature a distinctive ab-

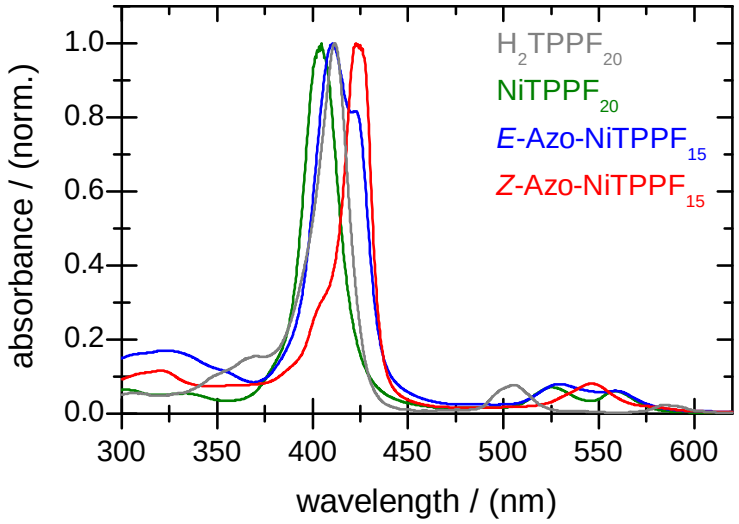

Figure 7.4: Static UV/VIS spectra H_2TPPF_{20} (gray), $NiTPPF_{20}$ (green), *E*-Azo-$NiTPPF_{15}$ (blue) and *Z*-Azo-$NiTPPF_{15}$ (PSS $\approx$ 80%) (red).

sorption band at $\lambda \approx 410$ nm, which is attributed to the $S_0 \rightarrow S_2$ transition (B or Soret band) and another one in the range of $\lambda = 500 - 600$ nm, which belongs to the transition from the S_0 to the S_1 state (Q_y and Q_x bands). The absorption spectra of *E*- and *Z*-Azo-$NiTPPF_{15}$ exhibit an additional band in the UV with maximum at $\lambda = 325$ nm, which is probably attributable to the $\pi\pi^*$ transition of the AB unit.

7.3.2 TIME-RESOLVED TRANSIENT ABSORPTION MEASUREMENTS

7.3.2.1 *H_2TPPF_{20}*

The two-dimensional spectro-temporal transient absorption maps of the metal free macrocycle H_2TPPF_{20} for delay times up to 10 ps and 1200 ps after excitation at $\lambda_{pump} = 520$ nm are given in Figs. 7.5 a and b), respectively. Immediately after the pump pulse, the negative ground state bleach (GSB) signals of the B, the Q_y and the Q_x absorption bands can be observed at $\lambda_{probe} \approx 370 - 385$ nm, $\lambda_{probe} \approx 510 - 540$ nm and $\lambda_{probe} \approx 575$ nm, respectively. Strong positive excited state absorption (ESA) bands appear at the same time in the detection wavelength ranges between $\lambda_{probe} \approx 420 - 500$

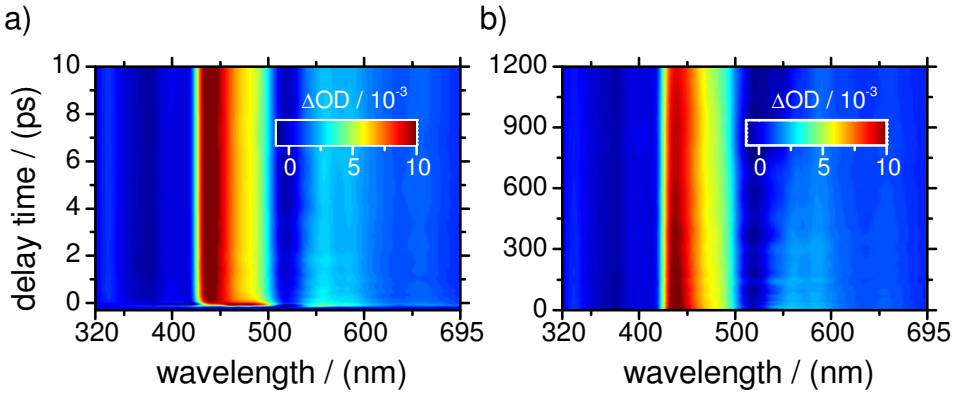

Figure 7.5: Two-dimensional transient absorption maps of H_2TPPF_{20} in cyclohexane as solvent after excitation at $\lambda_{pump} = 520$ nm in a probe wavelengths range of 320 nm $\leqslant \lambda_{probe} \leqslant$ 695 nm for delay times up to a) 10 ps and b) 1200 ps.

nm and above $\lambda_{probe} > 540$ nm. The GSB of Q_y appears to fluctuate both in intensity and width, which is caused by the overlap with the neighboring positive absorption bands. The small intensities of the bleach of Q_x are also related to the overlap with the surrounding ESA bands. In contrast, however, the B band bleach seems to remain nearly constant over the whole temporal detection range as well as the most pronounced ESA band around $\lambda_{probe} \approx 450$ nm. After an initial blue-shift of this intense ESA band and the B band GSB within the first 100 fs, all absorption bands remain virtually constant within the recorded time frame of 1.2 ns, except for a slight continuous decay and narrowing of the absorption bands.

7.3.2.2 *NiTPPF$_{20}$*

The spectro-temporal absorption maps recorded for the metal porphyrin $NiTPPF_{20}$ after excitation at $\lambda_{pump} = 520$ nm for delay times up to 10 ps and 1200 ps are shown in Figs. 7.6 a and b), respectively. At $\Delta t = 0$ several negative GSB and positive ESA absorption bands arise. The very early dynamics are dominated by a strong blue-shift of the ESA at $\lambda_{probe} \approx 420 - 520$ nm which narrows from a spectral width of $\approx$ 100 nm to a width of ≈ 30 nm ($\lambda_{probe} \approx 410 - 440$ nm) within the first $1 - 2$ ps. This absorption band decays slowly to nearly zero within the temporal detection range of 1.2 ns. Additional ESA bands decaying on the same time scale appear between $\lambda_{probe} \approx 340$ and 380 nm and $\lambda_{probe} \approx 445$ and 465 nm, respectively. A broad and much shorter lived ESA band can be observed above $\lambda_{probe} > 580$ nm, which overlaps with the GSB of the Q_x band at $\lambda_{probe} \approx 570 - 590$ nm. The bleach of the Q_y band can be observed at $\lambda_{probe} \approx 500 - 535$ nm and is overlapped by the intense ESA band at very early delay times. The B band GSB arises at $\lambda_{probe} \approx 380 - 410$ nm. The main changes occur within the first three ps and afterwards the dynamics reach a final level whereupon the population has reached the porphyrin ground-metal excited state (denoted as $|S_0, ^{1,3}(d, d)\rangle$). After 1.2 ns all elec-

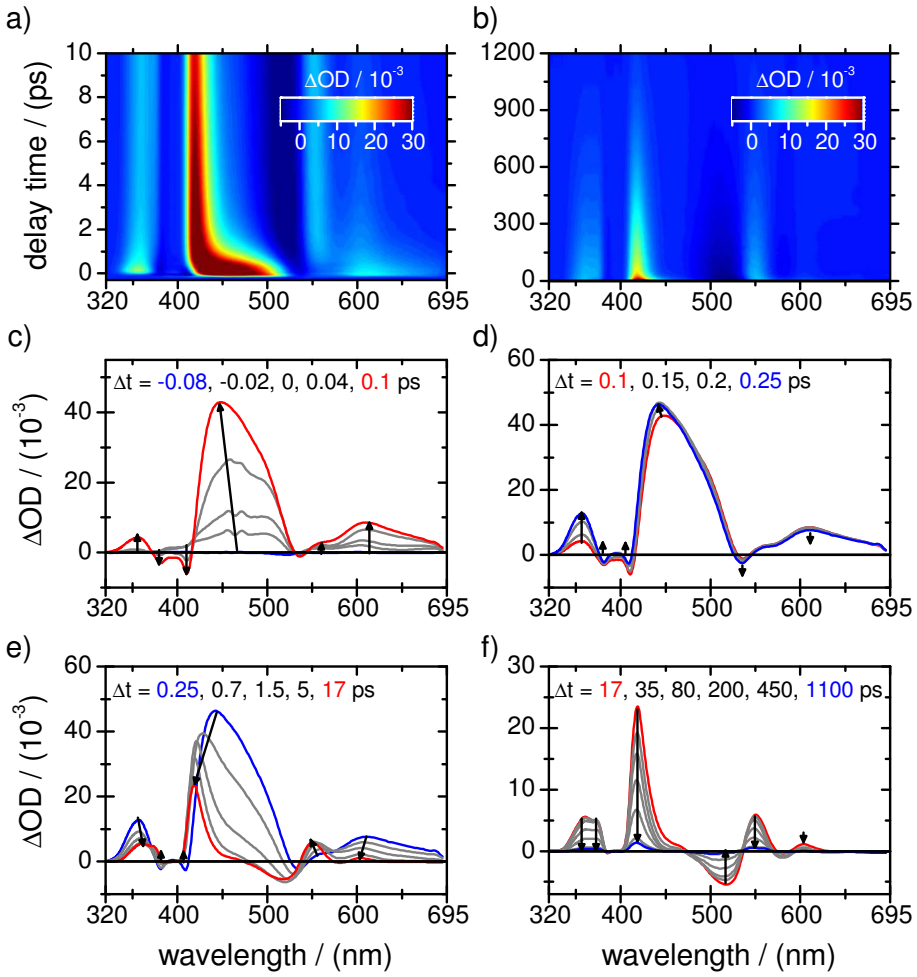

Figure 7.6: Two-dimensional transient absorption maps of $NiTPPF_{20}$ in cyclohexane as solvent after excitation at $\lambda_{pump} = 520$ nm in the probe wavelengths range 320 nm $\leqslant \lambda_{probe} \leqslant$ 695 nm for delay times up to a) 10 ps and b) 1200 ps and selected transient spectra of $NiTPPF_{20}$ at delay times between c) -0.08 ps $\leqslant \Delta t \leqslant 0.1$ ps, d) 0.1 ps $\leqslant \Delta t \leqslant 0.25$ ps, e) 0.25 ps $\leqslant \Delta t \leqslant 17$ ps and f) 17 ps $\leqslant \Delta t \leqslant 1100$ ps. The arrows indicate the temporal evolution of the spectra.

tronic and vibrational processes are completed and most of the ground state population is recovered. Nearly no final permanent absorption can be observed.

The transient absorption spectra of $NiTPPF_{20}$ for different delay times reveal the complex molecular dynamics in some more detail and are depicted in Figs. 7.6 c - f). Figure 7.6 c) shows the temporal evolution up to 100 fs. The dynamics up to 250 fs are shown in Fig. 7.6 d). The subsequent changes up to 17 ps and 1100 ps are shown in Figs. 7.6 e and f), respectively. The minimum of the GSB of the B band and the maximum of the positive absorption band above $\lambda_{probe} > 580$ nm are reached after $\approx$ 100 fs. At this time the GSB band appears divided into two bands which is probably caused by the overlap with positive contributions or by the ob-

servable splitting of the B_x and B_y bands in the planar macrocyclic plane of $NiTPPF_{20}$. The intense positive absorption band at $\lambda_{probe} \approx 420-520$ nm and the absorption band at $\lambda_{probe} \approx 340-380$ nm reach their maximum slightly delayed after $\approx$ 250 fs. The bleach signals of the Q bands are hardly visible due to the numerous overlapping bands. After $\approx$ 250 fs, the absorption at $\approx$ 430 nm shows a pronounced blue-shift and becomes much sharper, therefore the negative Q band GSB becomes more visible. In the same temporal window the absorption band at $\approx$ 360 nm shows a red-shift and seems to split into two separated bands. After a delay time of $\approx$ 17 ps no further shifting of the absorption bands can be observed. The spectra feature the two distinctive derivative-shaped band pairs each involving one of the Q band GSBs. At the maximum delay time of 1100 ps only very weak contributions can be observed.

Compared to H_2TPPF_{20}, $NiTPPF_{20}$ shows very different dynamics. While the band structure remains largely the same, the overall lifetime of $NiTPPF_{20}$ is considerably shorter and the dynamics appear more complex, showing pronounced shifts and changes in the shape of the absorption bands, whereas the absorption bands of H_2TPPF_{20} remained nearly constant over the 1.2 ns after an initial blue-shift within the first $\approx$ 100 fs.

7.3.2.3 *E-Azo-NiTPPF*$_{15}$

The 2D transient absorption maps up to delay times of 10 ps and 1200 ps and the respective transient absorption spectra at different delay times of *E*-Azo-$NiTPPF_{15}$ after Q band excitation at $\lambda_{pump} = 520$ nm are given in Figs. 7.7 a - f). The dynamics of *E*-Azo-$NiTPPF_{15}$ are very similar to those of $NiTPPF_{20}$, except for slight shifts of the absorption bands. The ESA at $\lambda_{probe} \approx 425-540$ nm shows a strong blue-shift and narrows from a spectral width of more than 100 nm to less than 40 nm ($\lambda_{probe} \approx 420-460$ nm) within the first $\approx$ 5 ps. The positive contribution at $\lambda_{probe} \approx 360$ nm partially overlaps with the GSB of the B band ($\lambda_{probe} \approx 390-425$ nm). Furthermore, a broad and less intense ESA band is present at $\lambda_{probe} > 570$ nm, showing a faster decay than the other ESA bands. The GSB of the Q bands $\lambda_{probe} \approx 520-575$ nm is only very weak in intensity due to the superposition with the positive absorption bands.

In the transient absorption spectra for delay times up to 100 fs and up to 250 fs in Figs. 7.7 c and d), respectively, it can be observed that the absorptions at $\approx$ 360 nm and at $\approx$ 475 nm rise slightly delayed compared to the GSB of the B band and the positive band at $\approx$ 625 nm which reach their maximum after $\approx$ 100 fs. The B band GSB shows two separated bands which are probably related to overlap with several positive bands or to splitting of the B_x and B_y bands in the planar macrocyclic plane. After $\approx$ 250 fs the ESA band at $\approx$ 475 nm shows a pronounced blue-shift and the shape of the band becomes very sharp. At the same time the absorption band in the UV at $\approx$ 360 nm begins red shifting to a maximum of $\approx$ 380 nm. Both the blue- and the red-shift are completed after $\approx$ 17 ps (cf. Fig. 7.7 e). During this time interval the ESA band at $\lambda_{probe} > 570$ nm decays nearly to zero resulting in the derivative-shaped band pair. This relatively

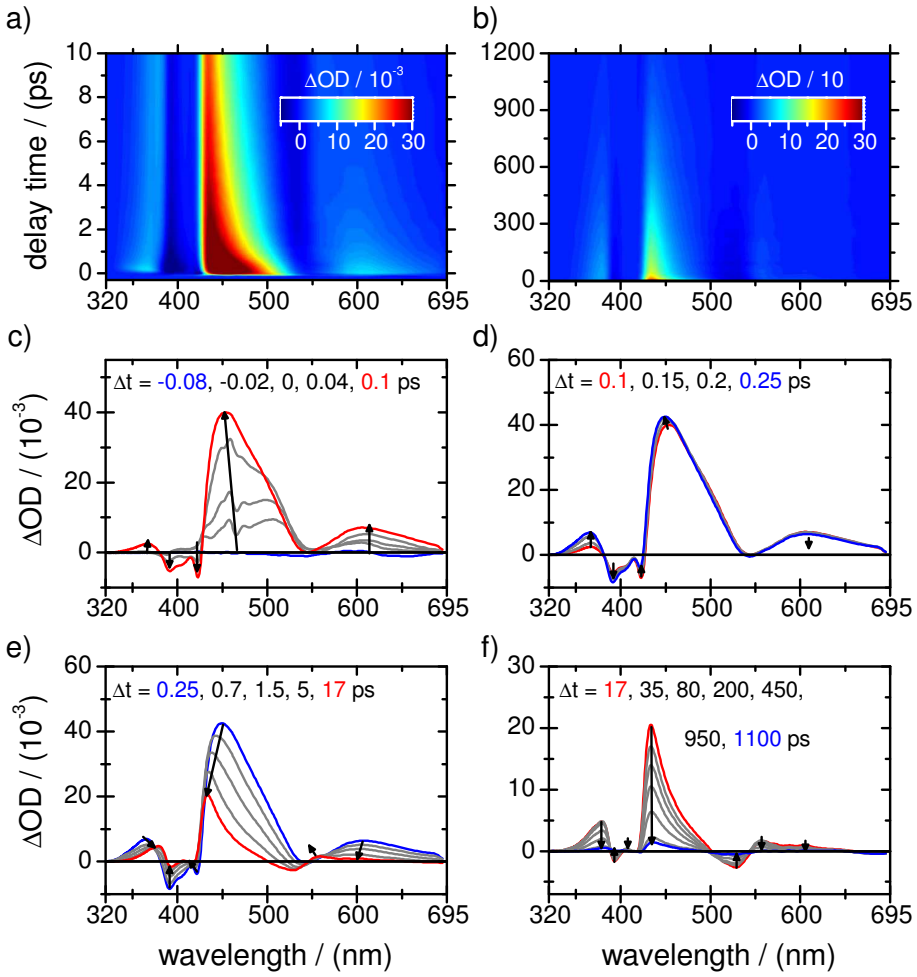

Figure 7.7: Two-dimensional transient absorption maps of *E*-Azo-NiTPPF$_{20}$ in cyclohexane as solvent after excitation at $\lambda_{pump} = 520$ nm in a probe wavelengths range of 320 nm $\leqslant \lambda_{probe} \leqslant$ 695 nm for delay times up to a) 10 ps and b) 1200 ps and selected transient spectra of NiTPPF$_{20}$ at delay times between c) -0.08 ps $\leqslant \Delta t \leqslant 0.1$ ps, d) 0.1 ps $\leqslant \Delta t \leqslant 0.25$ ps, e) 0.25 ps $\leqslant \Delta t \leqslant 17$ ps and f) 17 ps $\leqslant \Delta t \leqslant 1100$ ps. The arrows indicate the temporal evolution of the spectra.

broad unstructured band pair is caused by the overlapping Q_y and Q_x bands in the case of *E*-Azo-NiTPPF$_{15}$. After a delay time of $\approx$ 17 ps no shifts or changes in the structure of the absorption bands can be observed. After 1.1 ns the dynamics are virtually completed and the ground state is almost refilled.

7.3.2.4 *Z-Azo-NiTPPF$_{15}$*

The spectro-temporal absorption maps of the five-coordinate *Z*-Azo-NiTPPF$_{15}$ following excitation at $\lambda_{pump} = 520$ nm in a probe wavelengths range of 320 nm $\leqslant \lambda_{probe} \leqslant$ 695 nm for delay times up to 10 ps and 1200 ps are shown in Figs. 7.8 a and b). At first glance the dynamics appear very similar to those of NiTPPF$_{20}$ and *E*-Azo-NiTPPF$_{15}$. The very

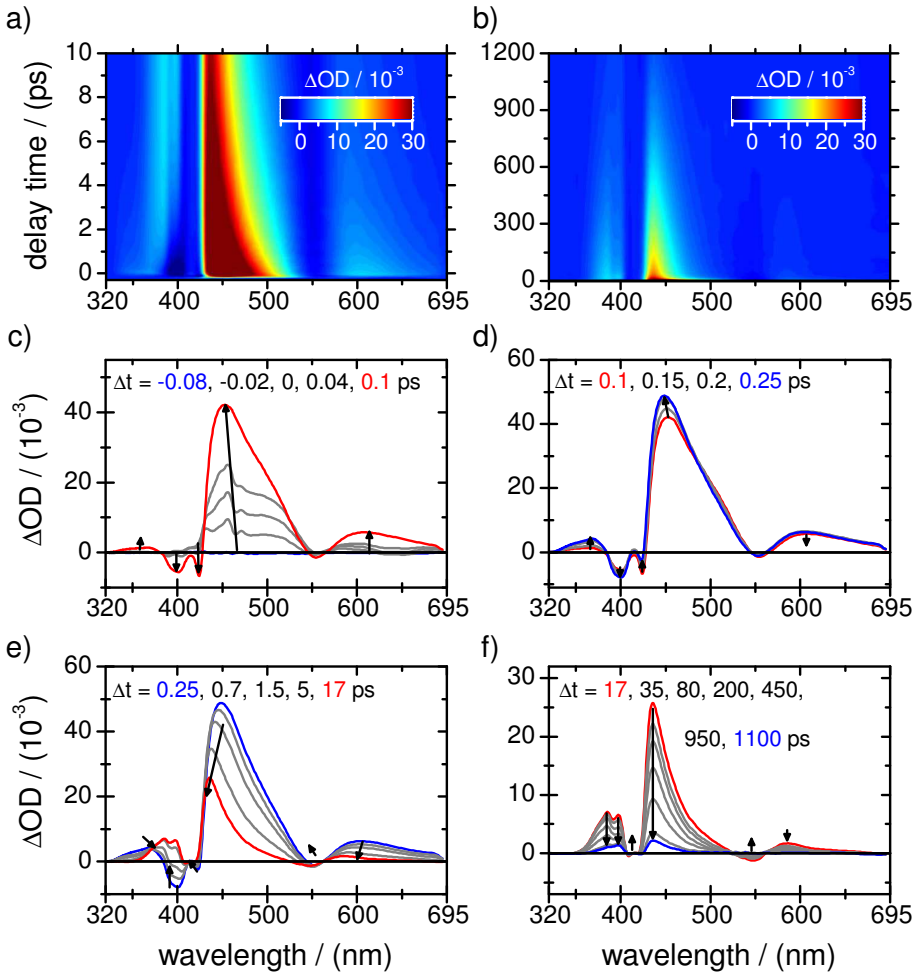

Figure 7.8: Two-dimensional transient absorption maps of *Z*-Azo-NiTPPF$_{20}$ (PSS $\approx$ 80%) in cyclohexane as solvent after excitation at $\lambda_{pump} = 520$ nm in a probe wavelengths range of 320 nm $\leqslant \lambda_{probe} \leqslant$ 695 nm for delay times up to a) 10 ps and b) 1200 ps and selected transient spectra of NiTPPF$_{20}$ at delay times between c) -0.08 ps $\leqslant \Delta t \leqslant$ 0.1 ps, d) 0.1 ps $\leqslant \Delta t \leqslant$ 0.25 ps, e) 0.25 ps $\leqslant \Delta t \leqslant$ 17 ps and f) 17 ps $\leqslant \Delta t \leqslant$ 1100 ps. The arrows indicate the temporal evolution of the spectra.

strong ESA band at $\lambda_{probe} \approx 425-540$ nm shows a strong blue-shift as well as a significant narrowing from a spectral width of $\approx$ 100 nm to $\approx$ 30 nm within less than 10 ps. The time scale for this process increases from $\approx$ 2 ps for NiTPPF$_{20}$ to $\approx$ 5 ps for *E*-Azo-NiTPPF$_{15}$ and finally to $\approx$ 10 ps for *Z*-Azo-NiTPPF$_{15}$. Another positive absorption band at $\lambda_{probe} \approx 340-400$ nm overlaps with the GSB of the B band ($\lambda_{probe} \approx 390-425$ nm). The ESA band at $\approx$ 600 nm shows less intensity and a faster decay compared to the other ESA bands. The GSB of the Q bands shows slight negative contributions at $\lambda_{probe} \approx 535-570$ nm but are mainly overlapped by several positive contributions.

The transient absorption spectra of *Z*-Azo-NiTPPF$_{15}$ for selected delay times are depicted in Figs. 7.8 c - f). The very early dynamics up to 100 fs

and 250 fs are reflected by the spectra shown in Figs. 7.8 c and d), respectively. The spectra reflecting the subsequent slower dynamics at longer delay times up to 17 ps and 1100 ps are depicted in Figs. 7.8 e and f), respectively. As for $NiTPPF_{20}$ and *E*-Azo-$NiTPPF_{15}$, the bleach signals of the B and the Q bands and the ESA $\lambda_{probe} > 570$ nm reach their maximum within $\approx$ 100 fs. The ESA bands at $\approx$ 460 nm is fully developed after $\approx$ 250 fs. Due to the overlap between the GSB of the B band and the positive absorption at $\approx$ 350 nm it is hard to say whether this band rises within 100 fs or also slightly delayed within 250 fs. Subsequently, the band at $\approx$ 460 nm shifts to the blue and becomes spectrally narrower, whereas the band at $\approx$ 350 nm moves to the red and splits into two bands. The derivative-shape of the transient spectra in the Q band region at $\lambda_{probe} \approx 525 - 625$ nm can be clearly observed in Fig. 7.8 f). At the maximum delay time at 1100 ps only a weak absorption can be observed.

7.4 DISCUSSION

The ultrafast photo-induced dynamics of the bistable molecular spin switch Azo-$TPPF_{15}$ in the *E*- and the *Z*-form, and the metal free porphyrin H_2TPPF_{20} and the Ni porphyrin $NiTPPF_{20}$ as the building blocks of the azopyrindine functionalized system have been investigated systematically by means of femtosecond time-resolved transient absorption spectroscopy after Q band excitation. The results of the AB-functionalized Ni complex will be discussed on the basis of the results for the Ni porphyrin and the metal free macrocycle. At first the differences in the UV/VIS absorption spectra will be explained.

7.4.1 UV/VIS ABSORPTION SPECTRA

The differences in the absorption spectra of the metal free porphyrin and the metal porphyrin can be explained by the absence of the Ni(II) ion in H_2TPPF_{20}.[18] In $NiTPPF_{20}$ the $e_g(\pi^*)$ LUMOs are higher in energy due to the interactions of the $a_{1u}(\pi)$ HOMOs with the d orbitals of the Ni(II) ion. Therefore the B band of the metal complex shows a blue-shift compared to the metal free system. The well separated Q bands in the spectrum of H_2TPPF_{20} are attributed to the comparatively low symmetry of the macrocyclic framework. In the case of the four-coordinate Ni(II)-porphyrin the Q_y and Q_x bands are much closer together due to a lower effective symmetry but still separated due to the saddled conformation of the porphyrin ring. Only the five-coordinated *Z*-isomer of Azo-$TPPF_{15}$ shows a single Q band because the macrocycle is nearly planar due to the interactions with the occupied $d_{x^2-y^2}$ orbital of the Ni(II) ion with the p orbitals of the porphyrin. In accordance with the four orbital model, the absorption bands of the five-coordinate *Z*-Azo-$NiTPPF_{15}$ are red-shifted compared to these of *E*-Azo-$NiTPPF_{15}$ and $NiTPPF_{20}$.[14] The shoulders in the red part of the B band of *E*-Azo-$NiTPPF_{15}$ as well as in the blue wing of the B band of *Z*-Azo-$NiTPPF_{15}$ cannot easily be explained by the

four orbital model[18] and are probably related to the broken symmetry in the porphyrin macrocycle after the substitution of the fluorinated phenyl ring by the azo-moiety.

7.4.2 ULTRAFAST DYNAMICS OF H_2TPPF_{20}

The observed dynamics of the metal free porphyrin H_2TPPF_{20} take place on an extremely long time scale. During the entire temporal detection range nearly no changes can be observed, except for the very early delay times up to 200 fs, where a blue-shift of the positive transient absorption bands can be observed. This behavior is typical for non-metallated derivatives of this compound.[32] After excitation to the Q_y state ($S_1(\pi\pi^*)$) at $\lambda_{pump} = 520$ nm an internal conversion to the vibrational excited states of the Q_x state occurs within tens of femtoseconds.[23,29,32,44,48] The resolution of this process is therefore instrument limited but visible in the 2D transient absorption map in Fig 7.5 a). Afterwards, vibrational relaxation in the electronic state occurs typically within several picoseconds.[29,32] The subsequent intersystem crossing to a lower lying triplet state is eventually followed by the recovery of the electronic ground state. These processes take place on the nanosecond time scale due to the spin-forbidden nature of the transitions.[32] The overall dynamics of the metal free system can be summarized as follows:

$$\begin{aligned} S_0 \xrightarrow{h\nu} S_1(\pi\pi^*)/Q_y \xrightarrow{IC/<IRF} Q_{x,hot} \\ \xrightarrow{VR/\sim ps} Q_x \xrightarrow{ISC/\sim ns} T_1 \xrightarrow{ISC/\sim ns} S_0. \end{aligned} \tag{5}$$

7.4.3 ULTRAFAST DYNAMICS OF $NiTPPF_{20}$

The observed dynamics of $NiTPPF_{20}$ are quite different from these of H_2TPPF_{20}, which can be easily explained by the existence of metal-centered (d,d)-excited states of the Ni(II) ion.[11,23,24,35,39] The initial population of the $S_1(\pi\pi^*)$ of the macrocycle is probably followed by an ultrafast radiationless transition into a state involving singlet or / and triplet (d,d) excited states in the metal manifold and the electronic ground state of the porphyrin.[34] However, Musewald *et al.* assume that the porphyrin remains still in the excited state after part of the excitation energy is transferred to the metal ion.[21] The involvement of triplet states of the porphyrin itself is also discussed up to now.[14,21,34] Nevertheless, it has been virtually proven that after excitation to the Q band definitely a (d,d)-excited state is reached in less than 1 ps.[11,14,23–27,31,34–36,38–40,45,46] The lifetime of the initially excited $Q_y(\pi\pi^*)$ state was also found to be shorter than the time-resolution of the used absorption and fluorescence experiments.[21,47] The first detectable state was then probably a combination of the porphyrin and (d,d) metal states. The first metal excited state in these experiments is given by the transient spectrum after 250 fs (cf. Fig. 7.6 d). Due to the good time-resolution of ≈ 40 fs of our setup the transient spectra up to 250

fs (cf. Fig. 7.6 c) probably also reflect the initially excited $\pi\pi^*$ state of the macrocycle. The subsequent blue-shift of the positive contributions can be assigned to the vibrational relaxation of excited metal states and probably also to the vibrational relaxation of the porphyrin in its electronic ground state leading to a $|S_0, {}^{1,3}(d,d)\rangle$ state on a time scale of ≈ 5 ps. Vibrational relaxation of the metal states has also been observed by other groups but often on a slightly longer time scale of tens of picoseconds.[23,24,34,39,49] The spectra after a delay time of 17 ps (cf. Fig. 7.6 f) belong to the electronic ground state of the macrocycle and excited state of the metal moiety, respectively. Since the metal ion remains in an excited state on a time scale of hundreds of picoseconds longer than the porphyrin, the subsequent interaction between the two manifolds of states leads to a red-shift of the observed ground state absorption and the typical derivative shape which can be observed particularly in the Q band region.[14,24,26,34,35] The overall ground state recovery eventually takes place within hundreds of picoseconds. The relaxation after $\pi\pi^*$ excitation of the macrocycle *via* the metal (d,d) states can be summarized as follows:

$$\begin{aligned} |S_0, (d_{z^2})^2\rangle &\xrightarrow{h\nu} |S_1, (d_{z^2})^2\rangle \xrightarrow{IC/ISC \ll 1ps} \\ |S_0, {}^{1,3}(d_{z^2}, d_{x^2-y^2})\rangle_{hot} &\xrightarrow{VR/\sim 5ps} \\ |S_0, {}^{1,3}(d_{z^2}, d_{x^2-y^2})\rangle &\xrightarrow{GSR/\sim 100ps} |S_0, (d_{z^2})^2\rangle. \end{aligned} \tag{6}$$

7.4.4 ULTRAFAST DYNAMICS OF E-AZO-NiTPPF$_{15}$

A comparison of the results for NiTPPF$_{20}$ and *E*-Azo-NiTPPF$_{15}$ reveals virtually identical dynamics for both systems, except for slight shifts of the GSB of the Q and B absorption bands. Therefore an identical relaxation pathway after excitation at $\lambda_{pump} = 520$ nm is suggested for both cases:

$$\begin{aligned} |S_0, (d_{z^2})^2\rangle &\xrightarrow{h\nu} |S_1, (d_{z^2})^2\rangle \xrightarrow{IC/ISC \ll 1ps} \\ |S_0, {}^{1,3}(d_{z^2}, d_{x^2-y^2})\rangle_{hot} &\xrightarrow{VR/\sim 5ps} \\ |S_0, {}^{1,3}(d_{z^2}, d_{x^2-y^2})\rangle &\xrightarrow{GSR/\sim 100ps} |S_0, (d_{z^2})^2\rangle. \end{aligned} \tag{7}$$

Regarding the very complex dynamics of the Ni complex itself with broad, intense and overlapping absorption bands over the entire spectral detection range, it is difficult to find and analyze possible contributions from the AB moiety, which would indicate a switching process of the AB and therefore the spin of the Ni(II) ion from low- to high-spin. The potential product absorption band of the AB and its derivatives, which would appear in the UV ($\lambda_{probe} = 320 - 400$ nm) is probably superimposed by the porphyrin signal. Typically the transient absorption signals of AB and its derivatives are very low in intensity and show a much shorter lifetime compared to the porphyrin derivatives.[16,51–56] Another indicator for spin switching could be found in the derivative shaped absorption bands in the transient spectra for very long delay times (cf. Fig. 7.7 f). Since the

porphyrin macrocycle is back in the electronic ground state and the metal remains excited, a pronounced red shifted ground state absorption can be observed whose specific shape could give evidence concerning the amount of the present isomers. A comparison of the shape of the derivative-shaped bands in the Q band region of the transient spectra with the shape of the static spectrum shows that no considerable spin switching has taken place. Previous investigations have shown that the coordination strongly depends on the ligand[27,34] and in the case of *E*-Azo-NiTPPF$_{15}$ two conditions must be fulfilled. First the excitation must lead to the isomerization of the azo moiety and second the azo moiety must be oriented correctly with the coordinating nitrogen very close to the Ni(II) ion. Due to the rotational motion of the AB unit there is a small number of possible orientations that would lead to a coordination upon *E*-*Z* isomerization of the AB. Another reason why the spin switch does not occur could be that at least a two-photon absorption is necessary and not only the absorption of a single-photon.

7.4.5 ULTRAFAST DYNAMICS OF Z-AZO-NiTPPF$_{15}$

Z-Azo-NiTPPF$_{15}$ differs from the previous compounds NiTPPF$_{20}$ and *E*-Azo-NiTPPF$_{15}$ due to its paramagnetic triplet electronic ground state of the five-coordinate metal ion with both the d_{z^2} as well as the $d_{x^2-y^2}$ orbitals being singly occupied. Nevertheless, the data for the *Z*-form are very similar to the *E*-isomer and the Ni complex. The relaxation after excitation in the Q_y absorption band can be summarized in the following scheme, which is discussed in the literature for the photo-induced decoordination of the respective ligands *via* a $(d_{z^2})^*$ metal excited state, which should be an unfavorable electronic configuration for axial ligands:[11,14,34]

$$\begin{aligned} |S_0,{}^3(d_{z^2}, d_{x^2-y^2})\rangle &\xrightarrow{h\nu} |S_1,{}^3(d_{z^2}, d_{x^2-y^2})\rangle \\ &\xrightarrow{IC/ISC \ll 1ps} |T_1,{}^3(d_{z^2}, d_{x^2-y^2})\rangle \\ &\xrightarrow{ISC/\sim 5ps} |S_0,{}^1((d_{z^2})^2)^*\rangle \\ &\xrightarrow{GSR/\sim 100ps} |S_0,{}^3(d_{z^2}, d_{x^2-y^2})\rangle \end{aligned} \tag{8}$$

The ultrafast internal conversion and / or intersystem crossing probably lead to a triplet $\pi\pi^*$ state of the porphyrin macrocycle with the d system of the metal remaining in the same ${}^3(d_{z^2}, d_{x^2-y^2})$ configuration. Within $\approx$ 5 ps the system reaches the doubly excited $(d_{z^2})^*$ state of the metal ion and the electronic ground state of the porphyrin. Afterwards the excited metal state return to the electronic ground state on a comparatively long time scale.[34] Despite these changes the dynamics are essentially the same as for *E*-Azo-NiTPPF$_{15}$ and also no specific switching dynamics can be observed. The derivative-shaped transient absorption bands (cf. Fig. 7.8 f) in the spectral range of the Q bands correlate well with the static absorption spectrum. No shoulders at either the blue or the red wing of the Q

bands appear which would indicate the formation of the *E*-isomer. The obtained results give no evidence for a possible switching of the AB or the spin state of the Ni(II) ion.

7.5 CONCLUSION

In conclusion we have presented a systematic study on the photo-induced ultrafast dynamics of the bistable Ni porphyrin based molecular spin switch Azo-NiTPPF$_{15}$ in the four-coordinate *E*-form (low-spin) and the five-coordinate *Z*-form and its respective building blocks, the Ni porphyrin NiTPPF$_{20}$ and the metal free porphyrin H$_2$TPPF$_{20}$, after Q band excitation by means of femtosecond time-resolved transient absorption spectroscopy. The interpretations of the results for the Ni(II)-complex and the metal free system could have been developed based on previous studies because of the close similarity. In the case of H$_2$TPPF$_{20}$ the excitation leads to the population of the $S_1(\pi\pi^*)$ / Q_y state of the macrocycle. Afterwards the system reaches vibrationally excited states of the Q_x state within a few tens of femtoseconds. The subsequent vibrational relaxation within this state is followed by two intersystem crossing transitions on the nanosecond time scale, first to a triplet state and then to the electronic ground state. The incorporation of the Ni(II) ion into the porphyrin leads to a combination of states of the macrocyclic π system and the d system of the metal moiety. The results for the four-coordinate derivatives NiTPPF$_{20}$ and *E*-Azo-NiTPPF$_{15}$ are virtually identical. Starting with the π and the d system in the respective ground states, excitation at $\lambda_{pump} = 520$ nm only affects the porphyrin ring, leaving the d system in its ground state. Ultrafast relaxation *via* IC/ISC transfers the excitation energy (partly) into the metal d electron system, resulting in a vibrationally hot excited state $|S_0, {}^{1,3}(d, d)\rangle_{hot}$ with the porphyrin back in its ground state. This configuration should be attractive towards axial ligands. Vibrational relaxation within $\approx 2-5$ ps leads to the formation of the vibrational ground states within the electronically excited Ni(II) states. This semi-excited state shows the typical derivative-shaped absorption bands and decays on a time scale of hundreds of picoseconds. The relaxation dynamics of the five-coordinate *Z*-Azo-NiTPPF$_{15}$ are very similar to those of the four-coordinate systems. However, the involved states are different. The electronic ground state is a triplet state and the deactivation occurs *via* a $(d_{z^2})^*$ state. Furthermore, a triplet state of the porphyrin is probably involved. The $(d_{z^2})^*$ state should actually be repulsive towards axial ligands.

Nevertheless, the principle aim of this work was the investigation of the switching dynamics of *E*- and *Z*-Azo-NiTPPF$_{15}$. The analysis of the obtained results especially regarding a possible switching process turned out to be difficult for several reasons. First of all the involvement of the porphyrin macrocylce leads to very complex dynamics and very broad, intense and superimposed absorption bands in the transient spectra over

the whole spectral detection range, which makes it impossible to follow the switching process.

Regarding these results it may be that it takes long-term irradiation or multi-photon absorption to reach any photoswitching or the photochemical equilibrium, while single-photon absorption experiments are not able to induce a significant population to the spin switch. Recent qualitative theoretical studies using ab initio methods suggest that Q band excitation does not lead to excited states involving the AB unit or AB character, thus concluding that in order to achieve a spin switch, vibrational excess energy has to be redistributed at the right point, making it an extremely rare event.[13]

Towards these ends, a systematic study of the four different molecules after excitation of the supposed $\pi\pi^*$ absorption band of the azobenzene at $\lambda_{pump} = 320$ nm yielded almost identical results and the entire spectral range was governed by the dynamics of the porphyrin macrocycle. Measurements after excitation to the B band are currently in progress in our laboratory. In this case the ground state bleach signals and the recovery of the ground states of *E*- and *Z*-Azo-NiTPPF$_{15}$ can probably be distinguished, allowing for a more detailed look at the switching dynamics.

ACKNOWLEDGMENTS

The support of this work by the Deutsche Forschungsgemeinschaft through the Sonderforschungsbereich 677 "Function by Switching" is gratefully acknowledged.

BIBLIOGRAPHY

[1] Kumble, R.; Palese, S.; Lin, V. S.-Y.; Therien, M. J.; Hochstrasser, R. M. *J. Am. Chem. Soc.* **1998**, *120*, 11489–11498.

[2] Nakano, A.; Osuka, A.; Yamazaki, T.; Nishimura, Y.; Akimoto, S.; Yamazaki, I.; Itaya, A.; Murakami, M.; Miyasaka, H. *Chem. Eur. J.* **2001**, *14*, 3134–3151.

[3] Song, N. W.; Cho, H. S.; Yoon, M.-C.; Jeoung, S. C.; Yoshida, N.; Osuka, A.; Kim, D. *Bull. Chem. Soc. Jpn.* **2002**, *75*, 1023–1029.

[4] Holten, D.; Bocian, D.; Lindsey, J. S. *Acc. Chem. Res.* **2002**, *35*, 57–69.

[5] Lee, T. H.; Gonzalez, J. I. .; Zheng, J.; Dickson, R. M. *Acc. Chem. Res.* **2005**, *38*, 534–541.

[6] Szacilowski, K.; Macyk, W.; Drzewiecka-Matuszek, A.; Brindell, M.; Stochel, G. *Chem. Rev.* **2005**, *105*, 2647–2694.

[7] Burdzinski, G.; Kubicki, J.; Maciejewski, A.; Steer, R.; Velate, S.; Yeow, E. In *Organic Photochemistry and Photophysics, Photochemistry and Photophysics of Highly Excited Valence States of Polyatomic Molecules: Nonalternant Aromatics, Thioketones, and Metalloporphyrins*; Ramamurthy, V., Schanze, K., Eds.; CRC Press Taylor & Francis Group, Boca Raton, Florida, 2006.

[8] Kadish, K., Smith, K., Guilard, R., Eds. *Handbook of Porphyrin Science (Volumes 1 -5)*; World Scientific, 2010.

[9] Kullmann, M.; Hipke, A.; Nuernberger, P.; Bruhn, T.; Götz, D. C. G.; Sekita, M.; Guldi, D. M.; Bringmann, G.; Brixner, T. *Phys. Chem. Chem. Phys.* **2012**, *14*, 8038–8050.

[10] Venkataramani, S.; Jana, U.; Dommaschk, M.; Sönnichsen, F.; Tuczek, F.; Herges, R. *Science* **2011**, *331*, 445–448.

[11] Kim, D.; Kirmaier, C.; Holten, D. *Chem. Phys.* **1983**, *75*, 305–322.

[12] Ake, R. L.; Gouterman, M. *Theoret. chim. Acta* **1970**, *17*, 408–416.

[13] Schönborn, J. B. Dynamics of photoinduced switching processes. Ph.D. Thesis, CAU Kiel, 2012.

[14] Rodriguez, J.; Holten, D. *J. Chem. Phys.* **1990**, *92*, 5944–5950.

[15] Siewertsen, R.; Neumann, H.; Buchheim-Stehn, B.; Herges, R.; Näther, C.; Renth, F.; Temps, F. *J. Am. Chem. Soc.* **2009**, *131*, 15594–15595.

[16] Siewertsen, R.; Schönborn, J. B.; Hartke, B.; Renth, F.; Temps, F. *Phys. Chem. Chem. Phys.* **2011**, *13*, 1054–1063.

[17] Bahrenburg, J.; Sievers, C. M.; Schönborn, J. B.; Hartke, B.; Renth, F.; Temps, F.; Näther, C.; Sönnichsen, F. D. *Photochem. Photobiol. Sci.* **2013**, *12*, 511–518.

[18] Gouterman, M. *J. Mol. Spectrosc.* **1961**, *6*, 138–163.

[19] Shelnutt, J.; Ortiz, V. *J. Phys. Chem.* **1985**, *89*, 4733–4739.

[20] Gouterman, M. *J. Chem. Phys.* **1959**, *30*, 1139–1161.

[21] Musewald, C.; Hartwich, G.; Lossau, H.; Gilch, P.; Pöllinger-Dammer, F.; Scheer, H.; Michel-Beyerle, M. E. *J. Phys. Chem. B* **1999**, *103*, 7055–7060.

[22] Nemykin, V. N.; Hadt, R. G. *J. Phys. Chem. A* **2010**, *114*, 12062–12066.

[23] Rodriguez, J.; Holten, D. *J. Chem. Phys.* **1989**, *91*, 3525–3531.

[24] Drain, C. M.; Kirmaier, C.; Medforth, C. J.; Nurco, D. J.; Smith, K. M.; Holten, D. *J. Phys. Chem.* **1996**, *100*, 11984–11993.

[25] Eom, H. S.; Jeoung, S. C.; Kim, D.; Ha, J.-H.; Kim, Y.-R. *J. Phys. Chem.* **1997**, *101*, 3661–3669.

[26] Drain, C. M.; Gentemann, S.; Roberts, J. A.; Nelson, N. Y.; Medforth, C. J.; Jia, S.; Simpson, M. C.; Smith, K. M.; Fajer, J.; Shelnutt, J. A.; Holten, D. *J. Am. Chem. Soc.* **1998**, *120*, 3781–3791.

[27] Uesugi, Y.; Mizutani, Y.; Kitagawa, T. *J. Phys. Chem. A* **1998**, *102*, 5809–5815.

[28] Gurzadyan, G. G.; Tran-Thi, T.-H.; Gustavsson, T. *J. Chem. Phys.* **1998**, *108*, 385–388.

[29] Akimoto, S.; Yamazaki, T.; Yamazaki, I.; Osuka, A. *Chem. Phys. Lett.* **1999**, *309*, 177–182.

[30] Mataga, N.; Shibata, Y.; Chosrowjan, H.; Yoshida, N.; Osuka, A. *J. Phys. Chem. B* **2000**, *104*, 4001–4004.

[31] Jeong, D. H.; Kim, D.; Cho, D. W.; Jeoung, S. C. *J. Raman Spectrosc.* **2001**, *32*, 487–493.

[32] Spencer Baskin, J.; Yu, H.; Zewail, A. H. *J. Phys. Chem. A* **2002**, *106*, 9837–9844.

[33] Enescu, M.; Steenkeste, K.; Tfibel, F.; Fontaine-Aupart, M.-P. *Phys. Chem. Chem. Phys.* **2002**, *4*, 6092–6099.

[34] Retsek, J. L.; Drain, C. M.; Kirmaier, C.; Nurco, D. J.; Medforth, C. J.; Smith, K. M.; Sazanovich, I. V.; Chirvony, V. S.; Fajer, J.; Holten, D. *J. Am. Chem. Soc.* **2003**, *125*, 9787–9800.

[35] Zamyatin, A. V.; Gusev, A. V.; Rodgers, M. A. J. *J. Am. Chem. Soc.* **2004**, *126*, 15934–15935.

[36] Rosa, A.; Ricciardi, G.; Baerends, E. J.; Zimin, M.; Rodgers, M. A. J.; Matsumoto, S.; Ono, N. *Inorg. Chem.* **2005**, *44*, 6609–6622.

[37] Gil, M.; Organero, J.; Waluk, J.; Douhal, A. *Chem. Phys. Lett.* **2006**, *422*, 142–146.

[38] Sorgues, S.; Poisson, L.; Raffael, K.; Krim, L.; Soep, B. *J. Chem. Phys.* **2006**, *124*, 114302.

[39] Zhang, X.; Wasinger, E. C.; Muresan, A. Z.; Attenkofer, K.; Jennings, G.; Lindsey, J. S.; Chen, L. X. *J. Phys. Chem. A* **2007**, *111*, 11736–11742.

[40] Chen, L. X.; Zhang, X.; Wasinger, E. C.; Attenkofer, K.; Jennings, G.; Muresan, A. Z.; Lindsey, J. S. *J. Am. Chem. Soc.* **2007**, *129*, 9616–9618.

[41] Lukaszewicz, A.; Karolczak, J.; Kowalska, D.; Maciejewski, A.; Ziolek, M.; Steer, R. P. *Chem. Phys.* **2007**, *331*, 359–372.

[42] Tripathy, U.; Kowalska, D.; Liu, X.; Velate, S.; Steer, R. P. *J. Phys. Chem. A* **2008**, *112*, 5824–5833.

[43] Liu, X.; Tripathy, U.; Bhosale, S. V.; Langford, S. J.; Steer, R. P. *J. Phys. Chem. A* **2008**, *112*, 8986–8998.

[44] Yeon, K. Y.; Jeong, D.; Kim, S. K. *Chem. Commun.* **2010**, *46*, 5572–5574.

[45] Chen, L. X.; Zhang, X.; Wasinger, E. C.; Lockard, J. V.; Stickrath, A. B.; Mara, M. W.; Attenkofer, K.; Jennings, G.; Smolentsev, G.; Soldatov, A. *Chem. Sci.* **2010**, *1*, 642–650.

[46] Chen, L. X.; Zhang, X.; Lockard, J. V.; Stickrath, A. B.; Attenkofer, K.; Jennings, G.; Liu, D.-J. *Acta Cryst.* **2010**, *A66*, 240–251.

[47] Pilch, M.; Dudkowiak, A.; Jurzyk, B.; Łukasiewicz, J.; Susz, A.; Stochel, G.; Fiedor, L. *Biochim. Biophys. Acta* **2013**, *1827*, 30–37.

[48] Retsek, J. L.; Gentemann, S.; Medforth, C. J.; Smith, K. M.; Chirvony, V. S.; Fajer, J.; Holten, D. *J. Phys. Chem. B* **2000**, *104*, 6690–6693.

[49] Yu, H.-Z.; Baskin, J. S.; Zewail, A. H. *J. Phys. Chem. A* **2002**, *106*, 9845–9854.

[50] Röttger, K.; Siewertsen, R.; Temps, F. *Chem. Phys. Lett.* **2012**, *536*, 140–146.

[51] Lednev, I. K.; Ye, T.-Q.; Hester, R. E.; Moore, J. N. *J. Phys. Chem.* **1996**, *100*, 13338–13341.

[52] Nägele, T.; Hoche, R.; Zinth, W.; Wachtveitl, J. *Chem. Phys. Lett.* **1997**, *272*, 489–495.

[53] Lednev, I. K.; Ye, T.-Q.; Matousek, P.; Towrie, M.; Foggi, P.; Neuwahl, F. V. R.; Umapathy, S.; Hester, R. E.; Moore, J. N. *Chem. Phys. Lett.* **1998**, *290*, 68–74.

[54] Hirose, Y.; Yui, H.; Sawada, T. *J. Phys. Chem. A* **2002**, *106*, 3067–3071.

[55] Satzger, H.; Root, C.; Braun, M. *J. Phys. Chem. A* **2004**, *108*, 6265–6271.

[56] Bahrenburg, J.; Röttger, K.; Siewertsen, R.; Renth, F.; Temps, F. *Photochem. Photobiol. Sci.* **2012**, *11*, 1210–1219.

8

ULTRAFAST DYNAMICS OF A BISTABLE INTRAMOLECULAR PROTON TRANSFER SWITCH

Julia Bahrenburg,[a] Michał F. Rode,[b] Andrzej L. Sobolewski,[b] and Friedrich Temps[a]*

[a] Institute of Physical Chemistry, Christian-Albrechts-University Kiel, Olshausenstr. 40, D-24098 Kiel, Germany

[b] Institute of Physics, Polish Academy of Science, al. Lotników 32/46, 02-668 Warsaw, Poland

J. Bahrenburg, M. F. Rode, A. L. Sobolewski and F. Temps *Ultrafast Phenomena XIX*, **2014**.

OWN CONTRIBUTIONS TO THIS MANUSCRIPT:

- Synthesis and characterization of the molecule
- Time-resolved fluorescence and transient absorption spectroscopy
- Static absorption spectroscopy
- Analysis of the data
- Writing of the manuscript

* To whom correspondence should be addressed. E-mail: temps@phc.uni-kiel.de

ABSTRACT

The stepwise formation of the proton transfer product of a bistable molecular switch was unambiguously revealed by femtosecond fluorescence and absorption spectroscopy. The interpretation was supported by ab initio excited-state calculations.

8.1 INTRODUCTION

Excited-state intramolecular proton transfer (ESIPT) reactions belong to the fastest chemical reactions known[1]. Moreover, many molecules showing proton transfer after UV excitation exhibit record photostabilities. ESIPT molecules thus offer huge advantages in numerous fields, e.g. as photostabilizers in sunscreens for protection against solar UV light[2] or for the development of novel photochromic molecular switches[3].

Here, we report on the stepwise ultrafast formation of the proton transfer product of the bistable ESIPT switch N-(3-pyridinyl)-2-pyridinecarboxamide (NPPCA, Fig. 1) by femtosecond fluorescence and absorption spectroscopy. The experimental results are complemented by ab initio excited-

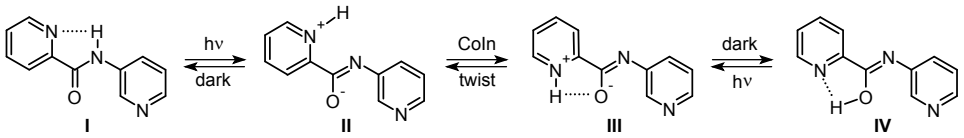

Figure 8.1: Molecular structures and reaction scheme of the ESIPT switch NPPCA after UV excitation.

state calculations at the MP2/cc-pVDZ, CC2/cc-pVDZ and ADC(2)/cc-pVDZ levels of theory.

8.2 RESULTS AND DISCUSSION

Measured fluorescence–time profiles, the two–dimensional (2D) transient absorption map and the transient absorption–time profiles at selected wavelengths after excitation of NPPCA in acetonitrile at $\lambda = 264$ nm are given in Figs. 2 a–e. The analysis of the fluorescence decay curves yielded lifetimes of $\tau_{fl,1} < 200$ fs as upper limit and $\tau_{fl,2} = 500 \pm 100$ fs mainly at longer emission wavelengths. The transient absorption map exhibits stimulated emission at $\lambda = 320 - 350$ nm and $450 - 550$ nm with lifetimes $\tau_1 = 100 \pm 10$ fs and $\tau_2 = 500 \pm 10$ fs, respectively, which correlate well with the fluorescence times. Additionally, we observe pronounced excited-state absorption (ESA) bands around $\lambda \approx 340$, 470 and 730 nm which feature a main decay time of $\tau_3 = 20 \pm 1$ ps next to the ultrashort τ_1 and τ_2 components.

The experimental data determined by a global analysis were assigned to sequential dynamical transformations of the photo-induced molecules as illustrated in Fig. 2f. Accordingly, the ≈ 100 fs component is the lifetime of

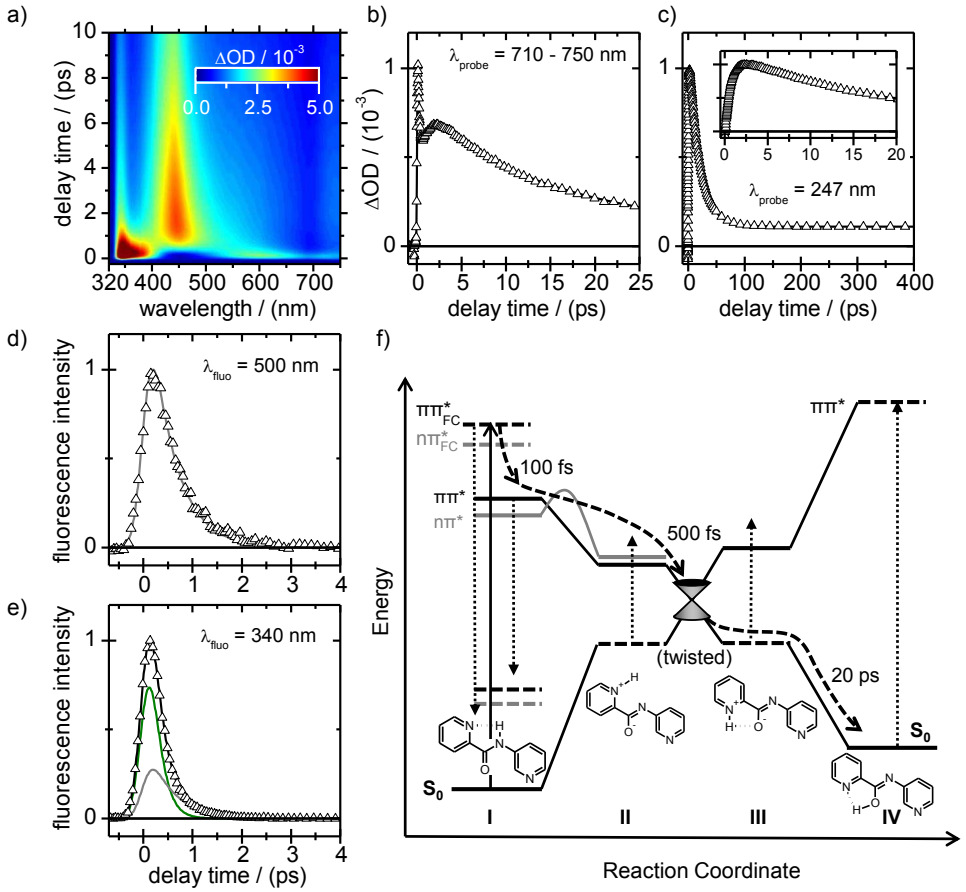

Figure 8.2: a) 2D transient absorption map. b) Transient absorption–time profile at $\lambda_{probe} = 710 - 750$ nm. c) Transient absorption–time profile at $\lambda_{probe} = 247$ nm. d) Fluorescence–time profile at $\lambda_{fl} = 500$ nm. e) Fluorescence–time profile at $\lambda_{fl} = 340$ nm. f) Scheme of the photo-induced proton transfer in the investigate switch NPPCA obtained by combination of the experimental and computational [CC2 and ADC(2)] results. The assigned time scales belong to the distinctive reaction steps denoted by the dashed arrows. Dotted arrows indicate the observed transient emission and absorption bands.

the initially excited Franck-Condon state of the keto isomer **I**. The applied electronic excitation induces the subsequent ultrafast proton transfer to the excited enol tautomer **II**. The observed 500 fs fluorescence lifetime has to be attributed to the barrierless transition of the enol **II** to the electronic ground state through the CoIn encountered at a twisted configuration of the pyridine moiety. The ESIPT from **I** to **II** should thus be completed in < 500 fs. The main decay time of 20 ps seen in the absorption experiment must belong to states **II** and **III** in the electronic ground state and the proton transfer to the final product **IV**. As can be seen from the data in Fig. 2 b and c, this 20 ps decay contribution features a 500 fs rise time precisely as expected by the observed 500 fs electronic deactivation time of the excited state. Last but not least, the formation of **IV** is confirmed by the weak positive permanent absorption ($\tau \gg 1$ ns) in the time profile at $\lambda = 247$ nm.

In conclusion, our experimental and computational results clearly demonstrate the stepwise proton transfer reaction in the bistable photochromic ESIPT switch NPPCA. The ultrafast fluorescence decay within a time $\tau = 500$ fs, the delayed rise within $\tau \approx 500$ fs of the absorption at $\lambda > 700$ nm and the persistent (permanent) absorption at $\lambda = 247$ nm provide unambiguous evidence for the proposed ESIPT switching process.

BIBLIOGRAPHY

[1] Douhal, A.; Lahmani, F.; Zewail, A. *Chem. Phys.* **1996**, *207*, 447–498.

[2] Elsaesser, T.; Bakker, H. J.; Kluwer in Ultrafast hydrogen bonding dynamics and proton transfer processes in the condensed phase; Dordrecht, 2002.

[3] Lapinski, L.; Nowak, M. J.; Nowacki, J.; Rode, M. F.; Sobolewski, A. L. *ChemPhysChem* **2009**, *10*, 2290–2295.

9

ULTRAFAST DYNAMICS OF A BISTABLE PHOTOCHROMIC ESIPT SWITCH

Julia Bahrenburg,[a] Michał F. Rode,[b] Andrzej L. Sobolewski,[b] Jacek Nowacki,[c] Christian Näther,[d] and Friedrich Temps[a]*

[a] Institute of Physical Chemistry, Christian-Albrechts-University Kiel, Olshausenstr. 40, D-24098 Kiel, Germany

[b] Institute of Physics, Polish Academy of Science, al. Lotników 32/46, 02-668 Warsaw, Poland

[c] Department of Chemistry, Warsaw University, Pasteura 1, Pl-03093 Warsaw, Poland

[d] Institute of Inorganic Chemistry, Christian-Albrechts-University of Kiel, Olshausenstr. 40, D-24098 Kiel, Germany

to be submitted

OWN CONTRIBUTIONS TO THIS MANUSCRIPT:

- Syntheses and characterization of the molecules
- Time-resolved fluorescence and transient absorption spectroscopy
- Static absorption spectroscopy
- Analysis of the data
- Writing of the manuscript

NOTE:

- The Chapter in its current form contains the experimental results and the discussion of the data based on the theoretical results of M. F. Rode and A. L. Sobolewski. For the final publication, it will be complemented with the computational methods and results.

* To whom correspondence should be addressed. E-mail: temps@phc.uni-kiel.de

ABSTRACT

The ultrafast dynamics of the bistable proton transfer switch N-(3-pyridinyl)-2-pyridinecarboxamide (NPPCA) following photoexcitation at $\lambda_{pump} = 264$ nm in acetonitrile (aprotic) and in water (protic) have been probed by means of femtosecond time-resolved fluorescence up-conversion and broadband and single color transient absorption spectroscopy. The interpretation of the data was supported by *ab initio* excited state calculations. The absorption- and fluorescence-time profiles in acetonitrile were analyzed in a global fashion and compared to those in water. The fit yielded four time constants, $\tau_1 = 0.10 \pm 0.01$ ps, $\tau_2 = 0.50 \pm 0.01$ ps, $\tau_3 = 5.80 \pm 0.40$ ps and $\tau_4 = 20.0 \pm 1.00$ ps for the transient absorption data and two decay times of $\tau_1 \leqslant 0.18 \pm 0.01$ ps and $\tau_2 = 0.50 \pm 0.01$ ps for the fluorescence data. τ_1 was assigned to the relaxation of the initially excited Franck-Condon state of the keto isomer. The subsequent ultrafast excited state intramolecular proton transfer (ESIPT) to the enol form and the deactivation to the electronic ground state *via* a conical intersection (CoIn) encountered at a twisted configuration of the molecule proceed within $\tau_2 = 0.50 \pm 0.01$ ps. The main component in all absorption traces decays within $\tau_4 = 20.0 \pm 1.00$ ps, features a rise time of $\tau_2 = 0.5$ ps and is therefore assigned to states in the electronic ground state. Absorption bands at $\lambda_{probe} > 700$ nm and at $\lambda_{probe} = 247$ nm and the calculated energies for the involved states confirm this suggestion. Finally, the stepwise formation of the proton transfer product is revealed by a permanent absorption at $\lambda_{probe} = 247$ nm.

9.1 INTRODUCTION

Proton transfer reactions belong to the most relevant chemical reactions and are known to play a crucial part in numerous biological processes.[1–8] In this context, artificial bistable photochromic molecular switches based on the excited state intramolecular proton transfer (ESIPT) phenomenon typically consist of at least one acidic and one basic functional group, which are connected *via* intramolecular hydrogen bonds. Upon electronic excitation, an intramolecular proton transfer from the proton donating to the accepting unit can occur.[9–13] Typically, the ESIPT process is ultrafast and reaction times have been found down to tens or few hundreds of femtoseconds.[5,14,15] Furthermore, bistable switches, which can be driven by the ESIPT process allow for record numbers of repeatable switching cycles due to their exceptional photostabilities. These properties lead to the high application potential of ESIPT switches, e.g., as photostabilizers in organic materials, UV absorbers and sunscreens.[16–20] One of the most common photostabilizers (2-(2'- hydroxy-5'-methylphenyl)benzotriazole, TINUVIN-P) for varnishes and adhesives shows an overall excited state lifetime of only $\approx$ 200 fs. The proton back-transfer in the electronic ground state occurs within less than $\approx$ 1 ps. Additionally, the reaction was found to be nearly unaffected by a polymeric environment, which is very impor-

tant for most applications.[21,22] Due to their particularly UV stabilities, for example, different derivatives of o-hydroxybenzaldehyde,[23–27] salicylic acid,[24,28–30] 3-hydroxyflavone,[5,28,31,32] 2-(2'-hydroxyphenyl)benzotriazole[21,22,24,28,33–36] hydroxyquinolines[11,37–41] and functionalized anthraquinones[28,42–44] have been investigated extensively both from the experimental and the theoretical point of view.[5,12,15,28] All these systems are based on the ultrafast UV induced ESIPT process in the electronically excited state from the respective proton donating to the proton accepting unit within less than a few hundred femtoseconds. The second important feature, is the (almost) barrierless subsequent radiationless deactivation to the electronic ground state. The photocycle is then typically closed by the proton back-transfer in the electronic ground state.[9,10,14,28,29] Since the formation of stable photoproducts is undesired for the function as photostabilizers the energy barrier between the two tautomers in the electronic ground state should be low to allow for an efficient back-reaction. The details of the underlying reaction steps of course depend strongly on the respective systems.[9,10,14,29]

Here, we report on a study of the photo-induced ultrafast dynamics of the bistable ESIPT switch N-(3-pyridinyl)-2-pyridinecarboxamide (NPPCA, Fig.9.1). The photochemical scheme of such bistable systems, which are

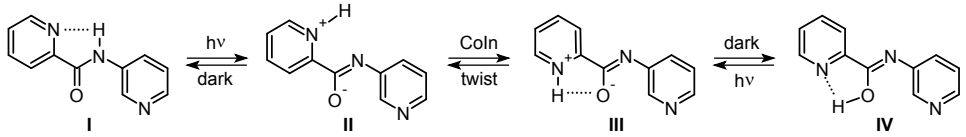

Figure 9.1: Molecular structures and reaction scheme of the bistable ESIPT switch NPPCA after UV excitation. Possible intramolecular hydrogen bonds are indicated by dotted lines.

based on the mechanistic principles of the ESIPT phenomenon, has been realized only recently.[9,10] In the case of NPPCA, $S_0 \rightarrow S_1$ optical excitation of the keto form **I** induces a proton transfer from the amide nitrogen as proton donating to the nearby pyridine nitrogen as proton accepting unit. The resulting form **II** evolves towards the $S_0 - S_1$ conical intersection (CoIn) and reaches the electronic ground state by a twist around the pyridine-carboxylic single bond. In the electronic ground state, the system thereafter can either continue the torsional motion to the final product **IV** or can return to the initial form **I**. Both **II** and **III** are unstable in the ground state.

To obtain experimental insight into the reaction pathways of the proton transfer switch NPPCA, its molecular dynamics were investigated by means of femtosecond time-resolved fluorescence up-conversion and broadband and single color transient absorption spectroscopy following excitation to the energetically lowest $\pi\pi^*$ state ($\lambda_{pump} = 264$ nm) in acetonitrile (AcCN) and in water (H_2O) as aprotic and protic solvent, respectively. The intramolecular proton transfer and therefore the formation of **IV** *via* configuration **II** is expected only in AcCN. In H_2O the formation of **IV**

is not impossible, but disfavored owing to preferential H-bonding and intermolecular proton exchange with the surrounding H_2O molecules. The experimental results are complemented by *ab initio* excited state calculations at the MP2/cc-pVDZ, CC2/cc-pVDZ and ADC(2)/cc-pVDZ levels of theory. Special attention is directed at the observation of the ultrafast ESIPT process from the photo-excited keto form **I** to the excited enol form **II** and the subsequent deactivation to the electronic ground state through the $S_0 - S_1$ CoIn as well as the formation of the final product **IV**. The obtained absorption and fluorescence-time profiles were analyzed in a global fashion and provide strong support for a stepwise formation of the final configuration **IV** in AcCN.

9.2 EXPERIMENTAL SECTION

NPPCA was synthesized according to a known protocol[45] and recrystallized from ethanol. The purity of the product (> 99 %) was checked by one- and two-dimensional NMR spectroscopy in D_2O and AcCN-d3. Additionally an X-ray diffraction structure was obtained (see Section 9.6). The time-resolved fluorescence measurements employed sample solutions at 0.3 mM concentration in a home-built flow cell of 1 mm optical path length and 0.2 mm quartz windows (ultrapure H_2O) or a 1 mm Hellma Analytics all-quartz flow cuvette with 1 mm windows (anhydrous AcCN). For the transient absorption measurements, which were performed on 6 mM sample solutions, flow cells of 0.1 mm path length with 0.2 mm (H_2O) resp. 0.4 mm windows (Hellma all-quartz cuvette for anhydrous AcCN) were used. All solutions in AcCN (supplied by Sigma-Aldrich and dried over molecular sieve) were prepared in a box purged with dry air.

The fluorescence up-conversion (FU) and transient absorption (TA) spectrometers have been described previously.[46–48] The excitation pulses of $\lambda_{pump} = 264$ nm for both experiments were delivered by frequency-doubled home-built non collinear optical parametric amplifiers (NOPAs) pumped by a 1 kHz regeneratively amplified 775 nm Ti:Sa laser (Clark MXR CPA 2001) and focused into the respective sample cells by dichroic mirrors. The pump-probe delay times were set using computer-controlled linear translation stages.

The fluorescence-time profiles were detected at three different wavelengths, $\lambda_{fl} = 340$, 430 and 500 nm. The excitation energies for the FU experiments was reduced to $\leqslant 100$ nJ per pulse. Scattered pump light was removed by a WG320 filter behind the sample cell. The emission by the excited molecules was collected and refocused into a BBO crystal for up-conversion by type I sum frequency generation with the 775 nm Ti:Sa gate pulses. After passing a double monochromator, the up-converted light was detected as a function of pump-gate delay time by a photomultiplier connected to a gated photon counter. Each recording was repeated twice. Background signals from impurities or unwanted coherent effects were ruled out by scans of the neat solvent. The time resolution determined by the pump-gate cross correlation was of the order of $\Delta t \approx 130$ fs.

The supercontinuum probe pulses for the TA experiment between 320 nm $\leqslant \lambda_{probe} \leqslant$ 750 nm were generated in CaF_2, split up into probe and reference paths, and focused into the sample cell, where the probe pulses were spatially overlapped with the pump pulses. The transmitted probe and reference spectra were detected with two FFT-CCD cameras. Single-color probe pulses at $\lambda_{probe} = 247$ nm were obtained from a third frequency-doubled NOPA, split again into probe and reference, and detected with two matched photodiodes. The excitation pulse energies were reduced to $\leqslant$ 150 nJ. Each pump-probe delay scan was repeated three times. For better comparison the measurements in H_2O and AcCN were performed directly one after the other. The signals due to pump-induced cross-phase modulation (XPM), multiphoton absorption (MPA) and solvated electron absorption (SEA) were measured independently for the pure solvent. The instrument response function (IRF) gave an experimental time resolution of $\Delta t \approx 50$ fs.

9.3 RESULTS

9.3.1 MOLECULAR STRUCTURE AND STATIONARY UV/VIS SPECTRA

The measured stationary UV/VIS absorption spectra of NPPCA in AcCN and in H_2O are shown in Fig. 9.2. They are in very good agreement with the calculated spectra[2]. The strong absorption band with its maximum at

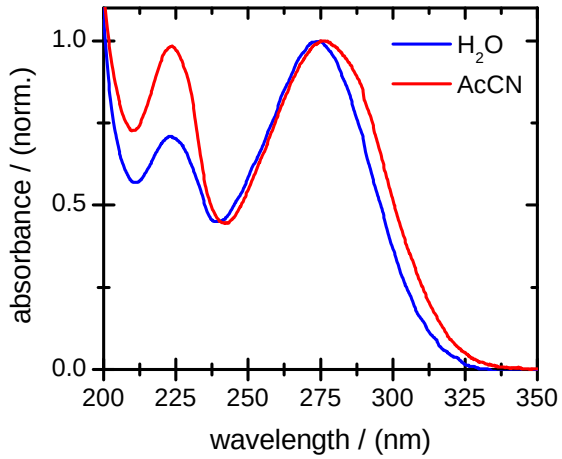

Figure 9.2: UV/VIS absorption spectra of NPPCA in AcCN (red) and in H_2O (blue).

$\lambda = 276$ nm and at $\lambda = 275$ nm in AcCN and in H_2O, respectively, is attributed to the lowest $\pi\pi^*$ transition, which carries the bulk of the oscillator strength. Excitation at $\lambda_{pump} = 264$ nm leads exclusively to the population of this state. The energetically higher absorption band at $\lambda = 224$ nm

2 The quantum chemical calculations were performed by A. L. Sobolewski and M. F. Rode.

in both solvents belongs to a second $\pi\pi^*$ transition. The X-ray diffraction structure (see Section 9.6) clearly shows the pre-orientation of the proton donating N-H unit towards the proton accepting nitrogen and leads to a planar configuration of the molecule according to the calculations.

9.3.2 TIME-RESOLVED FLUORESCENCE MEASUREMENTS

Measured fluorescence-time profiles at two selected emission wavelengths ($\lambda_{fl} = 340$ and 500 nm) after excitation at $\lambda_{pump} = 264$ nm are given in Fig. 9.3. The global fitting analysis of these data yielded two time constants

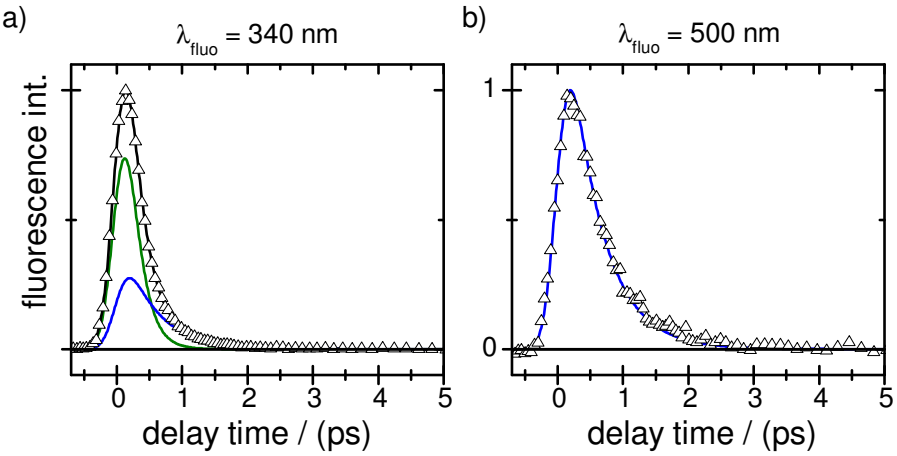

Figure 9.3: Fluorescence-time profiles of NPPCA in AcCN after excitation with $\lambda_{pump} = 264$ nm at two emission wavelengths of a) $\lambda_{fl} = 340$ nm and b) 500 nm. Open symbols are the data points, solid lines give the least-squares fit curves (green: τ_1, blue: τ_2).

(with 2σ error limits) of

$$\tau_1 = 0.18 \pm 0.01 \text{ ps},$$
$$\tau_2 = 0.50 \pm 0.01 \text{ ps}.$$

The lifetime $\tau_1 = 0.18 \pm 0.01$ ps should be seen as upper limit in view of the time resolution of the experiment. The relative amplitude of this component decreases rapidly with increasing emission wavelength. The time profile at $\lambda_{fl} = 340$ nm is almost completely determined by the fast component τ_1, whereas the decay curve at $\lambda_{fl} = 500$ nm can be fully described with the component decaying within τ_2. τ_2 can thus be taken as measure for the lifetime of the molecules in the excited electronic state.

9.3.3 TIME-RESOLVED TRANSIENT ABSORPTION MEASUREMENTS

The two-dimensional (2D) spectro-temporal maps of the change in optical density ΔOD of NPPCA in H_2O and in AcCN after excitation at $\lambda_{pump} = 264$ nm in the detection wavelengths range 320 nm $\leqslant \lambda_{probe} \leqslant$ 750

nm are displayed in Figs. 9.4 a and b, respectively. Both the transient ab-

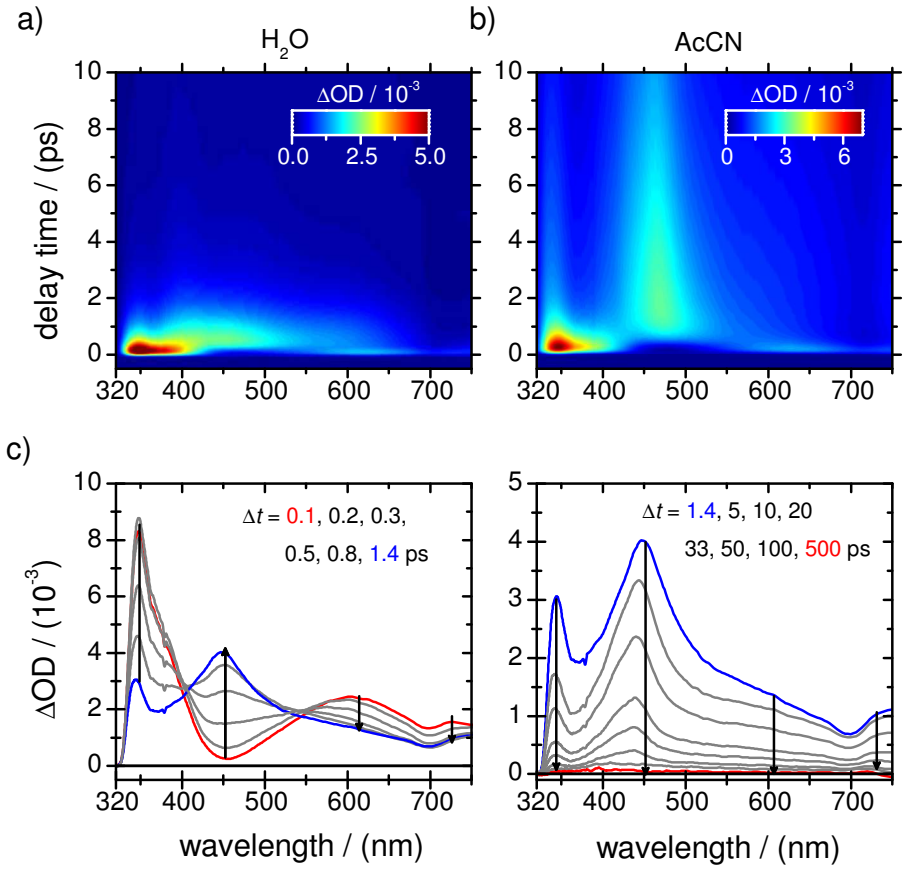

Figure 9.4: Two-dimensional maps of the transient absorption changes ΔOD of NPPCA in a) H_2O and b) AcCN after excitation at $\lambda_{pump} = 264$ nm for probe wavelengths in the range 320 nm $\leqslant \lambda_{probe} \leqslant$ 750 nm and delay times of $\Delta t \leqslant 10$ ps. c) Transient spectra of NPPCA in AcCN at delay times between 0.1 ps $\leqslant \Delta t \leqslant$ 1.4 ps (left) and between 1.4 ps $\leqslant \Delta t \leqslant$ 500 ps (right) after the pump pulse at $\lambda_{pump} = 264$ nm. The arrows indicate the temporal evolution of the spectra.

sorption maps in H_2O and AcCN exhibit very similar positive and negative absorption bands in virtually the same detection wavelength regions. At first glance, the only difference seems to be the significantly shorter lifetime of the absorption bands in H_2O compared to these in AcCN, where the formation of longer lived species can be observed. Since the intramolecular proton transfer and therefore the stepwise formation of the desired product can only be expected in the aprotic solvent AcCN and not in the protic solvent H_2O, we mainly focus on the measurements in AcCN and compare them with the measurements in H_2O if needed. The transient absorption map of NPPCA in AcCN exhibits negative features near time-zero at $\lambda_{probe} = 320 - 350$ nm and $420 - 540$ nm from stimulated emission (SE), which decay within $\approx$ 100 fs and $\approx$ 500 fs, respectively. Additionally, several positive excited state absorption (ESA) bands appear at $\lambda_{probe} \approx 350$ nm, $\approx$ 450 nm, $\approx$ 600 nm and at $\approx$ 730 nm. The transient spectra displayed

in Fig. 9.4 c reveal the ensuing molecular dynamics in some more detail. All positive and negative absorption bands are nicely featured in the distinctive spectral windows identified above. A very remarkable feature is the relatively long lived absorption band above $\approx$ 700 nm, which only exists in AcCN and not in H_2O.

The temporal evolution of the transient absorption features is reflected by the transient absorption-time profiles for four selected probe wavelength ranges representing the distinctive spectral windows (cf. Fig. 9.5). The absorption-time profiles were analyzed in a global fashion with a sum

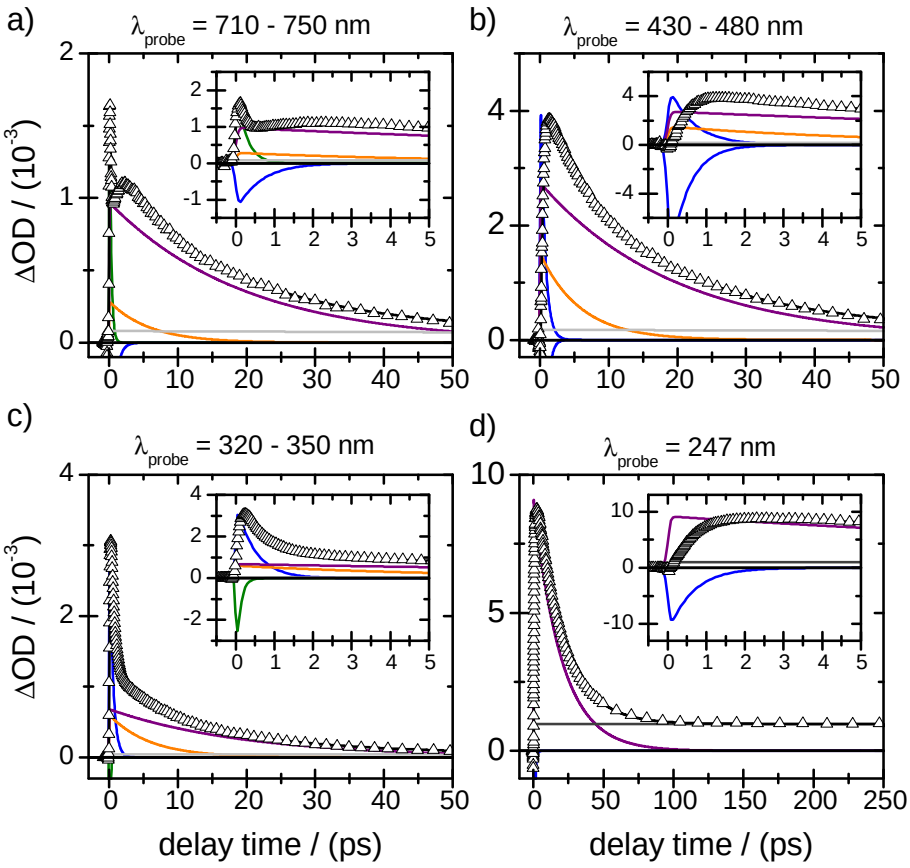

Figure 9.5: Transient absorption-time profiles of NPPCA in AcCN after excitation at $\lambda_{pump} = 264$ nm at four selected wavelengths. The open symbols are the data, solid black lines the overall least-squares fit curves. The different contributions are indicated by colored lines (green: τ_1, blue: τ_2, orange: τ_3, purple: τ_4, grey: τ_∞). The insets show the same data on a shorter time scale up to 5 ps.

of four exponentials for the single color measurement at $\lambda_{probe} = 247$ nm and for the data curves between $\lambda_{probe} = 710 - 750$ nm, $650 - 600$ nm, $430 - 480$ nm, $370 - 400$ nm and $320 - 350$ nm after spectral integration,

respectively. The global analysis yielded the four time constants (with 2σ error limits)

$$\tau_1 = 0.10 \pm 0.01 \text{ ps},$$
$$\tau_2 = 0.50 \pm 0.01 \text{ ps},$$
$$\tau_3 = 5.80 \pm 0.40 \text{ ps},$$
$$\tau_4 = 20.0 \pm 1.00 \text{ ps}.$$

The lifetimes of $\tau_1 = 0.10 \pm 0.01$ ps and $\tau_2 = 0.50 \pm 0.1$ ps, which can be observed as SE in the detection ranges of $\lambda_{\text{probe}} = 370 - 400$ nm and $430 - 480$ nm, respectively, correlate well with the two fluorescence times. The value of $\tau_1 = 0.18 \pm 0.01$ ps determined by the fluorescence measurements is an IRF-limited upper value and may be shorter ($\tau_1 \leqslant 0.18 \pm 0.01$ ps). Thus, these two decay times can be assigned to the early dynamics in the excited state. Additionally, some transients decay within $\tau_3 = 5.8 \pm 0.4$ ps, which do probably not belong to major processes because of their relatively small amplitudes. The main component, next to the ultrashort τ_1 and τ_2 components in all absorption traces around $\lambda \approx 340$, 470 and 730 nm exhibits a lifetime of $\tau_4 = 20 \pm 1$ ps and features a 0.5 ps rise time, which is consistent with τ_2. The absorption-time profile at $\lambda_{\text{probe}} = 247$ nm additionally features a constant positive absorption with a relative amplitude of $\approx 12\%$, which does not decay to zero within the temporal detection window and was described with a constant offset term (dark gray). The absorption-time profiles at $\lambda_{\text{probe}} = 710 - 750$ nm, $430 - 480$ nm and $320 - 350$ nm also show a long-lived component (light gray), but with very small amplitudes ($\leqslant 4\%$) (cf. Fig. 9.5 a and b). Fit attempts without these contribution were not satisfactory. It may belong to background shifts or slow processes in the electronic ground state.

9.4 DISCUSSION

Taking into account the quantum mechanical calculations[3], the global analysis of time-resolved fluorescence up-conversion and absorption measurements presented above provides explicit information on the ultrafast photo-induced reaction dynamics of the bistable ESIPT switch N-(3-pyridinyl)-2-pyridinecarboxamide (NPPCA) after excitation at $\lambda_{\text{pump}} = 264$ nm. The obtained results can be assigned to the stepwise sequential dynamic transformations of the molecules after UV excitation as illustrated in Fig. 9.6. Excitation at $\lambda_{\text{pump}} = 264$ nm projects the wavepacket from S_0 to the Franck-Condon (FC) region of the $\pi\pi^*$ state of the keto isomer **I**. The observed fluorescence and ESA components decaying with τ_1 and τ_2 probably belong to the excited keto isomer **I**. Emission from the excited enol tautomer **II**, which is subsequently formed after the photo-induced proton transfer, would be in the infrared according to the calculated energies of ≈ 1 eV. In addition, the calculations show that the conical intersection with

3 Performed by A. L. S. and M. F. R.

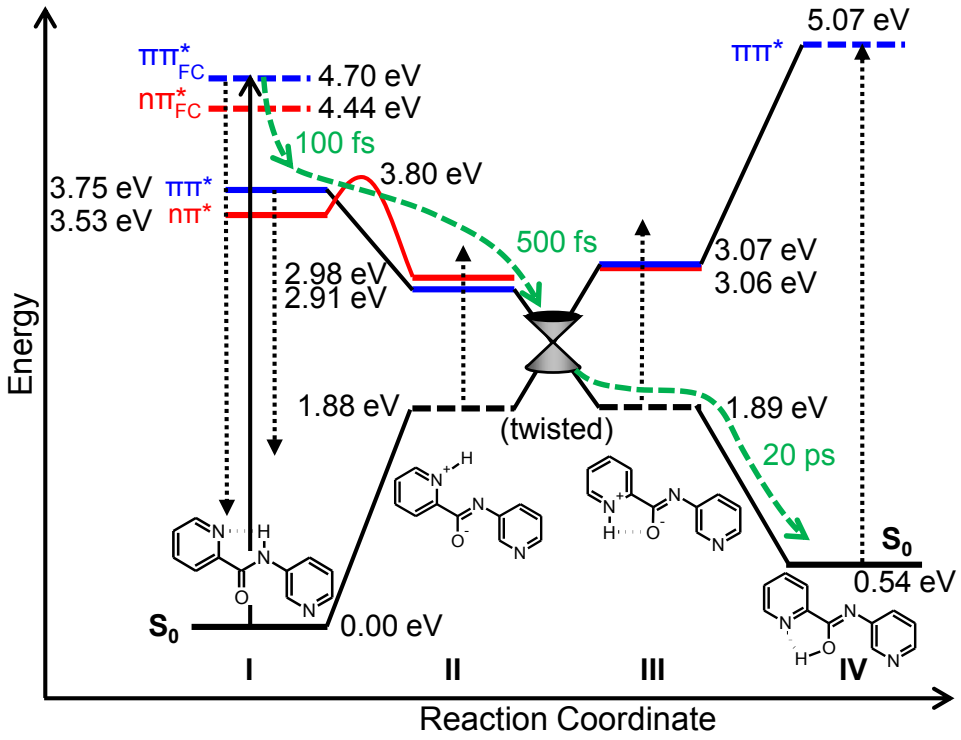

Figure 9.6: Proposed scheme of photo-induced proton transfer in the investigated switch NPPCA obtained by a combination of the experimental and computational (CC2 and ADC(2)) results. The electronic nature of the state is encoded by colors (black: S_0, blue: $\pi\pi^*$, red: $n\pi^*$). Solid lines represent the adiabatic (optimized) energy of a given state. The dashed blue and red lines give the "vertical" excitation energy of a given state computed at the respective ground state minimum. The dashed black lines represent the "vertical" excitation energy of the ground state computed at the optimized geometry of form **II** ($n\pi^*$). The assigned time scales belong to the distinctive reaction steps denoted by the dashed arrows. Dotted black arrows indicate the observed transient emission and absorption bands. The solid curved red line indicates a certain barrier, the height of which plays an important role in the electronic deactivation.

the electronic ground state can be reached from form **I** *via* form **II** without any significant barrier ($\leqslant$ 0.05 eV). The proton transferred $n\pi^*$ form is separated from the $n\pi^*$ state of form **I** by a barrier of 0.27 eV. The $n\pi^*$ state **I** may, in principle, be responsible for emission between $\lambda_{fl} = 340$ nm and 500 nm, but the barrier from the initially excited $\pi\pi^*$ state is much lower (0.05 eV). Therefore, the $\approx$ 0.1 ps component is associated with the rapid departure of the wavepacket from FC region of configuration **I**. The 0.5 ps time is attributed to the barrierless transition from **I** to the electronic ground state *via* **II** through the $S_0 - S_1$ CoIn encountered at a twisted configuration of the pyridine moiety linked to the carboxyl-carbon. The ESIPT from **I** to **II** should thus be completed in $<$ 0.5 ps.

The main decay time of 20 ps, which was only observed in the absorption and not in the fluorescence experiments, probably belongs to states **II**

and **III** in the electronic ground state and the proton transfer to the final product **IV**. The respective time profiles further feature a 0.5 ps rise time as would be expected by the observed 0.5 ps electronic deactivation time of the excited state and especially dominates the absorption at $\lambda_{probe} > 700$ nm and 247 nm. Next to the rise time, there are additional reasons why this component is assigned to dynamics in the electronic ground state and not to the excited state. First, the measurements in AcCN show an absorption band at detection wavelengths at $\lambda_{probe} > 700$ nm, which is dominated by decay component τ_4. In addition, the energy difference between the excited state and the ground state of form **II** and **III**, respectively, is only about ≈ 1 eV. Therefore, this absorption band should actually belong to the configurations **II** and **III** in the electronic ground state. The "direct observation" of the states **II** and **III** strongly hints at the stepwise formation of product **IV**. Furthermore, the measurements in H_2O, where the intramolecular proton transfer to **IV** is unlikely, do not show a comparable absorption band at > 700 nm. Fig. 9.7 a shows a comparison of the transient absorption-time profiles of NPPCA in H_2O and AcCN at $\lambda_{probe} = 710 - 750$ nm. In contrast to the time profile in AcCN, the time pro-

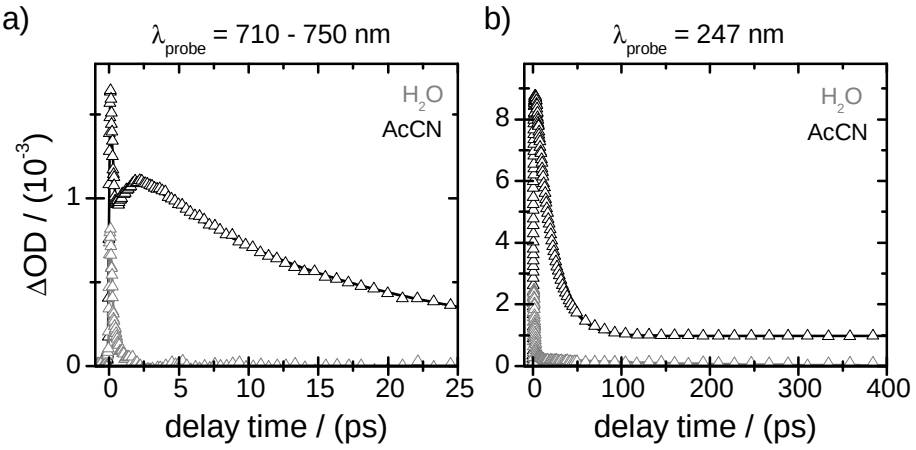

Figure 9.7: Comparison of the transient absorption-time profiles of NPPCA in AcCN and H_2O at a) $\lambda_{probe} = 710 - 750$ nm and b) $\lambda_{probe} = 247$ nm after excitation at $\lambda_{pump} = 264$ nm. The open symbols are the data and the solid lines are the overall least-squares fit curves. Since the measurements in H_2O and AcCN were performed directly one after the other, a direct comparison of the data is possible.

file in H_2O does not show the 20 ps component or any other longer-lived species. The absorption-time profiles in the two solvents at $\lambda_{probe} = 247$ nm are given in Fig. 9.7 b. The time profile in AcCN shows the main decay component τ_4 and this contribution does not exist in H_2O. Additionally, a permanent persistent absorption, which does not decay over the entire temporal detection range, can be observed in AcCN and not in H_2O. This permanent absorption is attributed to the difference in the UV absorptions between forms **I** and **IV**. However, the formation of long-lived triplet states is also not impossible for compounds like NPPCA. Mord-

zińisk *et al.* investigated the role of triplet states in the ESIPT reactions in 2-(2′-hydroxyphenyl)benzoxazole in degassed solutions and found triplet states to become more important at lower temperatures. At room temperature nearly no intersystem crossing was observed.[49] A study on the proton transfer in 2-(2′-hydroxyphenyl)benzothiazole in AcCN and pyridine as solvents by Elsaesser *et al.* revealed that internal conversion is the dominant process. The found time constants were found to be to short for intersystem crossing between singlet and triplet states.[50] Nevertheless, the permanent absorption in AcCN could also belong to a triplet state but due to air-saturation of the solvents the formation of triplet states is unlikely. Furthermore, no permanent absorption was observed in H_2O, even though the formation of triplet states in H_2O would not be less probable. In agreement with the calculated energies of the different states, the positive long-lived UV absorption may belong to the proton transfer product **IV**. The thermal lifetime of this product should be longer than the detection window of 400 ps. Thus the existence of this permanent absorption band supports the stepwise reaction from the keto tautomer **I** to the enol tautomer **IV**.

The present results and the observed stepwise reaction and formation of the proton transfer product fit well with previous theoretical studies on the ESIPT phenomenon in bistable proton transfer switches by Sobolewski *et al.*,[9,29] Lapinski et al.[10] and Rode *et al.*[11,13]

9.5 CONCLUSION

In conclusion, we have presented an experimental and computational study of the photo-induced dynamics of the bistable excited state intramolecular proton transfer (ESIPT) switch N-(3-pyridinyl)-2-pyridinecarboxamide (NPPCA) in solution in AcCN and in H_2O by means of femtosecond time-resolved fluorescence up-conversion and transient absorption spectroscopy following photoexcitation at $\lambda_{pump} = 264$ nm. The interpretation of the data was supported by *ab initio* excited state calculations[4]. The results clearly hint at a stepwise proton transfer reaction from the thermally stable keto tautomer to the desired enol tautomer in the aprotic solvent AcCN. A global analysis of the absorption-time profiles yielded four time constants of $\tau_1 = 0.10 \pm 0.01$ ps, $\tau_2 = 0.50 \pm 0.01$ ps, $\tau_3 = 5.80 \pm 0.40$ ps and $\tau_4 = 20.0 \pm 1.00$ ps. The two fast time constants were also found in the fluorescence data. τ_1 was assigned to the relaxation of the initially excited Franck-Condon state of the keto isomer (**I**, cf. Figs. 9.1 and 9.6). The applied electronic excitation induces the subsequent ultrafast proton transfer to the excited enol tautomer **II**. τ_2 is the almost barrierless (0.05 eV) radiationless deactivation to the electronic ground state *via* the $S_0 - S_1$ conical intersection encountered at a twisted configuration of the pyridine moiety, which is linked to the carboxyl-group. The ESIPT process from **I** to **II** is therefore completed in < 0.5 ps. The main decay time of $\tau_4 = 20.0 \pm 1.00$ ps only seen in the absorption experiment belongs to states **II** and **III** in

4 Performed by M. F. R. and A. L. S.

the electronic ground state and the proton transfer to the final product **IV**. These absorption traces feature a delayed rise time of 0.5 ps as expected for the observed deactivation time of the excited state. This component can be also observed at $\lambda_{probe} > 700$ nm, which matches well with the calculated energy differences of ≈ 1 eV for the states **II** and **III** in the excited and the ground state. In addition, the persistent absorption at $\lambda_{probe} = 247$ nm provides evidence for the proposed ESIPT switching process and the stepwise formation of the proton transfer product. In H_2O, where the intramolecular proton transfer is unlikely, no long-lived permanent absorption at $\lambda_{probe} = 247$ nm and no absorption at detection wavelengths above $\lambda_{probe} > 700$ nm can be observed.

Ongoing UV-pump/IR-probe experiments on NPPCA in our laboratory should allow for an unambiguous clarification of the reaction mechanism by the observation of different intermediate products and the final proton transfer product, respectively.

ACKNOWLEDGMENTS

The work of JB and FT has been supported by the Deutsche Forschungsgemeinschaft through SFB 677.

BIBLIOGRAPHY

[1] Heberle, J.; Riesle, J.; Thiedemann, G.; Oesterhelt, D.; Dencher, N. A. *Nature* **1994**, *370*, 379–382.

[2] Stowell, M.; McPhillips, T.; Rees, D.; Soltis, S.; Abresch, E.; Feher, G. *Science* **1997**, *276*, 812–816.

[3] Luecke, H.; Richter, H.-T.; Lanyi, J. K. *Science* **1998**, *280*, 1934–1937.

[4] Belevich, I.; Verkhovsky, M. I.; Wikström, M. *Nature* **2006**, *440*, 829–832.

[5] Han, K.-L.; Zhao, G.-J. *Hydrogen bonding and transfer in the excited state*; Wiley: Chichester, UK, 2011; Vol. 1&2.

[6] Hsieh, C.-C.; Chou, P.-T.; Shih, C.-W.; Chuang, W.-T.; Chung, M.-W.; Lee, J.; Joo, T. *J. Am. Chem. Soc.* **2011**, *133*, 2932–2943.

[7] Weinberg, D. R.; Gagliardi, C. J.; Hull, J. F.; Murphy, C. F.; Kent, C. A.; Westlake, B. C.; Paul, A.; Ess, D. H.; McCafferty, D. G.; Meyer, T. J. *Chem. Rev.* **2012**, *112*, 4016–4093.

[8] Migliore, A.; Polizzi, N. F.; Therien, M. J.; Beratan, D. N. *Chem. Rev.* **2014**,

[9] Sobolewski, A. L. *Phys. Chem. Chem Phys.* **2008**, *10*, 1243–1247.

[10] Lapinski, L.; Nowak, M. J.; Nowacki, J.; Rode, M. F.; Sobolewski, A. L. *ChemPhysChem* **2009**, *10*, 2290–2295.

[11] Rode, M. F.; Sobolewski, A. L. *J. Phys. Chem. A* **2010**, *114*, 11879–11889.

[12] Kwon, J. E.; Park, S. Y. *Adv. Mater.* **2011**, *23*, 3615–3642.

[13] Rode, M. F.; Sobolewski, A. *J. Chem. Phys.* **2014**, *140*, 084301.

[14] Douhal, A.; Lahmani, F.; Zewail, A. H. *Chem. Phys.* **1996**, *207*, 477–498.

[15] Elsaesser, T.; Bakker, H. J. *Ultrafast hydrogen bonding dynamics and proton transfer processes in the condensed phase*; Kluwer Academic Publishers: Dordrecht, 2002.

[16] Pospisil, J.; Nespurek, S. *Prog. Polym. Sci.* **2000**, *25*, 1261–1335.

[17] Kaczmarek, L.; Borowicz, P.; Grabowska, A. *J. Photochem. Photobiol. A* **2001**, *138*, 159–166.

[18] Zayat, M.; Garcia-Parejo, P.; Levy, D. *Chem. Soc. Rev* **2007**, *36*, 1270–1281.

[19] Baughman, B. M.; Stennett, E.; Lipner, R. E.; Rudawsky, A. C.; Schmidtke, S. J. *J. Phys. Chem. A* **2009**, *113*, 8011–8019.

[20] Kumasaka, R.; Kikuchi, A.; Yagi, M. *Photochem. Photobiol.* **2014**,

[21] Wiechmann, M.; Port, H.; Laermer, F.; Frey, W.; Elsaesser, T. *Chem. Phys. Lett.* **1990**, *165*, 28–34.

[22] Wiechmann, M.; Port, H.; Frey, W.; Laermer, F.; Elsaesser, T. *The Journal of Physical Chemistry* **1991**, *95*, 1918–1923.

[23] Sobolewski, A. L.; Domcke, W. *Chem. Phys.* **1994**, *184*, 115–124.

[24] Sobolewski, A. L.; Domcke, W. *Phys. Chem. Chem. Phys.* **1999**, *1*, 3065–3072.

[25] Lochbrunner, S.; Schultz, T.; Schmitt, M.; Shaffer, J.; Zgierski, M.; Stolow, A. *J. Chem. Phys.* **2001**, *114*, 2519–2522.

[26] Stock, K.; Bizjak, T.; Lochbrunner, S. *Chem. Phys. Lett.* **2002**, *354*, 409–416.

[27] Migani, A.; Blancafort, L.; Robb, M. A.; DeBellis, A. D. *J. Am. Chem. Soc.* **2008**, *130*, 6932–6933.

[28] Formosinho, S. J.; Arnaut, L. G. *J Photoch. Photobio A* **1993**, *75*, 21–48.

[29] Sobolewski, A. L.; Domcke, W. *Phys. Chem. Chem Phys.* **2006**, *8*, 3410–3417.

[30] Jankowska, J.; Rode, M. F.; Sadlej, J.; Sobolewski, A. L. *ChemPhysChem* **2012**, *13*, 4287–4294.

[31] Ameer-Beg, S.; Ormson, S. M.; Brown, R. G.; Matousek, P.; Towrie, M.; Nibbering, E. T.; Foggi, P.; Neuwahl, F. V. *J. Phys. Chem. A* **2001**, *105*, 3709–3718.

[32] Douhal, A.; Sanz, M.; Carranza, M.; Organero, J.; Santos, L. *Chem. Phys. Lett.* **2004**, *394*, 54–60.

[33] Lochbrunner, S.; Wurzer, A.; Riedle, E. *J. Chem. Phys.* **2000**, *112*, 10699–10702.

[34] Lochbrunner, S.; Wurzer, A. J.; Riedle, E. *J. Phys. Chem. A* **2003**, *107*, 10580–10590.

[35] Sobolewski, A. L.; Domcke, W.; Hättig, C. *J. Phys. Chem. A* **2006**, *110*, 6301–6306.

[36] Iijima, T.; Momotake, A.; Shinohara, Y.; Sato, T.; Nishimura, Y.; Arai, T. *J. Phys. Chem. A* **2010**, *114*, 1603–1609.

[37] Kim, T. G.; Topp, M. R. *J. Phys. Chem. A* **2004**, *108*, 10060–10065.

[38] Bhattacharya, B.; Samanta, A. *J. Phys. Chem. B* **2008**, *112*, 10101–10106.

[39] Schriever, C.; Barbatti, M.; Stock, K.; Aquino, A. J.; Tunega, D.; Lochbrunner, S.; Riedle, E.; de Vivie-Riedle, R.; Lischka, H. *Chem. Phys.* **2008**, *347*, 446–461.

[40] Vetokhina, V.; Nowacki, J.; Pietrzak, M.; Rode, M. F.; Sobolewski, A. L.; Waluk, J.; Herbich, J. *J. Phys. Chem. A* **2013**, *117*, 9127–9146.

[41] Vetokhina, V.; Nowacki, J.; Pietrzak, M.; Rode, M. F.; Sobolewski, A. L.; Waluk, J.; Herbich, J. *J. Phys. Chem. A* **2013**, *117*, 9147–9155.

[42] Neuwahl, F. V.; Bussotti, L.; Righini, R.; Buntinx, G. *Phys. Chem. Chem. Phys.* **2001**, *3*, 1277–1283.

[43] Schmidtke, S. J.; Underwood, D. F.; Blank, D. A. *J. Phys. Chem. A* **2005**, *109*, 7033–7045.

[44] Nagaoka, S.-i.; Uno, H.; Huppert, D. *J. Phys. Chem. B* **2012**, *117*, 4347–4353.

[45] Anand, J.; Singha, N. C.; Sathyanarayana, D. N. *J. Mol. Struct.* **1997**, *412*, 221–229.

[46] Pancur, T.; Schwalb, N. K.; Renth, F.; Temps, F. *Chem. Phys.* **2005**, *313*, 199–212.

[47] Schwalb, N. K.; Temps, F. *J. Phys. Chem. A* **2009**, *113*, 13113–13123.

[48] Röttger, K.; Siewertsen, R.; Temps, F. *Chem. Phys. Lett.* **2012**, *536*, 140–146.

[49] Mordziński, A.; Grellmann, K. *J. Phys. Chem* **1986**, *90*, 5503–5506.

[50] Elsaesser, T.; Schmetzer, B.; Lipp, M.; Bäuerle, R. *Chem. Phys. Lett.* **1988**, *148*, 112–118.

To verify and support the conclusion of the ultrafast ESIPT process in NPPCA, the closely related derivative N-(3-pyridyl)-benzamide (NPBA) was synthesized and investigated by means of static UV/VIS absorption and time-resolved fluorescence up-conversion spectroscopy in the context of this project. In NPBA the proton accepting nitrogen is substituted by a carbon atom so that the intramolecular proton transfer cannot take place. A comparison of the molecular structures and the obtained X-ray diffraction structures of NPPCA and NPBA are given in Figs. 9.8 a and c, and b and d, respectively. Due to the pre-orientation of the amide proton to-

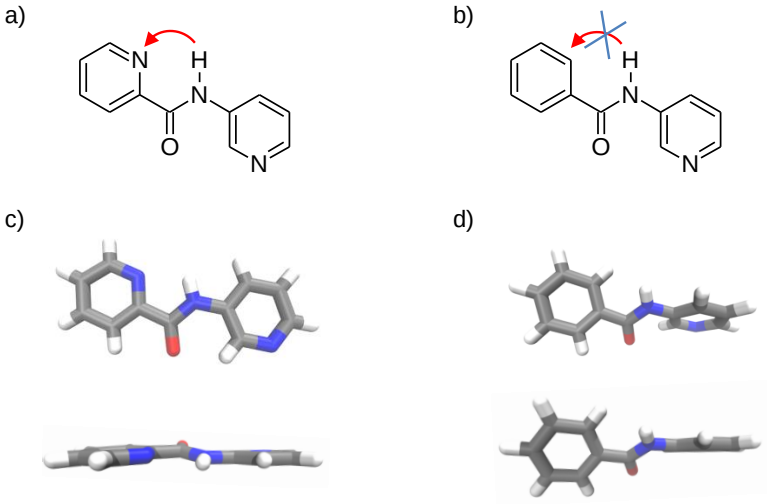

Figure 9.8: Comparison of the structures of the proton transfer switch NPPCA (a and c) and the closely related molecule NPBA where the proton donating nitrogen is replaced by a carbon (b and d) so that the intramolecular proton transfer cannot take place.

wards the proton donating pyridine nitrogen and the resulting intramolecular hydrogen bond between these units, NPPCA shows an almost planar configuration in its electronic ground state (cf. Fig. 9.8 c). In the case of NPBA the pyridine and the benzyl unit become more perpendicular to each other with an out-of-plane dihedral angle of $\approx 30°$ [A9.1]. During the X-ray diffraction experiments three polymorphic modifications of NPBA were found. To obtain insight into the rotational barriers and stabilities of the different modifications quantum chemical calculations on the B3LYP/6-311++G(d,p) level of theory were performed. Furthermore, differential scanning calorimetry (DSC), thermomicroscopy, X-ray powder diffraction (XRPD) and crystallization experiments were performed to resolve the thermodynamic relations between the three forms. As expected, one modification was found to be energetically favored. The other two forms were metastable and it was not possible to obtain phase-pure samples [A9.1].

Regarding the ESIPT process it was initially assumed that the ultrafast fluorescence lifetime for NPBA should be increased compared to NPPCA.

The fluorescence for NPPCA decays within < 500 fs. This time constant was assigned to the ESIPT process and the subsequent deactivation to the electronic ground state. The static UV/VIS absorption spectra of both molecules in the aprotic solvent AcCN are given in Fig. 9.9 a. The intense

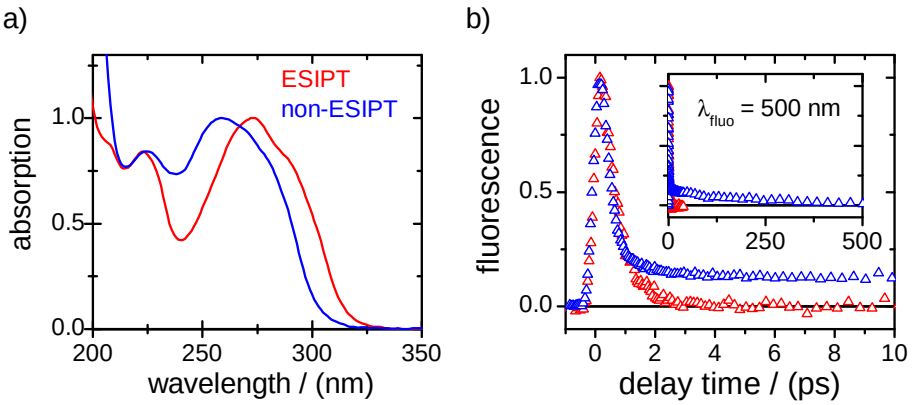

Figure 9.9: a) UV/VIS absorption spectra of NPPCA (red) and NPBA (blue) in AcCN as solvent. b) Fluorescence-time profiles of NPPCA (red) and NPBA (blue) in AcCN at a fluorescence wavelength of 500 nm after excitation at $\lambda_{pump} = 264$ nm.

absorption band of NPBA in the UV at $\lambda = 260$ nm shows a blue-shift of $\approx$ 15 nm compared to the maximum of NPPCA. Furthermore the absorption band becomes more unstructured.

The fluorescence-time profiles after excitation at $\lambda_{pump} = 264$ nm at a fluorescence wavelength of 500 nm for NPBA and NPPCA are depicted in Figs. 9.9 b. Next to an ultrashort $\approx$ 500 fs component, which was also observed for NPPCA, the data of NPBA reveal an additional much longer-lived component of $\approx$ 150 ps. Despite the fact that the 500 fs component also exists for NPBA, the ultrafast ESIPT for NPPCA is not excluded. The electronic ground state structures clearly demonstrate that NPBA and NPPCA are completely different molecules regarding their geometrical structure. Therefore, comparison of the data for NPBA and NPPCA has to be performed with caution.

REFERENCES

A9.1 Näther, C.; Jess, I.; Bahrenburg, J.; Bank, D., Temps, F. *CrystEngComm* **2014**, *16*,5633–5614.

Part III

CONCLUDING DISCUSSION

10

SUMMARY AND OUTLOOK

The first goal of this Thesis was the elucidation of the photochemical properties and the ultrafast molecular dynamics of several azobenzene (AB) derivatives under different circumstances, which might influence or compete with the desired photoisomerization. The potential impacts include inter- and intramolecular effects, such as steric interactions, geometrical constraints, external forces, excitonic coupling, charge-transfer (CT) or direct electronic coupling in π-conjugated systems. All these effects may occur in typical functional systems where multiple chromophores are embedded in complex environments in close proximity to each other. The second part was concerned with the nature of excited states and possible deactivation mechanisms of a recently designed molecular spin switch based on a nickel porphyrin and its building blocks. Previous studies of the magnetic bistability of the system at room temperature have shown that irradiation can induce coordination of the tethered azopyridine ligand leading to electronic rearrangement from a diamagnetic to a paramagnetic state. Finally, the molecular dynamics of a bistable photochromic excited state intramolecular proton transfer (ESIPT) switch have been revealed by femtosecond time-resolved spectroscopies. The interpretation of the data was supported by ab initio excited state calculations of A. Sobolewski and co-workers. The aim was to follow the sequential reaction pathways and the formation of the desired proton transfer product.

10.1 SUMMARY

AZOBENZENE SWITCHES UNDER THE INFLUENCE OF INTRA- AND INTERMOLECULAR EFFECTS

The strong influences of electron donating and accepting substituents on the AB core were investigated for the *push-pull* azobenzene Disperse Red 1 (DR1) shown in Fig. 10.1. The *push-pull* substitution induces a strong CT

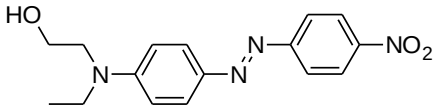

Figure 10.1: Structure of the *push-pull* azobenzene Disperse Red 1 (DR1).

character in the $\pi\pi^*$ excited state leading to a lower energy barrier between the *E*- and the *Z*-isomer in the electronic ground state. Consequently, the *Z*-isomer features a significantly shorter thermal lifetime. The ultrafast photoinduced dynamics after excitation to the $\pi\pi^*$ state at $\lambda_{\text{pump}} = 475$ nm

were followed by femtosecond absorption and fluorescence spectroscopy to obtain insight into the energetic order and nature of the excited states, which have been discussed controversially for years. The obtained transient absorption spectra for very early dynamics up to $\approx$ 300 fs feature a very fast rising and blue-shifting excited state absorption (ESA) band at $\lambda_{probe} \approx 570$ nm and in addition a delayed rise of the ESA bands at other detection wavelengths. Based on these observations, the subsequent quantitative analysis of the transient absorption- and fluorescence-time profiles was done in a global fashion using a consecutive kinetic model assuming a stepwise electronic deactivation and isomerization *via* an intermediate excited state. The fit of the transient absorption-time profiles yielded three time constants of

$$\begin{aligned}\tau_1 &= 0.08 \pm 0.03 \text{ ps},\\ \tau_2 &= 0.99 \pm 0.02 \text{ ps},\\ \tau_3 &= 6.00 \pm 0.10 \text{ ps},\end{aligned}$$

whereby τ_1 and τ_2 were also found in fluorescence. Therefore, τ_1 was assigned to the ultrafast radiationless deactivation of the initially excited $\pi\pi^*$ state to the intermediate $n\pi^*$ state. The electronic ground state is populated within τ_2 *via* the subsequent *E-Z* isomerization and deactivation. τ_3 describes the relaxation of vibrationally hot molecules in the electronic ground state. Since the measurements could not fully resolve the energetic order of the excited $\pi\pi^*$ and $n\pi^*$ states, two possible scenarios were proposed. In the first one the $\pi\pi^*$ state is higher in energy than the $n\pi^*$ state, in the second one the $\pi\pi^*$ state is energetically below $n\pi^*$ state. However, in both scenarios the $\pi\pi^*$ transition is the initially excited one. The interpretation of the data for DR1 in solution formed the basis for a time-resolved study on DR1 in polymer colloids.

To investigate the influence of intermolecular forces on the excited state lifetimes and the isomerization behavior of molecular switches, femtosecond fluorescence up-conversion spectroscopy was used to probe and compare the ultrafast dynamics of two AB derivatives in solution and in cross-linked polymeric micronetworks after excitation at $\lambda_{pump} = 475$ nm. The above DR1 was covalently attached as side chain of the 1:10 cross-linked polybutylmethacrylate (PBMA) colloids, whereas the bifunctional 4,4'-bis(acetamido)-azobenzene (BAAB) was covalently linked directly into the main chain of 1:10 and 1:50 cross-linked polymer networks (cf. Fig. 10.2). The obtained results reveal dramatic differences between the isomerization dynamics in solution and in the polymer. The excited state lifetimes in the polymer are drastically longer and can be controlled by varying the tightness of the surrounding matrix. In the case of DR1 the mean excited state lifetime increases by a factor of more than 10 from $\langle\tau\rangle = 0.5$ ps for the monomer in solution to $\langle\tau\rangle = 5.5$ ps for DR1 as side group in the polymer. Accordingly, the *E-Z* isomerization is substantially hindered by the increased microviscosity and mechanical forces in the cross-linked polymer compared to solution. Thus, the molecular motion on the excited

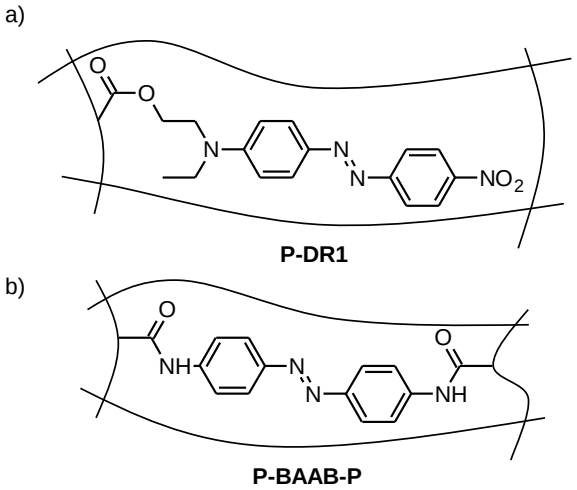

Figure 10.2: DR1 linked to the polymer side chain (P-DR1, a) and BAAB linked to the main chain of the polymer (P-BAAB-P, b).

potential energy surface en route to the conical intersection becomes more "diffuse". In effect, the large amplitude motion required for the *E-Z* transformation is slowed down. As expected, the influences on the photoisomerization dynamics of BAAB embedded into the main chain are even stronger. The lifetime of the photo-excited state increases strongly with increasing cross-linking ratio - the tighter the network, the longer the temporal fluorescence decay. The amplitude-weighted mean lifetime increases more than 20-fold from $\langle\tau\rangle = 3$ ps for BAAB in solution to $\langle\tau\rangle = 35$ ps for BAAB in the 1:50 cross-linked networks to $\langle\tau\rangle = 65$ ps for BAAB in the colloids with cross-linking ratio of 1:10. A fluorescence lifetime component of 430 ps with a relative amplitude of 12 % for the strongest cross-linked particles demonstrates that a sizable fraction of the molecules need almost 100-times longer to reach the electronic ground state. These results clearly show the effects of the strong mechanical restraining forces acting on the photo-excited AB in the tightly cross-linked polymer network.

To elucidate possible intramolecular interactions among chromophores, a systematic study on the photochemical properties of the two multi-azobenzene compounds bis[4-(phenylazo)phenyl]amine (BPAPA) and tris[4-(phenylazo)phenyl]amine (TPAPA) compared to the parent molecule 4-aminoazobenzene (AAB) was performed by means of static UV/VIS and NMR spectroscopy. The chemical structures of BPAPA and TPAPA are depicted in Fig. 10.3. The AB derivatives were synthesized by a less harsh variant of the Ullmann reaction and show a non-planar propeller-like configuration of the AB moieties around the central nitrogen in their electronic ground states. However, the twist angle is larger in TPAPA (42°) than in BPAPA (21°). The $\pi\pi^*$ absorption bands in the static UV/VIS spectra show a pronounced red-shift and an increase in intensity with increasing number of AB units, with the particularity that the observed effects are non-additive and more pronounced for BPAPA compared to AAB as for TPAPA compared to BPAPA, which strongly hints at specific intramolecu-

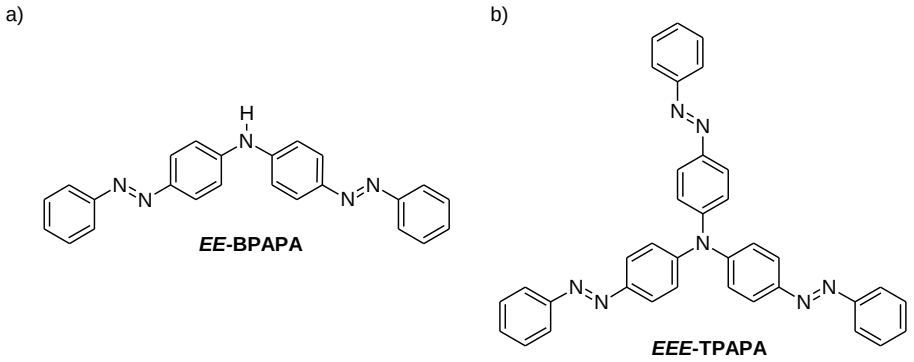

Figure 10.3: Schematic molecular structures of the respective all-*E* isomers of a) BPAPA and b) TPAPA.

lar interactions between the ABs. The three and four individual isomers of BPAPA (*EE*, *EZ*, *ZZ*) and TPAPA (*EEE*, *EEZ*, *EZZ*, *ZZZ*), respectively, were detected by 1D-^{1}H NMR and 2D-HSQC NMR experiments. The photostationary states (PSS385 for BPAPA and PSS455 for TPAPA) contain $\approx$ 20% of the all-*Z* isomer for BPAPA and $\approx$ 12% for TPAPA, which led to the conclusion that both BPAPA and TPAPA are efficient photoswitches. The thermal back-isomerization lifetimes of the two systems were also determined by 1D- and 2D-NMR spectroscopy at T = 35°C. The obtained kinetic profiles were analyzed using a consecutive kinetic model including the simultaneous back-reaction and formation of the respective isomers and yielded time constants of

$$\tau_{ZZ} = 0.5 \pm 0.1 \text{ h},$$
$$\tau_{EZ} = 2.4 \pm 0.2 \text{ h}$$

for BPAPA and of

$$\tau_{ZZZ} = 4.0 \pm 0.4 \text{ h},$$
$$\tau_{EZZ} = 6.4 \pm 0.9 \text{ h},$$
$$\tau_{EEZ} = 12 \pm 1 \text{ h}$$

for TPAPA. The thermal lifetime of the *Z*-isomer of AAB was determined under the same conditions by UV/VIS spectroscopy and was on the order of only $\approx$ 5 min. These drastic variances are related to the changes in the geometric and electronic structures of the molecules. The results on the electronic structures and the UV/VIS absorption spectra of AAB, BPAPA and TPAPA were supported by quantum chemical excited state calculations by J. B. Schönborn.

To understand the intramolecular chromophore-chromophore couplings between the AB units in BPAPA and TPAPA in more detail, femtosecond time-resolved broadband transient absorption and transient absorption anisotropy decay measurements were performed. A global analysis of the transient absorption data for BPAPA and TPAPA for parallel, per-

pendicular and magic angle pump-probe polarization after excitation at $\lambda_{pump} = 460$ nm yielded four time constants of

$$\tau_1 = 0.05 \pm 0.01 \text{ ps},$$
$$\tau_2 = 0.90 \pm 0.10 \text{ ps},$$
$$\tau_3 = 2.60 \pm 0.10 \text{ ps},$$
$$\tau_4 = 10.0 \pm 1.00 \text{ ps}$$

for BPAPA and

$$\tau_1 = 0.05 \pm 0.01 \text{ ps},$$
$$\tau_2 = 0.47 \pm 0.02 \text{ ps},$$
$$\tau_3 = 3.00 \pm 0.10 \text{ ps},$$
$$\tau_4 = 14.0 \pm 1.00 \text{ ps}$$

for TPAPA, respectively. The obtained decay times for each of the three polarizations for BPAPA as well as for TPAPA are virtually identical, whereas the relative amplitudes change depending on the pump-probe polarization. According to several previous studies, these results give reason to conclude that the relaxation to the electronic ground state of BPAPA and TPAPA are very similar to that of plain AB and AAB after $\pi\pi^*$ excitation. Therefore, the ultrashort 50 fs component was assigned to the transformation of the initially excited $\pi\pi^*$ state to the subsequent $n\pi^*$ state. The isomerization and radiationless deactivation to the electronic ground state occur within τ_2 and τ_3. The much slower process decaying with τ_4 belongs to the vibrational relaxation in the electronic ground state. Regarding the polarization dependent measurements, special attention was directed at the very early dynamics and the initial anisotropy values, which provide clear evidence for substantial electronic coupling between the two or three available AB units, respectively. The initial anisotropy value of $r(t) \approx 0.3$ for TPAPA is lower compared to that for BPAPA ($r(t) \approx 0.4$). The anisotropy decreases to values of $r(t) \approx 0.15$ for TPAPA and ≈ 0.3 for BPAPA on an instrument limited time scale of < 30 fs. The lower initial anisotropy for TPAPA as well as the ultrafast anisotropy decay to a value below 0.4 give unambiguous indication for electronic coupling and / or energy transfer between the ABs. The fact that the observed effects are more pronounced for the tris-AB compared to the bis-AB is in good agreement with previous theoretical and experimental studies, which have shown stronger intramolecular interchromophore coupling with increasing number of chromophores.

NI-PORPHYRIN BASED MOLECULAR SPIN SWITCH

The ultrafast dynamics of a magnetically bistable azopyridine functionalized Ni-porphyrin based molecular spin switch (*E*- and *Z*-Azo-NiTPPF$_{15}$) and its respective building blocks, the metal porphyrin NiTPPF$_{20}$ and the

metal free porphyrin H_2TPPF_{20} were followed by means of femtosecond time-resolved transient absorption spectroscopy after Q_y band excitation at $\lambda_{pump} = 520$ nm. The chemical structures of *E*- and *Z*-Azo-NiTPPF$_{15}$ are given in Fig. 10.4. Previous studies revealed that this molecule shows

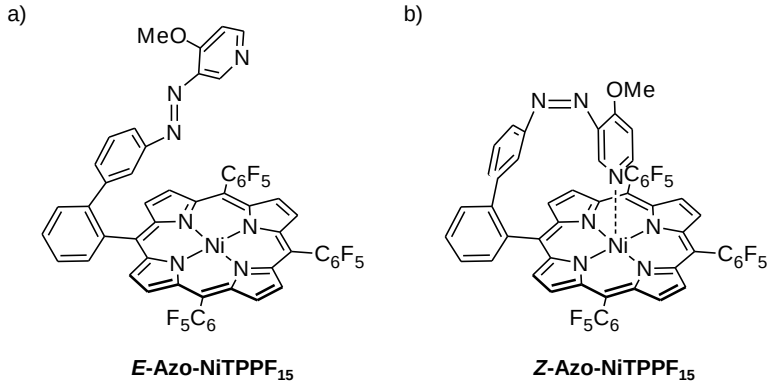

Figure 10.4: Schematic molecular structures of the respective all-*E* isomers of a) BPAPA and b) TPAPA.

magnetic bistability in solution at room temperature. The ground state of the four-coordinate *E* isomer is diamagnetic, whereas the ground state of the five-coordinate *Z* isomer was found to be paramagnetic. The magnetic state of the Ni(II) ion can be reversibly switched by the photo-induced $E \rightleftarrows Z$ isomerization of the azopyridine moiety and the resulting coordination or decoordination of the pyridine nitrogen.

The principle aim of the study performed in this Thesis was to obtain insight into the mechanisms of the photo-induced coordination of the azopyridine nitrogen and the resulting spin switch from low-spin (*E*-Azo-NiTPPF$_{15}$) to the high-spin state (*Z*-Azo-NiTPPF$_{15}$) of the Ni(II) ion. The results for H_2TPPF_{20} and $NiTPPF_{20}$ are very complex but could be analyzed and interpreted on the basis of published studies on the photochemical properties and the molecular dynamics of other metal and metal free porphyrin derivatives. In the case of H_2TPPF_{20}, the deactivation of the initially populated Q_y to the vibrationally excited Q_x state occurs within a few tens of femtoseconds. The subsequent vibrational relaxation occurs on the picosecond time scale and is followed by two very slow (nanoseconds) intersystem crossing steps to a lower triplet state and finally to the electronic ground state. S_1 / Q_y band excitation of the macrocycle of $NiTPPF_{20}$ only affects the porphyrin system while the d system of the Ni(II) ion initially remains in its $(d_{z^2})^2$ configuration. Afterwards, the energy is transferred into the metal ion within less than one picosecond leading to a $|S_0, {}^{1,3}(d,d)\rangle_{hot}$ singlet or triplet state with the porphyrin probably already back in its electronic ground state. The subsequent vibrational relaxation of the metal excited states occurs within ≈ 5 ps and causes a pronounced blue-shift of the respective ESA bands. Finally, this semi-excited $|S_0, {}^{1,3}(d,d)\rangle$ state shows the Ni-porphyrin specific derivative-shaped transient absorption bands and decays slowly on a

time scale of hundreds of picoseconds. The analysis of the obtained results for the *E*-Azo-NiTPPF$_{15}$ and *Z*-Azo-NiTPPF$_{15}$ turned out to be difficult, especially regarding a possible switching process. The broad and intense superimposed positive and negative transient absorption bands of the porphyrin macrocycle itself over the whole spectral detection range made it nearly impossible to find and analyze possible contributions of the AB unit, which could give an indication of (spin) switching and formation of the desired product. In addition, the derivative shaped absorption bands of the Ni(II) should be different for the four- and the five-coordinate reactant and product, respectively, but a comparison of these bands did not give any evidence on a spin switch of the system. Therefore, the results for the four-coordinate *E*-Azo-NiTPPF$_{15}$ were found to be virtually identical to those of NiTPPF$_{20}$ and were interpreted in the same way. Compared to NiTPPF$_{20}$ and *E*-Azo-NiTPPF$_{15}$, the electronic ground state of *Z*-Azo-NiTPPF$_{15}$ is a high-spin $|S_0, {}^3(d_{z^2}, d_{x^2-y^2})\rangle$ state and the electronic relaxation to the ground state occurs *via* a $((d_{z^2})^2)^*$ state and a triplet state of the metal system and the porphyrin, respectively. Despite these changes, no switching and decoordination could be observed for *Z*-Azo-NiTPPF$_{15}$, although the intermediate $((d_{z^2})^2)^*$ state should be repulsive towards axial ligands. A study on the dynamics of the four different molecules after excitation of the supposed $\pi\pi^*$ absorption band of the AB at $\lambda_{pump} = 320$ nm yielded similar results as obtained for the excitation at $\lambda_{pump} = 520$ nm and the entire spectrum was governed by the porphyrin absorption bands. Regarding these results, further investigations on the isomerization mechanism will be necessary to elucidate the details of this complex process.

PROTON TRANSFER SWITCH

A time-resolved study on the ultrafast dynamics of the bistable excited state intramolecular proton transfer (ESIPT) switch N-(3-pyridinyl)-2-pyridinecarboxamide (NPPCA) was performed following excitation at $\lambda_{pump} = 264$ nm in acetonitrile and water as aprotic and protic solvent, respectively. The molecular structures and the suggested reaction scheme of the switch after UV excitation are shown in Fig. 10.5. In water, the intramolecular

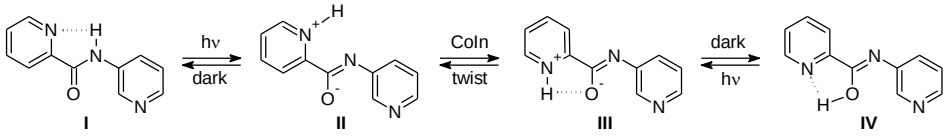

Figure 10.5: Molecular structures and reaction scheme of NPPCA after excitation in the UV.

proton transfer can be excluded, whereas it can be expected in acetonitrile. The interpretation of the data was supported by ab initio excited state calculations of A. Sobolewski and co-workers on this system. A combination of the obtained computational and experimental results provides insight

into the reaction pathway of the photo-excited keto tautomer of NPPCA **I** and the stepwise formation of the desired proton transfer product **IV** in the aprotic solvent. A global analysis of the transient absorption-time profiles yielded time constants,

$$\tau_1 = 0.10 \pm 0.01 \text{ ps},$$
$$\tau_2 = 0.50 \pm 0.01 \text{ ps},$$
$$\tau_3 = 5.80 \pm 0.40 \text{ ps},$$
$$\tau_4 = 20.0 \pm 1.00 \text{ ps}.$$

The two fast components τ_1 and τ_2 were also found in the analysis of the fluorescence-time profiles, whereas the longer processes decaying with τ_3 and τ_4 were only found in absorption. τ_1 was assigned to the relaxation out of the Franck-Condon region of the initially populated $\pi\pi^*$ state of **I**. The subsequent proton transfer to the excited enol tautomer **II** and the practically barrierless deactivation to the electronic ground state of **II** and / or **III** occur within τ_2. The S_1-S_0 conical intersection was found at a twisted configuration of the pyridine moiety linked to the carbonyl group. The processes decaying with τ_3 as well as τ_4 belong to the dynamics of **II** and **III** in the electronic ground state and the formation of the final product **IV**. τ_4 is the dominant contribution in all absorption traces, which also features a delayed rise time of τ_2 as would be expected for the observed excited state lifetime of 0.5 ps. The existence of transient absorption bands at $\lambda_{\text{probe}} > 700$ nm and at at $\lambda_{\text{probe}} = 247$ nm also with the main decay time of τ_4 confirms the assignment of τ_4 to the dynamics on the ground state potential energy hypersurface. Additionally, the absorption band at $\lambda_{\text{probe}} > 700$ nm is in good agreement with the calculated energy differences of ≈ 1 eV for the involved configurations of **II** and **III** in the electronic ground and excited states. The stepwise intramolecular formation of the final enol form **IV** is revealed by a permanent non-decaying absorption of the product at $\lambda_{\text{probe}} = 247$ nm. In water, where the intramolecular proton transfer is prevented, no long-lived permanent absorption at $\lambda_{\text{probe}} = 247$ nm and no absorption at detection wavelengths above $\lambda_{\text{probe}} > 700$ nm can be observed.

10.2 OUTLOOK

The obtained results form the basis for several ongoing and future works regarding the ultrafast dynamics of molecular switches in complex environments, chromophore-chromophore interactions, spin switches and proton transfer switches.

The photoswitching behavior and the ultrafast dynamics of promising molecular switches such as the bridged AB derivative dihydrodibenzodiazocine, which was designed in our work group, should be investigated in future in complex environments by means of static and time-resolved spectroscopies. Due to strong intramolecular forces in this system, the photoswitching efficiency and the isomerization quantum yields are much

higher compared to unsubstituted AB and the molecular dynamics are strongly accelerated. The diazocine can be covalently linked to the main chain of polymer colloids with different cross-linking ratios and embedded in amorphous glass films to obtain insight into the dynamics under the influence of competing intra- and intermolecular forces. The variation and the increasing of the dye content will hopefully allow for the investigation of additional interchromophore interactions. The syntheses and the characterization of the colloidal particles is already planned in collaboration with W. Richtering and co-workers.

In the multi-azobenzene compounds BPAPA and TPAPA, direct electronic coupling between the AB moieties is enabled *via* the nitrogen linker. Substitution of the nitrogen by a carbon would prevent the direct coupling. Another possibility is to add a boron instead of the nitrogen as an electron accepting core. In any case, the electronic structure of these system will be completely different. This allows for a systematic "core-dependent" study on possible intramolecular interchromophore interactions. Furthermore, the details of the molecular structure and the symmetry of TPAPA on Au(111) have been investigated by means of scanning tunneling microscopy (STM) (cf. Gopakumar, T. G.; Davran-Candan, T.; Bahrenburg, J.; Maurer, R. J.; Temps, F.; Reuter, K.; Berndt, R. *Angew. Chem.* **2013**, *125*, 1-5.). Further measurements of TPAPA on Ag(111) surfaces are underway in cooperation with the group of R. Berndt.

Since the observation of the photo-induced spin switch of Ni(II) in the azobenzene functionalized porphyrin has not yet given definite results, other molecules without a porphyrin backbone and with nickel as well as iron ions should be investigated in collaboration with the group of F. Tuczek. The static absorption spectra of these systems are mainly dominated by the absorption bands of the switch (e.g. AB) itself. Therefore, it would be easier to observe and analyze the respective transient signals regarding the switching of the molecular chromophore and the resulting switch of the spin state.

The unambiguous clarification of the reaction mechanism and the formation of different intermediate products and the final proton transfer product of the investigated ESIPT switch NPPCA will be possible with a UV-pump/IR-probe experiment, which is currently under construction in our laboratory. The aim of this project is to develop new bistable photoreversible proton transfer switches, which allow for proton transfer cascades in close collaboration with A. Sobolewski.

DANKSAGUNG

An erster Stelle möchte ich mich ganz herzlich bei meinem Doktorvater Prof. Friedrich Temps für die engagierte Betreuung und großartige Unterstützung während der gesamten Zeit bedanken. Seine motivierende und begeisternde Art, sein Glaube an die Sache und sein großes Interesse, auch an den ganz kleinen Fortschritten, haben diese Arbeit so erst möglich gemacht.

Der gesamten Arbeitsgruppe Temps danke ich für die schöne Zeit, das nette Arbeitsklima und die große Hilfsbereitschaft.

Ganz besonders möchte ich mich bei Ron Siewertsen für seine geduldige Einführung in das Thema und das Arbeiten im Labor bedanken. Ohne das Praktikum bei dir und deine wertvolle Hilfe hätte ich diese Arbeit vermutlich nie angefangen. Für zahlreiche Diskussionen und die Zusammenarbeit möchte ich mich außerdem bei Falk Renth bedanken.

Ganz großer Dank gilt Katharina Röttger für das schönste Büro (LMS8), die gute konstruktive Zusammenarbeit, die große Unterstützung in jeder wissenschaftlichen und nichtwissenschaftlichen Lage, die ausgeprägte Heiterkeit, das viele Lachen und ganz besonderes für eine tolle Freundschaft. Mayra Stuhldeier danke ich ebenfalls für ihre Hilfe, ihre Freundschaft und dafür, dass sie sich immer um alles (wichtige) gekümmert hat. Außerdem danke ich Alexander Thrun für seine Spaßigkeit, die "witzigen" Witze und dafür, dass wir Freunde sind. Vielen Dank ihr Drei - Es hat mir großen Spaß gemacht!

Außerdem bedanke ich mich bei Katharina und Anja Köhntopp für die gute Zeit im zweitschönsten Büro (MES1).

Ich möchte mich ganz herzlich bei Felix Plamper und Prof. Walter Richtering für die gute Zusammenarbeit, die wertvollen Diskussionen und die schöne und lehrreiche Zeit in Aachen bedanken. Besonders Felix danke ich dafür, dass er mich geduldig in die Welt der Synthese und Charakterisierung von Polymeren eingeführt hat und mir jederzeit mit Rat und Tat zur Seite gestanden hat.

Prof. Frank Sönnichsen danke ich für die vielen NMR Messungen, für die Hilfe bei der Auswertung der Daten und für die zahlreichen Diskussionen.

Großer Dank gilt Jan Boyke Schönborn, Ole Carstensen und Prof. Bernd Hartke für die Beantwortungen meiner Fragen und für die durchgeführten Rechnungen.

Special thanks to Prof. Andrzej Sobolewski and his co-workers for the interesting molecule and the important calculations.

I would like to thank Thiruvancheril Gopakumar and Prof. Richard Berndt for the fruitful collaboration and for introducing me to the importance of switches on surfaces and STM measurements. It was a pleasure to work with you.

Marcel Dommaschk und Prof. Rainer Herges danke ich für die mühevolle Synthese und das stete zur Verfügung stellen des "Plattenspielers".

Ich danke Prof. Christian Näther für das Lösen der Kristallstrukturen und die gute Zusammenarbeit.

Den Praktikanten, Bachelorstudenten und HiWis, Dennis Bank, Jessica Bahr, Hendrik Böhnke, Mats Bohnsack, Mark Dittner und Claudia Sievers danke ich für ihre tatkräftige Unterstützung.

Den technischen Mitarbeitern der Werkstatt und des Instituts danke ich für die schnelle und kompetente Hilfe bei allen großen und kleinen Projekten und die fachliche und persönliche Beratung in jeder Lebens- und Institutslage.

Bei unseren Sekretärinnen Ursula von der Heydt und Tanja Sharif bedanke ich mich für das schnelle Lösen aller kleinen und großen nichtwissenschaftlichen Probleme.

Für das Korrekturlesen der Arbeit bedanke ich mich bei Katharina Röttger, Hendrik Böhnke, Anja Köhntopp und Rebecca Marschan.

Bei meinen Freunden und bei meiner Familie bedanke ich mich für schöne Stunden, angenehme Abwechslungen und das große Verständnis. Besonderes großer Dank geht dabei an: Michelle und Christian, Käthe, Thrun, Mayra, Inga, Martin, Maren, Jenny, Lena, Mäddi, Betti, Nana und Paul mit Oskar und Madlen und Christian.

Bei meinen lieben Eltern bedanke ich mich für den bedingungslosen Rückhalt, den Glauben an mich, das immer offene Ohr und für das schöne Gefühl immer gerne nach Hause zu kommen.

Nicht zuletzt möchte ich mich bei Adrian bedanken. Um es kurz zu machen: Vielen, vielen Dank für alles. Du bist der Beste. Kocham cię.